767 1968b

NATIONAL AERONAUTICS AND SPACE ADMINISTRATION

Technical Report 32-1264

Surveyor VII Mission Report Part II. Science Results

Prepared by:

The Surveyor Investigator Teams, Scientific Evaluation Advisory Team, and Working Groups

JET PROPULSION LABORATORY
CALIFORNIA INSTITUTE OF TECHNOLOGY
PASADENA, CALIFORNIA

March 15, 1968

Technical Report 32-1264

Surveyor VII Mission Report Part II. Science Results

Prepared by:

The Surveyor Investigator Teams, Scientific Evaluation Advisory Team, and Working Groups

JET PROPULSION LABORATORY
CALIFORNIA INSTITUTE OF TECHNOLOGY
PASADENA, CALIFORNIA

March 15, 1968

TECHNICAL REPORT 32-1264

Copyright © 1968

Jet Propulsion Laboratory

California Institute of Technology

Prepared Under Contract No. NAS 7-100 National Aeronautics & Space Administration

Scanned and PDF created by the Space Imagery Center, Lunar and Planetary Laboratory University of Arizona, Tucson, AZ January 22, 2020.

Preface

This three-part document constitutes the Project Mission Report on Surveyor VII, the last spacecraft in a series of unmanned lunar soft-landing missions.

Part I of this Technical Report consists of a technical description and an evaluation of engineering results of the systems used in the *Surveyor VII* mission. Part II presents the scientific data derived from the mission, and the scientific analyses conducted by the *Surveyor* Scientific Evaluation Advisory Team, the *Surveyor* Investigator Teams, and the Associated Working Groups. Part III consists of selected pictures from *Surveyor VII* and appropriate explanatory material.

Results given in this report are based on data evaluation prior to March 15, 1968. It is expected that future evaluation and analysis of the *Surveyor VII* data will provide additional science results.

Contents

I.	Introduction	1
	Reference	4
II.	Principal Science Results From Surveyor VII	5
III.	Television Observations From Surveyor VII	9
	A. Television Camera	9
	B. Categories of Pictures Taken	. 10
	C. Location and Topography of Landing Site	. 11
	1. Location of Landing Site	. 11
	2. Orientation of Spacecraft	. 15
	3. Topography of Landing Site	. 15
	D. Geology of Landing Site	. 23
	1. Regional Geologic Setting	. 23
	2. Geology of Area Around Spacecraft	. 28
	3. Detailed Geologic Features Observed From Surveyor VII	. 44
	4. Photometric Observations of Lunar Surface	. 62
	5. Polarimetric Observations of Lunar Surface	. 62
	6. Interpretation of Geologic Observations	. 66
	E. Observations of the Earth	. 72
	References	. 75
IV.	Lunar Surface Mechanical Properties	. 77
	A. Spacecraft Landing	. 77
	1. Description	. 77
	2. Observations of Spacecraft/Soil Interactions	. 80
	3. Simulations and Analyses	. 98
	B. Post-Landing Spacecraft/Soil Interactions	. 111
	1. Bearing Strength From Sensor Head Imprints	. 111

Contents (contd)

	2. Bearing Strength From Rock Drop Test	1
	C. Soil, Rock, and Terrain Characteristics	21
	1. Rock Size and Distribution	21
	2. Rock Hardness	28
	3. Rock Fractures	31
	4. Terrain Characteristics	31
	D. Summary and Preliminary Conclusions	32
	References	33
٧.	Soil Mechanics Surface Sampler	35
	A. Lunar Surface Operations	35
	1. Subsystem Description	35
	2. Functional and Operational Description	38
	3. Mission Description	44
	B. Data Analysis	59
	1. Discussion of Tests	69
	2. Preliminary Analyses and Results	83
	C. Summary	84
	References	85
VI.	Lunar Surface Thermal Characteristics	87
	A. Thermophysical Properties of Landing Site, as Determined From	0-
	Earth-Based Observations	
	C. Spacecraft View of Lunar Surface	
	D. Compartment, Solar Panel, and Planar Array Antenna Data	
	E. Calculation of Lunar Surface Temperatures	
	F. Results and Comparisons	
	G. Discussion	
	References	U
VII.	Lunar Surface Electromagnetic Properties	09
	A. Radar Reflectivity Analysis	09
	1. Signal-Strength Data	0

Contents (contd)

	2. Cross Section as a Function of Beam Incidence Angle
	3. Tracks of Beams on Lunar Surface
	4. Comparison With Other Surveyor Flights
	B. Magnet Data
	1. Purpose and Design Description
	2. Data
	3. Laboratory Studies
	4. Interpretation and Conclusions
	References
VIII.	Chemical Analysis of the Moon at the Surveyor VII Landing Site: Preliminary Results
	A. Instrument Description
	1. General
	2. Characteristics of the Surveyor VII Alpha-Scattering Instrument 242
	B. Mission Description
	1. Pre-Launch Operations at Cape Kennedy
	2. Launch and Landing
	3. Post-Landing Operations
	C. Results
	1. Background Data
	2. Standard-Sample Data
	3. Sample 1 Data
	4. Sample 2 Data
	5. Sample 3 Data
	D. Discussion
	References
IX.	Lunar Theory and Processes
	A. Geologic Setting
	B. Discussion of Chemical Analyses
	1. Contrasts in Albedo
	2. Estimated Density of Lunar Surface Rocks

Contents (contd)

	3. Bulk Composition of the Moon										•		. 286
	4. On the Thermal Regime in the Moon												. 287
	5. On Chondritic Meteorites and the Moon												. 288
	6. On Tektites												. 289
	7. Solar System Implications						٠						. 290
	C. Rock Types												. 290
	D. Surface Material												. 303
	E. Post-Sunset Horizon "Afterglow"								٠				. 308
	References												. 312
X.	Post-Landing Tracking Data Analysis . F. B. Winn	•			•							٠	. 315
	A. Tracking Data Acquisition		٠										. 315
	B. Tracking Data Validity and Weighting $$.												. 317
	C. A Priori Parameter Constraints	٠			•	•		*					. 317
	D. Lunar Ephemerides												. 318
	E. Parameter Solution Vector												. 319
	F. Observed Minus Computed Residuals			٠					,	,			. 321
	G. Conclusions												. 326
	References									•	•		. 327
XI.	Laser Beam Pointing Tests	٠									٠		. 329
	A. Laser Transmitting Stations						٠						. 330
	B. Schedule of Lunar Tests												. 330
	C. Detection of Laser Beams						•						. 331
	D. Conclusions												. 331
	References		٠										. 334
XII.	Astronomy											٠	. 337
Арр	endix. Surveyor Science Teams and Cogn	izo	n	P	ers	on	ne	١.					. 341

I. Introduction

R. H. Steinbacher and L. D. Jaffe

Surveyor VII was launched from Cape Kennedy, Florida, at 06:30:00.54 GMT on January 7, 1968, using Atlas/Centaur launch vehicle 15. Surveyor and Centaur were placed in a parking orbit, from which Surveyor was injected into a lunar trajectory. Centaur/Surveyor separation occurred at 07:05:16 GMT. The spacecraft mass at injection was 1038.4 kg; after final touchdown, 305.7 kg.¹

The launch system guidance parameters, which require a long lead time before launch, were set for a trajectory to the area of Hipparchus (approximately 5°E longitude, 5°S latitude); the science landing site, selected as the most significant scientifically, was the ejecta blanket north of the rim of the crater Tycho, more than 1000 km to the southwest of Hipparchus.

At 23:30:10 GMT on January 7, a midcourse maneuver was executed, directing the spacecraft to the Tycho landing site, 11.37°W longitude and 40.87°S latitude. To place *Surveyor* within the site required that the trajectory be corrected to within 15-km radius at the moon. Although a second midcourse maneuver was anticipated,

midcourse tracking data indicated that the single maneuver had provided adequate trajectory correction.

The main retro ignition of the terminal descent occurred at 01:02:14 GMT, and resulted in a normal touchdown on the lunar surface at 01:05:36.3 GMT on January 10, 1968. Immediately after touchdown, a brief engineering interrogation was made; then a series of 200-line television pictures was transmitted to assist in positioning the spacecraft's planar array antenna toward earth accurately enough to transmit 600-line television pictures. To allow maximum use of time for the science experiments, all engineering sequences within the first few hours after touchdown were shortened. The first 600-line picture was received at 03:41:47 GMT.

Inflight radio tracking data gave an estimate of 11.41°W longitude and 41.01°S latitude for *Surveyor's* landed position. The position, determined by matching features on *Lunar Orbiter V* photographs with *Surveyor VII* pictures,² was 11.41°W longitude and 40.95°S latitude, according to Orthographic Atlas coordinates (Ref. I-1).³ Post-landing

¹A midcourse maneuver consumed about 4.2 kg of fuel; the propellant, main retro-engine case, altitude marking radar, and other hardware expended during the retro and touchdown sequences were responsible for the remaining 728.5-kg loss.

²Lunar Orbiter V, frame H-128, framelet 266, approximately half-way across the frame.

³Position determination by E. A. Whitaker, University of Arizona; see Section III of this Report.

tracking data placed the *Surveyor* at 11.53 ± 0.03 °W longitude and 40.86 ± 0.05 °S latitude in inertial coordinates.

The *Surveyor VII* payload (Fig. I-1), the most advanced of the *Surveyor* series, included:

- (1) A television camera.
- (2) An alpha-scattering instrument.
- (3) A surface-sampler instrument.
- (4) Three auxiliary mirrors to observe special areas of vernier-engine jet gas impingement on the surface, crushable block contact with the surface, and alphascattering-instrument deployment area.
- (5) A stereo mirror to provide a surface of stereoscopic coverage convenient for surface-sampler operations.
- (6) Seven dust mirrors to indicate whether lunar surface material was deposited on the spacecraft as a result of vernier-engine firing.
- (7) Magnets attached to two footpads and installed in the door of the surface-sampler scoop.

The television camera took 21,038 pictures. Of these pictures, 20,993 were transmitted during the first lunar day; the remaining 45 were transmitted during the second lunar day.

During the alpha-scattering-instrument operations, more than 100 hr of data were recorded, including analyses of three lunar samples: (1) the undisturbed lunar surface, (2) a rock, and (3) the disturbed lunar surface. During the first lunar day, more than 66 hr of data were recorded; at least an additional 34 hr of data were obtained on the disturbed surface during the second lunar day.

The sensor head of the alpha-scattering instrument was not deployed normally to the lunar surface on command, but remained in the background position, suspended on a nylon cord about 55 cm above the lunar surface. To assist the deployment procedure, the surface sampler performed operations that involved turning the alpha-scattering instrument, pinning it against spacecraft support members, and pushing it downward in a series of steps. The sensor head was deployed to the surface in good operating condition by the surface sampler, which was later used to pick up the sensor head and move it to two new sample positions on the lunar surface, and to trench the surface to provide a sample of subsurface material for chemical analysis. These operations demonstrated the versatility of the surface sampler as a remote manipulation tool.

Various types of data on mechanical properties and the density of the lunar surface material were obtained by the surface sampler, which performed static and dynamic bearing tests; trenching operations; rock extraction, weighing, and breaking. Some of these tests were made after sunset to take advantage of added torque from cold motors.

The magnets installed on the surface-sampler scoop made repeated contacts with the surface and accumulated some magnetic particles. At the completion of one drag test, a large particle was lifted from the surface by these magnets.

The altitude marking radar and radar altimeter and doppler velocity sensor (RADVS), used for terminal guidance and landing of the spacecraft, provided data on the surface microwave reflectivity.

A test of techniques was conducted for pointing narrow laser beams from earth to a specific site on the moon using the television camera as a detector. The beams were successfully recorded, during the period January 19 through 21, from two stations on several separate occasions.

The post-sunset television operation began at 06:06 GMT on January 25 when the sun set on the television camera, and extended 15 hr after local sunset at the end of the first lunar day. When the sun had set on the eastern terrain, the solar corona pictures were taken to as far as 50 solar radii; many of these pictures were taken through polarizing filters. Earth pictures and star surveys were taken throughout the first lunar day and during the post-sunset period.

Thermal data were taken with engineering interrogations until operations were terminated at 14:12 GMT on January 26, 80 hr after sunset.

Operations on the second lunar day began at 19:01 GMT on February 12, 1968, and continued until 12:24 GMT on February 21.

All Surveyor pictures may be obtained from the National Space Science Data Center, Goddard Space Flight Center, Greenbelt, Maryland. Individual pictures can best be identified by the day of year and GMT at which they were taken. January 10 was Day 010; February 21 was Day 052. Mosaics can best be identified by catalog number.

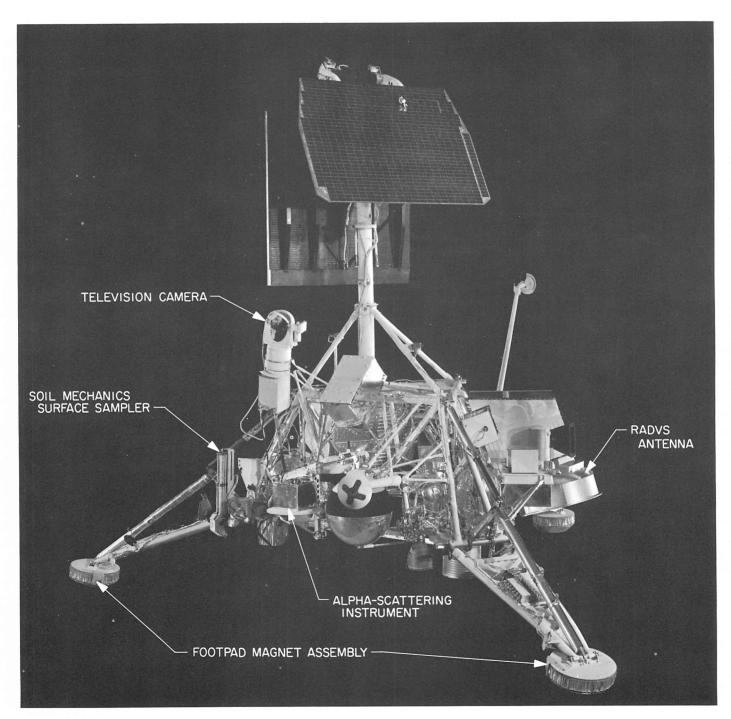


Fig. I-1. Surveyor VII spacecraft model in landed configuration. The alpha-scattering and surface-sampler instruments are in stowed positions. The hood on the television camera shown in this picture is not the box configuration actually flown on Surveyor VII. Also not shown is the stereo mirror, which is located at the base of the antenna mast.

Reference

I-1. Orthographic Atlas of the Moon, Supplement 1 to the Photographic Lunar Atlas, compiled by D. W. G. Arthur and E. A. Whitaker, University of Arizona Press, Tucson, Ariz., 1961.

Acknowledgment

E. M. Christensen, JPL, was responsible for an important portion of the organization and execution of the *Surveyor VII* science effort. A Filice, J. Strand, and D. Smythe, JPL, were responsible for site selection evaluation; J. Strand was responsible for television science data handling. S. Grotch, JPL, was responsible for the nontelevision science data handling. R. Hill, JPL, furnished facilities and support for the participating scientists.

II. Principal Science Results From Surveyor VII

L. D. Jaffe, C. O. Alley, S. A. Batterson, E. M. Christensen, S. E. Dwornik, D. E. Gault, J. W. Lucas, D. O. Muhleman, R. H. Norton, R. F. Scott, E. M. Shoemaker, R. H. Steinbacher, G. H. Sutton, and A. L. Turkevich

The rim of the crater Tycho, believed by scientists to be the most interesting highland area, was chosen as the *Surveyor VII* landing site. The selection of this particular site was made because the area around the rim of Tycho was thought to be the youngest sample of highland material; it was also believed possible that this material originated at depth and was ejected during the formation of the crater.

The exterior rim of Tycho consists of a belt of terrain, 80 to 100 km wide, that differs in topography, albedo, color, radar reflectivity, thermal characteristics, and other physical properties from the surrounding highland terrain. Extending outward a distance of 10 to 15 km is a ring characterized by hummocky topography and high luminance (high albedo, 16 to 17%). From 15 to about 40 km, the surface is marked by numerous subradial ridges and valleys superimposed on a broadly undulating surface and with a lower albedo (13 to 14%). Surveyor VII landed in this area, about 30 km north of the rim crest of Tycho. In the vicinity of the spacecraft are many smaller-scaled, irregular hillocks and swales.

Lunar Orbiter V photography shows that the rim of Tycho is composed of debris, presumably ejected from depth during the crater's formation, and a sequence of

flows that form mappable geologic units, several of which are visible from the *Surveyor VII* television camera. The flows range from those that appear to have been emplaced as highly viscous, steep-fronted flows to very fluid, low-viscosity, smooth-surface flows that have collected on the floors of closed depressions. *Surveyor VII* landed on one of the flows whose surface is composed of irregular, low hills and depressions ranging from 100 m to several hundred meters across with scattered blocks, small craters, and swarms of north-trending fissures that occur on the flow's crest.

A great variety of rock fragments is scattered about on the surface in the landing site area. Some of these fragments contain vesicles; others contain bright, irregular spots of various sizes and shapes. Most of the fragments appear to be dense, coherent rock; others appear less dense and porous. The surface rocks appear to have been subjected to an erosive, or abrasive, action; one of the rocks turned over by the surface sampler was smooth on the exposed side and angular on the subsurface side.

The size-frequency distribution of the fragmental debris determined from the *Surveyor VII* pictures indicates the average grain size is coarser at the *Surveyor VII* site than at the other *Surveyor* landing sites. Per unit area,

more fragments larger than 4 cm were observed at the Surveyor VII site than at the Surveyor VI site; however, no subsurface fragments of centimeter dimensions were observed in the material excavated by the surface sampler.

The distribution of small craters, 15 cm to 2 m, is similar to the distribution of small craters of this size observed at previous *Surveyor* sites; however, there are fewer craters larger than 8 m at the *Surveyor VII* site than observed at the previous sites, which indicates a young age for the Tycho rim material.

Photometric measurements made from the Surveyor VII pictures show the normal luminance factor of the undisturbed, fine-grained material near the spacecraft to be 13.4%, whereas the rock fragments scattered over the lunar surface are lighter and have estimated normal luminance factors ranging from 14 to 22%. The material ejected by the spacecraft footpads and excavated by the surface sampler is darker and has a normal luminance factor estimated to be 9.6%. Similar differences between the optical properties of the surface and subsurface material have been noted at all Surveyor landing sites. Its occurrence in different geological provinces, such as the lunar maria and highlands, suggests that the difference in luminance of the subsurface and surface material is not dependent on the intrinsic properties of local bedrock.

Polarimetric observations of the fine-grained material near *Surveyor VII* revealed a maximum polarization of 7 to 8% at 90- to 100-deg phase angles. This polarization of light, at a resolution of a few square centimeters, is similar to telescopic measurements which integrate over 100 km². Various rock surfaces, however, showed maximum polarization effects ranging from that of the fine-grained material at a 100-deg phase angle to a maximum of 30% polarization at a 120-deg phase angle. The variation in the rock polarization properties suggests variations in mineralogy and texture, or similar rocks covered with increasing amounts of fine-grained dust, or both.

The soil at the *Surveyor VII* site resembles that of the previous sites, since it is predominantly fine-grained, granular, slightly cohesive, and partially compressible; the static strength, and probably the density, increases with depth. The density of one typical surface rock fragment lies between 2.4 and 3.1 g/cm³, which is in the range of common, solid terrestrial rocks and is consistent with

estimates based on the chemical analysis. If the soil grains are derived from the rocks, the grains themselves cannot be highly porous. One rock fragment was broken by a moderately strong impact by the surface sampler.

On previous *Surveyor* missions, lunar soil adhered to spacecraft components primarily following the firing of the vernier rocket engines. During the *Surveyor VII* landing, lunar soil was thrown against an auxiliary mirror and adhered to it. Adhesion of the soil to the inside of the surface-sampler scoop was also observed. The adhesion seemed to increase with time during the first lunar day.

The bearing capacities of the lunar surface at the *Surveyor VII* landing site are:

At a depth less than 1 cm: 0.2×10^5 dynes/cm² (from imprint of alpha-scattering-instrument sensor head).

At depths of 2 to 5 cm: 2×10^5 to 3×10^5 dynes/cm² (from imprints of crushable block and footpads, and from surface-sampler operations).

These bearing capacities are in general agreement with results from previous *Surveyor* landings.

The surface sampler made it possible for the alphascattering instrument to analyze three lunar samples: (1) undisturbed lunar surface, (2) a small rock, and (3) a disturbed area exposing subsurface material. Within the present experimental errors, the composition of all three samples is similar to that of the mare material examined during the *Surveyor V* and *VI* missions, except that the amount of the iron group of elements (Ti to Ni) is significantly less in the highland samples than in those examined in the maria.

Whereas the maria were found to have a basaltic composition with a high iron content, the *Surveyor VII* chemical analysis may be grossly characterized as a basaltic composition with a low iron content. The chemical data from *Surveyors V*, *VI*, and *VII* clearly contradict a lunar origin for most meteorites. Moreover, although the origin of the material analyzed by the alpha-scattering instrument on *Surveyor VII* is subject to varied interpretations (i.e., impact and/or volcanic), these new data, together with results from *Surveyors V* and *VI*, establish that the moon is not an undifferentiated body of chondritic composition. The analyses are strong circumstantial evidence that some melting and chemical fractionation of lunar material has occurred in the past. The bulk composition of the moon, however, remains obscure. The lower iron

³The normal luminance factor of the undisturbed material on the maria varies from 7.3 to 8.2%; for the disturbed material, from 5.5 to 6.1%.

content for the highlands suggests a significantly lower rock density than that of the mare material, and may also provide an explanation for the albedo differences between the two major geologic units on the moon.

The presence of magnetic constituents, comparable in amounts to those found at the mare sites of *Surveyors V* and *VI*, was indicated by the magnet test of the soil near *Surveyor VII*. In addition, during the surface-sampler operations, a centimeter-size object was observed to adhere to a magnet attached to the door of the surface-sampler scoop. Objects possibly attracted in this manner include rocks containing significant amounts of magnetite or iron-bearing meteorites.

Lunar surface temperatures after sunset, obtained from spacecraft thermal data, were different in two directions viewed. An effective thermal parameter of about 240 was indicated in the direction of a nearby group of large blocks; a value of 385 was obtained for the area that did not contain the large blocks. The difference in the two values is qualitatively consistent with the supposition that the blocks are solid rocks. In contrast, the thermal parameter value obtained from Surveyors I, III, V, and VI was the same (about 500) in the two directions after sunset. The earth-based (telescope) thermal parameter value for the Surveyor VII region was 700; the difference between this value and those obtained from the spacecraft is comparable to the results from the previous Surveyors. Also in agreement with previous spacecraft, directional thermal emission from the lunar surface was clearly indicated and is qualitatively consistent with earth-based data.

Measured values of the radar signal strengths at a wavelength of 2.5 cm during descent from about 20 km to touchdown indicate that the angular dependence of the radar backscattering function in the Tycho region exterior to the crater is similar to that observed for the average lunar surface with earth-based radars. Assuming that this dependence is the same as that observed from the earth at 3.6-cm wavelength, the values of the angular cross sections observed suggest that the material radar reflectivity in the Tycho region is from 50 to 100% greater than that for the average moon. If this result is interpreted in the conventional way, we conclude that the effective dielectric constant in this region is in the range from 3.2 to 4.5, as compared with the earth-based result of 2.8 for the average moon.

A comparison of radar data from all *Surveyor* flights shows that the reflectivity at all observed angles is approximately twice as large for the rim flank of Tycho as for the mare regions. In general, a comparison of the angular reflectivities for the *Surveyor* flights over mare regions with those from the average moon from earthbased measurements shows that the effective dielectric constant is slightly below that of the mean lunar value.

A test for directing narrow, continuous laser beams from earth to a specified area on the lunar surface was successful. The two laser beams emitted from Kitt Peak and Table Mountain were detected by Surveyor; each beam transmitted about 1 W and yet appeared comparable in brightness to Sirius (magnitude, -1.4).

Observations of the faint outer (F) corona were conducted 8 to 14 hr after sunset. Seven pictures were obtained in polarized and unpolarized light, the later ones recording the coronal image to about 50 solar radii (12 deg). This is some five times farther than obtainable from eclipse photography, and 50% farther than earlier Surveyor data. It covers the previously unobserved transitional region between the solar corona and the inner zodiacal light.

III. Television Observations From Surveyor VII

E. M. Shoemaker (Principal Investigator), R. M. Batson, H. E. Holt, E. C. Morris, J. J. Rennilson, and E. A. Whitaker

Surveyor VII, the last spacecraft of the Surveyor series, successfully landed at 01:05:36 GMT, January 10, 1968, on the outer rim flank of the large crater Tycho, in the southern part of the moon. The spacecraft landed about 30 hr after local lunar sunrise and transmitted about 21,000 pictures during the remainder of the first lunar day of operation. On January 22, after local sunset, almost 700 pictures were taken of the earth, the sun's corona, and parts of the lunar surface illuminated by earthlight. On February 12, Surveyor VII was revived for operation on the second lunar day approximately 120 hr after local lunar sunrise. The camera was then operated in the 200line (low-resolution) mode because of loss in horizontal sweep in the 600-line (high-resolution) mode. About 45 pictures were taken in the 200-line mode during the second lunar day.

During the first lunar day, the *Surveyor VII* camera was operated extensively over the Goldstone, California; Canberra, Australia; and Robledo, Spain (near Madrid), Tracking Stations of the Deep Space Network; most of the pictures were received at the Canberra Station.

A. Television Camera

The television camera on *Surveyor VII* (Fig. III-1) is almost identical to that flown on *Surveyor VI* (Ref. III-1); in particular, a redesigned mirror assembly, first used on the *Surveyor VI* camera, was incorporated on the *Surveyor VII* camera. As on the *Surveyor VI* camera, the filter wheel in the mirror assembly contains three polarizing filters in place of the color filters used on *Surveyors I, III*, and *V*.

The polarizing filters on the Surveyor VII camera are glass-laminated, linearly polarizing, dichroic-type (KN-36) filters with transmission axes oriented successively at 0, 45, and 90 deg when they are rotated into the optical path. The 0-deg filter transmission axis is parallel to the mirror surface and perpendicular to the plane containing the mirror normal and the camera optical axes. As the filter wheel is an integral part of the mirror assembly, the orientation of the polarizing filters remains fixed with respect to the camera mirror and rotates with respect to the picture format during azimuth rotation of the mirror assembly. For a camera oriented vertically, the filter orientations are horizontal, at 45 deg, and vertical with

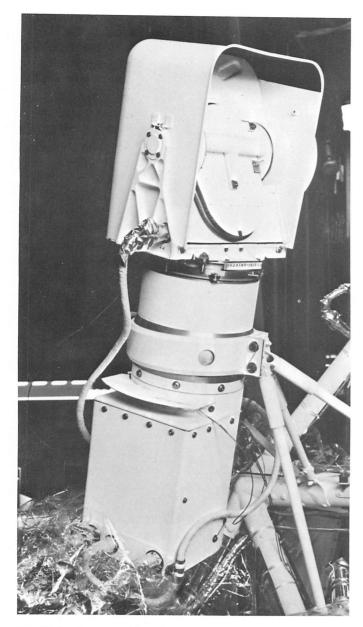


Fig. III-1. Surveyor VII television camera hood and mirror assembly. The mirror is open and reflects the image of the lens and filter-wheel assemblies. The hood, mirror, and filter-wheel assembly rotate in azimuth as a unit.

respect to a level horizon projected onto the plane of the vidicon target. In order that no iris changes would be required for pictures taken at different filter positions for a given field of view, the fourth position of the filter wheel is occupied by a piece of optical glass with an Iconel coating of sufficient density that the transmission of the clear-filter position is equal to that of the polarizing filters.

Surveyor VII was equipped with a 9- by 24-cm mirror, which was attached to the spacecraft mast and oriented

to provide a reflected view, as seen from the television camera, of a small area in front of the spacecraft within the operations area of the surface sampler. Stereoscopic pictures were obtained by recording direct images of this area and images reflected from the mirror.

The dynamic range and sensitivity of the Surveyor VII camera are slightly less than those of the Surveyor VI camera. The total range of response of the Surveyor VII camera, like the previous Surveyor cameras, is about 1,000,000 to 1, which is achieved by the combined use of various apertures and exposure times.

The resolution and quality of the pictures transmitted by the Surveyor VII camera are comparable to the resolution and quality of the pictures received from Surveyors V and VI.

B. Categories of Pictures Taken

An estimated 20,993 pictures were taken during the first lunar day of Surveyor VII operations (Table III-1). The first sequence, taken shortly after touchdown, consisted of 15 pictures taken in the 200-line mode; 20,978 pictures were taken in the 600-line mode.

Table III-1. Categories of pictures taken by Surveyor VII television camera

Type of survey	Approximate number of pictures during first lunar day	Approximate number of pictures ^b during second lunar day
Wide-angle panoramas ^a	1,323ª	
Narrow-angle panoramas	9,697	25
Stereo mirror	236	6
Polarimetric surveys	3,170	
Focus ranging	1,177	
Shadow progression	155	
Earth	472	
Laser test	358	
Stars	103	
Surface-sampler operations area	700	4
Surface-sampler operations	1,600	
Special area, magnet, and alpha- scattering-instrument surveys	1,902	10
Solar corona	100	
Total	20,993	45
alncludes fifteen 200-line pictures.	•	

b200-line pictures.

To record surface detail at a wide variety of angles of solar illumination, both narrow- and wide-angle panoramas were taken. Specially prepared command sequences were used to take pictures, under varying illumination, of the stereo mirror area, both directly and through the mirror; of the surface-sampler operations area; of the shadow of the spacecraft as it moved toward the horizon, late in the lunar day; and of special areas in which the contact of the spacecraft with the lunar surface is visible. Focus ranging surveys were taken, from which the detailed topography of the surface around the spacecraft has been measured along selected profiles. The polarizing properties of the surface material are being studied with pictures that were taken of selected target areas through each of three polarizing filters.

Numerous pictures of the earth were taken through polarizing filters at intervals throughout the lunar day to study the polarization of light scattered from the earth; pictures were also taken, using polarizing filters, of the solar corona after sunset. Other special pictures were taken of stars for determination of spacecraft orientation and of the area for deployment of the alpha-scattering instrument. An unusual sequence of pictures was taken to detect the radiation from lasers on earth, which were aimed through telescopes at the *Surveyor VII* landing site (see Section XI of this Report).

Television activity on the second lunar day was restricted because of difficulties with the camera and the spacecraft power system. About 45 pictures were taken, however, in the 200-line mode (Table III-1). During the lunar night, leg 1 compressed; the resulting tilt revealed, just north of the spacecraft, an area of large blocks which previously had been partially obscured by the electronics compartments. Approximately 25 pictures were taken of this previously obscured area.

C. Location and Topography of Landing Site

As in the Surveyor I, III, and VI missions, the combined data from the Surveyor pictures and from high-resolution Lunar Orbiter photographs has led to the discovery of the precise location of the landed Surveyor VII spacecraft and has permitted a much more complete analysis of the topography and geology of the landing site than would have been possible from the Surveyor data alone. We have drawn heavily, therefore, on data contained in the Lunar Orbiter photographs of the Tycho region, as well as on the Surveyor VII pictures, in the preparation of this report. Our confidence in the use of the Lunar

Orbiter data is based on Whitaker's identification of the Surveyor VII landing site in the Lunar Orbiter photographs (described below).

1. Location of Landing Site

The coordinates of the aiming point for the Surveyor VII spacecraft (Fig. III-2) were 40.87°S latitude, 11.37°W longitude, near the center of Lunar Orbiter V high-resolution photograph H-128. This point is the approximate center of the smoothest area on the rim flank of Tycho for which Lunar Orbiter high-resolution photographs were available.

From interim reduction of tracking data, the best estimate of the spacecraft's landed position was 40.96°S, 11.43°W, 3 km SSW of the aiming point (Fig. III-2). Further evidence used for precise location of the landed spacecraft was provided by the doppler radar beam, which swept the lunar surface from the northwest as the spacecraft approached its landing point (Fig. III-2). A broad enhancement of the reflected radar signal was observed to be centered some 4 km northwest of the landed position. Assuming the tracking coordinates to be fairly accurate, this enhancement was probably produced by reflections from the slope H-H (Fig. III-2).

From an examination of a complete wide-angle mosaic, and a narrow-angle mosaic of the horizon taken with the *Surveyor VII* television camera early in the lunar day, it was apparent that the horizon on the southeast, south, west, and northwest lay near the spacecraft and lacked easily identifiable features. In the remainder of the panorama, however, well defined ridges along the horizon, as well as several distant craters, rocks, and other features, could be recognized. Some of the features that were critical in the location of the landing site are shown in Fig. III-3.

On the basis of their apparent smoothness, ridges A, B, C, and E (Fig. III-3) were considered to lie at distances of not less than about 1 km. Initially, it was thought that ridge C, as seen from *Surveyor* (Fig. III-3) might be ridge D in the *Lunar Orbiter* photographs (Figs. III-2 and III-4). After further work, it became apparent that this was not the case, and the spacecraft's probable position was eventually narrowed down, after concentrated study, by the identification of rock G on the *Lunar Orbiter* photograph (Fig. III-4). Crater F was next identified, and then several other rocks and craters at different azimuths. Careful plotting of these azimuths on the *Lunar Orbiter* photograph allowed the *Surveyor* location to be pinpointed to within a few meters.



Fig. III-2. Part of Lunar Orbiter V photograph M-126. Aim point, tracking location (white crosses), and actual location (white circle) of Surveyor VII are indicated. The locations of features identified in Fig. III-3 are shown by corresponding letters. The dashed line r-r-r represents path swept by the doppler radar beam.

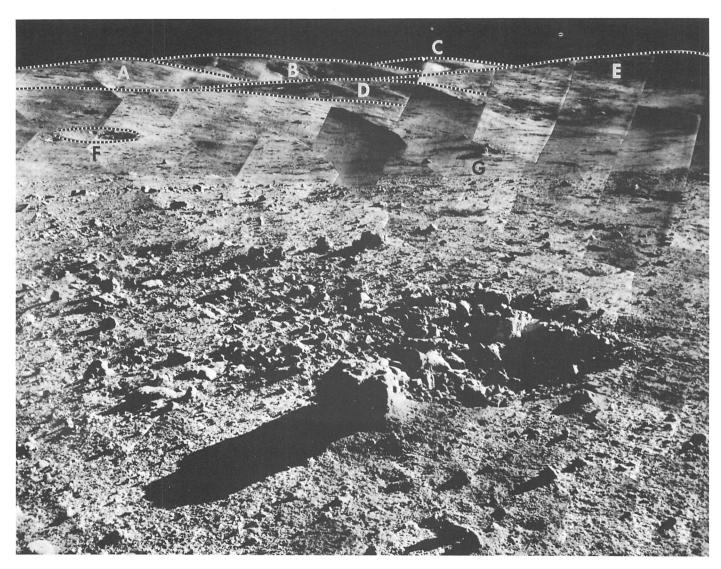


Fig. III-3. A mosaic of Surveyor VII narrow-angle pictures of the north-to-northeast part of the panorama. The locations of the lettered features are shown in Fig. III-2 on Lunar Orbiter V photograph M-126 and in Fig. III-4 on Lunar Orbiter V photograph H-128.

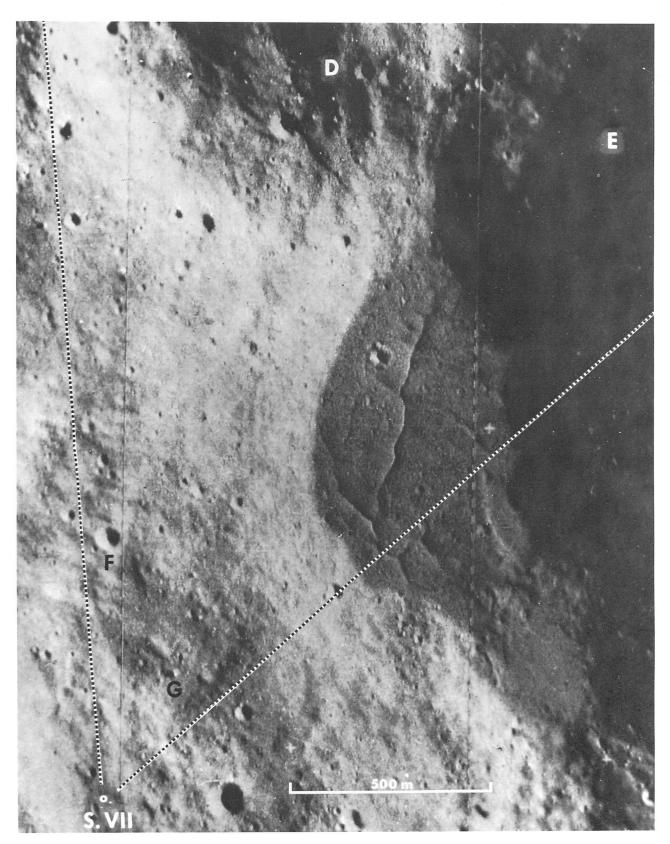


Fig. III-4. Enlargement of part of Lunar Orbiter V photograph H-128 showing the Surveyor VII landing site and nearby terrain. Lettered features correspond to those shown in Figs. III-2 and III-3.

Further study of the pictures led to the identification of ridges A, B, C, D, and E on the *Lunar Orbiter* photograph (Fig. III-2). Ridge C is 21 km from the spacecraft, a distance that is not apparent from an examination of the panorama alone.

By carefully plotting the position of the landed Surveyor VII on the Orthographic Atlas of the moon, the best estimate of the coordinates of the spacecraft is 40.95°S latitude, 11.41°W longitude, less than 1 km from the tracking position.

2. Orientation of Spacecraft

The orientation of the spacecraft on the lunar surface was determined from measurement in the television pictures of the positions of the earth, Jupiter, and the star Rigel in Orion; from the angular settings of the solar panel sun sensor; from the positional tuning of the spacecraft's planar array antenna; and from gyro data at touchdown. A solution for the orientation of the spacecraft, based on the integrated results of these measurements, indicates the spacecraft was tilted 3.17 deg at an azimuth of 349 deg from lunar north during the first lunar day. The -Y axis of the spacecraft was found to be oriented 20.23 deg west of north. As there is a slight difference (0.92 deg) between the camera 0-deg azimuth and the spacecraft -Y axis, the 0-deg azimuth of the camera was oriented 19.3 deg west of north. These estimated angles may have errors on the order of 1 deg.

3. Topography of Landing Site

Surveyor VII landed on the outer flank of the rim of the crater Tycho (Fig. III-5), one of the most prominent and well known features in the lunar highlands. The rim crest of the crater rises to an average height of about 2.5 km above the surrounding highland terrain; as the highland terrain surrounding Tycho is complex, and includes many close-spaced large craters, no widespread, natural level surface is present with which the elevation of the rim may be readily compared. The average exterior slope on the rim of Tycho is only a few degrees, but a variety of hills and valleys, with local steep slopes, is characteristic of much of the rim flank.

Near the crest and extending outward a distance of 10 to 15 km, the rim of Tycho is composed of irregular hills and intervening depressions (Fig. III-6), which give it a bumpy or hummocky appearance at the telescope. From 15 km to a radial distance of about 35 to 40 km, the surface of the rim is marked by numerous subradial ridges and valleys superimposed on a broadly undulating

surface. Surveyor VII landed about 30 km north of the rim crest of Tycho on the part of the rim flank marked by these linear ridges. Individual linear ridges are typically 2 to 5 km in length and ½ to 1 km in width. The broader undulations on which this ridge and valley pattern is developed have dimensions of 5 to 20 km. Some of these undulations clearly reflect ancient craters that have been buried, or partly buried, by the rim materials of Tycho. Still farther from the rim crest of Tycho the outline and form of buried ancient craters become more easily discerned, but these ancient features are also sculptured with smaller subradial ridges and valleys to distances as great as 100 km. This fine sculpture is evidence that the rim materials of Tycho extend at least as far as 100 km from the rim crest.

The local relief in the vicinity of the spacecraft is about 160 m (Fig. III-7). A narrow, north-trending ridge, about 2.5 km long, 0.5 km wide, and 90 m high, lies 1.5 km northeast of the spacecraft. An irregular, north-trending valley, several kilometers long, lies about 1 km to the east; another, much longer valley lies about 2 km to the west. Within the regional pattern of north-south ridges and valleys, the terrain consists mainly of irregular hillocks and swales.

The horizon, as seen from the *Surveyor VII* camera, is less than 200 m distant to the east, south, and west. The local surface slopes to the north, however, and much more distant features can be seen in that direction.

In the immediate vicinity of the Surveyor VII landing site, the Tycho rim terrain may be subdivided into several topographically distinctive units on the basis of detailed surface characteristics (Fig. III-8). These terrain units correspond, in part, to geologic units discussed below. The most widespread of the terrain units extends several tens of kilometers north and west of Surveyor VII. It is a rather smooth surface, as revealed in the Lunar Orbiter V high-resolution photographs, and is marked by a pattern of closely spaced shallow ridges and grooves. Individual ridges and grooves are typically a few hundred meters long, less than 100 m in width, and have amplitudes of several meters. The ridges and grooves are aligned mainly in three dominant orientations, and they give a strongly patterned appearance to the surface, as seen in the Lunar Orbiter V photographs.

Less extensive terrain units occur to the south and east of *Surveyor VII*. A unit of a very smooth, undulating terrain with irregular boundaries extends for a distance of about 4 km along the valley southeast of the spacecraft.

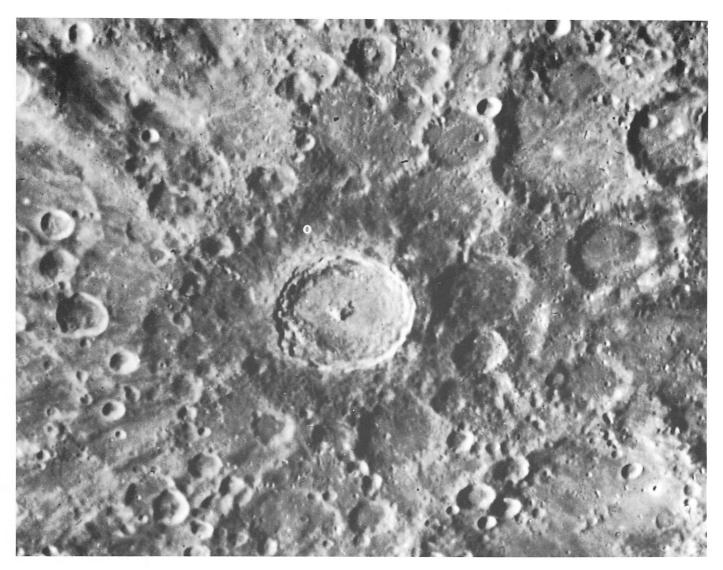


Fig. III-5. Lick Observatory photograph of Tycho. Note the bright, inner ring and dark halo around Tycho, and numerous small secondary craters extending outward from Tycho beyond the dark halo. The Surveyor VII landing site is indicated by the white circle.

Several distinct units of bumpy, blocky terrain, some forming pronounced ridges, extend 5 to 10 km south of the spacecraft. These units have the form and pattern of viscous flows.

Another distinctive class of terrain occurs widely in small local patches on the rim of Tycho. This terrain class is composed of nearly level, flat areas, the surfaces of which are locally marked by branching systems of sinuous grooves (Fig. III-7 and III-8); these flat areas are, in all cases, the floors of local closed depressions. Over a large part of the outer rim flank of Tycho, each closed depression larger than about 1 km² has such a level, flat floor. These flat floors strongly resemble terrestrial

playas¹, and we will refer here to the flat floors of closed depressions on the moon as *lunar playas*. One of the larger lunar playas on the northern flank of the rim of Tycho lies about 1 km northeast of the *Surveyor VII* spacecraft. It is about 0.8 km long and 0.5 km wide.

The lunar playas probably are formed by transportation and deposition of material in fluid or fluidized form onto the bottoms of the closed depressions, but we do not mean to imply, in using the name *playa*, that the fluids involved in this deposition were necessarily aqueous.

¹Playa (pla'ya), the flat-floored bottom of an undrained desert basin. Webster's New Collegiate Dictionary, 1953.

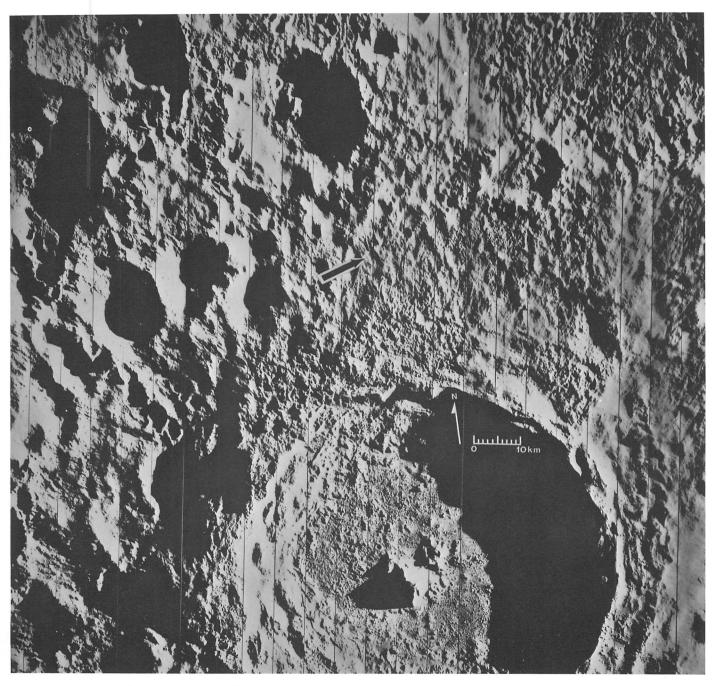


Fig. III-6. Lunar Orbiter V photograph M-127 of the crater Tycho and its northern flank. The arrow points to the Surveyor VII landing site.



Fig. III-7. Part of Lunar Orbiter V photograph H-128 showing the area around the Surveyor VII landing site. The arrow points to the location of the spacecraft. Compare with Figs. III-8 and III-12.

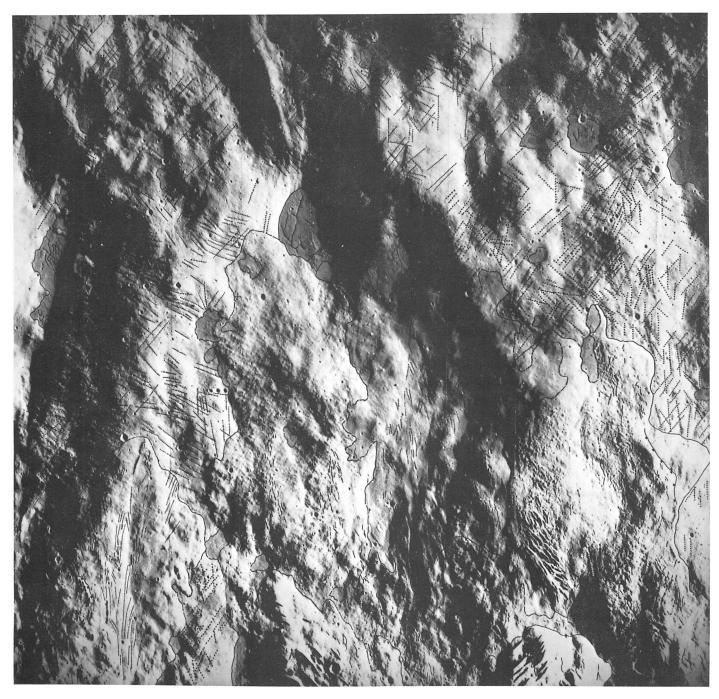


Fig. III-8. Part of Lunar Orbiter V photograph H-128 of an area on north rim of Tycho showing geologic features around Surveyor VII. See Fig. III-12 for explanation of annotations.

In addition to the lunar playas, other small, relatively smooth patches of terrain occur in the general vicinity of the *Surveyor VII* landing site. These patches are generally a few hundred meters across; they occur on benches as well as in very small, closed depressions. The surfaces of these patches are somewhat rougher than the surfaces of the playas, and they do not exhibit sinuous grooves. The smooth patches may, however, be related in origin to the playas.

Small craters are ubiquitous features of the landscape around Surveyor VII, but they are not nearly as abundant or conspicuous as on the lunar maria. The areal density of craters larger than 10 m in diameter is less than that observed on the maria. The largest craters within a radius of a few hundred kilometers of the landed spacecraft are about 100 m in diameter; the largest nearby crater visible from the Surveyor VII camera is about 75 m in diameter. Nearly all craters larger than a few tens of meters in diameter have sharply formed, raised rims and an approximately conical interior form. Craters smaller than about 10 m in diameter show a wide variety of forms; many of them are markedly elongate. The craters vary in abundance from one terrain unit to another.

In addition to craters, small fissures are a widespread feature of the landscape near *Surveyor VII* and occur in the terrain units that resemble flows. Typical fissures range from 50 to 150 m in length and from 5 to 10 m in width. In general, they are north-trending, parallel with the long direction of the flows, and tend to be clustered on the flow crests.

Detailed study of the topographic features of the *Surveyor VII* landing site is being conducted by a combination of techniques, including stereophotogrammetric methods, focus ranging, shadow measurement, and correlation of features identifiable in the *Lunar Orbiter V* photographs and *Surveyor VII* pictures.

Stereoscopic pictures, from which a very detailed reconstruction of the surface can be made, were taken of a small 0.25-m² area near the spacecraft by means of the small mirror mounted on the spacecraft mast near the camera. The mirror permitted pictures to be taken from two different points of perspective, as the point of intersection of the camera mirror rotation axes is separated from the virtual image of this point in the stereo mirror by about 1 m (Fig. III-9). Because the effective perspective center of the camera swings around the camera mirror axes, the effective points of perspective, both in the direct view and in the view reflected by the mirror on

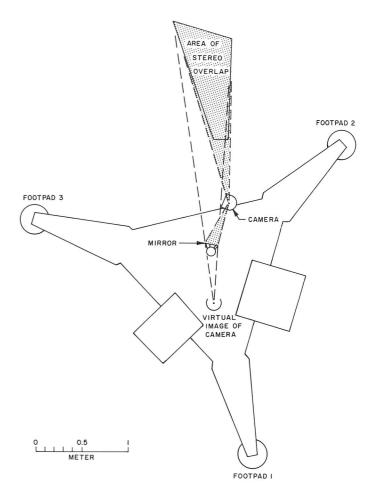


Fig. III-9. Geometry of area observed stereoscopically with the Surveyor VII stereo mirror. The surface in the stereoscopic overlap area is viewed directly by the camera and indirectly from a position corresponding to the virtual image of the camera in the mirror. This sketch has been simplified and does not show the effect of the camera mirror, which also reflects the field of view. Rotation of the camera mirror produces slight displacements of perspective centers, which vary with camera azimuth and elevation.

the mast, move with each motion of the camera mirror. Stereoscopic pairs of pictures with more than 35 possible combinations of relative orientations of the perspective points and lines of sight can be taken of the limited area reflected in the mirror on the mast.

The convergence of rays from the two perspective centers to an object on the surface varies between 50 and 250 mrad (about 3 to 14 deg). Test measurements of angles have been made with *Surveyor* pictures as accurately as ± 1 mrad (Ref. III-2). If there were no error in the

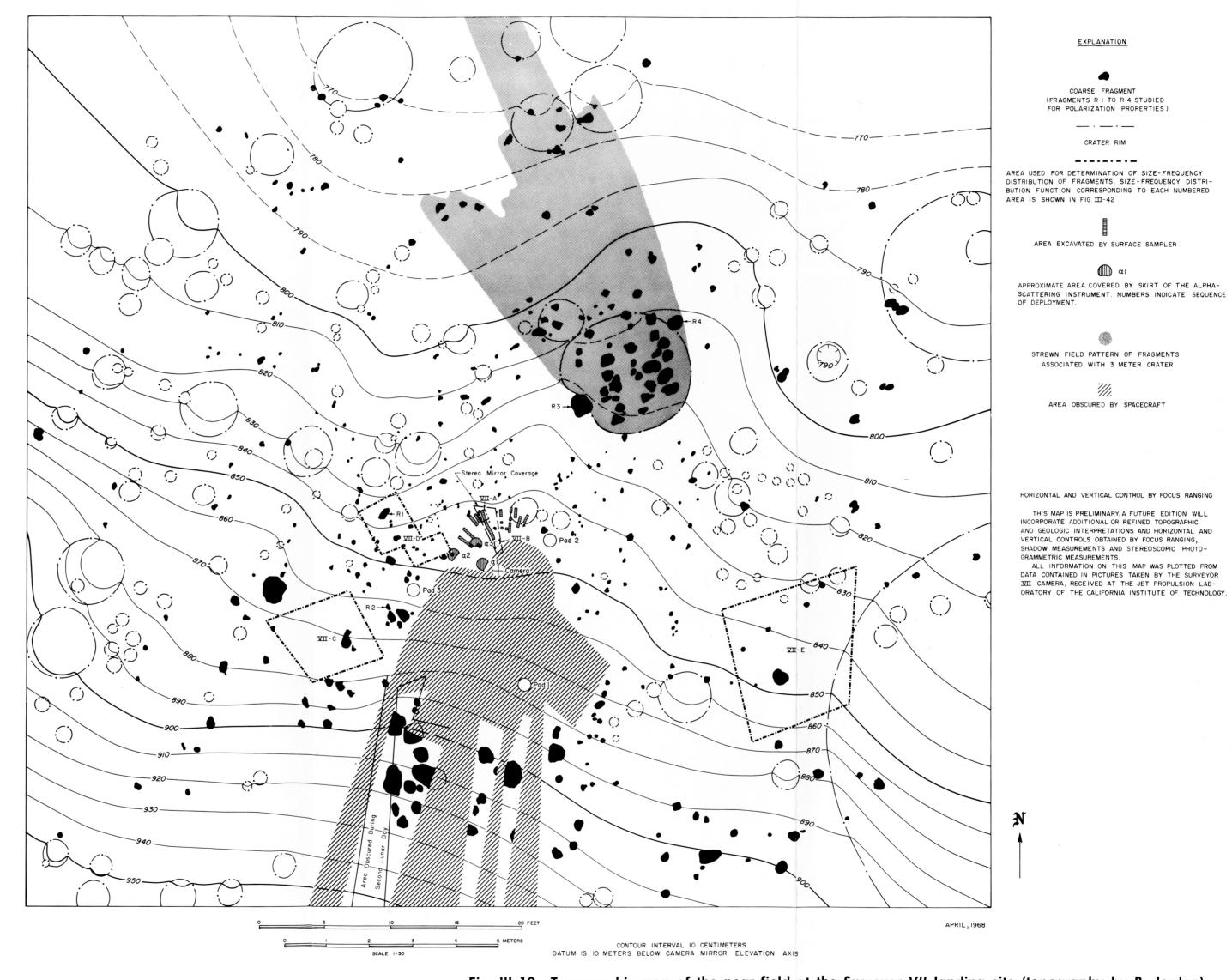


Fig. III-10. Topographic map of the near field at the Surveyor VII landing site (topography by R. Jordan).

JPL TECHNICAL REPORT 32-1264

determination of perspective point relative locations, measurement of distances from the camera would be accurate to about $\pm 0.4\%$ where convergence is 250 mrad, and about $\pm 2\%$ where convergence is 50 mrad.

Stereoscopic measurements can be made analytically, one point at a time, through the use of computer methods (Refs. III-3 and III-4). This method is tedious, but is being used in two modes for maximum efficiency. The first mode is used for the compilation of a generalized map of the entire stereo mirror area, and will require the annotation, computation, and plotting of approximately 500 data points. The part of the lunar surface reflected in the Surveyor VII stereo mirror lies between 1.7 and about 3 m from the camera. The accuracy with which individual measurements can be made of the distance from the camera to the surface varies from ± 7 mm to ±60 mm, depending on convergence. Convergence is a function of the location in the area of stereoscopic overlap of the surface to be measured. It will be practical to make the generalized map of the entire stereo mirror area with a contour interval of about 50 mm.

The second mapping mode involves the parts of the stereo mirror area that contain features of special interest, including surfaces disturbed by the surface sampler. Those features located in areas where convergence is large and which are included in a single pair of stereoscopic pictures are being mapped with contour intervals as small as 5 mm, enabling computation of approximate volumes of excavations and fragments. This mapping mode requires the computation and plotting of 50 to 100 data points per stereoscopic pair.

A generalized topographic map of the area within 10 m of the spacecraft was prepared by focus ranging (Fig. III-10). This technique utilizes pictures taken at nine or more focus settings at each camera elevation position along a given azimuth. Small areas in best focus in each picture are located on a mosaic of pictures taken at specific focus settings; the azimuth and elevation of the centers of each small area in best focus are determined by graphical measurement. The location of a point on the lunar surface with respect to the intersection of the camera mirror rotation axes is computed from azimuth, elevation, and calibrated focus distance. Focus-ranging surveys, consisting of about 75 pictures each, were taken along 14 camera azimuths during the Surveyor VII mission.

The preliminary focus-ranging map (Fig. III-10) shows that the spacecraft is resting on a gently concave surface

that has an average tilt of about 5 deg to the north. On the north side of the spacecraft, the surface is tilted away from the camera nearly 4 deg; on the east side, it is tilted away about 1.5 deg; on the south side, it is tilted about 6 deg, and on the west side, about 2 deg toward the spacecraft. Contour lines were interpolated in several areas where control is not available. The interpolation was roughly linear; no attempt was made to guess the shape of contour lines on surfaces obscured to the camera. The contour lines in the vicinity of footpad 1, for example, would require a larger spacecraft tilt than is actually observed. This anomaly could be explained if the footpad were resting in a small crater invisible to the camera.

The area near the spacecraft is littered with blocks and fragments; only the largest blocks were plotted on the map. A strewn field of blocks extending northwest of a crater about 5 m from the spacecraft is shown with a pattern. An area south of the spacecraft is also littered with blocks that may be associated with a crater obscured by the spacecraft. Most of this area was not visible to the camera during the first lunar day; the compression of leg 1 during the first lunar night allowed 200-line pictures to be taken of part of the previously obscured area during the second lunar day.

D. Geology of Landing Site

1. Regional Geologic Setting

The crater Tycho is one of the youngest, large ray craters on the moon (Fig. III-11) and is surrounded by the most conspicuous and extensive system of bright rays on the sub-earth side of the moon. The relatively young age of Tycho and its associated rim deposits and rays can be established from the superposition of these rays on a large number of other geologic units.

Both the form and the geology of the crater interior and Tycho's exterior rim appear to be representative of other large ray craters. As revealed in *Lunar Orbiter V* photographs, the details of the crater are strikingly similar to those of Aristarchus and Copernicus. Tycho seems to be the youngest of these three craters; the topographic and geologic details are less modified by still younger, superposed, small craters. Tycho has, therefore, become the type or standard area in which to study the detailed geological features of a large ray crater.

The crater of Tycho is about 85 km in diameter; the crater floor lies about 4½ km below the average level of

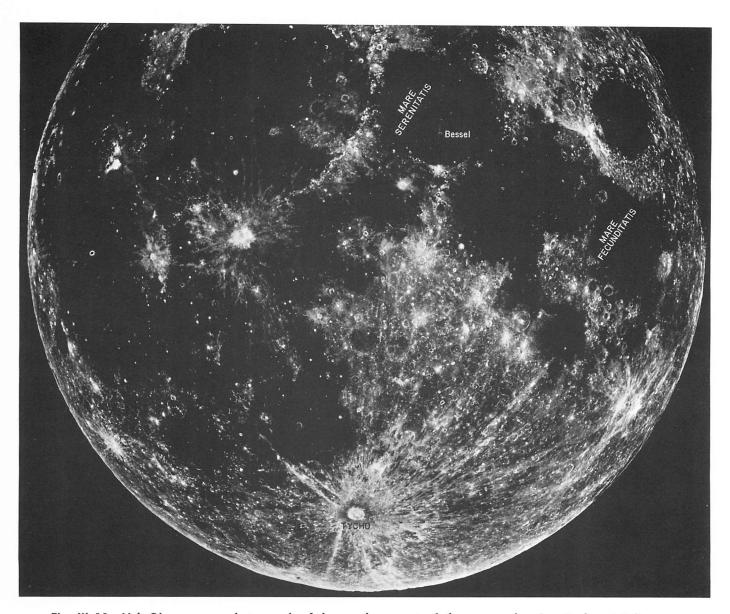


Fig. III-11. Lick Observatory photograph of the southern part of the moon showing Tycho at full moon.

the rim crest. A prominent central peak rises more than 2 km above the level of the floor, and subordinate hills are nestled against the northeast side of the peak. Along the wall of the crater is a well developed series of terraces, or steps, that are easily observed at the telescope. In these general topographic characteristics, Tycho is similar to a number of other craters of about the same size, such as Copernicus, Theophilus, and Aristoteles.

Among the most remarkable features revealed by the *Lunar Orbiter* photographs are extensive flows that extend down the terraced crater wall of Tycho and a major

flow that occupies the floor of the crater and surrounds the central peaks. This major flow forms a broad, approximately level, but very rough, surface on the floor of the crater. It is now recognized that the similar parts of the floors of other large ray craters probably also have been formed by flows. In detail, the large flow in the floor of Tycho is extensively fissured and cracked and appears to be partly draped or folded around small hills of preflow material protruding from the floor.

The exterior rim of Tycho comprises a belt of terrain 80 to 100 km wide that differs in topography, albedo, color, radar reflectivity, thermal characteristics, and other

physical properties from the surrounding highland terrain. This belt is underlain by a complex sequence of rim deposits. They are divisible, on the basis of both topography and albedo, into several distinct geologic facies, which form a series of concentric rings around the crater.

The inner ring is asymmetric with respect to the crater rim and is widest on the north side. This ring is characterized by irregularly hummocky topography and a high albedo (16 to 17% normal luminance factor, Ref. III-5). Within this ring are many well developed flows, some as long as 8 km. Surveyor VII landed a few kilometers north of one of the most distinctive of these flows recognizable in the Lunar Orbiter V photographs.

In the second ring, the topography is characterized by the radial sculpture superimposed on broader undulations that partly reflect old pre-Tycho topography; the albedo in this ring is significantly lower than in the other rings (13 to 14% normal luminance factor). The facies of this ring appears in full-moon telescopic photographs as a prominent, broad, dark halo around the crater (Fig. III-11).

Surrounding the dark-halo facies is still a third major facies in the rim deposits of Tycho characterized by abundant secondary or satellitic craters and a high albedo (15 to 17% normal luminance factor). Hundreds of secondary craters ranging from a kilometer to a few kilometers across may be readily resolved in this ring, under appropriate observing conditions at the telescope, and they are well portrayed in the *Lunar Orbiter* photographs. Beyond the third, or outer, ring, the rim deposits are discontinuous and grade outward into the ray system.

Lunar playas, which occur abundantly in the topographic depressions on the inner two facies of the Tycho rim, are occupied by smooth deposits with relatively low albedo. The largest of these playas occur on the eastern rim of the crater. In some of the large playas, part of the boundary of the filling material is a distinct scarp, and it is clear that the material has been emplaced, at least locally, as a flow with viscosity high enough for the scarp at the margin to be preserved.

Lunar Orbiter V photographs of the rim of Tycho have revealed that most parts of the rim in the inner two rings are broken by a mosaic of closely spaced faults. Most of these faults follow three principal patterns: (1) a radial pattern, (2) a concentric or circumferential pattern, (3) local crescent-shaped patterns. Displacement on the radial faults has produced many small radial troughs and

ridges in the inner ring. This pattern is similar to the much-larger-scale Imbrium sculpture (Refs. III-6 and III-7); the troughs are evidently graben, and the intervening ridges are horsts. Displacement on the circumferential faults is generally down, toward the center of Tycho. These faults probably are normal faults that have resulted from the settling of the crater's rim. The crescentic faults appear to be formed at the heads of very large slides or areas of large-scale mass movement relatively high on the eastern rim of Tycho. Displacement is generally down in the direction away from the center of Tycho, or down in the general direction of slope of the rim flank. Few faults appear to offset the flows on the rim; most of the displacement, therefore, probably antedates the flows.

Secondary, or satellitic, craters are one of the most characteristic features associated with the large ray craters. The secondary craters occur exclusively in the rim deposits and the ray system. Thousands of easily recognized, secondary craters occur around Tycho; the total number is unknown. The larger secondary craters (larger than 1 km in diameter) are most closely spaced in the outer ring of the rim deposits; at greater distances from Tycho, they occur in the rays and become more and more widely spaced. Smaller secondary craters, about 100 m to 1 km in diameter, were observed for the first time in the distant parts of the ray system of Tycho in the Ranger VII pictures in Mare Cognitum (Ref. III-8). These smaller craters occur in all of the rays.

The ray system of Tycho is strongly asymmetric (Fig. III-11). To the west, the rays extend only 200 to 300 km from the crater, whereas to the northeast and east, the rays extend at least 1000 km. A prominent, 200-kmlong, bright streak that crosses part of Mare Serenitatis in the vicinity of the crater Bessel is probably an element of one of the Tycho rays. If so, this particular ray extends about one-quarter the circumference of the moon. Part of another very long ray apparently extends across Mare Fecunditatis an equally great distance from Tycho.

The rays consist of a discontinuous series of bright streaks on the lunar surface. In more distant parts of the ray system, these streaks lie nearby along great circle arcs that pass through the parent crater. Close to Tycho, the pattern is more complex and includes broad, roughly linear, bright bands and numerous, bright ellipses and loops. Long axes of the ellipses tend to be radial with respect to the center of the crater, but the more nearly linear features are not radially aligned.

The pattern of the rays is superposed on nearly all the other topographic and geologic features of the lunar surface and is essentially independent of these other features. Except for the swarm of secondary or satellitic craters that occurs within the rays, the rays have no discernible intrinsic relief. They are essentially albedo patterns superimposed on the topography. The geologic units crossed by the rays include crater rim and floor units of the highlands; highland plains units; mare material in Mare Nectaris, Fecunditatis, Serenitatis, Nubium, and Cognitum; craters of Eratosthenian age; and crater units of Copernican age. From this superposition, the age of Tycho is readily established as Copernican; it is probably very late Copernican in age.

Tycho belongs to the general class of lunar craters that has been widely interpreted to be of impact origin (Refs. III-9 through III-11). In particular, the interior form and dimensions of the crater, the general characteristics of the crater rim, and the pattern of rays and secondary craters, all are consistent with an impact origin.

The terraces, or steps, on the walls of Tycho are thought to be formed by slumping (Ref. III-7). Each terrace, in this interpretation, is the top of a large landslide or fault block, and the risers are the scarps of normal faults along which the blocks have been displaced. On the basis of analogy with terrestrial craters of probable impact origin, the central peaks are probably formed of great brecciated masses of rock thrust up from fairly great depth in a late stage of opening of the craters.

The main features of the Tycho rim are probably produced in part by uplift of the local lunar crust and in part by deposition of debris ejected from the crater (Ref. III-12). The thickness of this debris layer is expected to be on the order of several hundred meters near the crest of the rim, thinning to only a few meters at distances on the order of 100 km (Ref. III-12). At a distance of 25 km from the rim crest, at the position of *Surveyor VII*, the average thickness of the ejected debris is probably a few tens of meters; it is at these distances that the subdued forms of the larger features in the buried pre-Tycho topography become easily recognizable.

The spatial association of the rays and the secondary craters implies a genetic association between the rays and these craters. Rays in a similar ray system around the crater Copernicus have been interpreted as thin, discontinuous deposits of ejecta from the secondary craters, and the pattern of the secondary craters and the rays has been shown to be consistent with a ballistic origin for the

craters (Ref. III-7). The secondary craters are probably formed by impact of large fragments or clots of ejecta from the primary crater.

The discovery in the *Lunar Orbiter* photographs of extensive flows, both on the interiors of the large ray craters and on the exterior flanks of the rims, has led to considerable new discussion and debate as to the origin of the flows and of the craters. At least three plausible hypotheses can be advanced for the origin of these flows:

- (1) The flows are volcanic and have been produced by extrusion of lava derived from depth, possibly formed or extruded in response to the forces that produced the craters.
- (2) The flows are relatively cold debris flows, which were mobile or fluid because they contained either liquid water or gas.
- (3) The flows are relatively hot debris flows, which were mobile because they contained molten, or partially molten, rock (and possibly some gas) heated by shock and by viscous flow during ejection of the debris from the craters.

If the flows are volcanic in origin, the volcanism may be a secondary phenomenon produced or triggered by the impact event that formed the craters. Or it may be argued by some observers that the craters are fundamentally of volcanic origin in the first place, and the observed flows are then cited as evidence for this volcanic origin.

Secondary volcanism, associated with impact, might occur as a result of:

- (1) Slight addition of heat by passage of a shock wave through an already hot substratum, the temperature of which was at, or near, the minimum melting point.
- (2) Triggering of an eruption from an existing magma chamber.

From theoretical analysis of attenuation of the shock associated with the formation of an impact crater the size of Tycho, it can be shown that the amount of shock heating would be exceedingly small at depth in the moon at which the average temperature gradient probably approaches the minimum melting point gradient. The peak shock pressure at these depths (a few hundred kilometers; see Section IX of this Report) is not likely to exceed a few kilobars. If the flows on the rim of Tycho are produced by secondary volcanism, it is much more likely that they

were extruded from an existing magma chamber or chambers, which might be present at considerable depth within the moon. The magma may have reached the surface either because these chambers were tapped by tensile fractures propagated in the shock wave from Tycho, or because of release of stress over the magma chamber in the region beneath the crater.

The possibility that wet debris flows might be formed in the interior and on the outer rim flank of a fresh impact crater arises as a consequence of the low average temperature at the lunar surface. The average temperature at the lunar surface in the equatorial region of the moon is about -28° C (Ref. III-13), and at the latitude of Tycho about -44° C. Materials in the subsurface at depths of a few meters, beneath the effective depth of penetration of the diurnal thermal wave, have nearly constant temperatures close to the mean temperature at the surface. Assuming the thermal gradients in the moon are not greater than those found on the earth (see Section IX of this Report), the rocks in the lunar subsurface are nearly everywhere below the freezing point of water to depths of 1 km or more. Any water escaping from the lunar interior, therefore, will tend to be frozen and trapped as ice when it reaches this cold layer. If the rate of escape of water from the lunar interior exceeds the rate of escape of water vapor through this, presumably semi-permeable, cold layer, then ice will tend to accumulate either in the interstices of the rocks or as veins and layers. Such accumulations of ice would tend to seal or decrease the permeability of the layer, and, once started, the process of accumulation might accelerate.

Ice may be widespread in the moon along the horizon corresponding approximately to the 0°C isotherm, and ice-impregnated rock could be ejected from a crater deep enough to intersect this isotherm. Material derived from near the center of such a crater would also be shockheated, and the ejected debris derived from this region might, therefore, contain abundant water in liquid form at the time it is deposited ballistically on the crater rim. This water-saturated debris might give rise to debris flows closely similar to the wet debris flows and mud flows that occur widely on earth. On the moon, such flows would have to be formed before the water escaped by evaporation into the tenuous lunar atmosphere. The time interval during which wet debris flows might form is fairly short unless a significant transient atmosphere is produced by the impact cratering event, as suggested by Urey (Ref. III-14).

The third explanation of the flows is based on the fact that the strongly shocked material ejected from a highspeed impact crater is heated, and, if the impact is at sufficiently high velocity, part of the ejected material is melted. From the effects of shock compression and subsequent decompression alone, the mass of material melted is many times the mass of the impacting body for shock pressures in rocks corresponding to typical lunar impact velocities of asteroidal and cometary objects. Additional material is melted owing to viscous dissipation of kinetic energy as heat in the flowing sheath of strongly shocked material produced in the rarefaction wave during the opening of the crater (Ref. III-15). The volume of material melted by both these processes, in a cometary impact crater the size of Tycho, probably exceeds the volume of the observed flows. Part of this melted material would be ejected at sufficiently great velocity to escape from the moon, and part of it would be widely scattered about the moon. It is an open question whether a significant amount of the melted material would be ejected at sufficiently low velocity to fall back on the outer flank of the rim and inner walls of the crater in sufficient volume to make the observed flows. The question cannot be decided on a purely theoretical basis without knowledge of the shock equations of state and other properties of the rocks.

On earth, a layer of melted and partially melted material, mixed with heated but unmelted debris, was formed around large impact craters such as the Ries Basin in Germany (Ref. III-16) and Lake Bosumtwi, Ghana. In other large craters of probable impact origin, such as the Clearwater Lake craters and the Manicouagan-Mushalagan Lakes crater of Canada, a fairly thick layer of melted material accumulated. There is a current debate as to whether this layer is of volcanic origin or was formed by melted, strongly shocked rocks. It may be noted, however, that most of the naturally occurring rocks that have been demonstrably shock-melted were originally misidentified as volcanic; the trend of studies of these rocks on earth has been to show that many rocks which superficially, or even rather closely, resemble volcanic rocks have been derived by impact processes.

The question of the origin of the flows associated with Tycho and other large, lunar ray craters is thus not an isolated problem, but part of a general problem of recognition and understanding of large impact craters, wherever they occur. It is of some interest to see whether the detailed data derived from the *Surveyor VII* television pictures provide any clues that help to resolve this larger controversy.

2. Geology of Area Around Spacecraft

Surveyor VII landed near the approximate boundary between the inner ring facies of the Tycho rim deposits and the second ring, or dark-halo facies. A variety of geologic units is present, therefore, within a few kilometers of the landed spacecraft; at least three of these units are visible from the vantage point of the Surveyor VII television camera. A detailed study of the geology of an 8- by 8½-km rectangular area around the landed spacecraft was undertaken to provide a basis for interpretation of the features observed. The study utilized the information contained in Lunar Orbiter V high-resolution photograph H-128, as well as the data applying to a more restricted part of this area, obtained directly from the Surveyor television pictures.

Eight mappable geologic units were recognized in the area studied. They include a widespread deposit of fragmental debris, a series of flows, the lunar playa material, and smooth patch material. The stratigraphic sequence of some of these units can be established from clear-cut superposition relationships, but for others, the relationships of superposition are not well defined, or are ambiguous. The units for which the stratigraphic sequence is known are described first, in the paragraphs that follow, and the units of uncertain stratigraphic position are discussed afterward. A plausible sequence for all eight units is then derived on the basis of some rather speculative arguments. As will be seen, there may be considerable overlap in the actual order of deposition and ages of some of the units.

a. Patterned debris. Patterned debris, the oldest and the most widespread geologic unit in the area mapped (Fig. III-12), occurs over a broad area north and west of the Surveyor VII spacecraft and extends for some tens of kilometers in each direction. It is the major geologic unit in the dark-halo facies of the Tycho rim deposits, and has a relatively low albedo, which accounts for the dark halo around Tycho.

The surface of the patterned debris is characterized by patterned terrain (Fig. III-13). This pattern, which consists of gentle ridges and intervening shallow, open grooves, probably reflects a closely spaced subsurface network of faults. In the vicinity of Surveyor VII, at least three prominent directions are represented in the pattern, reflecting three sets of faults, one trending approximately northwest, another approximately north, and a third approximately northeast. The north-trending set is approximately radial to the crater, whereas the northwest and northeast sets are apparently aligned along dominant

directions of major regional lineaments around Tycho. The shallow ridges and grooves of the patterned terrain are superimposed on somewhat larger hillocks and swales, a few hundred meters to half a kilometer across, and on the still larger north-trending ridges and valleys that characterize this part of the Tycho rim.

At a scale of a few tens of meters, the surface of the patterned debris is relatively smooth, but it is interrupted here and there by a few protruding blocks, large enough to be resolved on *Lunar Orbiter V* photograph H-128, and by relatively widely spaced, small craters. The blocks are rarely more than 10 to 20 m across; blocks of this size are generally spaced several hundred meters apart.

The crater density on the patterned debris is the highest of all the units in the area studied. The observed density of craters larger than 8 m in diameter is about 220 per km². The large craters have sharply formed, raised rims and are approximately conical in shape. Most of the smallest craters, however, are elongate in the north-south direction.

As seen in the Surveyor VII pictures, some of the larger craters with well defined, raised rims in the patterned debris have relatively smooth rims, which indicates the debris is both relatively fine-grained and, at most, weakly cohesive (Ref. III-17). A 60-m-diameter crater, about 650 m north of the spacecraft, exhibits such a rim (Fig. III-14). A few large blocks are scattered on the rim of this crater, but otherwise the rim is smooth and symmetrical in form, except for smaller superposed craters. The crater is slightly more than 10 m deep; the debris in which it is excavated is, therefore, mostly fine-grained and weakly cohesive, at least to a depth of 10 m, at the site of this crater.

The fact that only shallow ridges and grooves are present on the surface of the debris, rather than distinct fault scarps, suggests the faults are formed in more coherent rocks at depth and that the weakly cohesive debris is draped over the subsurface fault scarps. Ridges in the debris are probably formed over the upper edges of these scarps and the grooves at the bases of the scarps. Typical spacing between grooves is 100 to 200 m; the smooth profile and low relief of the ridges and grooves suggests the thickness of the weakly cohesive layer may be on the order of several tens of meters. This thickness is consistent with that expected for a layer of debris deposited ballistically from a lunar impact crater the size of Tycho, at the distance of the *Surveyor VII* site from the crater rim (Ref. III-12).

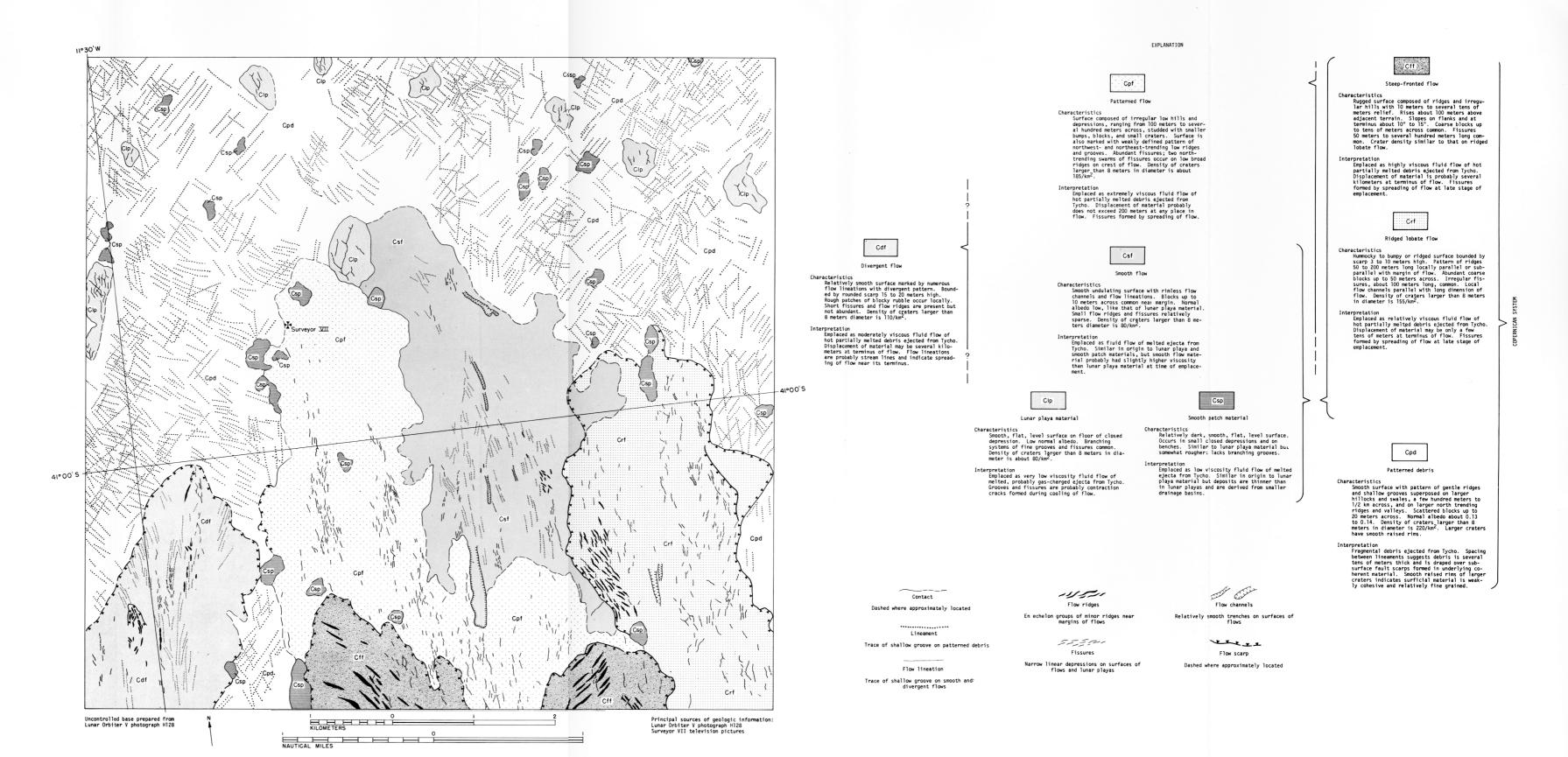
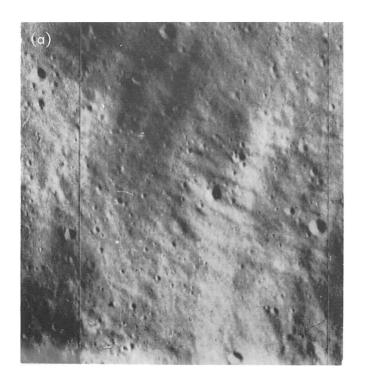


Fig. III-12. Preliminary geologic map of the Surveyor VII landing site (by E. M. Shoemaker and E. C. Morris).



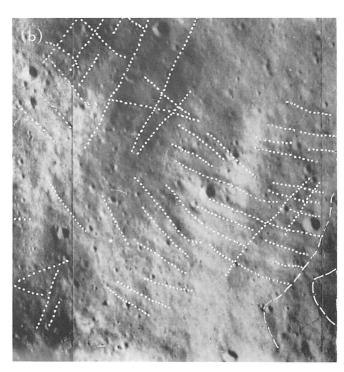


Fig. III-13. (a) Enlargement of part of Lunar Orbiter V photograph H-128 showing characteristics of patterned debris. Note the relatively smooth surface with pattern of gentle ridges and shallow grooves trending in two directions, from upper left to lower right and lower left to upper right. (b) Same area as III-13a, but with geologic annotations; see Fig. III-12 for explanation of annotations.

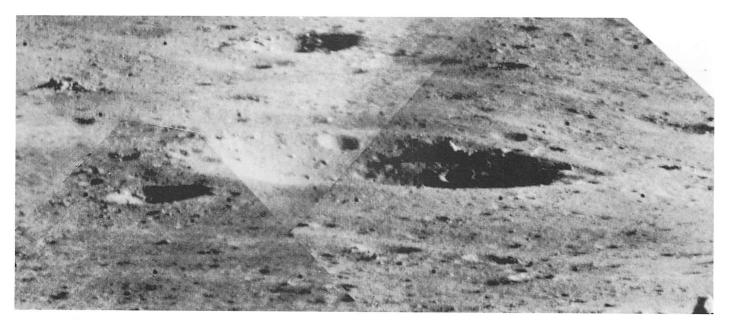


Fig. III-14. Mosaic of Surveyor VII pictures showing smooth, raised-rim crater, about 60 m in diameter and 650 m north of the spacecraft, formed in the patterned debris (Day 010, 06:58:34, 07:09:33, and 07:09:38 GMT).

b. Ridged lobate flow. A well defined lobate flow overlies the patterned debris in the southeast part of the area mapped (Fig. III-12). Its terminus is about 4 km east of the spacecraft. This flow may be traced a distance of 8 km from its terminus southward up the flank of the Tycho rim. Along the upper 2 km of its exposed length, it is bounded by a sharp, high, relatively straight levee on each side. The crests of the levees mark the boundary of a channel about 30 m deep and 400 m wide. Downslope from the levees, the flow expands abruptly to a width of at least 1½ km; it reaches a maximum width of about 2½ km near the lower terminus.

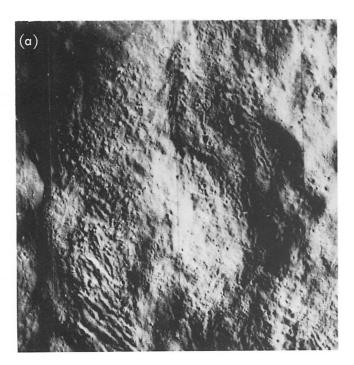
Just below the levee bounded channel, the flow is built up to a height of 50 to 70 m above the surrounding terrain. Here the surface of the flow is relatively smooth except for widely spaced fissures, and the flow has a hummocky topography. The relief of the flow diminishes gradually northward toward the lower end of the flow; the surface becomes bumpy and relatively rough and is locally marked with a well developed set of en echelon ridges (Fig. III-15). These ridges are 50 to 200 m long, about 2 to 5 m high, and are generally spaced about 50 m apart. They are locally parallel or subparallel with the margin of the flow. The margin of the flow along most of the

lower, northern part is a well defined, rounded scarp, ranging in height from about 3 to 10 m.

Coarse blocks, some as large as 30 to 40 m or, in some cases, even 50 m long, are common in the lower part of the flow. Irregular fissures, typically about 100 m in length, are also common. A few well defined channels or chutes, ranging in length from 100 to 400 m, occur in this part of the flow. In places, these have raised, levee-like edges; they all trend approximately north, parallel with the long direction of the flow.

Small craters are widespread on the surface of the ridged lobate flow. Craters about 30 m in diameter or larger are typically circular in plan and have well developed, raised rims. Most of the smaller craters, however, are elongate in a north–south direction approximately parallel with the direction of flow. The density of the craters larger than 8 m in diameter is about 155 to 160 per km².

c. Steep-fronted flows. Two prominent, high, steep-fronted flows, which extend into the southern part of the area studied, are among the largest and most easily recognized flows on the rim flank of Tycho. The termini of



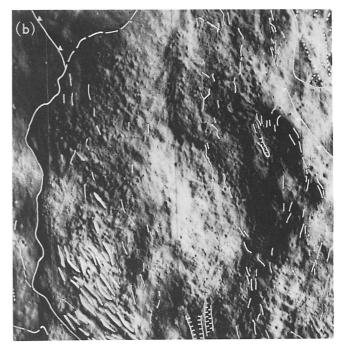


Fig. III-15. (a) Enlargement of part of Lunar Orbiter V photograph H-128 showing characteristics of ridged lobate flow. Note ridges and hummocky-to-bumpy surface. Flow is bounded on the left by a scarp about 10 m high. Ridges range from 50 to 200 m long, and large blocks up to 50 m across are abundant on the surface of the flow. (b) Same area shown in III-15a, but with geologic annotations; see Fig. III-12 for explanation of annotations.

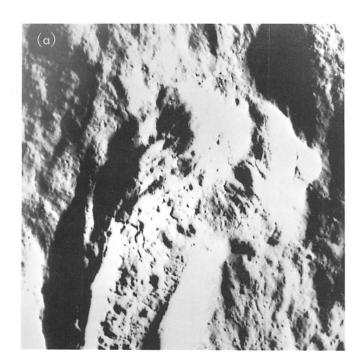
these flows lie about 3 and 5 km south and southeast of Surveyor VII. They can be traced about 7½ km southward, up the flank of the crater rim. Along most of their length, both flows are bounded by well defined levees on each side; along the easternmost flow, the levees extend to within 1 km of the terminus. The levees are exceptionally high along this flow and locally rise about 100 m above the top of the main part of the flow within the channel. The flows themselves have an average height of a little less than 100 m. Slopes on the flanks and at the termini of the flows are typically about 10 to 15 deg. The easternmost of the two flows cuts across the upper part of the ridged lobate flow, and the terminus of this steep-fronted flow rests partly on the ridged lobate flow (Fig. III-16). Thus, one of the steep-fronted flows is superposed on, and clearly younger than, the ridged lobate flow.

The surfaces of the steep-fronted flows are relatively rugged, both within the levee-confined channels and on the unconfined termini. In most places, the flow surfaces consist of a series of ridges and irregular hills with a relief of 10 m to several tens of meters. Generally, the ridges are roughly parallel with the margins of the flows; in some places, however, they lie perpendicular to the margin. Coarse blocks are fairly common on the flows; some of

these blocks have dimensions of many tens of meters. The surfaces of the flows are also cut by fissures ranging from 50 m to several hundred meters in length; locally, the westernmost of the two steep-fronted flows appears to be slightly offset along northeast-trending faults. These faults may be nothing more than extended fissures, which lie perpendicular to the direction of flow, along which the lower parts of the flow may have pulled away from the upper parts.

Small craters are fairly common on the steep-fronted flows; the density of the craters is similar to that observed on the ridged lobate flow. As on the lobate flow, the largest craters are circular in plan and have well defined, raised rims, whereas the smallest craters observed on the *Lunar Orbiter* photographs tend to be elongate in a north-south direction.

d. Lunar playa material. At least eight closed depressions in the area studied around the landed Surveyor VII have well developed flat floors, or lunar playas. The playas range from 300 m to about 1 km in length and from 200 m to about 500 m in width. The playa floors are occupied by relatively dark, smooth material, here referred to as lunar playa material. This material has the



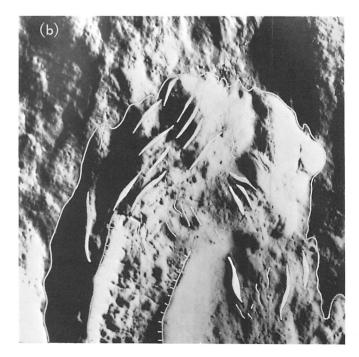


Fig. III-16. Enlargement of part of Lunar Orbiter V photograph H-128 showing the terminus of a steep-fronted flow. Flow rises about 100 m above adjacent terrain and has a rugged surface composed of ridges and irregular hills with 10 m to several tens of meters relief. (b) Same area shown in III-16a, but with geologic annotations; see Fig. III-12 for explanation of annotations.

lowest albedo of any of the geologic units recognized on the rim of Tycho, and, in general, it has the smoothest, most uniform surface. Except for the branching systems of fine grooves and a few superimposed craters, the surfaces are nearly flat and, as far as can be judged from Lunar Orbiter photographs, are also nearly horizontal. Relative to most of the other geologic units in the area studied, the surfaces of the lunar playas have a low density of small, superposed craters. Thus, in some respects, the lunar playas resemble miniature mare surfaces.

Branching grooves are characteristic features on the lunar playas (Fig. III-17). They range in length from a few tens of meters to as much as 800 m and are most strongly developed on the largest playa. In cross section, typical grooves have gently rounded edges and are convex on each wall; the slope on the wall steepens to more than 10 deg near the center of the groove. Along the largest grooves, a sharp-edged fissure lies at the center. The width of a groove, at its upper edge, is as much as several tens of meters, but the deep, sharp trough in the center is rarely more than 8 m across. Vertical relief along most parts of the grooves is less than 2 m. Both in profile and in areal pattern, the grooves resemble contraction cracks or fissures formed by desiccation in terrestrial playa beds

or by cooling and freezing in some basaltic lava pools in the Hawaiian volcanoes. The rounded edges of the grooves suggest that loss of volume has taken place in the underlying material along the crack. This loss may be due to compaction, perhaps as a result of escape of volatiles.

The observed density of craters larger than 8 m in diameter on the playa surfaces is about 80 per km². Because of the small total area of the playas and the small total number of craters counted, however, this density may not be representative of all the playas. Some of the observed craters have symmetrical form and well developed, raised rims; but, as in the case of some of the flows, many of the smallest craters are irregular or elongate in form, and they tend to be elongate in a north–south direction.

The age of the lunar playa material, relative to the other geologic units, can be established within broad limits only. The lunar playa material rests on, and is clearly younger than, the patterned debris. In most places, the lunar playa material is in contact only with patterned debris, so that the stratigraphic relationship between the isolated playa units and other geologic units studied cannot be determined. The largest playa studied, which lies



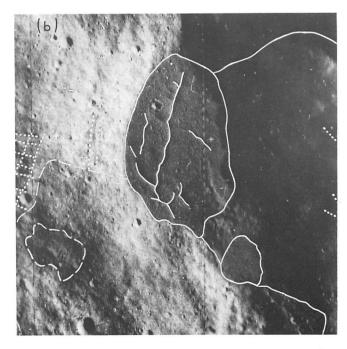


Fig. III-17. (a) Enlargement of part of Lunar Orbiter V photograph H-128 showing large lunar playa about 1 km northeast of Surveyor VII. Lunar playa material has a smooth, flat, level, dark surface and branching systems of grooves and fissures. (b) Same area shown in III-17a, but with geologic annotations; see Fig. III-12 for explanation of annotations.

about 1 km northeast of Surveyor VII, is in contact with two flows as well as with the patterned debris. Unfortunately, neither flow has a well defined scarp along the contact with the playa, and it cannot be determined whether either of the two flows overlaps the lunar playa material at the contact or is overlain by the playa material. On the basis of a speculative model of the origin of the playas, it is inferred that the playas were formed early in the period of emplacement of the flows, but that the playa material may have remained fluid during most of the time of this emplacement. If this hypothesis is true, the age of the playas may be thought of as actually spanning the ages of the flows.

e. Smooth patch material. Relatively dark, smooth material, somewhat similar to that found in the lunar playas, occurs in numerous small patches in the area studied (Fig. III-18). These smooth patches occupy small, closed depressions or, in some places, relatively small, level benches. Over two dozen such patches were observed in the 8- by 8½-km area studied. They range in length from 150 to about 700 m and in width from 100

to about 300 m. Although the smooth patch material resembles the lunar playa material in albedo, the surfaces of the patches, in general, are somewhat rougher than the surfaces of the playas, and they do not exhibit the branching systems of grooves found on the playas. In some cases, it is fairly clear that the material of the patch is thin, where large blocks protrude through it. A fairly large patch with protruding blocks occurs just north of Surveyor VII and is portrayed in some detail in the Surveyor pictures (Fig. III-19). The blocks are probably related to underlying geologic units. The lunar patch material is probably similar in origin and time of emplacement to the lunar playa material and may differ only in that the deposits in the patches are thinner than in the playas.

The smooth patch material is superposed on patterned debris; locally, it occurs along the terminus and is apparently superposed on the ridged lobate flow. It also occurs on a patterned flow described below. The smooth patch material is clearly younger than the patterned debris and is younger than the material of the flows on which it



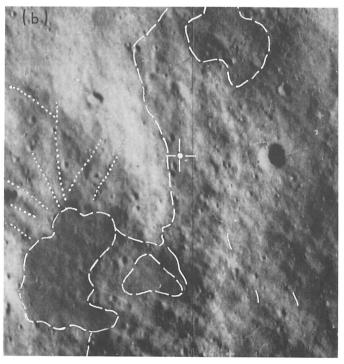


Fig. III-18. (a) Enlargement of part of Lunar Orbiter V photograph H-128 showing two areas of smooth patch material. Small patch in upper right of the picture can be seen in the Surveyor VII pictures (Fig. III-19). Surveyor VII landing site is located in the center of the picture just to the right of the small double crater. The smooth patch material has relatively dark, smooth, flat, level surface and generally is found in small, closed depressions and on benches. Similar to lunar playa material, but lacks branching grooves. (b) Same area shown in III-18a, but with geologic annotations; see Fig. III-12 for explanation of annotations.

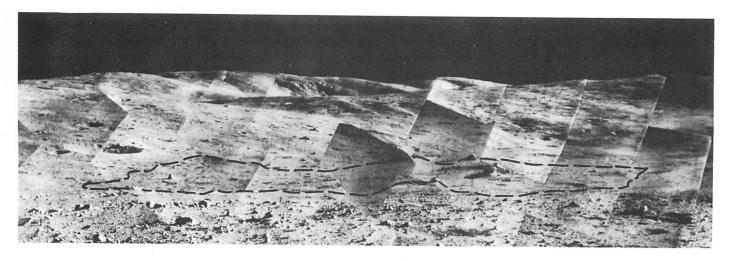


Fig. III-19. Mosaic of narrow-angle Surveyor VII pictures of an area northeast of the spacecraft. The boundary of the smooth patch material shown in the upper right of Fig. III-18b is indicated by a dashed line. Note the large block (block G) on the smooth patch and the fillet surrounding the block (Catalog 7-SE-22).

occurs, although it may have been emplaced before the movement of these flows occurred.

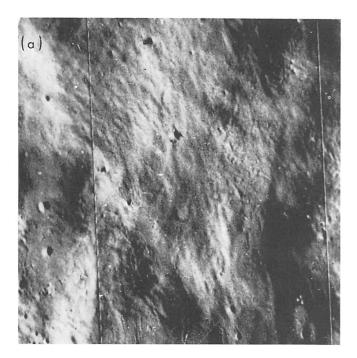
In any discussion of the origin of the smooth patches and lunar playas, it is important to note that nearly all closed depressions with a surface area of more than about 0.2 km² are occupied by either a smooth patch or a playa. Thus, essentially all closed drainage basins above a certain size have a recognizable deposit of dark, smooth material in them. In general, the larger the closed depression, the larger is the surface area of the dark, smooth deposit, and the largest depressions contain the playas, which are probably underlain by the thickest deposits. This strongly suggests that the dark, smooth deposits have been formed from fluids which were relatively uniformly spread over the surface and which subsequently drained into the local closed depressions.

f. Smooth flow. A remarkably smooth-surfaced flow occupies a north-trending irregular valley east of the Surveyor VII spacecraft. The flow extends down the length of the valley and is about 4 km long. At its lower, northern end, it bounds the east side of the large lunar playa northeast of the spacecraft.

Evidence on the stratigraphic relationship of the smooth flow is somewhat ambiguous. Along most of the length and at the upper end of the flow, the boundary of the smooth material is irregular in plan. Along its northeast margin, the smooth flow is in contact with the patterned debris and has a branching pattern along the contact; it is fairly clearly superposed on the patterned debris. Near this margin, many blocks about 10 m across protrude from the surface of the flow; these blocks are similar to the blocks on nearby parts of the patterned debris. It is inferred that they are, in fact, parts of the patterned debris which protrude through the flow along the margin where the flow is very thin.

Along part of the southeast margin, the smooth flow is overridden by the ridged lobate flow, which has a well defined 5- to 10-m-high scarp, but elsewhere the smooth flow extends over the scarp and onto the top of the ridged lobate flow. Thus, in one place, the ridged lobate flow rests on the smooth flow, and in another place, the smooth flow rests on the ridged lobate flow. These contradictory relationships are explicable if: (1) the smooth flow formed first; (2) the ridged lobate flow formed, or was displaced, afterward; and (3) locally, the ridged lobate flow overrode the smooth flow, but elsewhere only deformed the smooth flow without riding across it. This hypothesis requires that the material of the ridged lobate flow was not displaced very far, near its terminus, where the smooth flow extends unbroken across the scarp of the ridged lobate flow and up onto the flow top.

The surface of the smooth flow is, in most places, gently undulatory, and the material of the flow seems to be draped over an undulatory, slightly hummocky surface (Fig. III-20). A few swarms of fissures occur on the flow near the upper end and along the margins; near the southeast margin is one local cluster of small en echelon flow ridges, none of which is more than about 100 m long. Well defined channels, or chutes, occur along the length of the flow; the largest one occurs along the upper margin and is about 1 km in length and 200 m in maximum



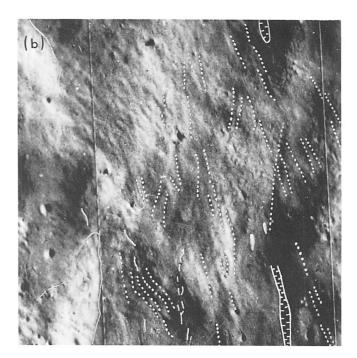


Fig. III-20. (a) Enlargement of part of Lunar Orbiter V photograph H-128 showing characteristics of smooth flow material. Smooth flow material has dark, undulating surface with rimless flow channels and flow lineations. Flow ridges and fissures are sparse. (b) Same area as III-20a, but with geologic annotations; see Fig. III-12 for explanation of annotations.

width. Unlike the chutes in other flows in the area, these channels are devoid of levees. In addition to the channels, there are a number of very shallow, open grooves on the surface of the flow. These grooves, which we have called flow lineations, may mark the sites of minor surges of movement in the flows, and are probably related in origin to the channels.

Some blocks protrude from the flow, particularly near the margins. The largest of these are 30 m across. It seems likely that these blocks are not intrinsic features of the flow, but belong to underlying geologic units and protrude throughout the relatively thin part of the flow. The distribution of these blocks suggests that, on the average, the flow is extremely thin over most of its extent. Its average thickness may be less than 5 m.

Small craters occur on the surface of the flow; the density of craters larger than 8 m in diameter is about the same as that observed on the lunar playas, about 80 per km². Many of the small craters are elongate in the north-south direction.

In many respects, the smooth flow resembles the lunar playa and smooth patch materials. It is so similar, in fact, that there is some difficulty in distinguishing local parts of the flow from smooth patch material. Not only is the surface smooth, but it has a relatively low albedo and a low crater density. It seems likely that the material of the smooth flow, the lunar playas, and smooth patches are all related in origin and that the difference between the flow and the dark, smooth materials underlying the level surfaces is principally one of viscosity at the time of emplacement.

g. Patterned flow. A patterned flow extends from the large lunar playa northeast of the spacecraft to about 6 km to the southeast. Surveyor VII landed on the patterned flow about 50 m from its western margin. The patterned flow is in contact with patterned debris along its western side and with the large lunar playa and the smooth flow along the north and eastern margin; on the south, it is overridden by the steep-fronted flows. An irregular scarp is present along the western margin of the flow about 2 km south of the spacecraft, but elsewhere there is little or no detectable relief at the contact of the flow with the patterned debris. Source deposits of smooth patch material occur in broad, shallow depressions along the margins of the flow, and a few also occur on benches and depressions on the flow.

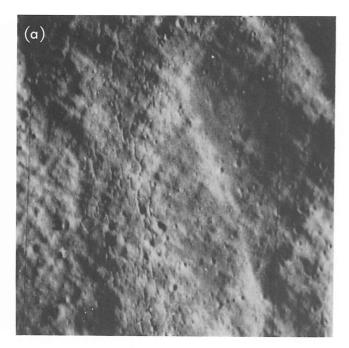
The surface of the flow is composed of irregular, low hills and depressions, ranging from about 100 m to several hundred meters across, studded with smaller bumps and blocks and small craters (Fig. III-21). Except for two low, rounded parallel ridges in the central part of the flow, these broader irregularities exhibit no conspicuous pattern. Superimposed on these broader irregularities, however, is a weakly defined pattern of low ridges and grooves, similar to that observed on the patterned debris but less well defined. Both northwest-trending and northeast-trending ridges and grooves are present on the flow. In addition, the surface of the flow is cut by numerous irregular, subparallel fissures. Individual fissures trend north-south, and two north-south-trending swarms of fissures occur along the two low, parallel ridge crests. The fissures range in length from a few tens of meters to about 250 m; where they are densely clustered in the swarms, they are typically spaced a few tens of meters apart.

Blocks are locally abundant on the surface of the flow. Those that are resolvable in the *Lunar Orbiter V* high-resolution photograph range in length from 5 to about 50 m. Blocks this size are spaced 20 to 30 m apart, where

they are most abundant. Abundant smaller blocks are strewn on the surface of the flow, as revealed in the $Surveyor\ VII$ pictures.

Craters are nearly as abundant on the patterned flow as on the patterned debris. The observed density of craters larger than 8 m in diameter is about 185 per km². The largest craters have well defined, raised rims and symmetrical form, but the majority of small craters are irregular to elongate in shape. The long axes of these small craters trend north–south, parallel with the north-trending fissures and with the long axis of the flow.

The evidence on the stratigraphic position of the patterned flow is subject to alternative interpretation. The flow appears to locally override and rest on the patterned debris. The material of the patterned flow is, in turn, overridden or overlain by the smooth flow, smooth patch material, and the steep-fronted flows. The amount of movement or displacement of the material in the patterned flow, however, may be very small, as suggested by the lack of a scarp around most of its margin and by the presence of the weak pattern of ridges and grooves.



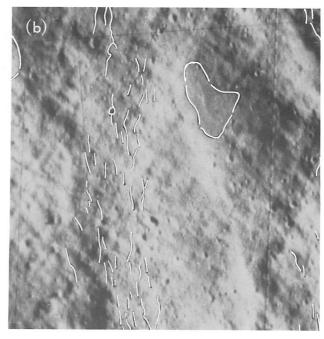


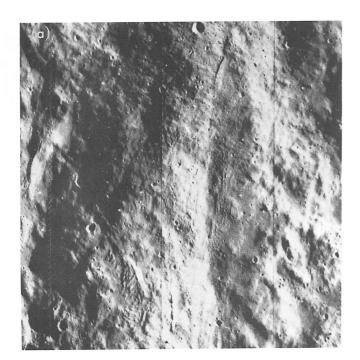
Fig. III-21. Enlargement of part of Lunar Orbiter V photograph H-128 showing abundant north-trending fissures on patterned flow. Swarms of fissures occur on low, broad ridges on the crest of the flow. The surface of the patterned flow is composed of low hills and depressions, ranging from 100 m to several hundred meters across, studded with smaller bumps, blocks, and small craters. Weakly defined pattern of northwest-trending low ridges and grooves extends from the upper left corner of the picture to the lower right side. (b) Same area shown in III-21a, but with geologic annotations; see Fig. III-12 for explanation of annotations.

The flow probably consists of debris similar in origin to the patterned debris, which flowed only slightly after it was deposited on the rim of Tycho. The material of the flow was clearly deposited before the superimposed flows and smooth patch deposits were formed, but flowage or displacement in the patterned flow could have taken place after the emplacement of the superimposed materials without significantly disrupting them.

h. Divergent flow. The terminus of a well developed flow of uncertain stratigraphic position extends into the southwest corner of the area studied. The surface of this flow is marked by numerous flow lineations that exhibit a striking divergent pattern near the terminus of the flow, which distinguishes it from the other flows in the area. Near the terminus, the flow is 1½ to 2 km wide, and it may be traced about 5 km to the south, up the rim flank of Tycho. Along the west side, the margin of flow is a rounded scarp, 15 to 20 m high. A low, much less well defined scarp is present at the terminus and along the east margin.

The surface of the divergent flow is relatively smooth and locally resembles the surface of the smooth flow to the east (Fig. III-22). Rough patches of blocks occur locally on the flow, however. In its overall topographic characteristics, the divergent flow is intermediate between the smooth flow and the ridged lobate flow. A few short fissures and flow ridges occur on the surface of the flow as well as the flow lineations. The flow lineations are shallow grooves ranging from 50 m to about 300 m in length and 10 to 40 m in width. One prominent, small flow scarp, which occurs on the crest of the flow, apparently was formed by a local surge of fluid. Small craters occur on the flow; the crater density is about 110 per km², intermediate between that of the smooth flow and that of the ridged lobate flow.

The part of the divergent flow in the area studied is in contact only with patterned debris and local smooth patch material. Its stratigraphic relation to the other flows in the area cannot, therefore, be determined. The divergent flow clearly overlies the patterned debris, but the stratigraphic position of the flow relative to the smooth patch material is indeterminate. If the sequence of emplacement of flows is controlled primarily by viscosity of the flow material, it is likely that the divergent flow is intermediate in age between the smooth flow and the ridged lobate flow.



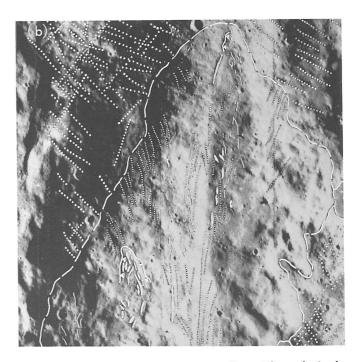


Fig. III-22. (a) Enlargement of part of Lunar Orbiter V photograph H-128 showing divergent flow. The relatively smooth surface of the flow is marked by numerous divergent flow lineations. Rough patches of blocky material occur locally. The flow is bounded on the west by a rounded scarp 15 to 20 m high. (b) Same area as III-22a, but with geologic annotations; see Fig. III-12 for explanation of annotations.

- i. Sequence of emplacement of geologic units. To infer the sequence of emplacement of the geologic units at the Surveyor VII landing site, two lines of evidence may be used:
 - (1) Relationships of superposition of one unit upon another.
 - (2) Relative density of craters observed on each unit mapped (Fig. III-23).

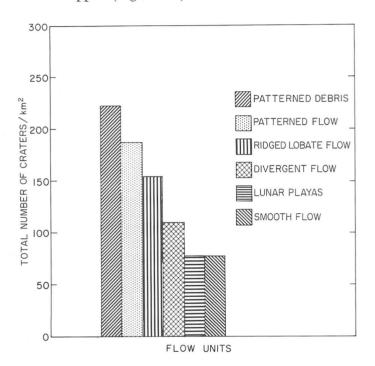


Fig. III-23. Areal density of craters larger than 8 m in diameter on six geologic units in the vicinity of the Surveyor VII landing site on the rim of the crater Tycho.

The evidence of superposition of one unit on another is insufficient to establish the sequence of emplacement for all of the units, and, in places, the evidence is conflicting. Therefore, the evidence from crater density on each unit or some model of the mechanism of emplacement of the units also must be used to arrive at a full interpretation of the emplacement sequence.

In general, there is fairly good agreement between the evidence based on superposition and the evidence based on crater density, where both lines of evidence can be used to obtain the relative sequence of two or more geologic units. For example, the patterned debris can be shown to underlie most, and probably all, of the other geologic units, and it has the highest density of craters, consistent with a greater age. The ridged lobate flow, the

divergent flow, the smooth flow, and lunar playa material, all of which are demonstrably superposed on the patterned debris, have lower crater densities. The smooth flow, the ridged lobate flow, and the steep-fronted flow are superposed on the material of the patterned flow; all have lower crater densities than the patterned flow.

In one case, there is a clear-cut contradiction in the relative ages derived from superposition and the ages derived from crater densities. The ridged lobate flow locally overlies the smooth flow, but the crater density is higher on the ridged lobate flow than on the smooth flow. Along most of its length, the contact of the ridged lobate flow with the smooth flow is a well defined scarp, where it has overridden the smooth flow (Figs. III-8 and III-12). Locally, the smooth flow extends over the scarp, however, and rests on the ridged lobate flow.

These observed relationships can be explained if the two flows were emplaced in rapid succession and the younger flow was formed while the older flow was still mobile. The smooth flow may be interpreted to have been emplaced first, partly on material that later became mobilized as the ridged lobate flow. The ridged lobate flow later overrode the smooth flow at most places, except where the displacement of the material was so slight that the older smooth flow was buckled, but not offset, along the flow scarp. This hypothesis requires that the material of the ridged lobate flow is locally derived from the debris already present on the surface and that parts of the flow near its terminus have moved, at most, only a few tens of meters rather than down the entire length of the flow.

An alternative hypothesis is that the ridged lobate flow was emplaced early and was followed by emplacement of the smooth flow. Then, renewed movement of the ridged lobate flow occurred after the smooth flow was formed, resulting in superposition of the ridged lobate flow on the smooth flow along most of the contact. Under this hypothesis, the material of the ridged lobate flow could have been derived from near the head of the flow, a distance of 8 km up the rim flank of Tycho. In either case, rapid succession of the emplacement of the flows is implied.

About twice as many craters occur per unit area on the ridged lobate flow as on the smooth flow. If the smooth flow and ridged lobate flow were emplaced in rapid succession, then about half or more of the craters on the ridged lobate flow probably were formed in a relatively short period of time. More craters may occur on the ridged lobate flow because: (1) the flow has not moved

very far at its lower end, and craters that were formed early were not destroyed by movement of the flow; or (2) the smooth flow remained fluid for a longer period of time than the ridged lobate flow, and only the craters formed after the smooth flow had become rigid were preserved on its surface.

The crater abundance on the patterned debris is almost three times as great as on the smooth flow and lunar playas. If all of the flows, including the smooth patch and lunar playa material, were emplaced in rapid succession and very shortly after deposition of the patterned debris, then about two-thirds of the craters on the patterned debris must have been formed during this period of emplacement.

If most of the craters on the patterned debris and older flow units were, in fact, formed in an extremely short time interval, the most likely explanation for their origin would be that they are secondary craters formed by fragments ejected from Tycho. They may represent, in other words, a record of the last stages of fallback or deposition of the Tycho ejecta. In this case, they were formed by fragments thrown to greater heights than most of the material deposited on the Tycho rim.

It is of interest to note that, on all of the geologic units, most craters between 8 and 16 m in diameter are elongate in shape and that the long axes of these craters are aligned radially with respect to the center of Tycho. It might be argued that the small craters are elongate in the northsouth direction because they were deformed during movement of the flows, but this argument is not likely to be applicable for the small craters on the patterned debris. Nor will it account for the fact that only the smallest craters are generally anomalous in shape, whereas the larger craters on both the flows and patterned debris tend to be approximately circular in plan. Some of the craters may be elongate simply because they have been formed or enlarged along fissures, but in this case, it is curious that there is no tendency for the elongate craters to be aligned in the two most prominent orientations of the lineaments in the patterned debris. The simplest explanation is that most of the elongate craters are secondary craters.

An imperfect analogy to the formation of secondary craters by late-falling fragments high on the rim of Tycho is provided by the formation of a swarm of secondary craters on the rim of the nuclear crater Sedan (Fig. III-24). These secondary craters at Sedan were formed by fragments, ejected at high velocities and high elevation angles

from the region near the center of the crater, which fell back onto the crater rim after the bulk of the rim material had been deposited and had come to rest. In the case of Sedan, the ejected fragments that formed the late secondary craters were derived from material that lay nearly directly above the buried nuclear device. The mechanism of ejection of this material has no direct analogy with the mechanisms of ejection of fragments from an impact crater. There may be other mechanisms, however, by which fragments that will produce late-forming secondaries on the crater rim can be ejected at fairly high velocities and high elevation angles from impact craters.

It is appropriate to inquire, therefore, what the time span might be for the sequence of emplacement of flows on the rim of Tycho, if most of the craters observed on these flows are secondaries. Plausible trajectories and times of flight of the main part of the ejecta from Tycho and possible trajectories of fragments which might have produced late-forming secondary craters can be derived from the standard ballistic equations. From a comparison of these times of flight, the time interval during which the flows and lunar playa deposits might have been emplaced can be estimated, and minimum values can be found for the flow velocities required for emplacement of the flows in this time interval. Finally, these velocities can be examined to see if they are compatible with the forms of flows.

From experimental studies of high-velocity impact, it has been found that the bulk, or a large fraction, of the material ejected from small impact craters is ejected at angles of about 45 deg from the original surface of the target. The final ejection velocity imparted to individual fragments is the vector sum of the velocities imparted by acceleration in the shock front and acceleration in the following rarefaction wave. As the geometric relationships between the shock front and shock wave are nearly independent of scale, it is reasonable to assume that the bulk of the material ejected from an impact crater the size of Tycho will also be thrown out at elevation angles of about 45 deg.

It is further assumed that the final crater is produced partly by ejection of material and partly by collapse of the walls of the crater in the late stage of its formation. The cumulative width of terraces along the walls of Tycho suggests that as much as 15 km of the final radius may be attributed to widening of the crater by the collapse. The range of radial distances, from the center of the crater, from which material was launched into ballistic trajectories is about 27 km. Fragments that arrived in the vicinity of the *Surveyor VII* landing site, therefore, trayeled

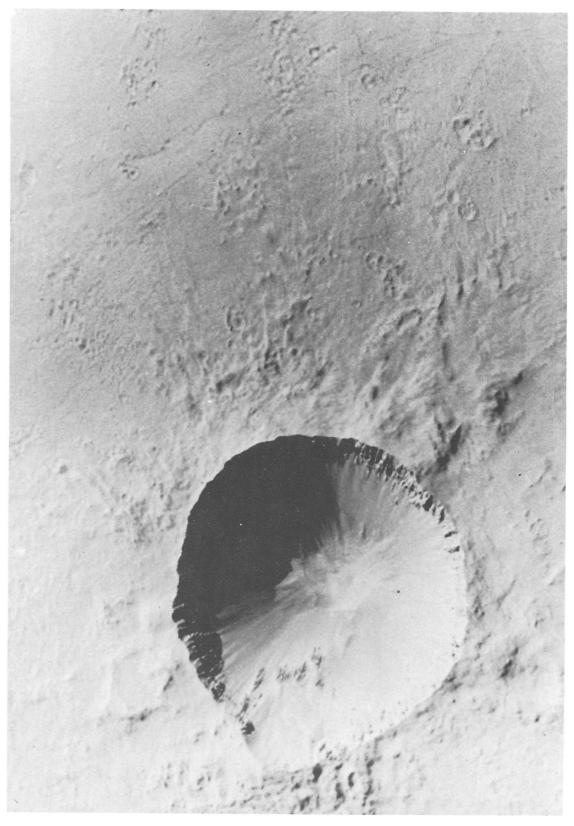


Fig. III-24. Aerial photograph of the Sedan nuclear explosion crater (Nevada) showing numerous secondary craters on its rim. Main crater is about 400 m across (photograph by courtesy of the Lawrence Radiation Laboratory, University of California).

horizontal distances not less than 45 km nor greater than 72 km.

For an ejection angle of 45 deg, the time of flight of a fragment to the Surveyor VII landing site must lie between about 220 and 290 sec, corresponding, respectively, to trajectories of 45 and 72 km in length. These times of flight correspond to ejection velocities of 0.27 km/sec and 0.35 km/sec. The difference in the two extreme values in the time of flight derived under these assumptions is only 70 sec; the difference in the vertical components of the ejection velocities is only about 50 m/sec. It is not likely, however, that fragments producing late-forming secondaries would be derived from the region near the center of the crater and ejected at such low velocities. The peak shock pressure and acceleration of material decrease rapidly, as the shock propagates away from the path of penetration of the projectile. Fragments derived from close to the path of penetration, therefore, tend to be ejected at much higher velocities than the fragments ejected from the region near the edge of the final crater. For this reason, most fragments follow over-arcing trajectories; most of the material derived from the central region of the crater is thrown the farthest, as shown by the arrangement of fragmental debris at Meteor Crater, Arizona (Ref. III-18).

It is much more probable that fragments which fall late, but high, on the rim flank of an impact crater are ejected at relatively high velocities and at high elevation angles. The greater the height reached by the fragment, the longer its time of flight. Fragments thrown to an apselene of 100 km above the lunar surface, for example, have a time of flight of about 700 sec. A fragment, thrown from a region near the center of Tycho to a height of 100 km and landing in the vicinity of the Surveyor VII landing site, would be ejected from the crater at a velocity of 0.59 km/sec and at an angle very close to 80 deg from the horizontal. If a fragment that landed in the vicinity of the Surveyor VII landing site were thrown to an apselene of 100 km from a point at a radial distance of 27 km from the center of Tycho, it would leave with nearly the same velocity, but at an angle of about 83.5 deg.

The question remains as to how the fragments might be thrown out at such steep angles. One possibility is that some of the anomalous high-flying fragments result from collision between fragments in the general spray of ejected material. Physical evidence for collision and overtaking of one fragment by another in the spray is found at Meteor Crater and at nuclear craters, where individual fragments that are formed by coalescence of materials from different

horizons have been recovered on the crater rims. Another possibility is that fragments are ejected, at a fairly late stage in the development of the crater, at very high or nearly vertical ejection angles from the region that becomes the central peak.

From impact experiments in the laboratory, using dense rock targets, Charters and Summers (Ref. III-19) found that, at a late stage in the opening of a small impact crater, a column of material is ejected, in a direction nearly normal to the target surface. Gault² has observed velocities of fragments as high as 200 to 300 m/sec in similar columns ejected from small, high-speed impact craters in basalt. The precise mechanism by which this column is formed is not presently understood, and it is observed experimentally only when the targets are composed of dense, coherent rock. The mechanisms by which central peaks are formed in terrestrial craters from material that has been raised from depths considerably below the crater floor is not understood either. In large, natural craters, a shock reflected from a lower, dense substratum may contribute significantly to the lifting of the rocks in central peaks, and it may also contribute to ejection of fragments at high elevation angles and moderately high velocities from the region of the central peaks.

Whatever the mechanism, if fragments can be ejected at elevation angles on the order of 80 deg and velocities on the order of 500 m/sec, then the difference in time of flight between these fragments and the main part of the ejecta is on the order of 400 to 500 sec, at distances from the center of the main crater corresponding to the Surveyor VII landing site. In other words, a time interval of several hundred seconds is then available for the emplacement of the flows prior to the fallback of the highervelocity ejecta. A time interval of 500 sec would require a flow velocity on the order of 10 m/sec for flows such as the steep-fronted flows, if the material at the termini of the flows all came from the regions near the heads of the flows. If material that now resides at the termini was derived from areas further down the length of each flow, then lower flow velocities are required. A flow velocity on the order of 10 m/sec seems compatible with the evidence of viscosity of the flows based on the final shapes of the flows as they came to rest.

A plausible sequence for the emplacement of the flows and the lunar playas and smooth patch materials can be derived from the qualitative evidence on the relative viscosity of these materials at the time that they were

²D. E. Gault, personal communication to E. M. Shoemaker, April 1968.

emplaced. The demonstrable relative sequences based on superposition relationships, are consistent with the hypothesis that the flows were emplaced in order of increasing viscosity. One of the steep-fronted flows, for example, cuts across and overlies the ridged lobate flow. From the heights of the flow fronts and the relief on the flows, it may be inferred that the steep-fronted flows were more viscous during most of their period of emplacement than was the lobate flow.

The inferred sequence of emplacement illustrated in the explanation of the geologic map (Fig. III-12) has been based on the available evidence on superposition and on a model of emplacement in which it is assumed that all of the units were emplaced in the time period on the order of 10³ sec or less. During this period, late-falling fragments ejected from Tycho were "raining down" and producing secondary craters on units that had become relatively stable. In general, the materials with lowest viscosity were emplaced first, and materials with highest viscosity last.

The oldest unit in the inferred sequence is the patterned debris. Patterned debris is demonstrably overlain by most of the other units and is inferred to be composed of Tycho ejecta, which was stable after ballistic deposition. The next units to be emplaced were the lunar playa and smooth patch materials, and the smooth flow. As shown by the low local relief on the surfaces of these units, these deposits were probably emplaced either as a fluid of very low viscosity or as fluidized systems. The general absence of flow fronts or other relief at the margins of these units and the apparent thinness of these units at their margins suggests their emplacement as fluidized systems. The occurrence of fissures with rounded edges in the lunar playas suggests deflation of the playa material owing to loss of gas after emplacement. If these units are the deposits of arrested, hot-gas solid systems (nueés ardentes), the flow velocities may have been as high as the velocities of terrestrial nueés ardentes (up to 30 or 40 m/sec). These units probably remained hot and semimobile for a considerable time after their emplacement, and they exhibit the lowest crater abundances of all the units mapped, probably because the secondary craters that formed early on these deposits were unstable and disappeared fairly rapidly.

On the basis of smoothness of form, it is inferred that the divergent flow was emplaced next. The surface of this flow is, in some places, nearly as smooth as the smooth flow, but the divergent flow has a distinct flow front and more intrinsic relief on its surface. It was probably emplaced as a viscous fluid and probably solidified earlier than the smooth flow and lunar playa and smooth patch materials. For this reason, more secondary craters were retained on its surface. Emplacement of the divergent flow probably was followed by emplacement of the ridged lobate flow. The ridged lobate flow was apparently emplaced as a still more viscous fluid. Some secondary craters that may have been formed even before the flow had come to rest may be preserved on its surface. The steepfronted flows were probably emplaced very shortly after the ridged lobate flow, inasmuch as they exhibit a similar crater abundance.

The patterned flow is inferred to have been emplaced last. In all probability, the displacement in this flow does not exceed a few tens of meters in most places. The pattern of lineaments weakly preserved on its surface is assumed to be inherited from the patterned debris from which the flow was probably derived. The abundance of craters on the patterned flow is only about 15% less than that observed on the patterned debris. A high density of craters occurs on this flow, probably because very few of the secondary craters formed on it were lost during the minor movement of the material. Flow units, which were emplaced earlier and superposed on the material of the patterned flow, probably were carried along a short distance by the patterned flow.

3. Detailed Geologic Features Observed From Surveyor VII

Features observable from the vantage point of the Surveyor VII camera include parts of several geologic units, most of which were seen in the distance at very low, oblique angles. The units observed in the distance include patterned debris to the west, north, and northeast of the spacecraft, and one patch of smooth patch material to the northeast. Craters and very coarse blocks are observable on the distant geologic units, and provide insight into some of the physical characteristics of these units. In the foreground, detailed features in the immediate vicinity of the spacecraft were observed on the surface of the patterned flow. These features include small craters and a great variety of rocky-appearing fragments, some more than 1 m across.

a. Craters. The craters visible from the Surveyor VII television camera range in diameter from about 13 cm to about 100 m. Craters larger than 30 m across are observed only in the far field, primarily on the patterned debris. A crater as large as 17 m across is visible on the smooth patch material northeast of the spacecraft.

Nearly all of the craters observed on the patterned debris have relatively smooth, raised rims. Scattered blocks occur on these raised rims and within the craters, but the spatial density of blocks is not substantially higher than it is on the areas between the craters. The absence of strewn fields of coarse blocks associated with these craters indicates that the patterned debris consists of weakly cohesive, fragmental material at least as thick as the depths of the observed craters and that the fragmental material has a mean grain size sufficiently small that most of the individual fragments are not resolved by the Surveyor camera (in general, less than 0.5 to 1 mm in diameter). As noted previously, these observations are consistent with the interpretation that the patterned debris consists of relatively loose, or uncemented, ejecta from Tycho. The minimum thickness of this loose debris layer, indicated by the observations from Surveyor VII, is about 20 m, the estimated depth of the largest crater with a smooth, raised rim.

In contrast to craters formed on the patterned debris, the craters observed from *Surveyor VII* on the smooth patch material have blocky rims; these craters range from 5½ m to 17 m across. This indicates that either the smooth patch material or the patterned flow material, which underlies the smooth patch deposit, is more coherent or coarser-grained than the patterned debris and that the coherent material lies at depths not greater than 2 m.

In all the geologic units mapped on *Lunar Orbiter V* photograph H-128 (Fig. III-8), most of the craters with diameters in the range from 8 to 16 m have anomalous shapes. Most are elongate in a north–south direction, approximately radial to the crater Tycho. Some of these craters are elliptical in plan; many are pear-shaped. The narrow part of most pear-shaped craters occurs at the south end of the crater, although a few craters were observed in which the small end was at the north. North-trending fissures, which are common in the patterned flow on which *Surveyor VII* landed, cross some of the craters.

Most of the craters observed in the foreground near Surveyor VII are between 13 cm and 4 m in diameter. Craters smaller than 15 cm are difficult to recognize because of the abundance of coarse, fragmental debris covering the surface of the patterned flow. In the pictures taken at low sun elevation angles, which are best for recognizing small craters, the shadows cast by the fragments tend to hide very small craters or make them difficult to recognize. Most of the small craters are shallow, cup-shaped, and have low, subdued rims.

The rims of most of the craters 13 cm to 4 m in diameter are composed of fragmental material of about the same grain size as the surface material in the inter-crater areas; a few craters about 3 to 4 m across have raised rims of blocky debris. Two craters, one about 20 m in diameter and the other about 30 m, which occur in the patterned flow southwest of the spacecraft, have coarse, blocky rims with blocks up to ¾ m across.

An irregular crater, about 5 m north of the spacecraft and about 3 m in diameter, is filled with coarse blocks ranging from a few centimeters to 60 cm across: a strewn field of blocks extends northwest from the crater (Fig. III-3). This crater probably is of secondary impact origin, formed by low-velocity impact of a block of material ejected from a larger crater southeast or east of the spacecraft. A crater, 100 m in diameter, that lies 300 m to the east of the spacecraft is a likely source from which the block may have been derived. Most, or many, of the fragments within the secondary crater and in the strewn field to the northwest may be pieces of the impacting block. Similar secondary impact craters with asymmetric patterns of ejecta have been observed around ballistic missile impact craters at White Sands Missile Range, New Mexico.

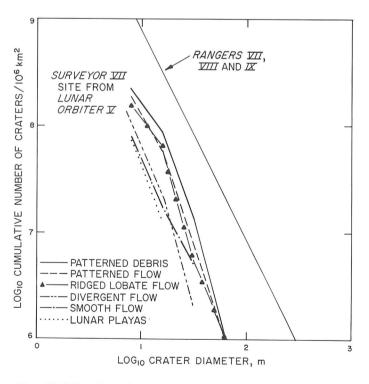


Fig. III-25. Cumulative size-frequency distribution of craters on six geologic units near the Surveyor VII site, compared with the general distribution of small craters on the lunar maria determined from Ranger pictures.

The size-frequency distribution of 8- to 128-m-diameter craters recognizable in *Lunar Orbiter V* photograph H-128 was determined in 1-km² areas on most of the geologic units mapped at the *Surveyor VII* landing site. An aggregate area of 0.53 km² was studied to obtain the size-frequency distribution of craters on the lunar playas; the steep-fronted flows were not studied because the relief on the surfaces of the flows severely limits the study of crater distribution. The size-frequency distribution of craters is slightly different on each geologic unit, but, in all units, it lies considerably below the *Ranger* curve and has an average slope that is somewhat steeper than the

Ranger curve (Fig. III-25). If account is taken of the normal dropoff in number of recognizable craters, as the diameters of the craters approach the limit of resolution of the photograph, then extrapolation of the distribution observed on the *Lunar Orbiter V* photograph suggests the crater size-frequency curve for the patterned flow probably joins the *Ranger* curve at a crater diameter of about 10 m.

The size-frequency distribution of small craters ranging in size from 13 cm to 4 m was investigated in a 209-m² area on the patterned flow, close to *Surveyor VII* (Fig. III-26).

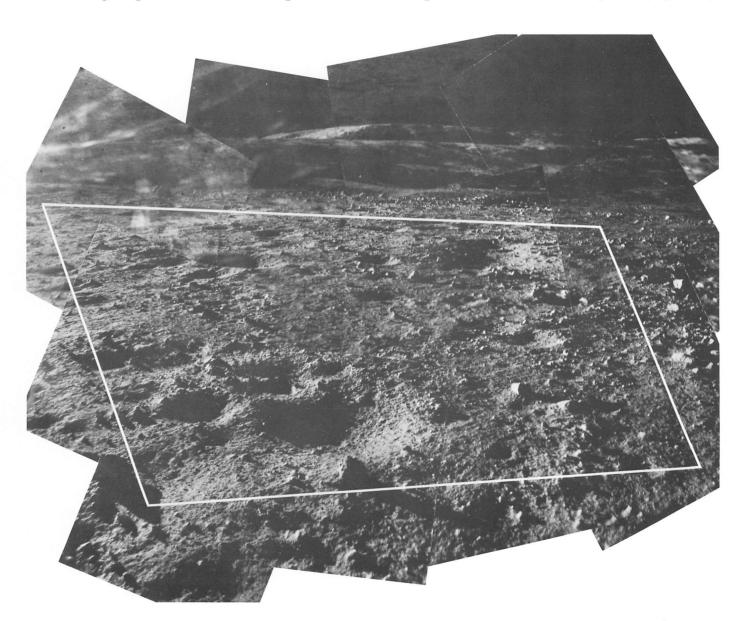


Fig. III-26. Mosaic of narrow-angle Surveyor VII pictures, taken at low sun elevation, of an area north of the space-craft. The area from which the size-frequency distribution of small craters 16 cm to 5 m was determined is outlined (Catalog 7-USGS-100).

A total of 75 craters was counted in the Surveyor VII pictures of this area. The cumulative size-frequency distribution of the small craters, normalized to 10⁶ km², is closely similar to the size-frequency distribution of craters of similar size found at the previous Surveyor landing sites (Fig. III-27). This distribution follows the general size-frequency distribution of craters on lunar plains determined from the Ranger pictures.

b. Thickness of regolith. The lunar regolith has been defined (Ref. III-5) as a layer of fragmental debris of relatively low cohesion which overlies a more coherent substratum. It covers nearly all parts of the lunar surface observed on the maria by Surveyors I, III, V, and VI;

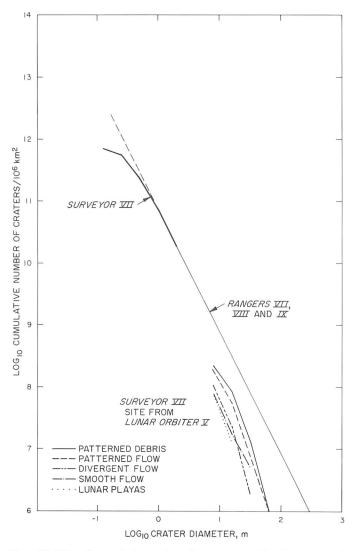


Fig. III-27. Cumulative size-frequency distribution of small craters on the lunar surface in the vicinity of Surveyor VII, determined from Surveyor VII pictures and. Lunar Orbiter V photographs.

it is inferred to have been derived primarily by a process of repetitive bombardment, which also produced the majority of small craters observed nearly everywhere on the lunar surface. The apparent thickness of this layer on the various mare sites investigated with the *Surveyors* ranges from about 1 or 1½ m to more than 10 m. In most places on the maria, it is very fine-grained; at the surface, about 90% of the regolith consists of fragments finer than 1 mm.

At the Surveyor VII landing site, on the rim flank of Tycho, there is an ambiguity both in prior definition and in observational evidence that may be used to interpret the presence, thickness, and characteristics of the regolith. The difficulty arises from the fact that possibly several, and at least one, of the geologic units that make up the rim of the crater are fragmental debris. In the case of the patterned debris, one of the most widespread units on the Tycho rim, the material of this geologic unit also appears to have relatively low cohesion.

We do not intend to apply the term regolith to such widespread blankets of fragmental ejecta associated with large, individual craters on the moon. These units, inferred to be formed by a single event, or by a sequence of a small number of events, during a well defined, short interval of time in lunar history, are more appropriately treated as mappable, regional, geologic units. They may be expected to have certain internal consistencies of structure and to exhibit systematic lateral variations in grain size, shock metamorphism, and other characteristics.

The regolith, on the other hand, is conceived here as a thin layer of material that forms, and progressively evolves, over a longer period of time as a result of an extremely large number of individual events, and possibly as the result of interaction of a number of different processes. The regolith is a strictly surficial layer of debris that conceals underlying geologic units in most places on the moon. Its thickness and other characteristics are a function of total exposure time of the different parts of the lunar surface to a number of surface processes. Among the principal processes are bombardment of the lunar surface by small, solid, interplanetary objects and secondary lunar fragments; mass wasting; and irradiation by high-energy particulate and electromagnetic radiation. Alteration by gases escaping from the lunar interior and other processes not yet recognized may also contribute to the evolution of the regolith.

A new surface freshly formed by a volcanic flow or ash fall or by deposition of an extensive ejecta blanket around a new crater has no regolith; the process of its development, however, begins almost immediately, and the regolith gradually becomes thicker with the passage of time. In this respect, we consider the regolith as a surficial layer analogous to soils on the earth.

Where a regolith has developed on a fragmental geologic unit such as a regional ejecta blanket or a debris flow, the practical distinction between the regolith and the underlying fragmental material must be based on differences in grain size, and aspects of physical and chemical alteration that can be recognized through the data at hand. In particular, the presence of numerous, small craters; a photometrically observable alteration profile or coatings or alteration rinds on individual fragments; or a grain size distribution of the surficial material similar to that observed elsewhere on the regolith can be used as evidence for its presence. At the *Surveyor VII* landing site, there is good evidence for the presence of a thin regolith. The most important evidence is the presence of abundant craters smaller than 4 m in diameter.

The probable mean thickness of the lunar regolith at the *Surveyor VII* landing site can be predicted on the basis of the model of origin by repetitive impact. The observed frequency distribution of the small craters corresponds to that which has been interpreted as an equilibrium or steady-state crater distribution, on the basis of the *Ranger* observations of the lunar plains (Refs. III-8 and III-20) and the television observations of small craters at various *Surveyor* landing sites (Refs. III-1, III-5, III-21, and III-22). The upper crater-diameter limit of the steady-state population on the patterned flow on which *Surveyor VII* landed is evidently about 10 m. At larger crater diameters, the frequency of craters rapidly falls below the steady-state crater distribution curve.

On the basis of experimental crater populations produced by repetitive impact and the observed crater frequency distribution on the lunar plains, the upper crater size limit of the steady-state crater population is found to be about 30 times larger than the lower size limit of all the craters formed whose aggregate area would just cover the surface. The depth of craters at this lower size limit represents the approximate average depth to which the lunar regolith has been overturned, just once, by cratering. This depth is the predicted or theoretical depth of the regolith at any given locality and, in general, corresponds fairly closely to the observed depth. At the Surveyor I landing site, for example, the observed upper limit of the steady-state crater population is at a crater diameter of approximately 200 m; the predicted thickness

of the regolith is, therefore, the characteristic depth of a fresh crater 7 m in diameter. The smallest observed crater, which just penetrates the regolith at the *Surveyor I* site, is 8 m in diameter and about 2 m in depth.

At the Surveyor VII landing site, the surface of the patterned flow should have been turned over, just once, by craters with a diameter of 30 cm or larger; the predicted depth of the regolith is, therefore, on the order of 10 cm. A slightly greater depth would be predicted for the regolith on the patterned debris, and a lesser depth on the other flows and on the smooth patch and lunar playa materials.

In contrast with prediction, the smallest crater with a conspicuously blocky rim observed on the patterned flow is about 3 m in diameter. If the underlying flow were coherent material, this observation would suggest that the thickness of the regolith was on the order of a meter. The patterned flow probably is composed of only weakly coherent, fragmental material, and the actual average thickness of the regolith probably is closer to the predicted 10 cm.

On the basis of the large blocks on the patterned flow that are resolvable in the Lunar Orbiter V photographs and the scattered, very large blocks observed in the Surveyor VII pictures, it seems likely that the material composing the patterned flow is significantly coarsergrained than the material of the regolith. If this is true, it may be expected that individual craters are occasionally formed in, or penetrate, the upper parts of buried, large blocks in the flow; apparently, it is only in these cases that blocky rims are formed around the craters. If the large blocks are relatively widely spaced, then the diameter of the smallest, blocky-rimmed crater observed will be significantly larger than that predicted for a regolith formed on a coherent substratum.

Additional evidence bearing on the thickness of the regolith is provided by the results obtained with the operation of the surface sampler (see Section V of this Report). In one trench excavated by the surface sampler, an object too large to be moved was encountered at a depth of about 3 cm. This object may be a large block in the underlying patterned flow.

c. Fragmental debris. One of the most striking features of the Surveyor VII landing site is the abundance of coarse, relatively angular debris that litters the surface in

the immediate vicinity of the spacecraft. Nearby fragments range from less than 1 mm to several meters across; blocks as much as ten to several tens of meters long occur on the patterned flow on which the spacecraft landed, as well as on more distant geologic units. Most of the blocks more than a meter across probably are original clasts embedded in the patterned debris or in the flows on which they are observed. Most fragments less than 10 cm across, on the other hand, appear to be pieces in the regolith. They probably have been derived by comminution of the coarser fragments or of more coherent material comprising the various geologic units at the *Surveyor VII* landing site.

Fragments coarser than 1 mm in diameter occupy about 18% of the surface; fragments coarser than 10 cm in diameter occupy about 10% of the surface and are an order of magnitude more abundant than fragments of similar size at the *Surveyor VI* landing site in Sinus Medii. It is this much greater number of large fragments that contributes to the distinctive appearance of the *Surveyor VII* landing site (Fig. III-28).

Many of the larger blocks are partly, or entirely, surrounded by a fillet or embankment of material. In general, the best developed fillets occur around the largest

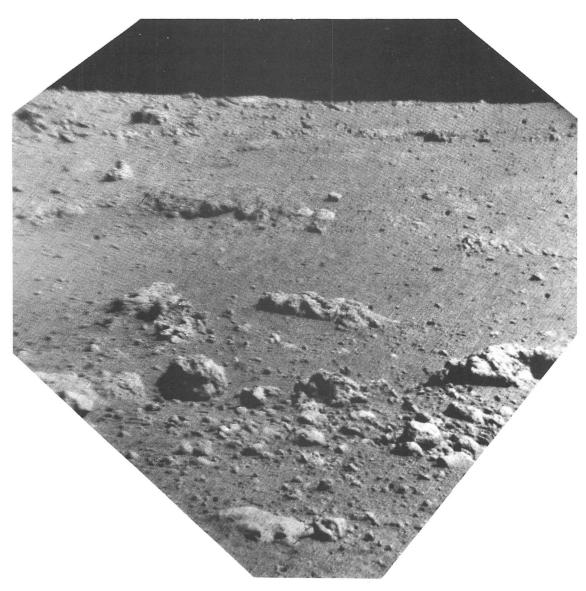


Fig. III-28. Narrow-angle picture of an area west of Surveyor VII showing typical field of fragmental debris. Largest blocks are several meters across (Day 018, 06:48:01 GMT).

blocks. An excellent example of a well developed fillet occurs around block G (Fig. III-5) on the smooth patch of material north of the spacecraft. Block G is about 5 m in diameter and has nearly vertical sides more than 2 m high. The fillet surrounding the block is about 20 m in diameter at the base and about 1 m high at the contact with the block (Fig. III-29). It is possible that this large fillet has a different origin than most of the fillets observed. Block G is probably a large block embedded in the patterned flow underlying the smooth patch material; the fillet could have been produced mainly by the deflation of the smooth patch material around the block during cooling. Fillets observed around smaller blocks close to the spacecraft are composed of fine-grained material. These fine-grained fillets probably are formed by the ballistic trapping of small particles sprayed out from nearby parts of the lunar surface.

Most of the blocks larger than 1 m in diameter are relatively rounded, for the most part, they seem also to be fairly deeply embedded in the units on which they are found. Fragments less than ten or a few tens of centimeters across, however, exhibit a wide range of shapes, and many are conspicuously angular. Some of the smaller fragments seem to have been broken along joint planes and tend to have planar surfaces with rectangular outlines, but others are highly irregular in shape. Some fragments exhibit fresh-appearing chonchoidal spall or

fracture surfaces. Surprising numbers of smaller fragments are resting on the fine-grained matrix of the surface without being significantly embedded in this material.

Fragments in the near vicinity of the spacecraft exhibit a wide range in normal luminance factor (normal albedo) and a wide variety of surface textures and structures. Some fragments are plain, but other fragments are spotted. Some fragments appear to be massive, but others exhibit well developed linear structures on their surfaces, which probably correspond to internal planar or linear structures. Most fragments appear to be relatively dense, but some are clearly vesicular. Most of the fragments probably are pieces of coherent rock, and the variety of observable characteristics probably indicates a variety of lithology. Many, but not all, of the observed characteristics of the rocks have also been observed at the Surveyor landing sites in the maria. The rocks at the Surveyor VII landing site, however, exhibit a far greater variety of textural and structural characteristics than the rocks observed on any single mare site.

Most angular fragments scattered over the surface near the landing site are conspicuously brighter than the finegrained matrix of the regolith at nearly all angles of solar illumination. As observed on the maria, the photometric function of most fragments appears to be more nearly like

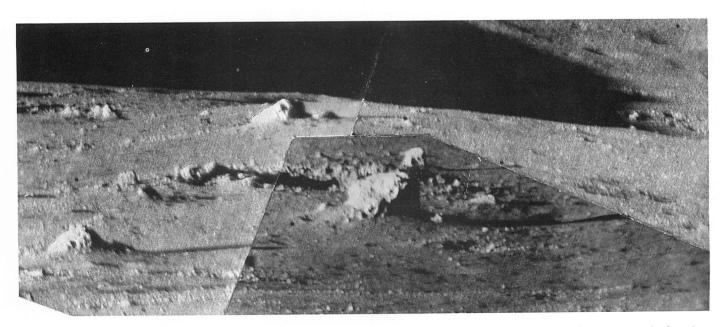


Fig. III-29. Mosaic of narrow-angle Surveyor VII pictures of an area about 350 m northeast of the spacecraft showing large block about 5 m across (block G) on smooth patch material. Swarm of fragments in back of the block are on the rim of a crater about 17 m across (Day 022, 18:29:49 and 18:31:05 GMT).

that of a lambertian scatterer than like that of the finegrained matrix. This shows that the surfaces of most of the fragments are less porous than the surface of the finegrained debris or the surfaces of clods, or aggregates, of fine-grained material.

The normal luminance factor of the angular fragments varies by as much as 50%. The lightest fragments have a normal luminance factor more than 50% greater than that of the fine-grained matrix of the regolith. A few angular

fragments (Fig. III-30), on the other hand, are nearly as dark as the fine-grained material of the surface. These dark, angular fragments appear to be pieces of rock, and not aggregates of fine-grained material. One small, dark fragment was attracted to magnets on the surface sampler (see Section VII-B of this Report); it is possible that most of the dark, angular fragments are rocks rich in magnetite or minerals of high magnetic susceptibility, or that they are mineralogically different in other respects from most of the other rock fragments on the surface.

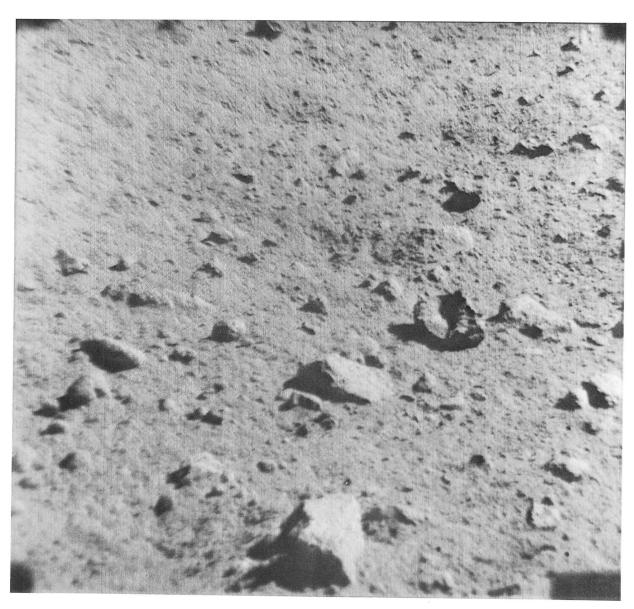


Fig. III-30. Narrow-angle picture of an area about $3\frac{1}{2}$ m from Surveyor VII camera showing a variety of fragments on the lunar surface. Note dark, elliptical fragment about 8 cm across in right center of the picture. Some fragments are angular and others are rounded; some are nearly buried by fine-grained material and others are on the surface (Day 018, 06:22:40 GMT).

Spots, which occur on a large number of fragments (Fig. III-31), are most easily observed on relatively smooth, clean fracture surfaces. In most cases, the spots on a given fragment have irregular, diffuse margins and vary widely in size. In many cases, the light material forms slight bumps, or protrusions, from the surfaces of the fragments; the raised relief of the light material suggests it is more resistant to processes of erosion occurring on the moon.

A densely spotted fragment, which lies about 2 m from the camera, has spots ranging in size from less than 1 mm to about 30 mm. The spots occupy about 30% of the surface of the fragment. The size-frequency distribution of these spots (Fig. III-31d) suggests they may be fragments,



Fig. III-31a. Angular, spotted fragment about 17 cm across, $1\frac{1}{2}$ m from Surveyor VII camera. Bright spots vary in size from less than 1 mm to about 7 mm across (Day 013, 13:58:10 GMT).

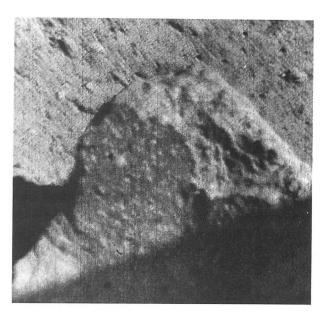


Fig. III-31b. Spotted fragment about $1\frac{1}{2}$ m from Surveyor VII camera. Bright spots have indistinct boundaries and vary from less than 1 mm to about 8 mm across (Day 015, 11:51:05 GMT).

possibly xenoliths, which were partly assimilated in the dark matrix material. The slope of the integral size-frequency function, however, is somewhat steeper than that expected for most fragmentation processes. A more likely explanation for the light spots is that they represent parts of the fragment that differ in crystallinity, or in composition or size of constituent crystals, from the matrix. Somewhat similar spots occur in partially crystallized, volcanic rocks and in a variety of metamorphic rocks on earth.

Small, elongate spots, ranging from 1 to 5 mm in length, were observed on a conchoidal fracture surface on one fragment close to the spacecraft (Fig. III-32). They occupy a few percent of the surface of the fragment, and the long axes of the spots tend to be oriented parallel with one another. Their orientation suggests a flow lineation or flow foliation fabric; their relatively high albedo suggests they may be feldspar. This suggestion is consistent with chemical analyses of both the fine-grained matrix of the regolith and an individual rock at the *Surveyor VII* landing site (see Section VIII of this Report). These analyses indicate the rocks at the *Surveyor VII* landing site are rich in the elemental constituents of plagioclase feldspar.

Some rocks scattered about *Surveyor VII* exhibit one or more sets of linear ridges and grooves on their surfaces. Good examples are found on some of the fragments in the crater of probable secondary impact origin, about

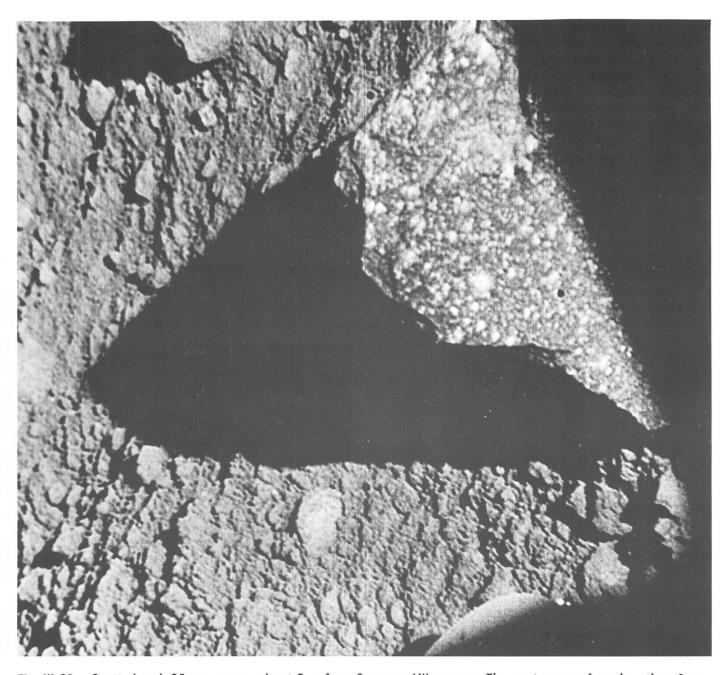


Fig. III-31c. Spotted rock 25 cm across, about 2 m from Surveyor VII camera. The spots range from less than 1 mm to 3 cm in size. Note the indistinct boundaries and irregular shape of most spots (Day 011, 06:29:29 GMT, computer-processed).

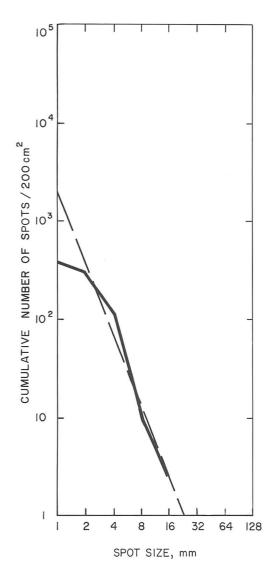


Fig. III-31d. Cumulative size-frequency distribution of bright spots on spotted rock shown in Fig. III-31c. The dashed line represents the mean distribution of the bright spots and is the plot of the function $N=2\times 10^3\,D^{-2.6}$, where N is the cumulative number of spots and D is the diameter of spots in millimeters.

5 m north of the spacecraft. Many of these fragments have nearly planar surfaces with rectangular outlines (Fig. III-33). On some of the fragments, low ridges and grooves occur that are parallel with the edges of some of the larger planar surfaces. These ridges and grooves probably were developed by slight, differential erosion of the exposed edges of planar structures within the blocks.

Intersecting sets of ridges and grooves observed on the surfaces of some blocks are among the most interesting, and perhaps among the most critical, features for inter-

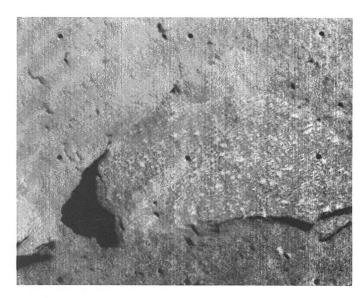


Fig. III-32. Angular block about 18 cm across, about $2\frac{1}{2}$ m from Surveyor VII camera. Block has a conchoidal fracture surface and bright elongate spots that are roughly parallel and range from 1 to 2 mm wide and up to 10 mm long (Day 013, 10:31:04 GMT).

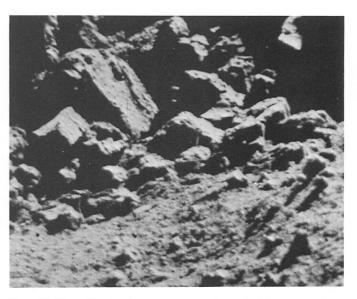


Fig. III-33. Blocks in a crater of probable secondary impact origin, about 5 m from Surveyor VII camera. The largest block is about 40 cm across. Note parallel, elongate ridges about 1 to 2 cm long on surfaces of some blocks (Day 010, 06:52:33 GMT).

pretation of the origin of the flows on the flank of Tycho. One small block with rectangular faces (Fig. III-34) exhibits two sets of linear structures on the side of the block facing toward the camera. One set consists of ridges parallel with the edge of the top surface of the block and

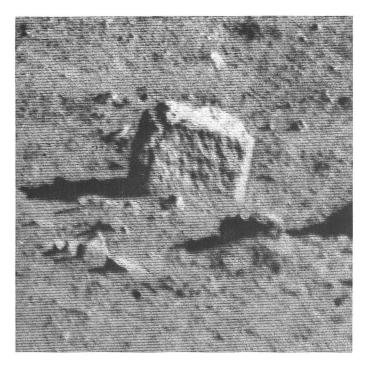


Fig. III-34. Angular block about 10 cm across, about 9 m from Surveyor VII, with two sets of structures on the surface facing the camera. One set consists of ridges parallel with the top edge of the block; the other set consists of ridges and grooves that intersect the first set at an angle of about 70 deg (Day 011, 23:56:00 GMT).

probably reflects planar structures parallel with this surface. The other set consists of ridges and grooves that intersect the first set at an angle of about 70 deg. This second set is not parallel with the edges of any of the observable, nearly planar faces of the block; it cannot be determined whether this second set of structures reflects a second set of internal planar structures or whether it may possibly reflect a set of internal linear structures in the block. In either case, the rock exhibits evidence of two intersecting, distinct sets of structures.

Another small fragment with rectangular faces (Fig. III-35) exhibits two sets of linear features on the top surface of the block. One set consists of ridges parallel with the edge of one side of the block, and the other set consists of short, deep grooves that intersect the first set at an angle estimated to be about 45 deg, as measured on the surface of the block. Again, this second set is not parallel with the edges of any of the observed faces of the block.

The presence of intersecting sets of structures suggests the observed fragments have been dynamically metamorphosed. One set of structures in these fragments prob-

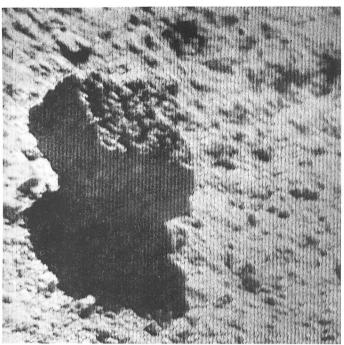


Fig. III-35. Angular block 10 cm across, about $3\frac{1}{2}$ m from Surveyor VII camera. Two sets of intersecting structures form a pattern on the surface of the block. One set consists of ridges parallel with the edge of one side of the block; the other set consists of short, deep grooves that intersect the first set at an angle estimated to be about 45 deg (Day 011, 10:11:26 GMT).

ably corresponds to an original, or primary, structure such as flow banding or rythmic layering, and the other set may correspond to a secondary structure produced by metamorphism such as slaty cleavage. Slaty cleavage that intersects primary structures at a wide range of angles is a common characteristic of shock-metamorphosed rocks.

A few rounded blocks relatively close to the spacecraft are cut by prominent, deep cracks. The appearance of these cracks on one of the blocks (Fig. III-36) suggests it has broken into smaller fragments that have been jostled apart slightly. This jostling may have been caused by impact, by seismic events that slightly disturbed the cracked block, or possibly by thermal expansion and contraction.

Many of the fragments in the vicinity of the Surveyor VII spacecraft have deep pits on their surfaces ranging from a fraction of a millimeter to a centimeter across. These pits are almost certainly vesicles produced by exsolution of a volatile phase at the time the material was molten. A good example of a vesicular fragment is

shown in Fig. III-37a. The vesicles on this fragment are 2 to 10 mm across and most of them appear to be slightly

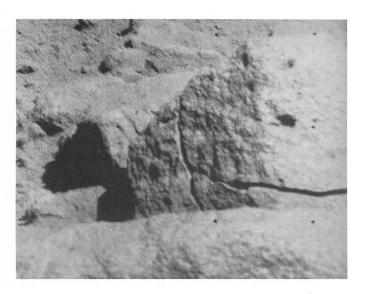


Fig. III-36. Broken block 30 to 40 cm across, about $2\frac{1}{2}$ m from Surveyor VII camera. Note the large cracks on the block. Separation of the pieces of the block may be due to thermal expansion and contraction or to seismic events (Day 015, 11:51:36 GMT).

(a)

Fig. III-37a. Vesicular fragment about 10 cm across, about $2\frac{1}{2}$ m from Surveyor VII camera. Vesicles are 3 to 5 mm across and up to 10 mm long. Most of the vesicles are elongate, with the long axes oriented approximately parallel to one another (Day 018, 13:56:36 GMT).

elongate, with the long axes oriented parallel, or approximately parallel, to one another. Parallel orientation of the vesicles is a common feature of the observed vesicular fragments. In some cases, the vesicles are extremely elongated, as shown in Fig. III-37b. This fragment has fairly large, nearly equidimensional vesicles about a centimeter across, and smaller vesicles as much as 1 cm long but only 1 to 2 mm wide.

One of the most remarkable fragments observed at the Surveyor VII landing site, just south of the spacecraft, seems to be a member of a pile of fragments partially obscured by the spacecraft (Fig. III-38). This fragment has two kinds of surfaces: One side is a smooth, undulating, slightly concave surface; the rest of the surface is relatively rough or porous in texture and is partly occupied by vesicles. A row of vesicles parallel with the edges of the smooth surface occurs along the side of the fragment facing the camera. Some of the vesicles observed on this side of the fragment are elongate and oriented parallel to one another; the orientation of their long axes intersects the row of vesicles and the edge of the smooth surface at a fairly large angle. Thus, in this fragment, there is evidence both of melting and of intersecting structures. The smooth, undulatory surface may be a chilled margin, as

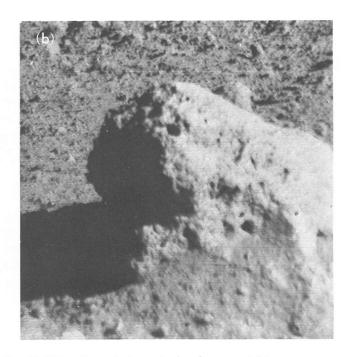


Fig. III-37b. Rounded, vesicular fragment 16 cm across, about 3 m from Surveyor VII camera. The large vesicle near the bottom is about 1 cm across. The small vesicles are up to 10 mm long, but are only a few millimeters across (Day 011, 23:50:47 GMT).



Fig. III-38. Vesicular block about 50 cm long and 15 cm thick, about $4\frac{1}{2}$ m from Surveyor VII camera. Vesicles are up to 1 cm across and 2 cm long. Note smooth, undulating, slightly concave surface on the bottom side of the block and the parallel band of elongate vesicles whose long axes intersect the edge of the smooth surface at a large angle (Day 011, 14:04:59 GMT).

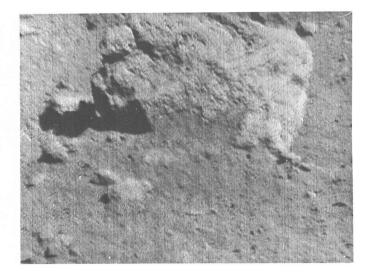


Fig. III-39. Vesicular fragment about 35 cm across, about 7 m from Surveyor VII camera. Note the slight banding due to subdued ridges and grooves that extend from the upper right to the lower left of the block. The long axes of the vesicles are oriented at an angle of about 70 deg to the banding (Day 015, 12:15:11 GMT).

found on the surfaces of volcanic bombs and shock-melted ejecta from impact craters.

Another fragment, about 35 cm across, that lies about 7 m from the camera exhibits both a faint banding and elongate vesicles (Fig. III-39). The banded appearance is due to subdued ridges and grooves on the sides of the fragment. The long axes of the vesicles are oriented at an angle of about 70 deg to the banding. Thus, this fragment also shows evidence of both dynamic metamorphism and melting.

The combined evidence of dynamic metamorphism and melting, observed in a number of fragments at the Surveyor VII landing site, suggests these fragments have been shock-metamorphosed. Analogies to the features observed in these fragments on the rim flank of Tycho may be found in the shock-metamorphosed ejecta at Meteor Crater, Arizona. The fragment shown in Fig. III-40, for example, exhibits two sets of planar structures, as well as vesicles. This fragment is an impactite derived from shocked Coconino sandstone. One set of planar structures consists of relict bedding of the sandstone. The other set is relict slaty cleavage produced in the sandstone during plastic flow of the material under relatively high shock pressure. The relict slaty cleavage intersects the relict bedding in this specimen at an average angle of about 80 deg. The shocked material became molten during decompression in the rarefaction wave that followed the shock front, and vesicles were formed by exsolution of water vapor from the melt. Some vesicles, a fraction of a millimeter to about 2 mm across, are nearly equidimensional, but much larger elongate vesicles were formed parallel with the relict slaty cleavage. Rows, or bands, of vesicles follow the primary planar structure of the material.

To study the size-frequency distribution of the resolvable fragmental debris, five sample areas near Surveyor VII were chosen so that the resolution and area covered would provide particle counts spanning different, but overlapping, parts of the particle size range. The areas are on parts of the lunar surface undisturbed by the spacecraft. A total of 2077 particles, ranging in size from 1 mm to 70 cm, was counted. All recognizable fragments were counted in each area. The estimated mean cumulative distribution of fragments determined in the five sample areas is shown by the heavy line in Fig. III-41. This line is the plot of the equation $N=7.9\times10^5D^{-1.8}$, where N is the cumulative number of fragments per 100 m² and D is the diameter of fragments in millimeters.

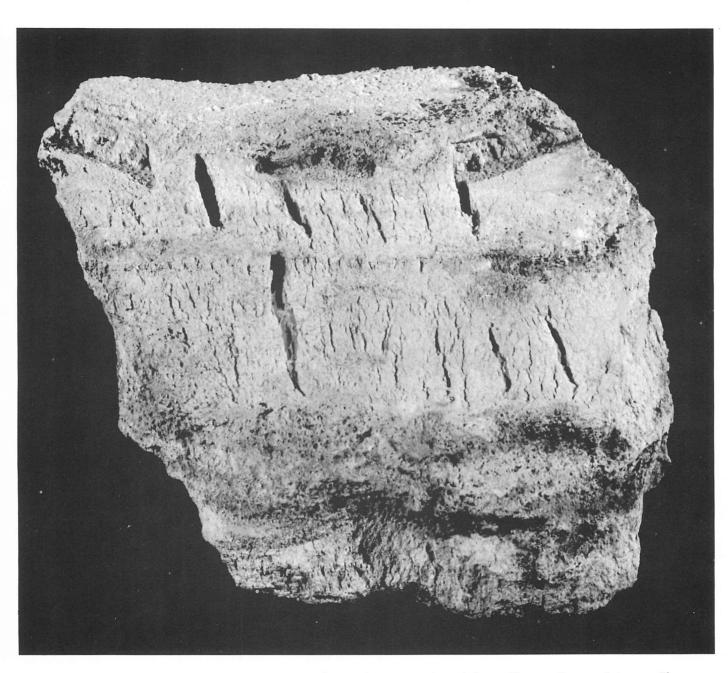


Fig. III-40. Vesicular, shock-melted Coconino sandstone fragment ejected from Meteor Crater, Arizona. Elongate vesicles have formed along the relict slaty cleavage planes. Note relict bedding that parallels the top of the fragment. Slaty cleavage produced in the sandstone during plastic flow under high shock pressures intersects the relict bedding at an angle of about 80 deg.

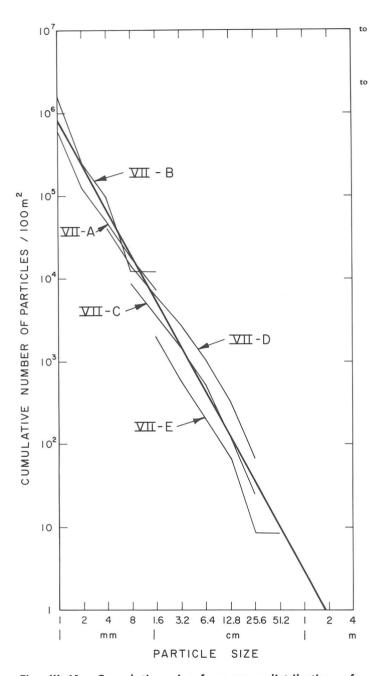


Fig. III-41. Cumulative size-frequency distribution of fragments determined from the Surveyor VII pictures for five sample areas. The locations of the sample areas are shown in Fig. III-10.

The size-frequency distribution curve for the resolvable fragments on the surface around *Surveyor VII* (Fig. III-42) has a much gentler slope than the curves obtained for the mare surfaces around *Surveyors I* and *VI*. There are more fragments larger than 4 mm at the *Surveyor VII* site than at the *Surveyor VII* site, and fewer fragments smaller than 4 mm.

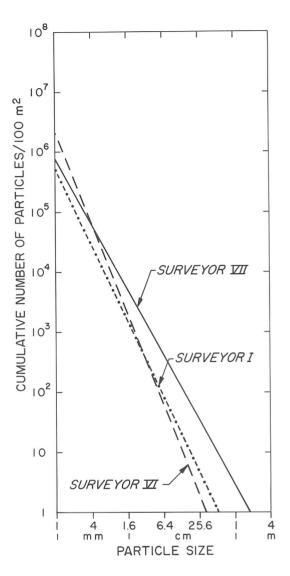


Fig. III-42. Mean cumulative size-frequency distribution of fragments on the lunar surface near Surveyor VII compared with the mean cumulative size-frequency distribution of fragments on the lunar surface near Surveyors I and VI.

As the absolute value of the slope of the size-frequency distribution of particles at the *Surveyor VII* landing site is less than 2, the bulk of the volume and mass of the resolvable fragmental material is represented by the coarser fragments. More than 80% of the material on the surface of the regolith, however, has a particle size less than 1 mm. The size-frequency distribution of particles finer than 1 mm, therefore, must be represented by a different function than the larger fragments, and the overall particle size distribution of the regolith, from the finest unresolved grains to the coarsest fragments, must have at least two modes, one in the submillimeter range and one in the resolvable size range.

The size distribution observed for the resolvable fragments corresponds fairly well to that expected for fragments produced by individual cratering events. As the regolith apparently is only about 10 cm thick, fragments in the regolith much coarser than 10 cm tend to lie essentially on the surface. Larger fragments that are buried to a significant extent must be part of the underlying fragmental geologic units and not a part of the regolith. Thus, the observed coarse blocks probably are formed in two ways:

- (1) By the cratering event that produced Tycho.
- (2) By the individual, subsequent, smaller cratering

events that contributed large fragments scattered on the surface.

Fragments smaller than 10 cm in diameter probably represent: (1) reworked fragmental debris derived from the various geologic units on the flank of Tycho; (2) fragments from the smaller, individual cratering events; and (3) fine-grained material produced by a very large number of impact events by very small meteoroids and micrometeoroids. The size distribution of the submillimeter particles in the matrix of the regolith probably corresponds fairly closely to the particle size distribution that

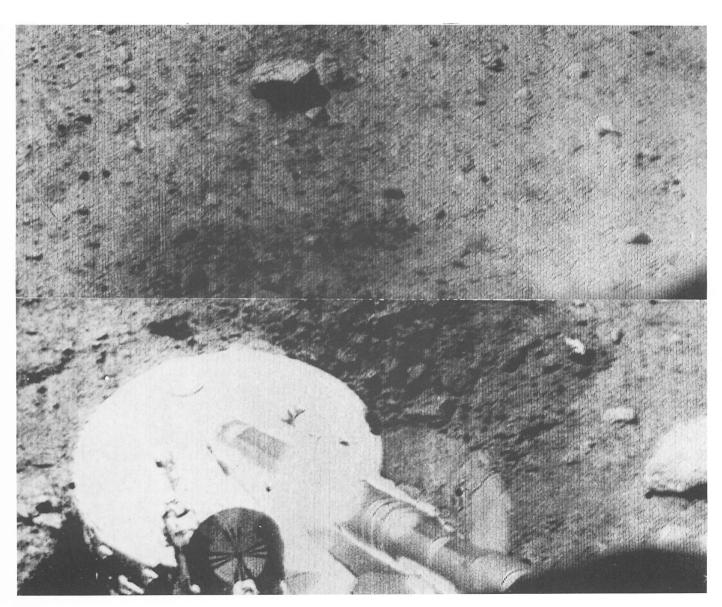


Fig. III-43. Dark material ejected by the impact of footpad 2 during the Surveyor VII landing (Day 015, 08:21:21 and 08:21:27 GMT).

would be produced by multiple small impacts; it could be represented by a power function with a slope of -2.47 over the size range of 1μ to 1 mm.

d. Disturbances of the surface. The lunar surface near Surveyor VII was disturbed by the impact of the footpads during landing and by surface-sampler operations. As observed at each of the Surveyor landing sites on the maria, dark, fine-grained material was exposed at each disturbed-surface area. Material ejected by the footpad impact consists primarily of dark clods or aggregates of fine-grained particles (Fig. III-43). The surface sampler exposed dark material at depths as shallow as a few millimeters.

On the basis of observations at the Surveyor I and Surveyor III landing sites, the hypothesis was advanced (Ref. III-5) that the subsurface material, exposed by landing of the Surveyor spacecraft and by manipulation of the surface, is dark because the subsurface particles are coated with a dark substance called lunar varnish. Under this hypothesis, the rocky fragments are generally brighter than the fine-grained particles on the surface and conspicuously brighter than the subsurface, fine-grained material because they are devoid of varnish. It is supposed that, if the varnish, at one time, had been deposited on these fragments, it has subsequently been scrubbed off by the same processes of erosion that produce round-

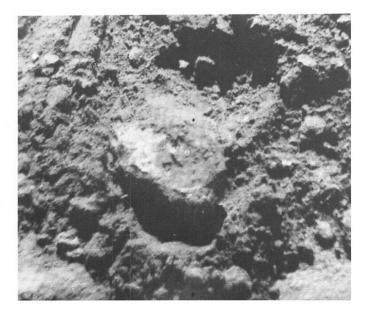


Fig. III-44. Small fragment, about 6 cm across, turned over by surface sampler on Surveyor VII, exposing dark underside. Part of dark coating has been scraped away by surface sampler (Day 018, 06:03:17 GMT).

ing of the fragments. A thin layer of fine particles on the undisturbed parts of the lunar surface is lighter than the subsurface material because these particles also tend to be scrubbed, but the surface layer of fine particles is darker than the exposed surfaces of the rocks because the scrubbing is incomplete, owing to relatively rapid turnover of the particles. Under this hypothesis, the deposition of varnish must take place on the surfaces of fragments at depths as shallow as a millimeter, or the abrupt decrease of albedo with depth would not persist in the face of repetitive cratering. It may be expected, on the basis of the lunar varnish hypothesis, that the buried undersides of the coarser fragments are coated with the varnish.

A test of the hypothesis was provided at the Surveyor VII site when the surface sampler overturned a number of coarse fragments. Two of the overturned fragments are shown in Figs. III-44 and III-45; in both

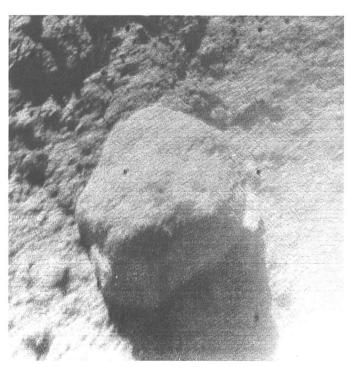


Fig. III-45. Small, rounded fragment, about 5 cm across, picked up and turned over by Surveyor VII surface sampler. Contact between a dark coating on underside of fragment that has been turned up and the bright top surface that has been turned down can be seen along the front surface of the fragment in shadow, which is partly illuminated by sunlight scattered from the spacecraft. The contact between the bright and dark surfaces can also be seen along the sides of the fragment (Day 019, 06:47:40 GMT).

cases, the undersides of these objects proved to be dark. On the object shown in Fig. III-44, most of the dark material may simply be dark, fine-grained particles adhering to the rock. The coating was partly scraped away by the surface sampler, which exposed material of much higher albedo beneath the coating. On the rounded, rock-like object shown in Fig. III-45, the coating evidently is very thin; however, it proved to be resistant to abrasion and scraping by the surface sampler. This coating may be the postulated layer of varnish.

4. Photometric Observations of Lunar Surface

Preliminary photometric measurements have been made from the Surveyor VII television pictures of the undisturbed lunar surface, of fine-grained material disturbed or ejected by the spacecraft footpads and the surface sampler, and of several coarse fragments. The photometric measurements are estimated to be within 15% of the correct values.

The estimated normal luminance factor (normal albedo) of the undisturbed, fine-grained surface material near the spacecraft is 13.4%; coarse fragments scattered over the nearby lunar surface, on the other hand, have estimated normal luminance factors ranging from 14 to 22%. In contrast to the photometric relations observed at the mare landing sites, some of the coarse fragments at the highland site are difficult to distinguish from the fine-grained matrix near zero phase angle because the difference is very small between the reflectance of the fine-grained material and that of some of the fragments. The observed range of normal luminance factor of the coarse fragments examined is similar to that observed in the mare areas, but fine-grained material at the Surveyor VII site has nearly twice as high a normal luminance factor as the fine-grained material at the mare landing sites.

The photometric function of the fine-grained material at the *Surveyor VII* site has been estimated from measurements made at ten different sun angles on a series of selected target areas. The form of the photometric function of the fine-grained material observed at the *Surveyor VII* landing site is similar to that observed at the other *Surveyor* landing sites.

Debris ejected by the spacecraft footpads is noticeably darker than the undisturbed surface (Fig. III-43); the normal luminance factor of the dark material is estimated to be 9.6%. Fine-grained material excavated by the surface sampler also has an estimated normal luminance factor of about 9.6%. The ratio of the normal luminance factor of

the disturbed material to that of the undisturbed material at the $Surveyor\ VII$ landing site (0.72) is very similar to ratios observed on the maria at the $Surveyor\ I$ (0.75) and $Surveyor\ VI$ (0.74) landing sites. Curiously, the optical effects of the alteration processes, which form the observed profile of dark and light material in the fine-grained matrix of the regolith, tend to be proportional to the normal luminance factor of the material. Furthermore, these effects appear to be independent of the type of bedrock. In this respect, the alteration processes are somewhat like the processes that produce soil profiles on earth.

5. Polarimetric Observations of Lunar Surface

Polarizing filters were mounted on the Surveyor VII television camera to serve as analyzers for the detection and measurement of the linearly polarized component of the light scattered from the lunar surface. Pictures of selected areas of the lunar surface were taken through the polarizing filters during most Goldstone passes of the moon. In order to obtain measurements of the variation of the polarized component as a function of phase angle, pictures for polarization measurements were usually taken 25 to 30 hr apart, an interval during which the sun moves 13 to 15 deg. After lunar sunset, pictures of the lunar surface illuminated by earthlight were taken in order to measure the depolarization of earthlight scattered from the lunar surface.

a. Method of polarimetric measurements. Pictures of the lunar terrain were taken with the three polarizing filters rotated sequentially in front of the camera lens while the aperture and other camera conditions were held constant. Variations in apparent radiance of an image element contained in the three pictures are due to a polarized component in the light incident on the filters. The greater the degree of polarization, or percentage of linearly polarized light in the light scattered from the lunar surface, the greater the variation in apparent radiance of image elements in pictures taken through the three filters. Laboratory tests with a slow-scan television camera and three polarizing filters have shown that as little as 5% linearly polarized light can be measured with moderate precision and as little as 3% can be detected.

The orientation of the polarizing filters remains fixed with respect to the camera mirror and rotates with respect to the picture format. The camera was tilted approximately 16 deg from lunar vertical, 290 deg toward lunar azimuth. Pictures taken in the direction of the camera tilt plane will have the polarization axis of filter 2 parallel to the horizon and the axis of filter 4 normal to the horizon.

At other camera viewing positions, the axes of filters 2 and 4 are inclined to the left or right, reaching the maximum inclination of 16 deg at viewing positions at right angles to the camera tilt plane.

For a first approximate analysis, the degree of polarization was computed by dividing the difference between the luminances observed through filters 2 and 4 by the sums of the luminances. The percentage of polarized light estimated by this rough method of analysis and reported here includes polarization introduced by the camera mirror. Final corrections for the polarization introduced by the camera mirror will be based on further tests of mirrors of the type used in the *Surveyor* camera.

b. Polarization of sunlight scattered from the lunar surface. The degree of polarization of sunlight scattered

from fine-grained areas of the lunar surface was found to depend principally on the phase angle. One target area was selected for measurement to the west, another to the northeast, and the third to the east of the spacecraft. Wihin each of these target areas, a smaller, approximately level area was selected and measured in a sequence of pictures for which the phase angles varied from 6 to 120 deg.

Although individual polarization measurements from Surveyor VII pictures exhibit considerable scatter, the degree of polarization of light scattered from the fine-grained parts of the lunar surface (Fig. III-46) is similar to that observed in the lunar highlands at the telescope (Ref. III-23). Most telescopic polarization measurements have been made of the integrated light scattered from areas of more than 100 km² of the lunar surface.

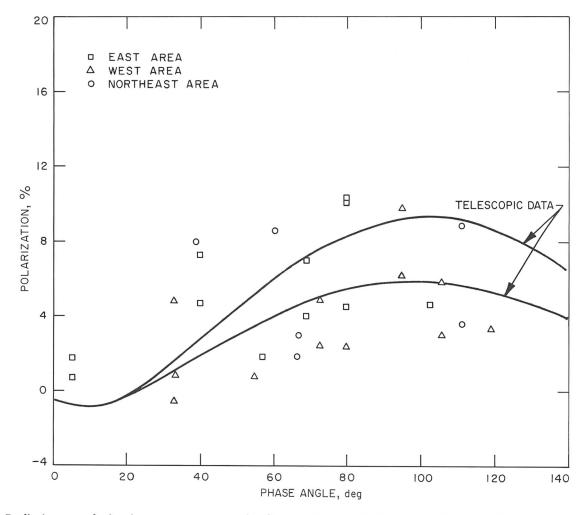


Fig. III-46. Preliminary polarization measurements for fine-grained material on the lunar surface near Surveyor VII compared with polarimetric functions derived from telescopic measurements. The two curves based on telescopic data represent the limits of the range of polarimetric functions reported in Refs. III-23 and III-24.

Maximum polarization observed at the telescope occurs at about 93-deg phase angle and varies from 6 to 9% over the different parts of the terrae. Measurements from the Surveyor VII pictures were made of sample areas of a few square centimeters. An average curve drawn through the Surveyor data points has a maximum of about 7% polarization between 90- and 110-deg phase angles.

The surfaces of some large fragments in the vicinity of *Surveyor VII* exhibit a different polarimetric function than that of the fine-grained material, but other fragment surfaces have nearly the same polarimetric properties as the fine-grained material. The light scattered from the

surfaces of some fragments is as much as 25 to 30% polarized at phase angles of 120 to 125 deg. An abrupt increase in polarization near 120-deg phase angle, observed on several fragments, seems to occur close to the angle of specular reflection for the observed surfaces.

Light scattered from the pitted surface of one slightly rounded, rock-like fragment, about 3.5 m to the northwest of the spacecraft (R-1, Figs. III-47 and III-48), was less than 5% polarized at phase angles below 60 deg. The degree of polarization increased rapidly to 34% at 125-deg phase angle (Fig. III-48). Light scattered from the fresh, conchoidal fracture surface of another fragment, about

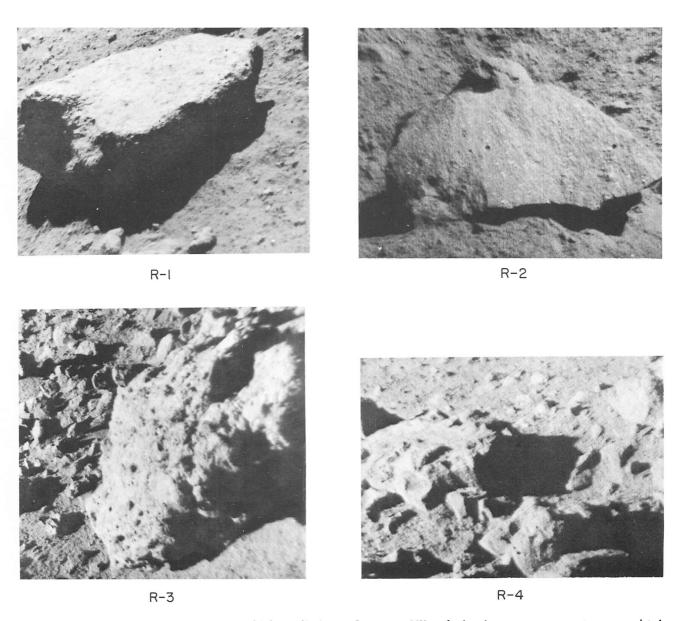


Fig. III-47. Four rock-like fragments for which preliminary Surveyor VII polarization measurements were obtained.

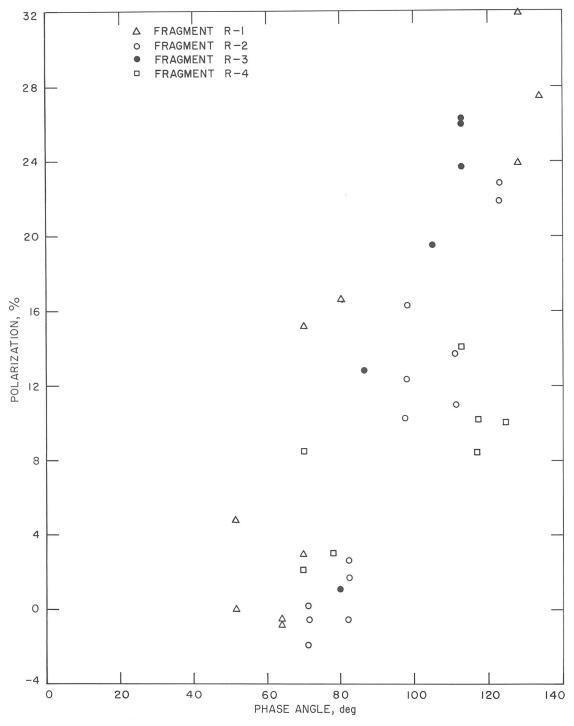


Fig. III-48. Preliminary polarization measurements of light scattered from surfaces of four rock-like fragments near Surveyor VII. Locations of the four fragments are shown in Fig. III-10, and the fragments are illustrated in Fig. III-47.

2 m west of the spacecraft (R-2, Figs. III-10 and III-47). exhibited less than 4% polarization at phase angles of 71 and 82 deg. Polarization increased to 12% at 100-deg phase angle, and then to 23% at 123-deg phase angle (Fig. III-48). These measurements are for the fragment with small, elongate, light spots; similar high polarization, 25% at a phase angle of 120 deg, was observed for the light scattered from the surface of a rounded, vesicular fragment (R-3, Figs. III-10 and III-47). This fragment may be partly, or wholly, glassy. Light scattered from another fragment (R-4, Figs. III-10 and III-47) shows 14% polarization at a phase angle of about 115 deg (Fig. III-48). The highest degrees of polarization probably are observed where light is scattered or reflected from the surfaces of crystalline or glassy rocks and where these surfaces are relatively free of a dust coating.

Surfaces of most fragments examined polarimetrically do not cause a high degree of polarization at phase angles above 100 deg or at angles near which specular reflection might occur. In part, this may be due to unfavorable orientation of most fragment surfaces; it also may be due to a partial coating of dust on the surfaces of some of the fragments. Other fragments observed may consist of shock-lithified, fine-grained material that contains few crystalline grains of sufficient size and proper surface characteristics to strongly polarize the scattered light. It is expected that these fragments would have a polarimetric function similar to that of the fine-grained material of the lunar surface.

In summary, the few preliminary polarization measurements reduced from *Surveyor VII* pictures indicate that the polarimetric function of the undisturbed, fine-grained lunar surface material is similar to the polarimetric function of the lunar highlands measured at the telescope. The polarimetric functions of fragments on the lunar surface, however, have maxima which, in some cases, are several times greater than those observed for the fine-grained material, and at phase angles as much as 20 deg higher. Many of these fragments may be crystalline or glassy rocks.

c. Depolarization of earthlight scattered from the lunar surface. Pictures were taken through the polarizing filters of a target area on a fine-grained part of lunar surface near the spacecraft about 12 hr after sunset. The lunar surface was illuminated by earthlight; the degree of polarization of the incident integrated earthlight was estimated to be 14 to 16% from a series of pictures taken of the earth a few minutes later. Preliminary reduction of the pictures of the lunar surface indicates that the polarization of earth-

light scattered from the lunar surface at a phase angle of 90 deg is about $10 \pm 3\%$. Depolarization of the scattered earthlight probably is due to multiple scattering from the surfaces of grains composing the upper few hundred microns of the surface layer.

d. Post-sunset bright line on the western horizon. As late as 1 hr after the upper limb of the sun had set on the western horizon, a bright line with several bright beads was observed along the western horizon (Fig. III-49). The beads disappeared by groups as the sun dropped lower behind the local horizon. A similar phenomenon was also observed after sunset at the Surveyor VI landing site on Sinus Medii (Ref. III-1). This bright line might be due to the diffraction of sunlight by minute irregularities on the western horizon, to refraction by translucent or transparent particles, to forward (Mie) scattering by particles above the surface, or possibly to a combination of these effects.

During several periods of observation of the bright line, the polarizing filters were sequentially rotated in the camera to measure polarization of this light. If the bright line were caused by diffraction, the light might be partially polarized to a degree that could be measured with the polarizing filters, whereas if the bright line were caused by forward (Mie) scattering or by refraction, a lower degree of polarization would be expected. Preliminary measurements do not reveal any polarized light component along the bright line and the beads. These observations favor the suggestion that the bright line and beads along the horizon are produced primarily by forward (Mie) scattering or by refraction. A detailed analysis of these phenomena will be required, however, before a final assessment can be made as to the cause of the bright line.

6. Interpretation of Geologic Observations

Two major problems can be attacked on the basis of the combined evidence from the *Lunar Orbiter* photographs of Tycho and the *Surveyor VII* television pictures:

- (1) The origin of the geologic units, particularly the flows and the lunar playa and smooth patch materials, on the rim flank of Tycho.
- (2) The origin and evolution of the lunar regolith.

The target for the *Surveyor VII* landing site was selected, in part, with the expectation that the *Surveyor* data would aid in the understanding of these problems, and it is appropriate, therefore, to review the extent to which this expectation has been realized.

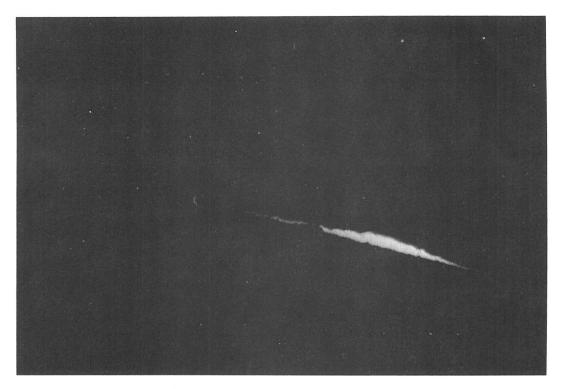


Fig. III-49. Discontinuous bright line, which appeared along the western horizon shortly after sunset. The line gradually became shorter and fainter and disappeared about 2 hr after sunset (Day 023, 06:35:57 GMT).

a. Origin of geologic units at Surveyor VII landing site. Data are available, from both the Surveyor pictures and the Lunar Orbiter photographs, on each of the three types of geologic units known to occur on the rim of Tycho: (1) patterned debris, (2) flows, and (3) smooth patch and lunar playa materials. Part of one geologic unit belonging to each type is observable from Surveyor VII.

The combined evidence from Surveyor pictures and Lunar Orbiter photographs of the patterned debris strengthens the interpretation that this widespread geologic unit is a deposit of fragments ejected from Tycho. Surveyor VI pictures of the raised rims of craters formed on the patterned debris reveal relatively few coarse blocks. This indicates that the debris in which these craters are excavated is comparatively fine-grained and has very low cohesion. From the depths of the craters with smooth, raised rims observed in the Surveyor pictures and from the manner in which the patterned debris, as seen in the Lunar Orbiter photographs, appears to be draped over subsurface scarps, the thickness of material with low cohesion is estimated to be a few tens of meters. This thickness corresponds to that expected for a deposit of fragments ejected on ballistic trajectories from an impact crater the size of Tycho, at a distance from the crater rim corresponding to the position of Surveyor VII (Ref. III-12). The bulk of the material composing the patterned debris at any one place probably landed in a very short interval of time, perhaps on the order of a few seconds. It may be expected that the fragments did not come to rest immediately upon landing on the flank of the crater rim, however. The loose material probably continued to move or flow a short distance, in the general direction of the fragment trajectories, until the kinetic energy of the fragments was finally spent in frictional heating. This brief stage of movement or flow, after ballistic deposition, may account for the relatively smooth surface on the patterned debris.

Several lines of evidence suggest the flows are also derived from fragmental debris ejected from Tycho, but the flows differ from the patterned debris in that the material of the flows moved farther after ballistic deposition on the rim flank of Tycho, and probably for a longer period of time. The size and distribution of blocks coarse enough to be resolved in the *Lunar Orbiter V* photographs suggest the flows are composed largely of fragmental material similar to the patterned debris. No well defined vent, such as a cinder cone or other common kind of volcanic vent, occurs at the upper end of any of the flows. Instead, there is a channel or scarp at the head of some flows, where the Tycho rim material seems to have pulled or flowed away. In other cases, it is difficult to determine the

precise upper limit of the flows. The conflicting evidence of superposition suggests the material of some flows has moved only a short distance from the site at which it was first deposited. Other flows, however, may have moved several kilometers down the Tycho rim flank from their source area.

The great variety of fragments observed in the Surveyor VII pictures of the patterned flow suggests the flow is composed of mixed debris, similar in some respects to the suevite at the Ries Basin, Germany (Ref. III-16). Debris ejected from an impact crater the size of Tycho might be expected to be lithologically diverse, whereas many, but not all, volcanic flows are more homogeneous.

It is of particular interest that the iron content of the fine-grained matrix of the regolith is unusually low at the Surveyor VII site, compared with that at the mare sites, and that the iron content of a relatively bright fragment near Surveyor VII is still lower (see Section VIII of this Report). On the other hand, a dark fragment was found near Surveyor VII that was demonstrably attracted to the surface sampler (see Section VII-B of this Report). The manner in which the dark fragment was held to the magnets indicates the dark fragment probably is unusually rich in iron minerals. These observations suggest that some of the light and dark fragments found on the patterned flow may have been derived from a stratiform complex composed of layers of rocks alternately rich in iron minerals and poor in iron minerals. The composition of the fine-grained matrix of the regolith matches fairly closely that of some feldspathic gabbros of the Stillwater stratiform complex in Montana.3 Tycho may have been excavated partly in a pre-existing gabbroic stratiform complex in the lunar crust.

The presence of numerous fragments that show evidence of having been melted or dynamically metamorphosed, or both melted and dynamically metamorphosed, supports the comparison of the material in the patterned flow with the suevite of the Ries Basin. Many individual fragments strongly resemble impactites. The abundant vesicular fragments on the patterned flow suggest the flow was hot and that it was mobile because of the presence of molten and possibly gaseous constituents.

It seems likely that movement of the flows began immediately upon deposition of most of the fragmental debris on the rim flank of Tycho. Individual fragments probably never stopped moving between the moment of landing and the beginning of movement of the flows; the radial

momentum of the flying fragments may have contributed significantly to setting the flows in motion.

Flows containing the highest proportion of molten ejecta probably had the lowest viscosity and the highest rate of movement. The fronts of these flows would tend to reach downslope positions earlier than the more-viscous flows, and the more-viscous flows would tend to override the upper parts of the lower-viscosity flows. The low-viscosity flows probably remained fluid longer than the high-viscosity flows, but, judging from the observed flow lengths, both high- and low-viscosity flows traveled comparable distances downslope. Some low-viscosity flows spread out more near their termini than the higher-viscosity flows. Movement of the flows may have been arrested as much by spreading and thinning of the flows as by cooling and increase of viscosity.

The lunar playa and smooth patch deposits probably were emplaced as fluids or fluidized systems with very low viscosities. The smooth surfaces of these deposits, the general lack of scarps at their margins, and the local thinness of the deposits, revealed by the protrusion of underlying blocks through the smooth patch deposits, all indicate low viscosity at the time of emplacement.

Two kinds of features suggest the lunar playa and smooth patch deposits were gas-charged at the time of their emplacement and that they may have been emplaced, therefore, as fluidized systems. The rounded edges of branching systems of fissures on the lunar playas suggest that the lunar playa deposits were partially deflated by loss of gas through the walls of the fissures. Similarly, the 1-m-high fillet observed in the Surveyor pictures around block G suggests the surface of the smooth patch deposit surrounding this block may have dropped as much as 1 m, owing to deflation and compaction during cooling. Significant compaction of the deposits may have been accompanied by welding, as in terrestrial nueés ardentes. If the lunar playa and smooth patch deposits were emplaced as fluidized systems, it may be expected that they were emplaced early in the sequence of flows, unless the ejecta from which they were derived landed much later than the material from which the other flows were derived.

The correlation between the occurrence and size of the lunar playa and smooth patch deposits and the occurrence and size of closed depressions suggests strongly that these deposits were derived from material that was relatively uniformly spread over the rim flank of Tycho. If so, this material must have been a relatively thin layer, covering units such as the patterned debris, and it must have been

E. D. Jackson and H. G. Wilshire, personal communication.

laid down after most of the Tycho ejecta had already landed. Such a layer might correspond to the thin fallout layers observed around the nuclear craters Teapot Ess and Jangle U and in Meteor Crater, Arizona (Ref. III-18). These fallout layers are rich in shock-melted material at the time they are deposited. They are composed of relatively fine-grained debris that has been aerodynamically decelerated, and they form the uppermost deposit in the craters and on the crater rims on which they are found. A similar fallout layer may have formed around large lunar craters such as Tycho if a large amount of gas was formed or liberated by impact, which retarded the flight of small lapilli of shock-melted material.

A survey of the rim of Tycho shows that lunar playa deposits tend to be somewhat more abundant and larger near the rim crest than lower on the rim flanks and that the largest playas occur high on the eastern rim. This distribution suggests the initial fallout layer was somewhat thicker near the rim crest of Tycho than farther out on the rim flank, as it is around the nuclear craters. It is of interest that the largest playas occur on the side of the crater from which the longest rays extend. The distribution of both the rays and large playas suggest the spray of strongly shocked ejecta from Tycho was asymmetrical; more strongly shocked material was ejected toward the east, than in other directions. Such an asymmetry in the spray may be the result of high zenith angle of impact (Ref. III-7).

The question may be asked whether the volume of the flows and lunar playa and smooth patch deposits is consistent with the energy available for melting of material in the formation of an impact crater the size of Tycho. Assume, for purposes of calculation, that flows (including the lunar playas) cover the rim flank of Tycho in all directions from the rim crest out to a distance comparable to the position of Surveyor VII. Assume, further, that the mean thickness of the flows is on the order of 10 m. The total volume of the flows is, then, on the order of 120 km². This is equivalent to a sphere with a radius of 3.5 km, which is about the size of an object, with a density like that of stony meteorites, required to produce a crater the size of Tycho, if it is traveling in an orbit like that of the Apollo group of asteroids. The mass of material melted by impact of objects traveling at velocities corresponding to the atmospheric entry velocity of these objects, if they were to strike the earth (16.0 to 31.7 km/sec, Ref. III-25), may be expected to be many times the mass of the impacting body; it varies as a function of the impact velocity and the porosity of the target material and impacting bolide. The specific kinetic energy of each of these objects, if it were all converted to internal energy, would be sufficient to melt a mass of rock one to two orders of magnitude greater than the mass of the impacting bolide. Only a fraction of this energy, of course, actually goes into melting of the target material and the impacting object.

The volume of the flows calculated above probably is an upper bound for a realistic estimate of the volume of molten material. The average thickness of the flows might be greater, but probably only a fraction of the typical flow material, perhaps not more than 50%, may have been molten. It also should be remembered that the melted material was vesicular, and the density of the flows may be well below the density of individual nonvesicular rock fragments.

A volume of flow material comparable to that found on the crater rim flanks may occur within Tycho. This volume should be added to that estimated for the rim, if all the flows are to be accounted for by impact heating. This additional volume does not, however, constitute a difficulty for the hypothesis.

Of more serious concern is the possible volume of melted rock that may have been ejected on lunar escape trajectories or spread very widely over the moon. This may well exceed the volume of flows in the crater and on the rim of the crater. In fact, the most difficult problem with the hypothesis that the flows are derived from impact-melted ejecta lies in explaining how a large volume of melted material was deposited so high on the crater rim. Available experimental evidence and cratering theory suggest it should have been deposited at greater distances from the crater.

b. Evolution of the lunar regolith. The data obtained at the Surveyor VII landing site provide an important test of hypotheses about the origin and evolution of the lunar regolith. We have proposed (Ref. III-5) that the regolith has been formed mainly by the process of repetitive bombardment of the lunar surface by meteoroids and by secondary lunar fragments; other processes such as creep (mass movement) and high-energy radiation, are considered, in our hypothesis, as playing a subordinate role in the evolution of the regolith on the maria. If the regolith is formed primarily by bombardment, certain correlations should be observed between characteristics of the regolith, from one part of the moon to another, and the abundance and size distribution of craters. Because the abundance of craters is much lower on the rim flank of Tycho than it is on the maria, the Surveyor VII landing site is a critical place to study these correlations.

Thickness is one characteristic of the lunar regolith that may be expected to have a direct correlation with crater abundance and that can be estimated from the data obtained at each Surveyor landing site. A rough positive correlation between thickness and crater abundance was observed on the maria (Ref. III-1). There the estimated thicknesses vary from 1 to 2 m to 10 to 20 m. On the basis of the observed crater distributions on the rim flank of Tycho, the thickness of the regolith was expected to be about 10 cm or less, much less than that found on the maria. This expectation proved to be somewhat difficult to verify, because of difficulties in determining the thickness of a regolith that has developed on pre-existing units of fragmental material. The observations of craters with blocky rims appear to be consistent in a general way, however, with the prediction.

Secondary cratering may have been a major process in the formation of the observed regolith at Tycho. The sizefrequency distribution of the craters observed on each geologic unit is consistent with either a primary or secondary origin of the craters (see Ref. III-8). If all the geologic units were emplaced in rapid succession, then more than half of the craters observed in the Lunar Orbiter V photographs on the patterned debris and on the patterned flow probably are Tycho secondaries. A significant fraction of the small craters (smaller than a few meters in diameter) that have been formed on the patterned flow might be Tycho secondaries as well. Thus, the rim flank of a large crater like Tycho may have a thin regolith produced very early by late-falling secondary fragments. At present, we know of no way to distinguish such a regolith from one produced over a much longer time interval by meteoroid bombardment, except possibly by the presence or degree of development of alteration profiles.

Size-frequency distribution of the fragmental debris is another characteristic of the regolith that is correlated with crater abundance and with thickness. From the rough correlation observed on the maria (Ref. III-1), the absolute value of the exponent of the size-frequency distribution function for the fragments in the regolith on the rim flank of Tycho was expected to be lower than that observed for the regolith on the maria. It was expected also that more coarse fragments would be observed in the regolith on the rim flank of Tycho than on the maria. Both of these expectations were confirmed by Surveyor VII, but, as in estimating the thickness of the regolith, there is an ambiguity in the results because the regolith has been formed on pre-existing units of fragmental material.

On a coherent substratum, the regolith should be very thin in the earliest stages of its development, and the individual coarse fragments ejected from craters excavated in the substratum will project above the general level of the surface of the regolith or tend to rest nearly on the surface. The size-frequency distribution of these coarse fragments (fragments larger in diameter than the thickness of the regolith) should correspond approximately to the sizefrequency distribution observed in strewn fields of fragments found around individual fresh impact craters. It is of some interest, therefore, that the size distribution of the coarser fragments observed around Surveyor VII is closely similar to the size distributions observed in strewn fields of fragments around two craters at the Surveyor III site (Fig. III-50). At neither the Surveyor III or VII landing sites are the observed fragments likely to have been excavated from a coherent substratum, but they probably are derived from still coarser fragmental material underlying the regolith at both sites. The observed sizefrequency distributions of the coarse fragments at both sites corresponds closely to that expected for the debris ejected from individual impact craters in coherent material (Ref. III-5).

The fine-grained material between the coarser, protruding fragments at the *Surveyor VII* landing site, on the other hand, is not comparable to the fine-grained debris ejected from individual impact craters in coherent rock. As shown by comparison with ejecta from impact craters (Fig. III-50), the matrix of the regolith is too fine-grained to have been produced by one or a small number of impact cratering events. It probably is the product of an extremely large number of impacts of small meteoroids and micrometeoroids.

The observed size-frequency distribution of particles smaller than ½ m at the *Surveyor VII* landing site is interpreted to be mainly the product of two somewhat different processes: (1) deposition of fragments ejected from a relatively small number of craters, a few meters to a few tens of meters across; and (2) repetitive bombardment of the Tycho rim flank by large numbers of small meteoroids and micrometeoroids. The first process probably has produced most of the fragments coarser than a few centimeters, and the second process most of the fragments finer than a few centimeters. Most fragments coarser than about ½ m probably are part of the debris units underlying the regolith and are ejecta from Tycho.

A thick, mature regolith, such as found on the maria, is composed predominantly of the fine-grained debris produced by repetitive bombardment of the moon by small meteoroids and micrometeoroids and by small secondary

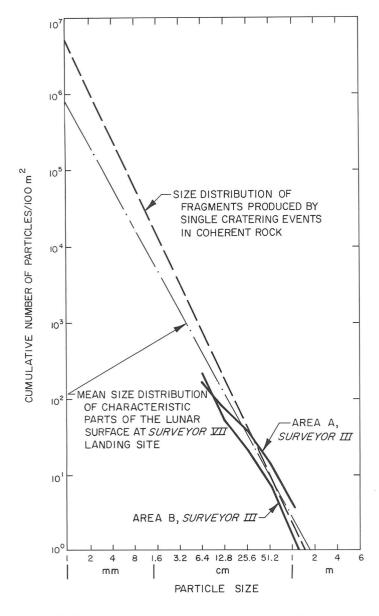


Fig. III-50. Cumulative size-frequency distribution of fragments on the lunar surface near Surveyor VII compared with size distribution of fragments produced by cratering events in coherent rocks. Curves labeled area A and area B are the size-frequency distributions of fragments in strewn fields of blocks around two craters near Surveyor III.

particles. Fewer coarse fragments are observed on, or protruding from, the surfaces of the maria, because craters deep enough to penetrate the regolith are much more widely spaced on the maria than on the rim flank of Tycho.

The presence of comparatively dark, fine-grained, subsurface material, exposed where the surface was disturbed by the *Surveyor VII* spacecraft, shows that the regolith

has been altered on the rim flank of Tycho, as it has been on the maria. Observations of coatings on the undersides of rocks overturned by the surface sampler lends support to our hypothesis that the particles in the subsurface are darker than those on the surface because they are coated with lunar varnish.

The principal photometric differences between the regolith at the Surveyor VII landing site and at the previous mare landing sites are in the fine-grained matrix, as seen both on the undisturbed surface and in the subsurface. The coarse fragments have about the same range of normal luminance factor on the rim flank of Tycho as on the maria, but the fine-grained matrix has a much higher normal luminance factor on the rim flank of Tycho than on the maria. Tycho is such a prominent bright feature, when observed through the telescope at low phase angles, because the fine-grained matrix of the regolith is bright.

The fact that fine-grained particles on both the undisturbed surface and in the subsurface have a higher normal luminance factor than the corresponding surface and subsurface particles on the maria suggests that the fine particles are less thoroughly coated with varnish in a young regolith like that on the rim flank of Tycho. As time passes, the particles probably become more and more thoroughly coated. Scrubbing of the particles on the surface by impact and by radiation tends to remove a certain proportion of the coating on the particles exposed at the surface, but this loss is more than compensated by deposition of more varnish on the particles in the subsurface. Thus, with increasing age, the regolith matrix becomes increasingly dark, both on the surface and in the subsurface. This darkening may continue until the subsurface particles are almost completely coated.

In terms of our hypothesis, the principal reason why the crater and rim deposits of Tycho and of other bright ray craters have a relatively high albedo is that these craters are mantled with a thin regolith that is only partly altered or in which the particles are only partly coated. Ray craters are young features on the lunar surface; with the passage of time, the albedo of their surfaces probably changes gradually and approaches that of other craters that lack rays.

The presence of both light and dark fragments of possibly different iron content around *Surveyor VII* suggests that other differences in albedo of the lunar surface may be due to differences in composition (see Section VIII of this Report). Whereas some differences in albedo seem clearly related to differences in age and alteration of the

regolith, other differences such as the general contrast in albedo between the maria and the lunar highlands may be due primarily to differences in composition. Most parts of the moon, as it is observed through the telescope, probably are covered with a mature, altered regolith. After a period of time, the albedo of the regolith probably approaches a steady value that is controlled by the composition of the material on which the regolith is formed. It is not yet clear, however, just how the albedo is controlled by composition.

E. Observations of the Earth

The relatively high latitude (41°S) of the Surveyor VII landing site made it possible to observe the earth throughout the lunar day. Pictures of the earth were taken several times before conjunction and about every 22 to 25 hr afterward (Fig. III-51). Each time, a series of pictures was taken for polarization measurements of earthlight. The pictures are being used to study the integral photometric and polarimetric functions of the earth.

Starting at 17:11 GMT on Day 022, a series of earth pictures was taken every 2 or 3 hr (Fig. III-52). The final series was taken on Day 023 at 19:37 GMT. This resulted in a sequence of earth pictures at 12 different periods during 26 hr; these pictures provide the information needed to study the variation in reflectance of the earth as a func-

tion of rotation and changing cloud distribution during a single day. The reflectance of the earth observed from the *Surveyor* pictures was about 15 to 20% higher than expected. Digital data processing procedures are being carried out to provide more accurate measurement of the earth's reflectance as viewed from the moon during the January 1968 lunation.

Preliminary polarization measurements indicate that the polarized component of the earthlight varies as a function of cloud cover and the changing patterns of oceans and continents during rotation. Specular polarization appears to occur over an area of about $2\times 10^6~\rm km^2$ in the approximate geometric center of the earth's illuminated crescent. The degree of polarization of earthlight from the specular reflection area varied from 26 to 30% over clear parts of the oceans, 12 to 16% over clear parts of the continents, and 4 to 8% over clouds. Thus, the cloud distribution over the specular reflection area has a strong effect on the degree of polarization of earthlight. The degree of polarization of earthlight from areas beyond the zone of specular reflection is much less; it averages from 3 to 6%.

The maximum polarization of integrated earthlight occurs at about 90-deg phase angle and decreases almost linearly to nearly zero at 0- and 180-deg phase angles. Digital data processing procedures are being carried out to determine more accurately the polarimetric function of the earth.

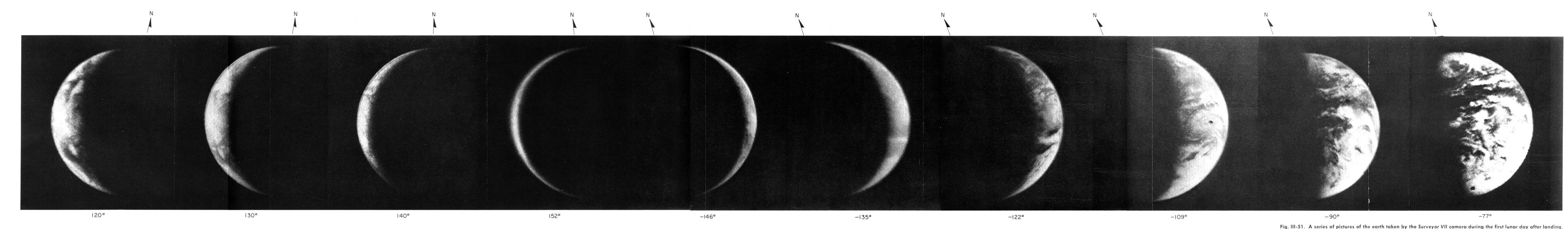


Fig. III-51. A series of pictures of the earth taken by the Surveyor VII camera during the first lunar day after landing. The first four frames show a waning earth; the later frames show a waxing earth. The phase angle is shown below each picture.

JPL TECHNICAL REPORT 32-1264

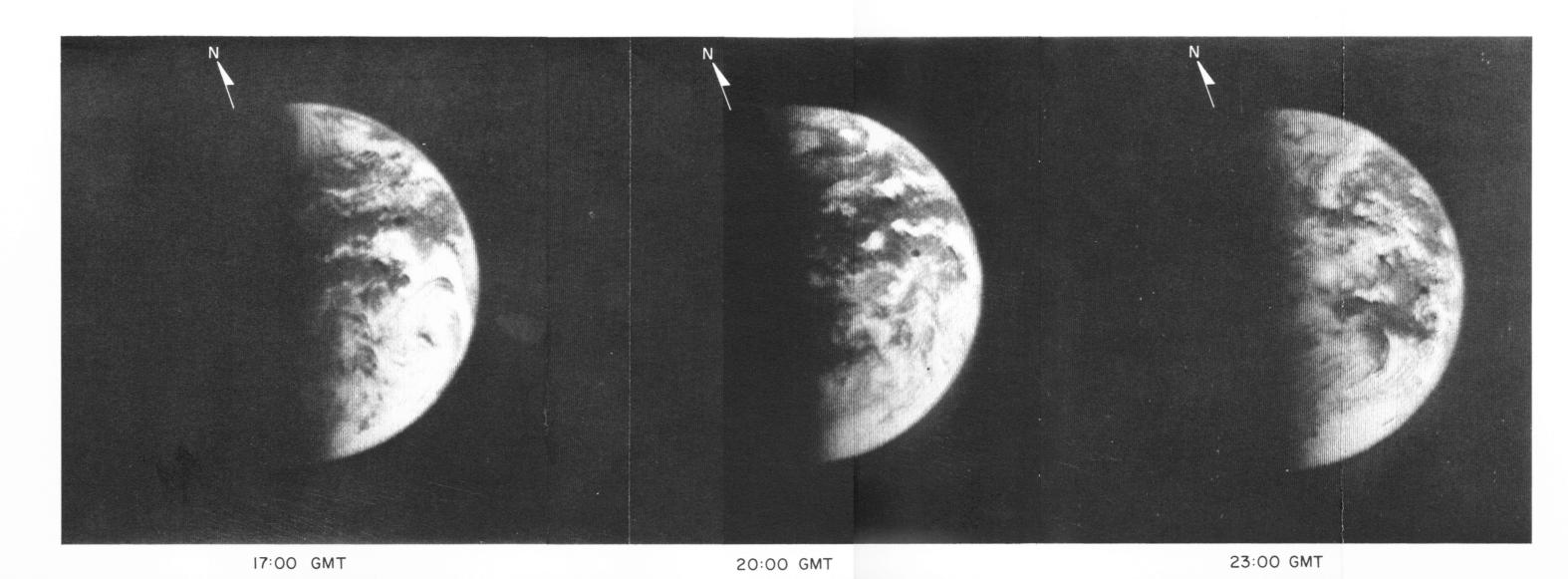
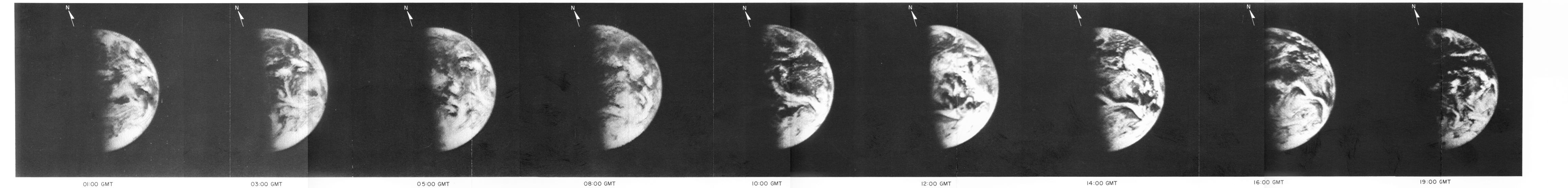


Fig. III-52. Twelve pictures, covering a 26-hr period on Days 022 and 023, of the partially illuminated earth taken by the Surveyor VII camera. The earth rotated 180 deg from left to right during the 26-hr viewing period, or about 30 deg between successive pictures. Sunrise occurs on eastern Australia at about 20:00 GMT. At 03:00 GMT, sunrise occurs along the east coast of Africa; most of the Indian Ocean is covered by clouds.

JPL TECHNICAL REPORT 32-1264



References

- III-1. Morris, E. C., Batson, R. M., Holt, H. E., Rennilson, J. J., Shoemaker, E. M., and Whitaker, E. A., "Television Observations from Surveyor VI," Surveyor VI: A Preliminary Report, Special Publication 166, pp. 11-40, National Aeronautics and Space Administration, Washington, D. C., 1968.
- III-2. Batson, R. M., "Surveyor Spacecraft Television Photogrammetry," Photogrammetric Engineering, pp. 1365–1372, December 1967.
- III-3. "Calibration of the Surveyor VII Stereo Mirror," Flight Projects, Space Programs Summary 37-50, Vol. II, pp. 96–103, Jet Propulsion Laboratory, Pasadena, Calif., March 31, 1968.
- III-4. Benes, M., "Complete Error Analysis of Relative and Absolute Orientation Methods for Extraterrestrial Stereophotogrammetric Mapping Purposes," *American Society of Photogrammetry* (in press).
- III-5. Shoemaker, E. M., Batson, R. M., Holt, H. E., Morris, E. C., Rennilson, J. J., and Whitaker, E. A., "Television Observations from Surveyor III," Surveyor III: A Preliminary Report, Special Publication 146, pp. 9-60, National Aeronautics and Space Administration, Washington, D. C., 1967.
- III-6. Gilbert, G. K., "The Moon's Face; A Study of the Origin of Its Features," Bull. Phil. Soc. Wash., Vol. 12, pp. 251–292, 1893.
- III-7. Shoemaker, E. M., "Interpretation of Lunar Craters," *Physics and Astronomy of the Moon*, Academic Press, New York, 1962.
- III-8. Shoemaker, E. M., "Preliminary Analysis of the Fine Structure of the Lunar Surface," *Ranger VII. Part II: Experimenters' Analyses and Interpretations*, Technical Report 32-700, pp. 75–134, Jet Propulsion Laboratory, Pasadena, Calif., February 10, 1965.
- III-9. Baldwin, R. B., *The Face of the Moon*, Chicago University Press, Chicago, 1949.
- III-10. Urey, H. C., "The Origin and Development of the Earth and Other Terrestrial Planets," *Geochim. et Cosmochim. Acta.*, Vol. 1, pp. 209–277, 1951.
- III-11. Kuiper, G. P., "On the Origin of the Lunar Surface Features," *Proc. Nat. Acad. Sci. Wash.*, Vol. 40, No. 12, pp. 1096–1112, 1954.
- III-12. Shoemaker, E. M., "Ballistics and Throwout Calculations for the Lunar Crater Copernicus," Proceedings of the Geophysical Laboratory, Lawrence Radiation Laboratory Cratering Symposium, UCRL-6438, Part II, pp. Q 1–31, University of California, Lawrence Radiation Laboratory, Livermore, Calif., March 1961.
- III-13. Wesselink, A. J., "Heat Conductivity and Nature of the Lunar Surface Material," *Bull. Astron. Institutes of the Netherlands*, Vol. X, No. 390, April 23, 1948.
- III-14. Urey, H. C., "Water on the Moon," Nature, Vol. 216, No. 5120, pp. 1074–1075, December 16, 1967.

References (contd)

- III-15. Shoemaker, E. M., Gault, D. E., Moore, H. J., and Lugn, R. V., "Hyper-velocity Impact of Steel into Coconino Sandstone," Am. Jour. Sci., Vol. 261, No. 7, pp. 668–682, 1963.
- III-16. Shoemaker, E. M., and Chao, E. C. T., "New Evidence for the Impact Origin of the Ries Basin, Bavaria, Germany," *J. Geophys. Res.*, Vol. 66, No. 10, pp. 3371–3378, 1961.
- III-17. Moore, H. J., "Cohesion of Material on the Lunar Surface," Rangers VIII and IX. Part II: Experimenters' Analyses and Interpretations, Technical Report 32-800, pp. 263–270, Jet Propulsion Laboratory, Pasadena, Calif., March 15, 1966.
- III-18. Shoemaker, E. M., "Impact Mechanics at Meteor Crater, Arizona," *The Moon, Meteorites, and Comets—The Solar System*, Vol. IV, pp. 301–336, Chicago, Chicago University Press, 1963.
- III-19. Charters, A. C., and Summers, J. L., "Some Comments on the Phenomena of High Speed Impact:" Proceedings of the Decenial Symposium, White Oak, Md., U. S. Naval Ordnance Laboratory, 1959.
- III-20. Trask, N. J., "Size and Spatial Distribution of Craters Estimated from Ranger Photographs," Ranger VIII and IX. Part II: Experimenters' Analyses and Interpretations, Technical Report 32-800, pp. 249–338, Jet Propulsion Laboratory, Pasadena, Calif., March 15, 1966.
- III-21. Rennilson, J. J., Dragg, J. L., Morris, E. C., Shoemaker, E. M., and Turkevich, A., "Lunar Surface Topography," Surveyor I Mission Report. Part II: Scientific Data and Results, Technical Report 32-1023, pp. 7-44, Jet Propulsion Laboratory, Pasadena, Calif., September 10, 1966.
- III-22. Shoemaker, E. M., Batson, R. M., Holt, H. E., Morris, E. C., Rennilson, J. J., and Whitaker, E. A., "Surveyor V: Television Pictures," Science, Vol. 158, No. 3801, pp. 642–652, November 3, 1967.
- III-23. Dollfus, A., "The Polarization of Moonlight," *Physics and Astronomy of the Moon*, pp. 131–160, Academic Press, 1962.
- III-24. Wright, F. E., Wright, F. H., and Wright, H., "The Lunar Surface: Introduction," *The Moon, Meteorites, and Comets—The Solar System*, pp. 1-47, University of Chicago Press, 1962.
- III-25. Whipple, F. L., and Hughes, R. F., "On the Velocities and Orbits of Meteors, Fireballs, and Meteorites," *Meteors*, presented at a symposium on meteor physics in July 1954, special supplement (Vol. II) to *J. Atmos. Terr. Phys.*, pp. 149–156, 1955.

IV. Lunar Surface Mechanical Properties

R. Choate, S. A. Batterson, E. M. Christensen (Chairman), R. E. Hutton, L. D. Jaffe, R. H. Jones, H. Y. Ko, R. L. Spencer, and F. B. Sperling

The Surveyor VII landing site, a highland region near the rim of the crater Tycho, provided an opportunity to investigate the lunar surface mechanical properties¹ of an area thought to be quite different from the previous mare landing sites. The influence of the greater rock population on the mechanical properties at this landing site, compared with that of previous Surveyor landings, is presented, along with properties derived from telemetry data and from studies of pictures of surface disturbances caused by the landing impact. Analyses and laboratory simulations were performed to assist in the interpretations.

A. Spacecraft Landing

1. Description

An assessment of the *Surveyor VII* lunar landing, based on touchdown telemetry data and on the post-landing attitude determination, shows that the spacecraft attitude and

 1 In this section, centimeter-gram units are used. To convert to foot-pound units, the following factors apply: 1 m = 3.28 ft; 1 cm = 0.394 in.; 1 N (newton) = 10^{5} dynes = 0.225 lb; 1 N/cm² = 1.45 lb/in.².

landing velocities at touchdown were close to the optimum design values.

The basic configuration (Fig. IV-1) and landing mechanism for *Surveyor VII* were essentially the same as for previous *Surveyors* (Refs. IV-1 through IV-4). During landing impact, the three landing legs rotate upward against the resistance of shock absorbers. Following initial impact, the shock absorbers re-extend, returning the legs to their pre-touchdown positions. Additional capability for energy dissipation is provided by crushable honeycomb blocks mounted on the underside of the spaceframe, inboard of each leg, and by crushable footpads.

Figure IV-2 shows the axial loading histories of the three shock absorbers, as measured by strain gages, throughout the landing phase. Peak loadings and times of initial footpad contact are given in Table IV-1. An evaluation of these data and other engineering telemetry has resulted in the following reconstruction of events during the final descent and landing sequence. The 3.1-m/sec velocity mark was generated about 7.4 sec before touchdown at an altitude of 13 ± 1 m. Immediately following

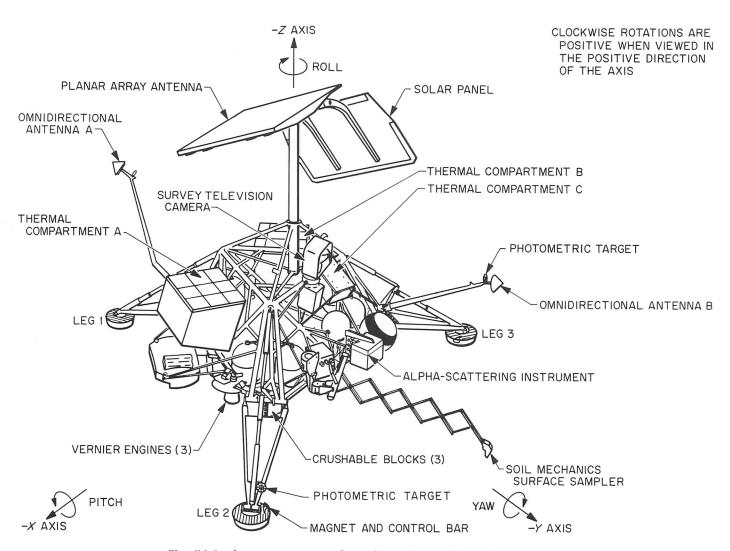


Fig. IV-1. Surveyor spacecraft configuration and coordinate system.

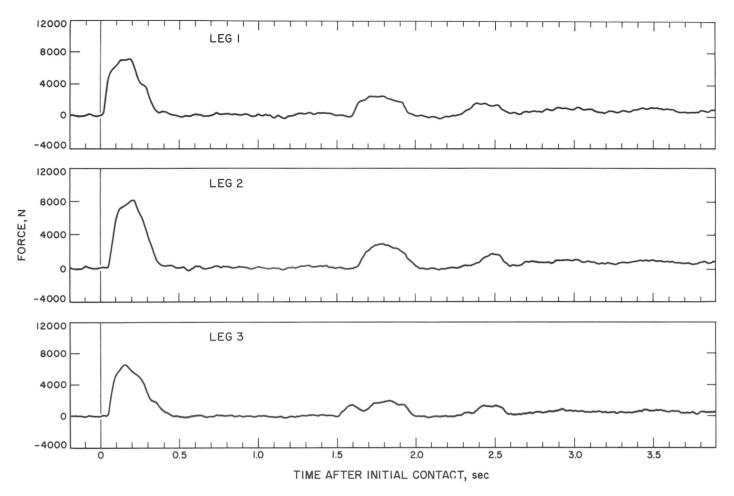


Fig. IV-2. Strain-gage telemetry data showing shock-absorber axial load histories during landing.

Table IV-1. Maximum shock-absorber forces and footpad impact times

Leg	Maximum shock-absorber force, N	Time of impact after initial contact, sec
1	7300 ±400	O ^a
3	6550 ±400	0.022 ± 0.004
2	7800 ±400	0.048 ± 0.004
"Leg 1 impact time was 01:05:37.612 ±0.0002 GMT (the time of receipt of signal		

 $^{\mathrm{a}}$ Leg 1 impact time was 01:05:37.612 \pm 0.0002 GMT (the time of receipt of signal on earth).

this mark, the spacecraft was slowed to a constant descent velocity of 1.6 ± 0.2 m/sec, which was maintained until an altitude of 3.6 ± 0.3 m was reached about 1.3 sec before touchdown. At this time, all three vernier engines were shut off, resulting in a free-fall period until ground contact, during which the vertical velocity increased to 3.8 ± 0.2 m/sec. Changes in angular orientation between the spacecraft attitude at the 3.1-m/sec mark (spacecraft attitude during descent, just before engine cutoff, was

constant) and the spacecraft attitude after settling were 3.1 ± 0.1 deg in pitch, -1.7 ± 0.1 deg in yaw, and 0.0 ± 1 deg in roll.

An analytical simulation, using the observed leg impact sequence 1-3-2 and times between leg impacts, indicated that, at initial touchdown, there was an angle of 3.3 deg between the spacecraft X–Y plane and ground and that the mast was tilted down in a direction 213.3 deg clockwise from leg 1 (from the +Y axis, looking down on the spacecraft, Fig. IV-3). Star, planet, and sunset sightings with the television camera after landing established the final spacecraft tilt, due to the local ground slope, as 3.1 deg in a direction 189 deg clockwise from leg 1.

At the time of initial touchdown, the attitude of the spacecraft, with respect to the local vertical, was determined by subtracting the angular motion between initial touchdown and final position from the post-landing attitude. This relative, angular motion was calculated from the landing simulation and from gyroscope telemetry data.

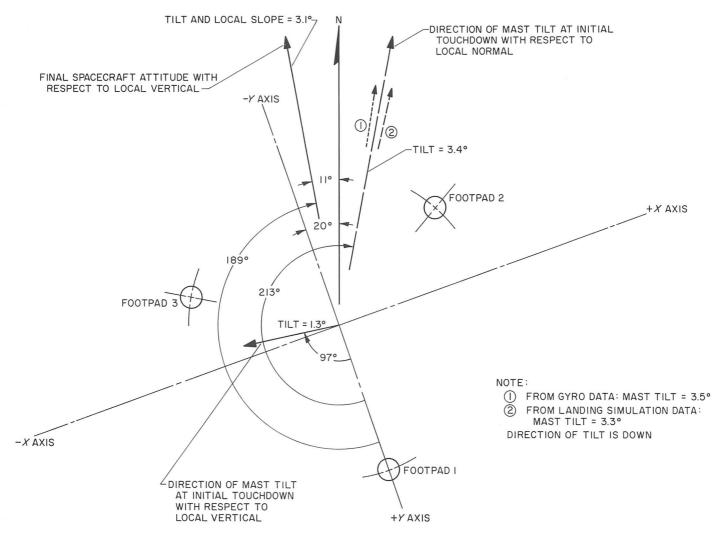


Fig. IV-3. Sketch showing landed spacecraft attitude, local slope, and lunar north.

Since these calculations deviated slightly, the arithmetic mean was used (Fig. IV-3). By this procedure, the spacecraft attitude (relative to the local vertical) at initial touchdown was determined to be $+1.2\pm0.1$ deg in yaw and -0.1 ± 0.1 deg in pitch. This attitude indicates horizontal components of the landing velocity were $+0.1\pm0.03$ m/sec in the spacecraft X direction and 0.0 ± 0.03 m/sec in the Y direction.

The shock-absorber force histories (Fig. IV-2) exhibit initial high-force periods of 0.30- to 0.35-sec duration, followed by zero-force readings of 1.0 to 1.2 sec in length. The zero-force readings indicate that the spacecraft rebounded after initial impact, raising the footpads to a height of 20 to 28 cm from their first impact positions. Spacecraft reimpact, registered 1.5 to 1.6 sec after initial impact, was followed by a second slight rebound and ring-out oscillations. Finally, the shock-absorber loads settled at

static load levels reflecting the lunar weight of the spacecraft. The *Surveyor VII* ring-out oscillations are lower in amplitude and frequency than those of previous *Surveyor* landings. As yet, this difference is unexplained.

2. Observations of Spacecraft/Soil Interactions

Television pictures transmitted from *Surveyor VII* were used to reconstruct landing events and to assess the lunar soil mechanical properties at this landing site. These pictures provide the principal data on footpad and crushable block penetration, nature and extent of soil ejecta resulting from landing impacts, and soil contamination on the spacecraft.

No landing problems were encountered by Surveyor VII in spite of the greater number of rocks occurring in the immediate vicinity of the spacecraft. Although study of

the surrounding terrain reveals several places where a landing could have caused damage, the only known permanent landing effects on the spacecraft were small holes in the crushable honeycomb footpads, rupture of the aluminum foil covering the bottom of crushable block 2, dust on the auxiliary mirrors, and small amounts of soil deposited on other spacecraft components.

a. Footpad/soil interactions. Figure IV-4 is a mosaic of narrow-angle pictures² showing footpad 2 and the surrounding ejecta. The imprint beside the lower-right-hand part of the footpad was made during the first impact.

Details of the imprint are shown under two different lighting angles in Fig. IV-5. The soil forming the beveled side wall of the imprint was subjected to the near-vertical motion of the footpad at impact and the lateral motion caused by leg extension. The right side of the imprint was compressed and then fractured as the footpad pushed outward (Fig. IV-5b). The far side, adjacent to the footpad in the picture, was compressed during maximum extension of the leg during the first impact, before the first spacecraft rebound (Fig. IV-2). The wall of the imprint (Fig. IV-5a) consists of a series of flattened soil surfaces formed en echelon as the footpad moved past them. This flattened wall, best seen in Fig. IV-5a, indicates that not only does undisturbed soil have cohesion but that recently disturbed soil particles have the ability to readhere.



Fig. IV-4. Footpad 2 and surrounding area. Sun elevation was 24 deg. The footpad imprint just to the right of the footpad, made during first impact, is illuminated by sunlight reflected off the footpad (Day 010; Catalog 7-SE-20G).

²Unless otherwise specified, all individual pictures and all mosaics used in this section are from narrow-angle television pictures.

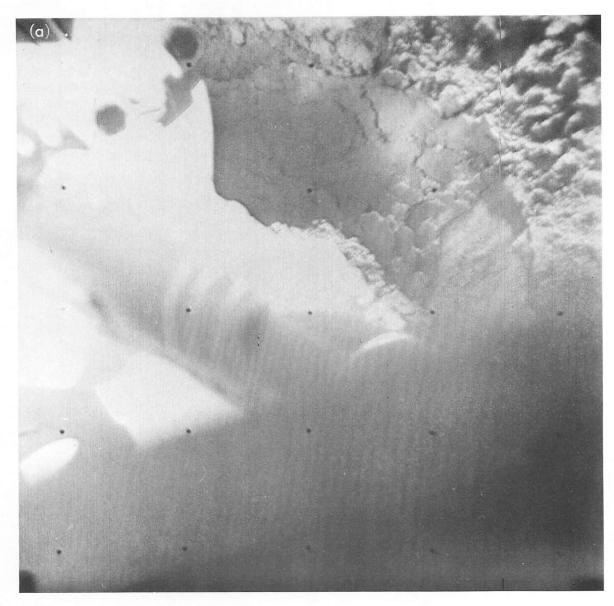


Fig. IV-5. Imprint caused by footpad 2 during first impact, at different lighting angles. The fine-grained nature of the soil is illustrated by the smoothed and flattened wall and floor of the imprint. Cohesiveness of the soil is demonstrated by the presence of open fractures, soil clumps, and side walls that stand at 45-deg angles. (a) Day 011, 12:28:52 GMT. (b) Day 013, 10:18:45 GMT, computer-processed.

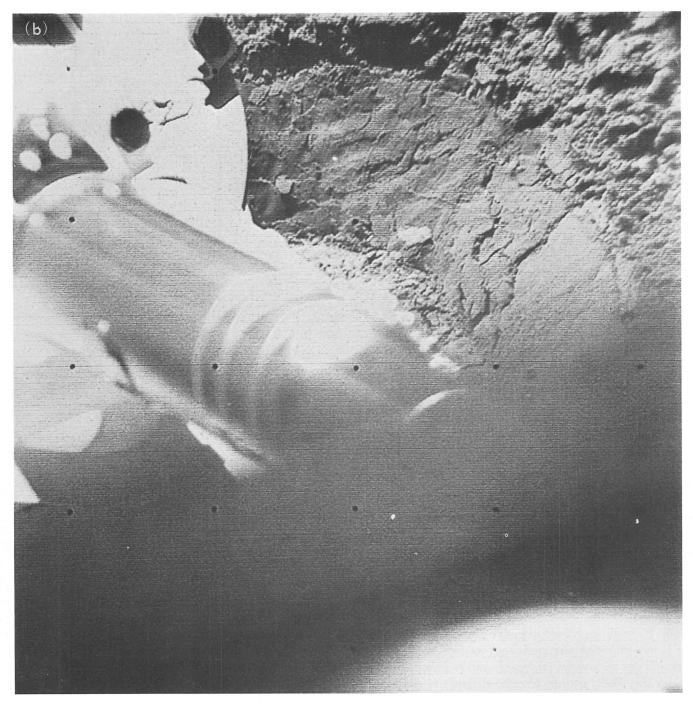


Fig. IV-5 (contd)

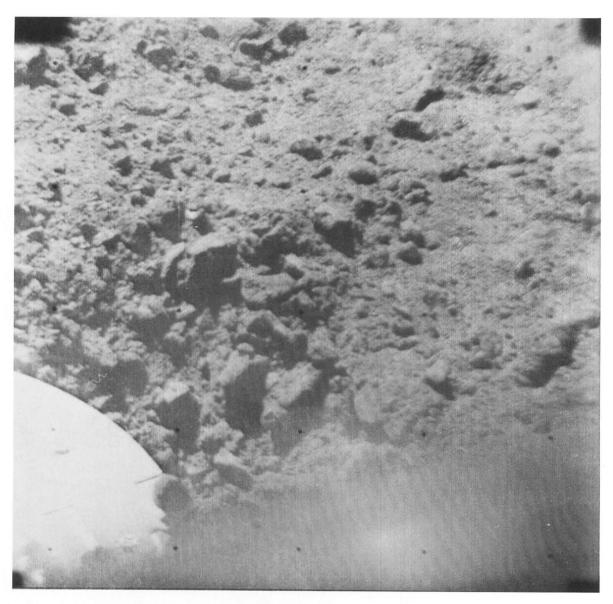


Fig. IV-6. Dark soil clumps, up to 3 cm in diameter, ejected by footpad 2 during landing. This area can be seen outboard from the footpad in Fig. IV-4 (Day 014, 01:26:23 GMT).

Lunar soil ejected by the footpads has a darker appearance than the undisturbed soil, as seen in the ejecta, which extend 20 to 40 cm from footpad 2 (Fig. IV-6). The lighting under different sun angles shows that some of this dark soil was deposited on top of, and beyond, the large rock in Fig. IV-7 (also see Fig. IV-4). The soil around the base of the rock appears disturbed (Fig. IV-8), indicating that the rock was moved, either by direct contact with footpad 2 or by impinging soil ejected during footpad impact. Ejected material also lies adjacent to the rock edge away from the footpad (Fig. IV-9). It is possible that this soil was displaced by the movement of the rock. Pictures of the near side of footpad 2 taken under low sun

angle show the fine detail of soil clumps and surface fractures that resulted from the landing impact (Fig. IV-10). At the lower left of Fig. IV-10a, 10b, and 10c, are two soil clumps, which, after they were ejected by the footpads, broke on impact without disintegrating.

Outboard of footpad 2 is a smooth, flat area, which is covered by fine ejecta and which terminates in a curved rim (Figs. IV-4 and IV-11). To the right, this rim merges into the wall of the imprint produced at the first landing impact. The rim may have formed during soil relaxation following retraction of the footpad.

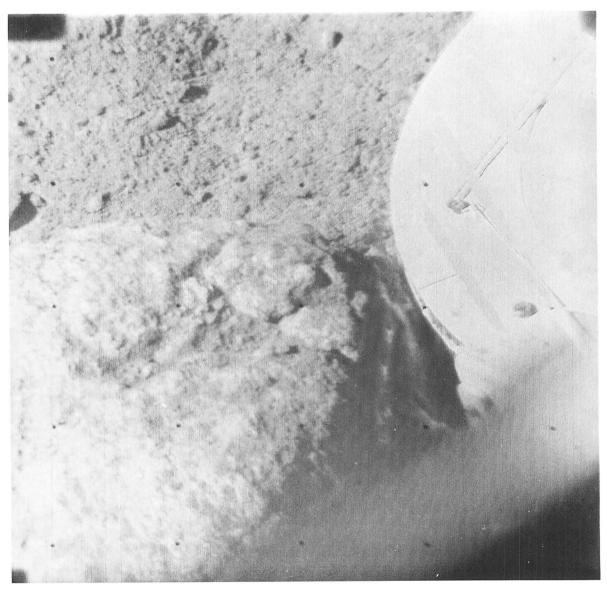


Fig. IV-7. Upper surface of the rock beside footpad 2. Dark ejecta cover parts of the rock (Day 018, 07:52:24 GMT).

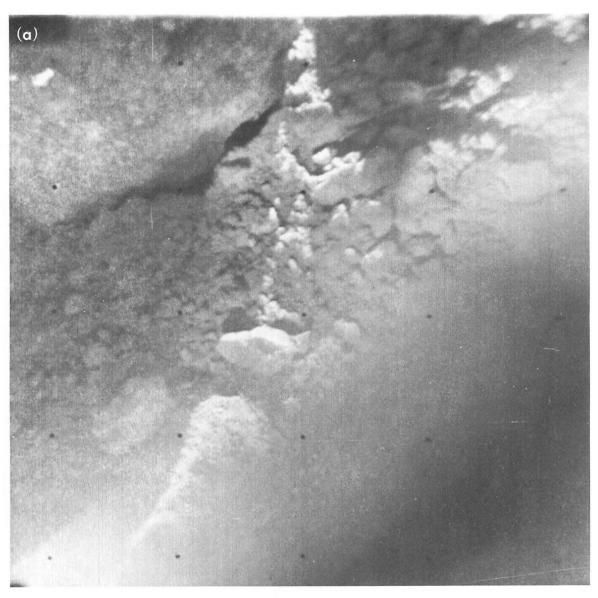


Fig. IV-8. Bottom of the rock adjacent to footpad 2, at two different lighting angles. The disturbed soil around the rock indicates that it was moved during landing. (a) Day 011, 06:14:49 GMT. (b) Day 022, 18:24:17 GMT.

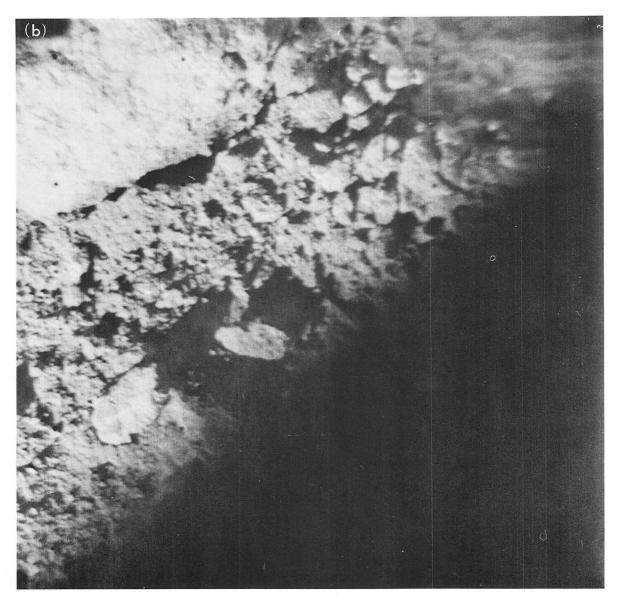


Fig. IV-8 (contd)

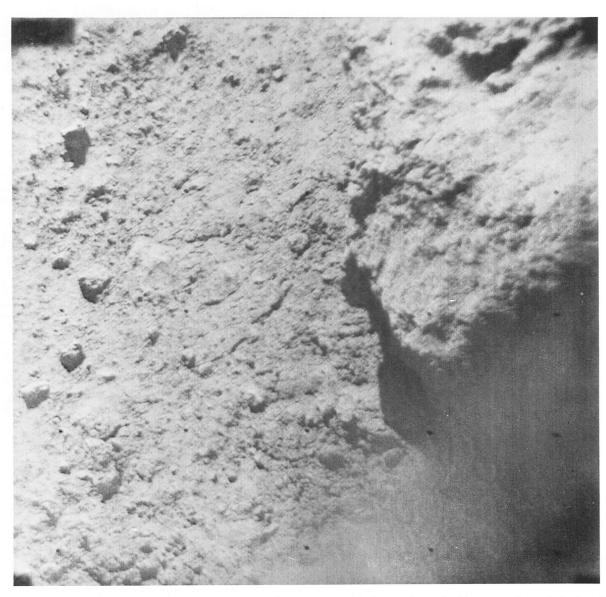


Fig. IV-9. Rock beside footpad 2. The dark soil beside and beyond the rock probably was ejected during landing (Day 013, 10:19:18 GMT).



Fig. IV-10. Ejected material on the near side of footpad 2, shown under different lighting conditions. A circular depression, probably caused by footpad rebound during the second landing impact, can be seen adjacent to the footpad. Soil clumps, fractured on impact after they were ejected by the footpad at landing, can be seen at the lower left. (a) Day 013, 10:21:44 GMT. (b) Day 020, 18:13:34 GMT. (c) Day 022, 16:08:35 GMT.



Fig. IV-10 (contd)

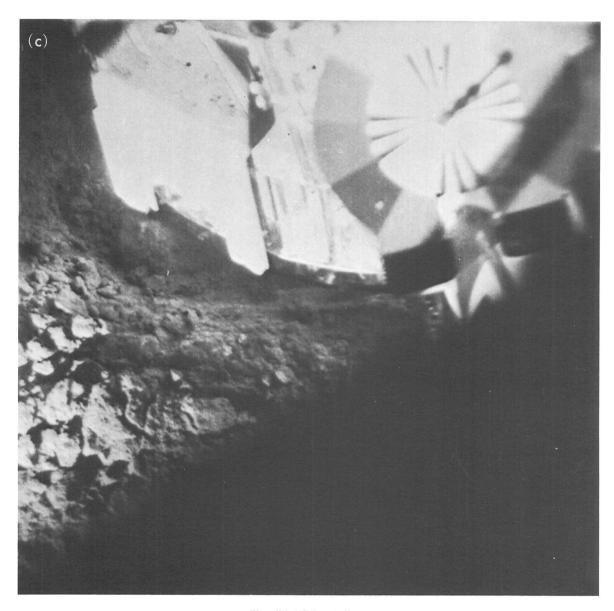


Fig. IV-10 (contd)

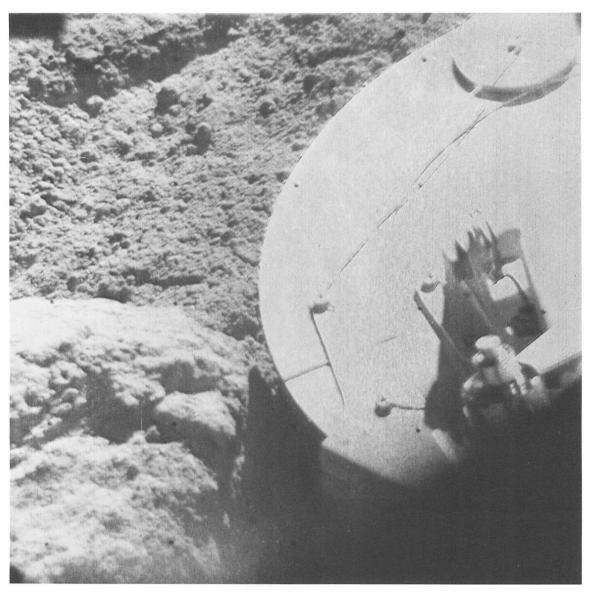


Fig. IV-11. A portion of the curved rim that bounds the smooth flat area outboard of footpad 2. The rim may have been formed by soil relaxation during retraction of the shock absorber as the spacecraft came to rest after landing (Day 011, 06:10:50 GMT).

The large rock to the left of footpad 2 is about 18 cm long and over 10 cm high. The small rocks near the footpad range in size to 10 cm.

Footpad 3 and the adjacent lunar surface are shown in the mosaic of Fig. IV-12. The edge of the first imprint can be seen between the leg and the shock absorber to the left of the footpad. A small, partly buried rock is visible beneath the footpad. The larger rocks to the right of the footpad range in size from 5 to 16 cm. Some crushing and deformation of the footpad occurred along its lower-right edge. Most obvious is the hole in the aluminum honeycomb directly behind the magnet assembly. The torn edges of aluminum around this hole in the foot-

pad can be seen clearly in Fig. IV-13. Footpad 3 ejecta, concentrated in two patches directly outboard from leg 3, extend about 40 cm beyond the footpad (Fig. IV-12). A thin layer of fine ejecta also can be seen on the near side of the footpad below the antenna boom.

The ejected material from footpads 2 and 3 is similar in amount and character to soil thrown out by the footpads of previous *Surveyors* that landed in flat mare regions with little horizontal motions. For example, the *Surveyor I* and *VI* (original landing) footpad ejecta are almost identical to those of *Surveyor VII* (Refs. IV-1 and IV-4). The depth of footpad penetration, amount of ejecta, size of ejecta pattern, and size of the resulting soil clumps are similar in all three landings.

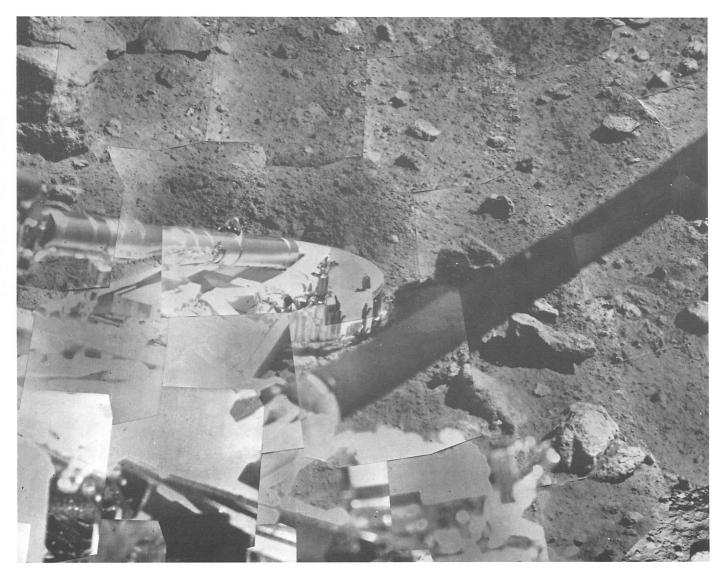


Fig. IV-12. Mosaic showing footpad 3 and dark, ejected material. The top edge of the first landing imprint can be seen above the leg structure and below the shock absorber (Day 017; Catalog 7-SE-20E).

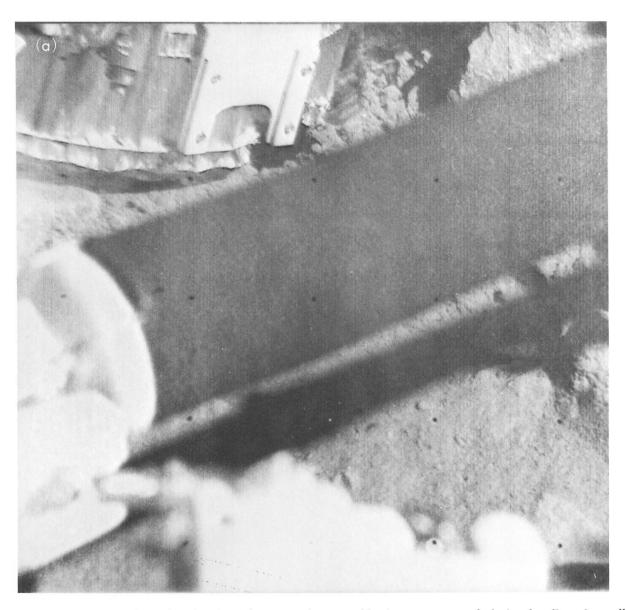


Fig. IV-13. Footpad 3. (a) Hole in the aluminum honeycomb, caused by impact on a rock during landing. A small rock under the footpad can be seen at the left of the picture (Day 015, 05:40:03 GMT). (b) Edges of the broken honeycomb highlighted by the sun (Day 020, 20:25:20 GMT).

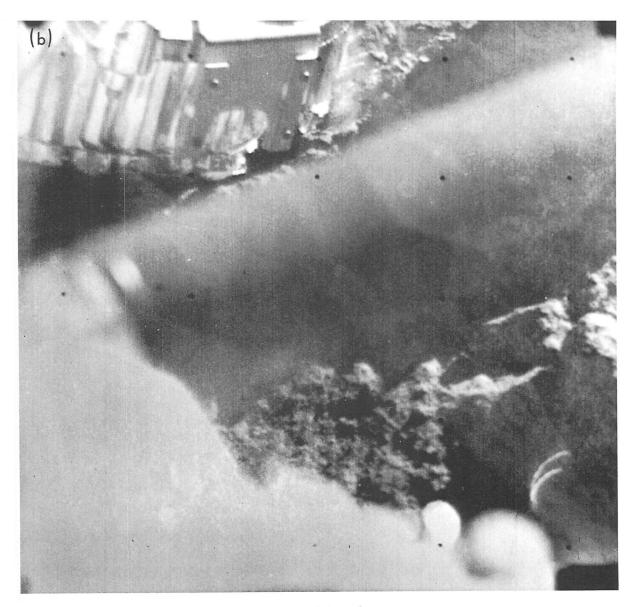


Fig. IV-13 (contd)

The footpad ejecta differed in the Surveyor landings with considerable horizontal spacecraft motion after impact. For example, during the landings of Surveyor III (10- to 14-deg surface slope), Surveyor V (19- to 20-deg surface slope), and the second landing of Surveyor VI (lunar hop), the footpads "plowed through" the soil, penetrating deeper than in landings without appreciable horizontal motion. There was a greater amount of ejecta, the ejecta were thrown further, and the average size of the soil clumps in the ejecta was larger. The larger size of the soil clumps, with their greater shear strength, possibly is due to their greater depth of origin. Such an increase of shear strength with depth could have a threefold explanation:

- Because the soil bulk density increases with depth (Ref. IV-4), there would be a greater number of individual soil bonds per unit volume.
- (2) Because of the increase in pressure with the increase in depth of overburden, the strength of the individual soil bonds should be greater.
- (3) Because most soil at depth has been undisturbed longer than the soil at the surface, the strength of the individual bonds should increase with geologic age.

Soil ejected by the footpads during landing appears darker than the undisturbed soil (Refs. IV-1 through IV-4), possibly because of the differences in the effective soil fragment size and not because of differences in color, mineral composition, or moisture content with depth. Since soil ejected by the footpads forms clumps that are larger than the average size of fragments on the undisturbed lunar surface, the surfaces of the footpad ejecta are rougher than the soil of the undisturbed surface and reflect less sunlight. Evidence that fragment size and surface roughness account for this phenomenon is provided by the sidewalls and bottoms of the many footpad imprints made during the Surveyor landings. In each of these imprints, the smooth bottoms and sidewalls not only appear brighter than the soil ejected from these same imprints, but are also brighter than the nearby undisturbed (and rougher) lunar surface.

b. Crushable block/soil interactions. Crushable blocks 2 and 3 are visible to the television camera through two auxiliary mirrors mounted on the spacecraft structure. Crushable block 2 left a distinct imprint in the soil (Fig. IV-14). The low cone of soil in the center of the imprint resulted from the rupture of the thin sheet of aluminum, which covers the hollow core of the crushable block. Laboratory tests have shown that failure of this

aluminum sheet occurs when the loading stress exceeds $2.4~\mathrm{N/cm^2}$ (Ref. IV-4). Although the image of the imprint is small and somewhat degraded by dust on the mirror, all three pictures of Fig. IV-14 indicate that there is no raised rim around the imprint. This lack of a raised rim, also apparent in the imprint of crushable block 3 on Surveyor VI (Ref. IV-4), indicates that the soil at the Surveyor VII landing site is compressible, at least in its upper few centimeters.

It was expected that all crushable blocks would impact in a similar manner on this relatively flat landing site. However, because the area beneath crushable block 3 was obscured by spacecraft shadows during most of the lunar day (Fig. IV-15), the expected imprint is not visible. Figure IV-16, a picture taken through the spaceframe, shows the surface near crushable block 3; the soil fractures probably were caused by the block impact.

c. Soil contamination on the spacecraft. A small auxiliary mirror was positioned for viewing the deployment area of the alpha-scattering instrument; however, only a uniform gray field was visible in the mirror. Pictures of this mirror under direct sunlight indicate that a layer of fine lunar soil covered the entire mirror surface. In Fig. IV-17, shadows of small clumps of soil can be seen on the mirror's surface. This mirror contains the greatest amount of soil contamination detected on Surveyor VII.

Figure IV-18 shows the upper part of the crushable block 2 auxiliary mirror under direct sunlight. The bright, cloudy appearance of the mirror top, in contrast to the bottom, suggests that a thin layer of dust was deposited on parts of this mirror. Contamination of the auxiliary mirrors probably was caused by fine soil and small soil clumps ejected by a crushable block, or by a footpad, during landing. Previous examples of such soil adhesion had been observed only after soil was eroded by vernier engine firings on the lunar surface (Refs. IV-2 through IV-4). With the exception of the dust on the mirrors, the spacecraft was relatively free from soil contamination, as shown by the tops of the footpads and the electronic compartments (Fig. IV-19a through 19d). A few small soil fragments can be seen on top of footpad 2 and on the bracket of its magnet assembly (Fig. IV-19a and 19b).

d. Objects of uncertain origin on the lunar surface. Some strangely shaped, fibrous-like objects, much brighter than the surrounding lunar surface, can be seen in Fig. IV-20. Because of their proximity to the spacecraft, their brightness, and because they resemble no soil or rock fragments observed during any Surveyor mission, these objects are thought to be pieces of the footpad

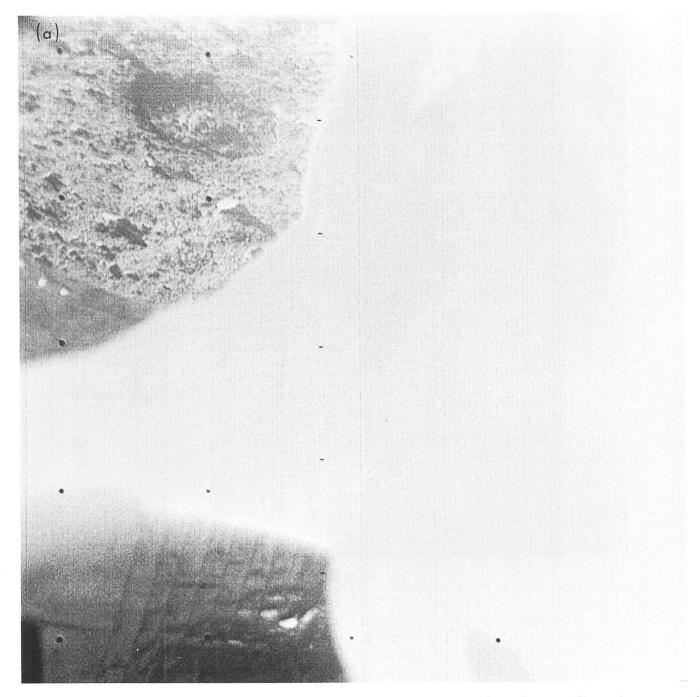


Fig. IV-14. Surface imprint caused by crushable block 2 during touchdown, seen through an auxiliary mirror mounted on the spaceframe. These three pictures show shadows across the imprint under different sun angles. (a) Sun angle, relative to the local surface, 15 deg (Day 010, 05:45:23 GMT, computer-processed). (b) Sun angle, relative to the local surface, 26 deg (Day 011, 06:57:42 GMT). (c) Sun angle, relative to the local surface, 36 deg (Day 019, 18:00:51 GMT).

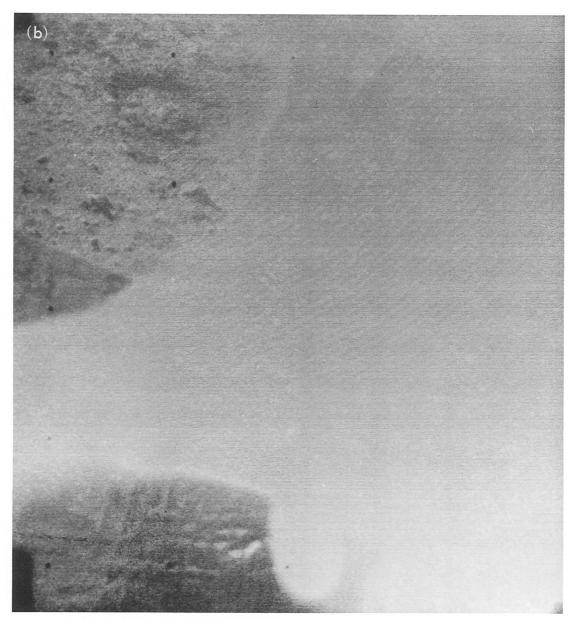


Fig. IV-14 (contd)

honeycomb. The best evidence of this is that the object in Fig. IV-20a appears to be resting on top of footpad 2 ejecta. The linear groove ending at the fragment cuts through footpad 2 ejecta.

3. Simulations and Analyses

a. Computer simulations.

Rigid surface. Landing simulations, assuming a rigid lunar surface, resulted in shock-absorber force histories matching the Surveyor VII landing data within $\pm 20\%$ with respect to peak forces, and within $\pm 20\%$ with respect to reimpact timing. Similar agreements with rigid-surface

simulations were obtained in the landings of *Surveyors I*, *III*, and *VI*. The surface on which *Surveyor V* landed produced shock-absorber forces that were lower than those of other *Surveyors*.

Soft surface. Landing simulations have utilized several simple analytical soil models; however, most results obtained to date have been derived from the compressible soil model described in Ref. IV-3 in which bearing strength variation is expressed by

$$p=p_{_{0}}\left(1+cs
ight) +rac{
ho _{1}
ho _{2}}{
ho _{2}-
ho _{1}}\dot{s}^{2}$$

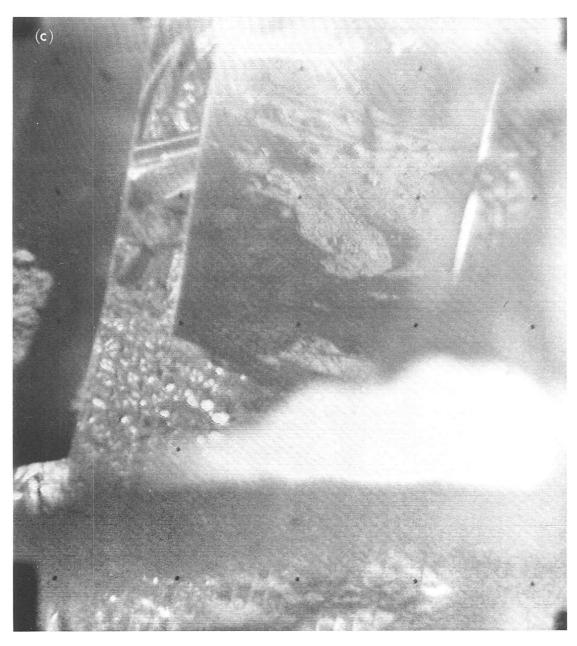


Fig. IV-14 (contd)

where

p =pressure exerted upon the penetrating object

 p_0 = static bearing pressure

c = frictional constant

s = penetration

 ρ_1 = initial density of the soil

 $\rho_2 = \text{compressed density of the soil}$

The best correlation with lunar data achieved to date with this model is shown in Fig. IV-21 for Surveyor VII landing velocity components of 3.7 m/sec vertical and 0.3 m/sec horizontal, and a 3-deg spacecraft incidence angle. The soil parameters used are $p_0 = 3.4 \text{ N/cm}^2$; $c = 3.3 \text{ m}^{-1}$; $\rho_1 = 1.2 \text{ g/cm}^3$; and $\rho_2 = 1.6 \text{ g/cm}^3$. These same values gave the best correlations for Surveyors I, III, and VI; for the Surveyor V landing site, the best correlations using this model were obtained with a softer surface $(p_0 = 2.7 \text{ N/cm}^2, \rho_1 = 1.1 \text{ g/cm}^3$; see Ref. IV-3).



Fig. IV-15. Lunar surface under crushable block 3 and vernier engine 3, visible because of an auxiliary mirror mounted on the spaceframe. Positive evidence of crushable block contact in this area has not been verified; however, spaceframe shadows obscured much of this area throughout the lunar day (Day 020, 18:42:14 GMT).

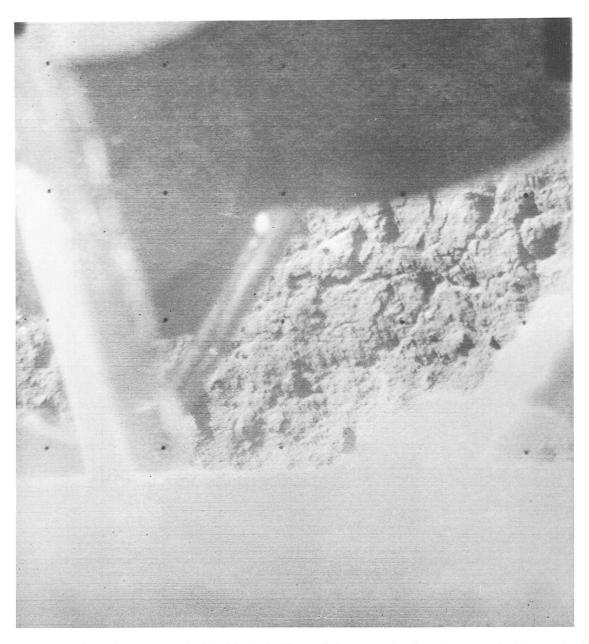


Fig. IV-16. Lunar surface close to crushable block 3. The soil fractures in the picture probably resulted from the impact of the crushable block out of camera view (Day 020, 18:16:20 GMT).



Fig. IV-17. Small auxiliary mirror positioned to view the alpha-scattering-instrument deployment area. The mirror was coated with a thin layer of lunar soil during the spacecraft landing. This picture, taken while sunlight was illuminating the mirror, also shows several small, dark clumps of soil on the mirror (Day 015, 06:30:04 GMT).



Fig. IV-18. Upper half of the crushable block 2 auxiliary mirror. The bright glare is caused by sunlight striking a thin layer of fine soil that was deposited on the mirror during the landing. The lunar surface area is the same as in Fig. IV-14c; the crushable block 2 imprint can be seen in both pictures (Day 020, 18:42:48 GMT).



Fig. IV-19. Relative lack of soil contamination on the spacecraft during landing is shown by the clean tops of the footpads and electronic compartments. Tops of both footpads were painted gray with 1.2-cm-wide white strips to improve visibility of any soil deposited on them. (a) Top of footpad 2 with a few small soil fragments (Day 020, 18:08:57 GMT). (b) Top of footpad 2 (Day 013, 10:15:12 GMT). (c) Top of footpad 3 (Day 019, 17:46:14 GMT). (d) Top of electronic compartment A (Day 015, 08:17:05 GMT).

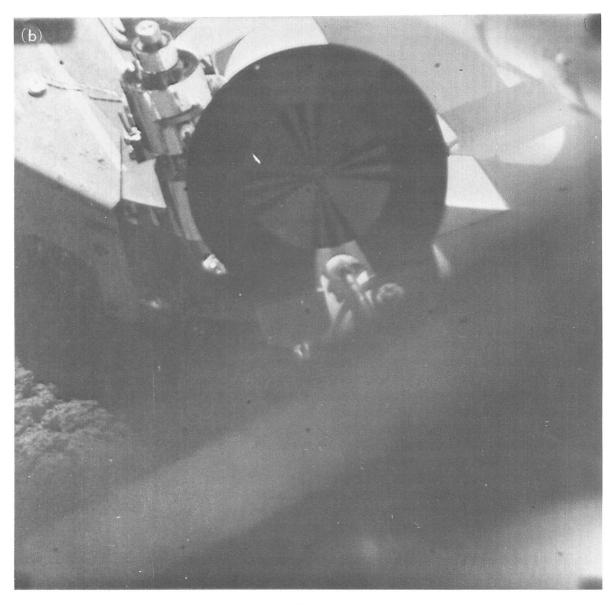


Fig. IV-19 (contd)

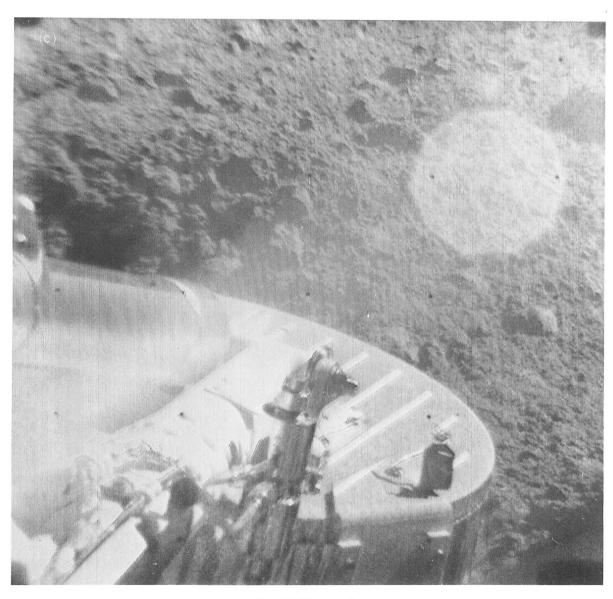


Fig. IV-19 (contd)

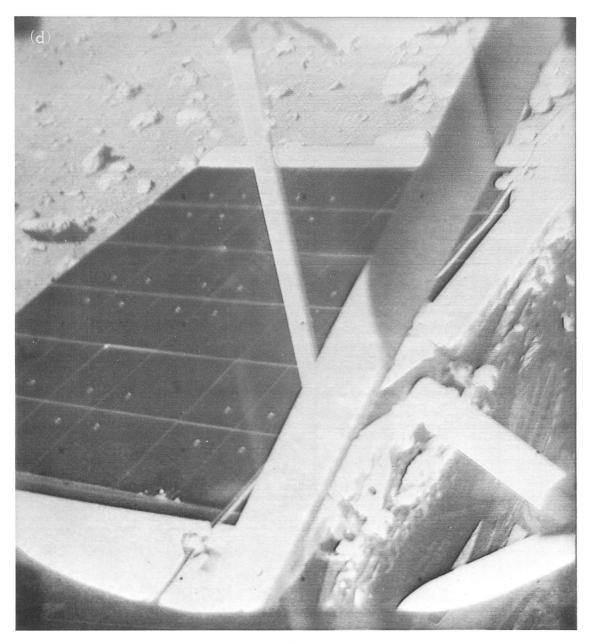


Fig. IV-19 (contd)

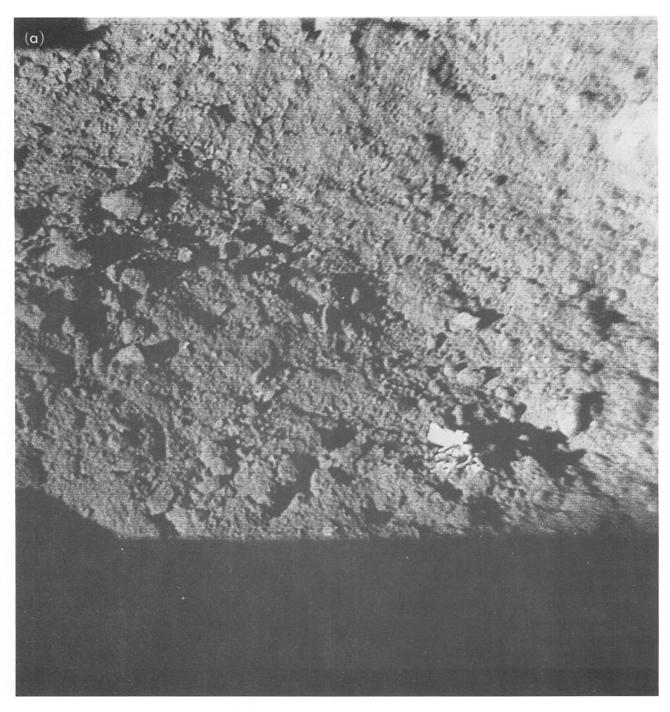


Fig. IV-20. Fibrous-like objects to the right of footpad 2. The bright appearance and unusual shape, unlike that of other fragments on the lunar surface, indicate that the objects probably originated from the spacecraft. (a) Day 020, 19:33:56 GMT, computer-processed. (b) Day 019, 19:42:37 GMT, computer-processed.

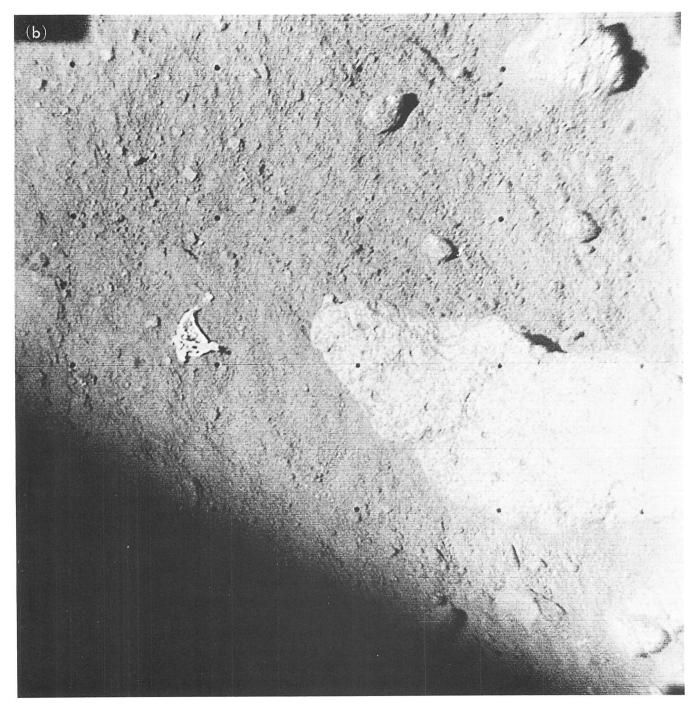


Fig. IV-20 (contd)

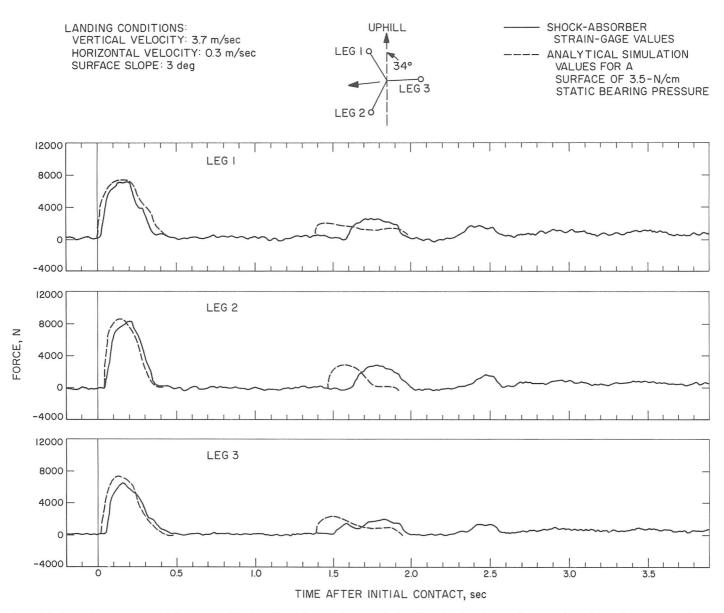


Fig. IV-21. Comparison of Surveyor VII landing data with analytically obtained shock-absorber force/time histories.

These results indicate that the mechanical properties at the *Surveyor VII* site are similar to the mechanical properties of the *Surveyor I*, *III*, and *VI* landing sites.

b. Footpad and crushable block imprint analyses. Estimates of the depths of footpad 2 and 3 penetrations have been made by two different methods. The first of these methods is based on measurement of shadows in pictures taken under various sun angles (Ref. IV-5). The second method is a laboratory simulation using a full-scale Surveyor model with an operational television camera system. In this method, footpad imprints in crushed basalt, similar in appearance to lunar soil, are photographed by the test vehicle camera and then compared with the Surveyor lunar pictures. Measurements also

have been made of footpad tilt angles, spacecraft motion between first impact of the leg and final position, and penetration of crushable block 2.

Both footpads are tilted with the outward edge down, footpad 2 by 5 to 10 deg and footpad 3 by 12 to 15 deg. Because of the tilts, the penetration measurements are referenced to the footpad centers at the tilt axes. The listed tolerances reflect the estimated accuracies of the measurements made from shadows adjacent to the footpads. In areas where shadow data were not available because of existing sun angles or where areas were not visible to the television camera, measurements were extrapolated from adjacent visible areas. Tolerances, in those cases, would be larger than listed here.

Footpad 2 penetration

First imprint

From shadow analysis and image simulations:

 $4\pm1\,\mathrm{cm}$

Final position

From shadow analysis: $4.5\pm1\,\mathrm{cm}$

Footpad 3 penetration

First imprint: obscured by leg structure

Final position

From shadow analysis and image simulations:

 $4\pm1\,\mathrm{cm}$

The movement of the spacecraft from first contact to final position is estimated to be 15 to 20 cm; the movement was toward the north, subparallel to the spacecraft Y axis, almost directly downslope. The depth of the crushable block 2 imprint is estimated to be 2.5 to 3.0 cm (Fig. IV-14).

B. Post-Landing Spacecraft/Soil Interactions

1. Bearing Strength From Sensor Head Imprints

During the Surveyor VII mission, the sensor head of the alpha-scattering instrument was picked up twice by the surface sampler and moved to a new position, thereby exposing the areas on which it had rested. The first position is shown in Figs. IV-22 and IV-23, the second position in Fig. IV-24. At the first position, the sensor head left a smooth, discontinuous, annular imprint (Fig. IV-23). Because the mechanism did not deploy normally, the surface sampler was used to force the sensor head to the lunar surface (see Sections V and VIII of this Report). During the deployment, the nylon cord holding the alphascattering instrument remained taut, making it difficult to determine the time of contact with the lunar surface. Because the surface sampler pushed both downward and sideward on the alpha-scattering instrument, the value for the total vertical load on the alpha-scattering instrument while the imprint was being formed cannot be determined accurately.

At the second position, the imprint on the surface is much narrower (Fig. IV-24). When the sensor head was moved to the second position, the cord had relaxed; the surface sampler exerted little, if any, load on the alphascattering instrument.

An estimate of the pressure exerted by the sensor head on the lunar surface, including the force exerted by the surface sampler at the first position, can be made as follows. The weight of the instrument is approximately 4.4 N; the surface sampler could have exerted an additional maximum downward force of about 8.9 N. The area of the irregular imprint made by the sensor head was measured by sketching a similar area, placing the sketch in proper position with respect to a full-scale model spacecraft, and photographing it with the spacecraft television camera. The size and shape of the sketch were adjusted until it matched the Surveyor VII pictures. The area of the imprint, as measured with a planimeter, is 37 cm². The depth of penetration of the edge of the sensor head's tapered circular plate, at its deepest point, was 6 ±1 mm, as measured by duplicating the imprint in soil. Because depth of penetration from the maximum point grades to zero in three perpendicular directions, average depth of penetration of the imprint area would be 1.5 mm. As seen by the imprint shape, the back, or straight edge, of the circular plate did not penetrate the surface, but apparently was resting on the small rock shown in Fig. IV-23. Assuming that half of the force was taken by the rock and half by the imprint, the maximum average pressure on the flattened surface would be about 0.2 N/cm² for an average penetration of 1.5 mm.

An estimate of the area of the imprint made by the sensor head in its second position is less accurate (Fig. IV-24). The sensor head made a wide, double imprint about 10 cm long on one side, and a narrow imprint about 25 cm long on the other. The estimated area of the inner part of the short imprint is $15~\rm cm^2$, and of the long, narrow imprint is $7~\rm cm^2$. The pressure exerted by the instrument only is estimated to about $0.2~\rm N/cm^2$. Penetration for the narrow imprint is less than 1 mm, and for the wide imprint approximately 2 mm.

Details of the first imprint are shown in the enlargement of a part of a narrow-angle picture (Fig. IV-25). The fine-grained nature of the soil is demonstrated by the smooth imprint. This same smoothness is visible in pictures of footpad imprints (Figs. IV-4, IV-5, and IV-12) and in the walls of the trenches excavated by the surface sampler (Fig. IV-26).

2. Bearing Strength From Rock Drop Test

During surface-sampler operations, a rock (rock A) was picked up and dropped from a height of about 60 cm above the surface (see Section V of this Report). After forming a small depression upon impact, the rock bounced, or rolled, about 12 cm upslope of the shallow crater in which it landed. Figure IV-27 shows the rock on the surface before it was picked up by the surface sampler.



Fig. IV-22. Sensor head of the alpha-scattering instrument in position for the first sample. Note imprint to right of sensor head which was made at first contact (Day 018, 09:22:54 GMT).

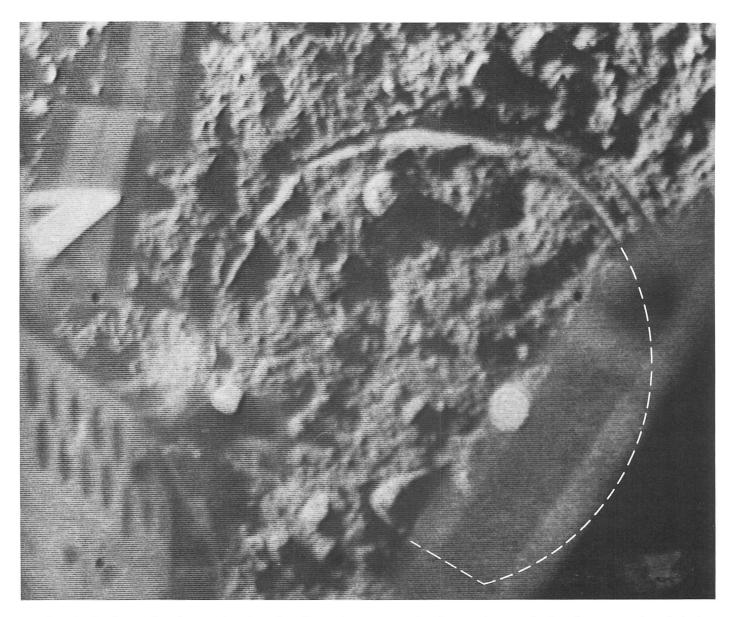


Fig. IV-23. Wide-angle picture showing the discontinuous annular impression made by the sensor head during deployment to the first sample position. The size of this imprint was used in estimating the bearing strength of the top-most layer of soil (Day 021; Catalog 7-SE-26).



Fig. IV-24. Mosaic showing the second sample position. Note short, wide imprint at upper left and long, narrow imprint at lower right (Day 022, Catalog 7-SE-25).

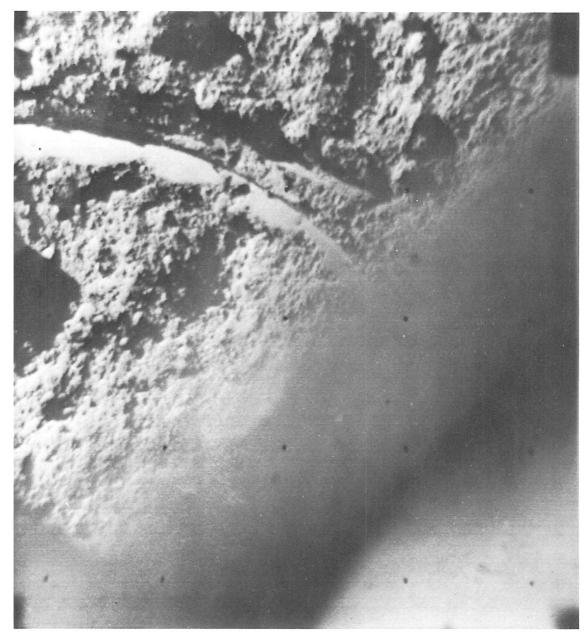


Fig. IV-25. Enlargement showing smooth surface of sensor head imprint at the first sample position (Day 021, 21:53:37 GMT). See Fig. IV-23.

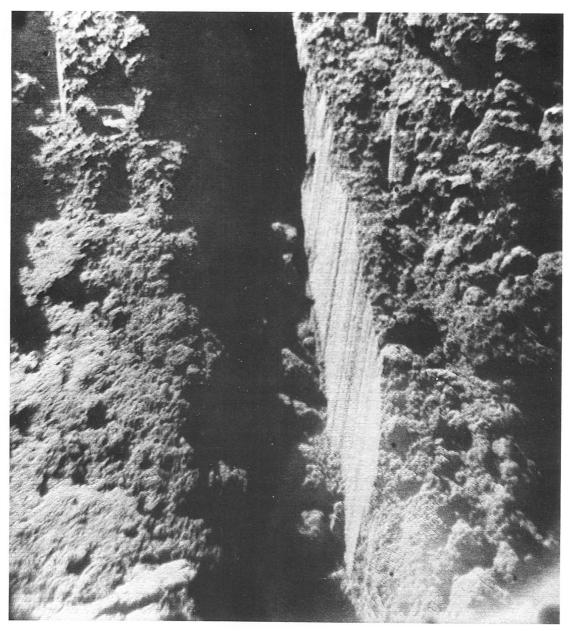


Fig. IV-26. Smooth, vertical wall and floor of the trench excavated by the surface sampler demonstrate the fine-grained, cohesive nature of lunar soil (Day 020, 09:51:50 GMT).

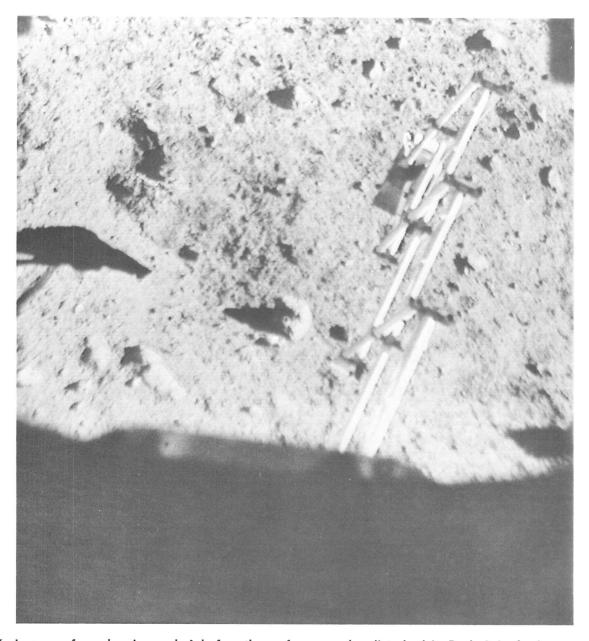


Fig. IV-27. Lunar surface showing rock A before the surface sampler disturbed it. Rock A is the large rock in the lower center of the picture to the left of the surface sampler and in line with the shadow of the surface-sampler scoop (Day 012, 02:06:06 GMT).

The size of the rock is indicated in Fig. IV-28, which shows the rock and the 5-cm-wide surface-sampler scoop. Figure IV-29 shows the rock before it was dropped; Fig. IV-30 shows the rock after it was dropped. Comparison of pictures taken before and after the drop shows that the rock came to rest on the upslope side (to the left) of the small, triangular rock seen in Fig. IV-29. The shallow track made by the rock as it moved upslope can be seen between the impact point and the final position of rock A (Fig. IV-30). The surface slope at this point is about

10 deg, as indicated by the sun angle when the sun line is tangential to the surface.

The depression formed during impact can be used to estimate the average bearing strength of the soil over the observed penetration depth. An estimate is made here by assuming that the difference in the potential energy of the rock at its release and at its final position is equal to the energy expended in deforming the soil during impact and as the rock moved along the surface

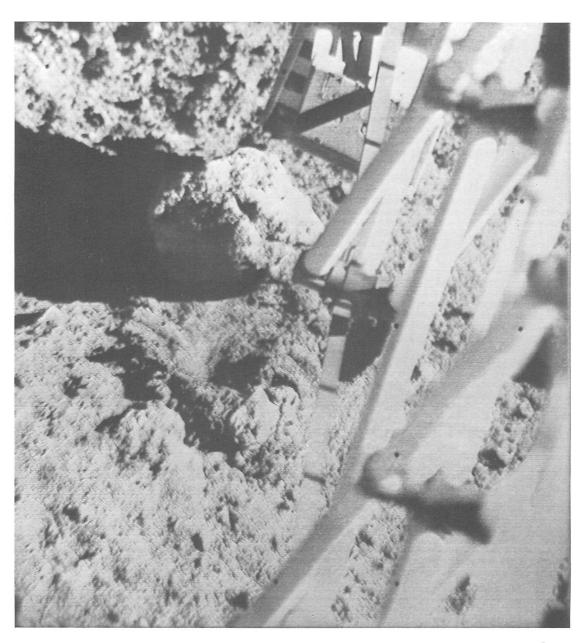


Fig. IV-28. Surface-sampler scoop after initial attempt to pick up rock A. The rock is approximately the same size as the 5-cm width of the scoop (Day 012, 02:29:00 GMT).

against a frictional resistance. If σ represents the soil dynamic bearing capacity (including both static and dynamic contributions), then

$$\sigma = \frac{mg\left(h_0 - h_1 - \mu l\right)}{V} \tag{1}$$

where mg is the lunar weight of the rock, h_0 is the release height, h_1 is the final height above the impact point, l is the horizontal distance the rock moved after impact, μ is the coefficient of friction between the rock and sur-

face, and V is the volume of soil compressed. The value of σ obtained from Eq. (1) should be an upper-bound estimate of the dynamic bearing stress because the energy expended in imparting momentum to displaced soil particles is neglected. For a spherical rock of radius R, the volume of soil compressed (expressed in terms of the radius of the rock and radius of the depression, R_1) is

$$V = \frac{2}{3} \pi R^{3} \left\{ 1 + \frac{1}{2} \left[1 - \left(\frac{R_{1}}{R} \right)^{2} \right]^{1.5} - \frac{3}{2} \left[1 - \left(\frac{R_{1}}{R} \right)^{2} \right]^{0.5} \right\}$$
(2)

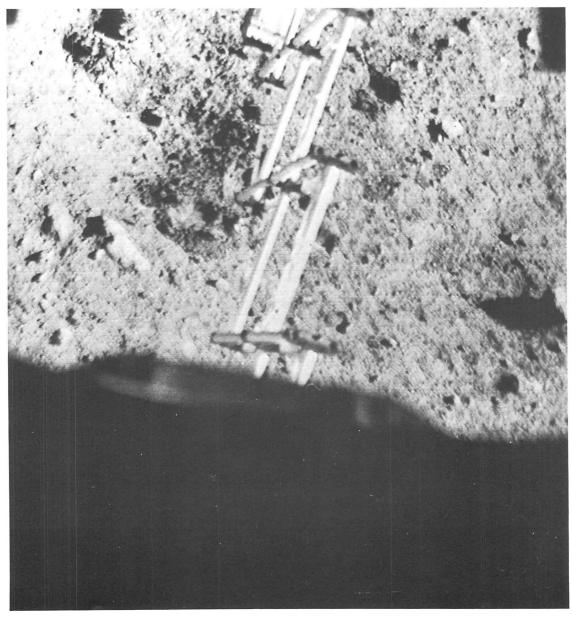


Fig. IV-29. Wide-angle picture of surface sampler just before rock A was dropped; rock A is inside the scoop (Day 012, 03:44:17 GMT).

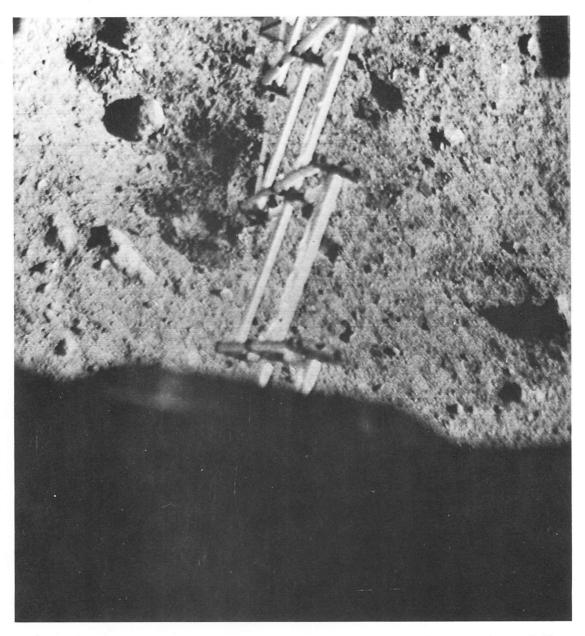


Fig. IV-30. Wide-angle picture of surface sampler and lunar surface after rock A was dropped. The rock impact depression is in the center of the picture between rock A and the surface sampler and above the original location of rock A (Day 012, 03:45:56 GMT).

The radius of the rock is approximately 2.8 cm, and the radius of the surface depression is estimated from Fig. IV-30 to be 2 cm. Hence, $R_1/R = 0.7$ and V = 5.4 cm³. The other parameters are estimated to be (see Section V of this Report for the rock mass and surface-sampler geometry)

$$m\mathrm{g}=0.36\,\mathrm{N}$$
 $h_0=61\,\mathrm{cm}$
 $h_1=l\sin10\,\mathrm{deg}=2\,\mathrm{cm}$
 $l=12\,\mathrm{cm}$
 $\mu=1$

For these values, the average bearing stress from Eq. (1) becomes

$$\sigma = 3.1~\mathrm{N/cm^2}$$

The corresponding penetration depth (for $R_1 = 2$ cm) is 0.8 cm. According to these results, 3.1 N/cm² becomes an upper-bound estimate of the average dynamic bearing strength for the top 0.8 cm of the lunar surface.

C. Soil, Rock, and Terrain Characteristics

The size and distribution of rocks can be studied in Fig. IV-31, which is a 360-deg panorama of the terrain around Surveyor VII, together with the keyed rock index sketch (Fig. IV-32). The panorama was obtained by mounting about 900 16-centimeter-square television pictures on a spherical surface in the form of a mosaic, which was then photographed in ten segments. Prints of these ten segments were flat-mounted and rephotographed to give the mosaic of Fig. IV-31. The individual pictures were positioned on the spherical surface such that the lunar terrain appears as it would have to a spacecraft camera that was vertical instead of tilted. The sizes of rocks and other objects can be estimated by using the scale at the right edge of Fig. IV-31; the two converging lines define a width of 1 m for each point in elevation (assuming a flat lunar surface). Thus, at this landing site, measurements of objects can be made for distances up to about 18 m from the spacecraft (camera elevation, -5 deg).

An enlarged view of the cluster of rocks (numbered 1 through 17) visible above electronics compartment B (Fig. IV-31) is shown in Fig. IV-33. These rocks are close

enough to the compartment to provide a cross-sectional area sufficiently large to have acted as a heat source that slowed the normal cooling rate of the compartment (see Section VI of this Report). The cross-sectional area of these 17 rocks is 2.7 m². Distance of the rocks from compartment B ranges from 3 to 18 m; the average distance is about 8 m. If the spacecraft had landed on this cluster of rocks, severe damage to the spacecraft could have occurred; for example, crushing of the bottoms of the electronic compartments would have destroyed the thermal balance of the electronic components within the compartments.

1. Rock Size and Distribution

A count was made of rocks larger than 5 cm, which are visible in the full panorama of Fig. IV-31 and within the circle defined by -5-deg camera elevation. For a flat lunar surface, -5-deg elevation occurs at 18.4-m distance from the camera; the bottom of the mosaic is at -35-deg camera elevation, or a distance of 2.3 m. The area of lunar surface in the panorama, below -5 deg and excluding the 40 m² obscured by the spaceframe, is 1004 m².

Rocks larger than 20 cm are numbered in Fig. IV-32; the sizes of these rocks are given in Table IV-2. The average width was 34 cm; the largest rock was 80 cm across.

The rock population and percentage of lunar surface covered for the size ranges (diameter in centimeters) of 5–10, 10–15, 15–20, and 20–80, given in Table IV-3, are based on a total number of 1266 rocks counted. As shown in Table IV-3, 0.6% of the lunar surface around Surveyor VII is covered by rocks larger than 20 cm, 1.2% by rocks larger than 10 cm, and 2.8% by rocks larger than 5 cm.

These preliminary data present a lower rock population than indicated by data presented in Section III of this Report. This discrepancy may be due to differences in areas selected for counting, or in counting technique; the differences in the scale of pictures used with resulting differences in resolution; or the assumption of a horizontal lunar surface. It is known that the surface is not horizontal; it slopes down to the north and up to the south. Though these slopes tend to be self-compensating, the amount of error introduced by this assumption is not yet known. It is noted, however, that all five points, represented by the size ranges in Table IV-3, lie on a straight line when plotted log-log (Fig. IV-34). If error is present in the data, it would seem to be systematic, not random.

Table IV-2. Rocks larger than 20 cm across, within 18 m of the spacecraft (identified in Fig. IV-32)^a

Rock	Width, cm	Rock	Width, cm	Rock	Width, cm	Rock	Width, cm			
1	50	18	20	35	20	52	30			
2	60	19	30	36	70	53	20			
3	60	20	20	37	20	54	40			
4	80	21	40	38	30	55	40			
5	50	22	40	39	20	56	20			
6	40	23	40	40	20	57	30			
7	50	24	40	41	20	58	20			
8	50	25	30	42	20	59	40			
9	50	26	30	43	20	60	40			
10	60	27	40	44	50	61	30			
11	40	28	20	45	40	62	20			
12	40	29	40	46	20	63	40			
13	30	30	20	47	30	64	30			
14	20	31	20	48	20	65	20			
15	40	32	20	49	40	66	40			
16	30	33	40	50	20	67	40			
17	20	34	20	51	50	68	20			
^a Average width = 34 cm.										

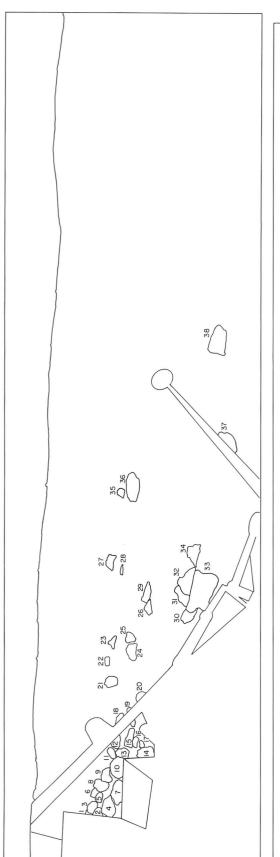
Table IV-3. Size distribution and lunar surface area covered by rock fragments (based on Fig. IV-31)

Rock width,	Number of rocks per 1000 m ²	rocks per		Lunar surface area covered per 1000 m², m²	Cumulative area covered per 1000 m², m²	Percentage of area covered	Cumulative percentage of area covered
80	1ª	1	80	0.5	0.5	0.05	0.05
20 to 80	67°	68	33	5.7	6.2	0.6	0.6
15 to 20	106°	174	16¼°	2.2	8.4	0.2	0.8
10 to 15	347°	521	111/4°	3.5	11.9	0.4	1.2
5 to 10	5,100 ^b	5,621	61/4°	15.6	27.5	1.6	2.8

aValue determined by actual count of rocks in the 1000 square meters of lunar surface visible in the panorama of Fig. IV-31, below -5-deg camera elevation.

 $^{^{}b}$ Value extrapolated from 745 rocks counted in 146 square meters of lunar surface visible between -10- and -35-deg camera elevation for six of the ten segments of the panorama in Fig. IV-31, i.e., for those segments where view of the lunar surface is not partly blocked by the spaceframe.

^cAverage diameter, for rocks not measured directly, was taken as the quarter point in the size range (Fig. IV-34).



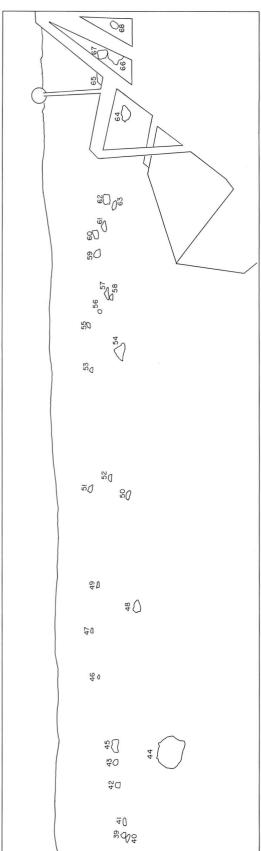
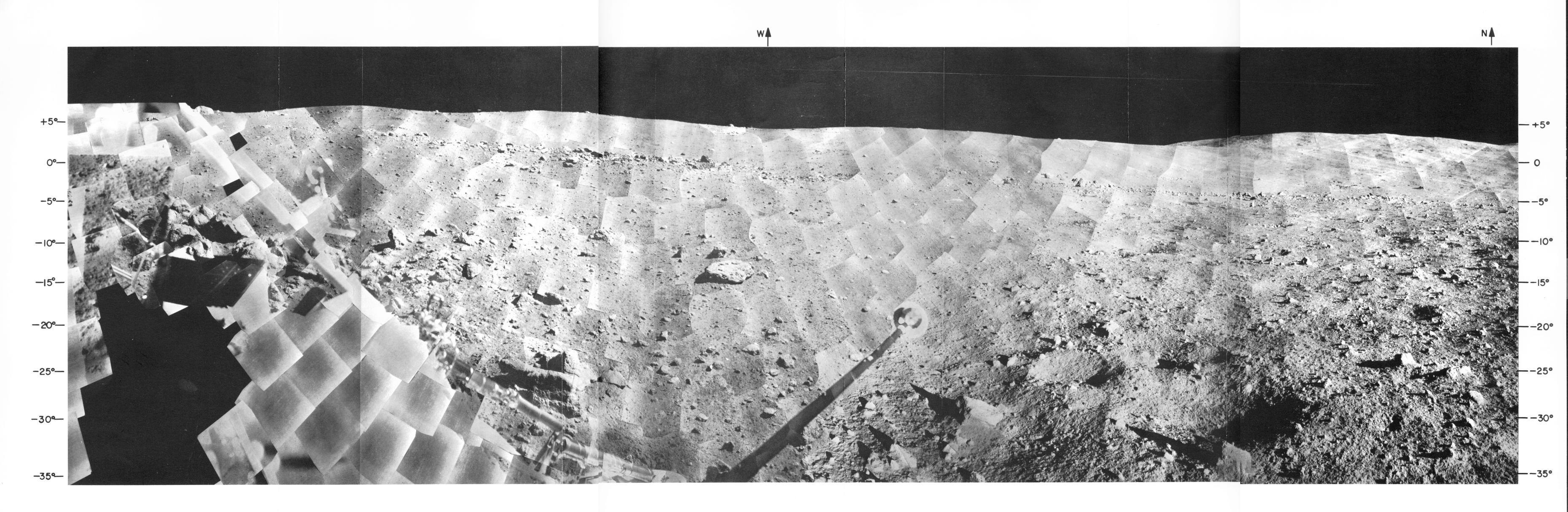


Fig. IV-32. Index sketch showing the locations of the rocks, visible in Fig. IV-31, which are larger than 20 cm in diameter and within 18 m of the spacecraft.



JPL TECHNICAL REPORT 32-1264

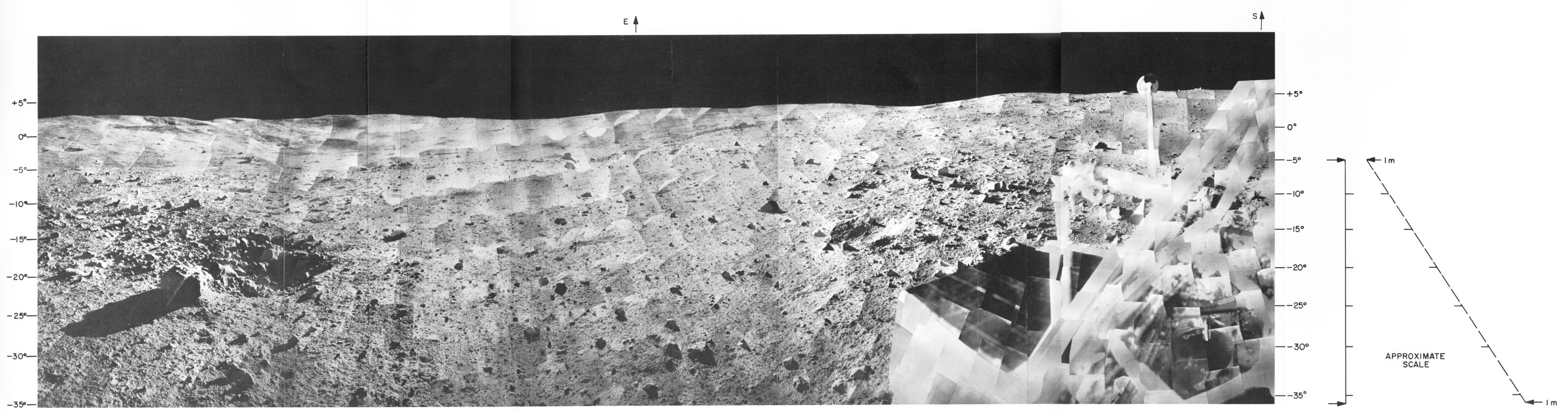


Fig. IV-31. Mosaic of narrow-angle pictures comprising a 360-deg panoramic view around the spacecraft. The scale at the right is based on a flat lunar surface (Days 010, 011, 013, 017, and 018; Catalog 7-SE-22).

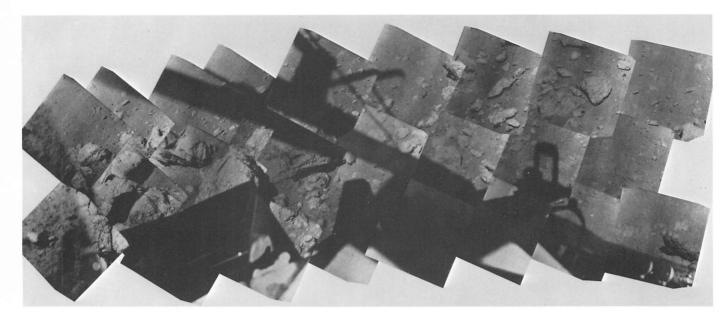


Fig. IV-33. View of rocks 1 through 17, visible above electronic compartment B in Fig. IV-32 (Day 013; Catalog 7-SE-19).

These data, as well as the observations described in the previous paragraphs (and in Refs. IV-1 through IV-4) indicate that the lunar soil is composed of a fine-grained matrix in which a small percentage of rock fragments is suspended. Tests of terrestrial soils indicate that comparable small percentages of coarse fragments suspended in a fine-grained soil normally do not affect significantly mechanical properties such as bearing strength. Therefore, it is not surprising that, even though many more rocks can be seen on the surface at the Surveyor VII highland landing site, the mechanical properties of the soil are not significantly different from those of previous mare sites.

2. Rock Hardness

Although quantitative data are scarce, it is desirable to draw possible conclusions on the hardness of the large fragments (rocks) observed by the television camera in Fig. IV-31 and of large fragments encountered in previous *Surveyor* missions. It is possible to conclude that large fragments are hard, not weak; i.e., they would be resistant to crushing if impacted by a landing spacecraft or moving vehicle.

During the Surveyor III mission, the surface sampler exerted a pressure of about 2×10^7 dynes/cm² on a 1.2-cm-diameter rock fragment, without breaking it (Ref. IV-2). This pressure is sufficient to crush weak terrestrial rocks

such as some tuffs, siltstones, claystones, and friable sandstones (Ref. IV-2).

During the Surveyor VII mission, the rock used in the drop test (Fig. IV-27) was also squeezed by the surface sampler and did not break. During landing, footpad 3 struck a rock, which made a hole in both parts of the footpad aluminum honeycomb. The lower section has a crushing strength of 6.9 N/cm²; the upper section has a crushing strength of 13.8 N/cm². However, at least some of the larger rock fragments can be broken by a sharp blow, as indicated during Surveyor VII operations when the surface sampler was allowed to fall from a height of 35 to 40 cm upon a 5-cm-diameter rock (rock E), which broke upon impact (see Fig. V-30 of Section V of this Report).

It can be demonstrated that most large rock fragments are hard, as shown by their resistance to erosion. The rocks above the leg 3 shock absorber in Figs. IV-31 and 35, for example, appear to have undergone extensive erosion. The planar surfaces of the rocks are almost certainly fracture surfaces that have been modified by erosion. The rounded edges of the rocks and the nonvesicular, but pitted, surfaces indicate a long period of erosion from impact by small fragments.

Fragments, formed by agglomerated, fine soil particles ejected by footpads and crushable blocks during *Surveyor* landings, are weak and do not exceed a few centimeters in diameter.

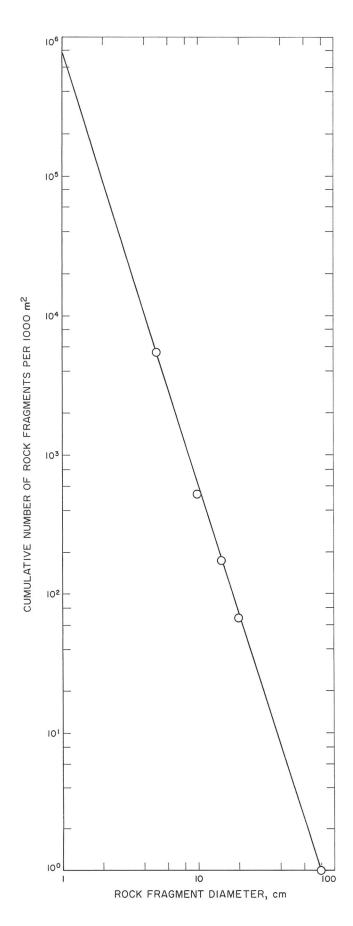


Fig. IV-34. Size-frequency distribution of rock fragments within 18 m of Surveyor VII. The graph represents the data in Table IV-3. The number of rocks larger than any specific size per unit area can be estimated from this graph. For example, there are approximately 1200 rocks larger than 7 cm in diameter per 1000 square meters of lunar surface.



Fig. IV-35. View of rocks 30 through 34 of Fig. IV-32. The fractures in rock 32 (Fig. IV-32) are the best developed fractures observed during the Surveyor missions (Day 013; Catalog 7-5E-28).

3. Rock Fractures

Of special interest are the fractures in rock 32 (Figs. IV-31 and IV-35). The fractures could have been caused by impact of another rock. However, it seems unlikely that the impacting rock would have had just enough energy to fracture rock 32, without any excess energy that would have dislodged the resulting fragments. It may be more likely that these fractures were caused by expansion and contraction during lunar day and night temperature cycling. The width of the fractures in the rock indicate that the fragments have separated by

several millimeters and are loose. Another rock with similarly well developed fractures is rock 14, located beside compartment B (Figs. IV-31 and IV-36).

4. Terrain Characteristics

As shown in Fig. IV-31, most of the surface visible to the camera has gentle slopes less than 10 deg. The steepest slope on the flank of the ridge north of the spacecraft, just below the horizon, is 34 deg. The angle of repose of most loose material is 35 to 37 deg.



Fig. IV-36. Fractures in rock 14 (Day 013, 14:45:18 GMT). See Fig. IV-32.

The slopes and the lack of distinct bedrock outcrops indicate that the visible lunar surface is almost entirely composed of fine-grained matrix material.

D. Summary and Preliminary Conclusions

First evaluations of television and telemetry data, aided by analytical and laboratory simulations, have provided the following conclusions:

- (1) The soil is predominantly fine-grained; granular; and slightly cohesive, similar to that found at the previous *Surveyor* landing sites. Not only is the soil cohesive, but soil particles, once disturbed, tend to readhere.
- (2) Soil ejected by the footpads is darker than undisturbed soil on the surface, possibly because recently disturbed soil has a rougher surface and a larger effective grain size than undisturbed soil, and therefore reflects less light.
- (3) Imprints of footpads and crushable blocks indicate that the soil is compressible, at least in its upper few centimeters.
- (4) Static bearing strength of the lunar soil increases with depth as follows:
 - (a) In approximately the upper millimeter: less than $0.1~\mathrm{N/cm^2}$ (from imprints of small rolling fragments).
 - (b) At a depth of 1 to 2 mm: 0.2 N/cm² (from imprints of the sensor head of the alpha-scattering instrument).
 - (c) At a depth of about 2 cm: 1.8 N/cm² (from *Surveyor VI* and *VII* imprints of crushable blocks).
 - (d) At a depth of 5 cm: 5.5 N/cm² (from Surveyor I footpad penetration).

- (5) An average 3.4-N/cm² lunar surface static bearing strength, determined from *Surveyor VII* footpad penetration into an assumed compressible soil model, is similar to that observed in the *Surveyor I*, *III*, and *VI* landings.
- (6) Dynamic bearing stress developed on crushable block 2 exceeded 2.4 N/cm² during penetration to a depth of 3 cm, as evidenced by the mound of soil in the center of the imprint; the mound indicates the aluminum sheet on the bottom of the crushable block was ruptured during landing.
- (7) The depression caused by a rock dropped from the surface sampler provided an upper bound estimate of 3.1 N/cm² for the dynamic bearing strength of the top 0.8 cm of the soil; static bearing strength would be less.
- (8) During landing, lunar soil was thrown against an auxiliary mirror and adhered to it. During previous missions, lunar soil adhered to the spacecraft principally when the soil impacted with substantial velocity, primarily during firing of the vernier engines while the spacecraft was on the ground.
- (9) Only 0.6% of the area at the Surveyor VII site (within an 18-m radius of the camera) is covered by rocks larger than 20 cm in diameter, 1.2% by rocks larger than 20 cm, and 2.8% by rocks larger than 5 cm (see Table IV-3).
- (10) In summary, soil at this highland site is generally similar in its mechanical properties to that at the mare landing sites of previous Surveyors except that there is a higher rock population within the soil and on the surface. Though individual large rocks and clusters of small rocks will substantially increase bearing strength locally, the higher rock population, in general, does not increase appreciably the bearing strength of soil at the Surveyor VII site.

References

- IV-1. Christensen, E. M., Batterson, S. A., Benson, H. E., Chandler, C. E., Jones, R. F., Scott, R. F., Shipley, E. N., Sperling, F. B., and Sutton, G. H., "Lunar Surface Mechanical Properties," Surveyor I Mission Report. Part II: Scientific Data and Results, Technical Report 32-1023, pp. 69–85, Pasadena, Calif., September 10, 1966.
- IV-2. Christensen, E. M., Batterson, S. A., Benson, H. E., Choate, R., Jaffe, L. D., Jones, R. H., Ko, H. Y., Spencer, R. L., Sperling, F. B., and Sutton, G. H., "Lunar Surface Mechanical Properties," Surveyor III Mission Report. Part II: Scientific Results, Technical Report 32-1177, pp. 111-153, Jet Propulsion Laboratory, Pasadena, Calif., June 1, 1967.
- IV-3. Christensen, E. M., Batterson, S. A., Benson, H. E., Choate, R., Hutton, R. E., Jaffe, L. D., Jones R. H., Ko, H. Y., Schmidt, F. N., Scott, R. F., Spencer, R. L., and Sutton, G. H., "Lunar Surface Mechanical Properties," Surveyor V Mission Report. Part II: Science Results, Technical Report 32-1246, pp. 43–88, Jet Propulsion Laboratory, Pasadena, Calif., November 1, 1967.
- IV-4. Christensen, E. M., Batterson, S. A., Benson, H. E., Choate, R., Hutton, R. E., Jaffe, L. D., Jones, R. H., Ko, H. Y., Schmidt, F. N., Scott, R. F., Spencer, R. L., Sperling, F. B., and Sutton, G. H., "Lunar Surface Mechanical Properties," Surveyor VI Mission Report. Part II: Science Results, Technical Report 32-1262, pp. 47–108, Jet Propulsion Laboratory, Pasadena, Calif., January 10, 1968.
- IV-5. Spencer, R. L., Determination of Footpad Penetration Depth from Surveyor Spacecraft Shadows, Technical Report 32-1180, Jet Propulsion Laboratory, Pasadena, Calif., October 1967.
- IV-6. Shoemaker, E. M., Batson, R. M., Holt, H. E., Morris, E. C., Rennilson, J. J., and Whitaker, E. A., "Television Observations from Surveyor V," Surveyor V Mission Report. Part II: Science Results, Technical Report 32-1246, pp. 7–45, Jet Propulsion Laboratory, Pasadena, Calif., November 1, 1967.

Acknowledgment

We thank Dr. Ronald F. Scott, Caltech, for providing data on surface-sampler operations, and Mr. F. I. Roberson, JPL, for his help in their interpretation; Mr. Charles Goldsmith and Mr. William Peer, JPL, for constructing the mosaics that appear in this section of this Report (including the unique Fig. IV-31), as well as for their support in mission operations and laboratory simulations; Mr. Lloyd Starks, JPL, for supporting mission operations and assisting in laboratory simulations.

We also thank Dr. George Sutton, University of Hawaii, for his continuing work on analysis and interpretation of lunar soil elastic properties from shock-absorber strain-gage data; and Dave Conway, Margaret Dove, and John Hinchey, HAC, for help in the landing dynamic simulations.

V. Soil Mechanics Surface Sampler

R. F. Scott (Principal Investigator) and F. I. Roberson

A. Lunar Surface Operations

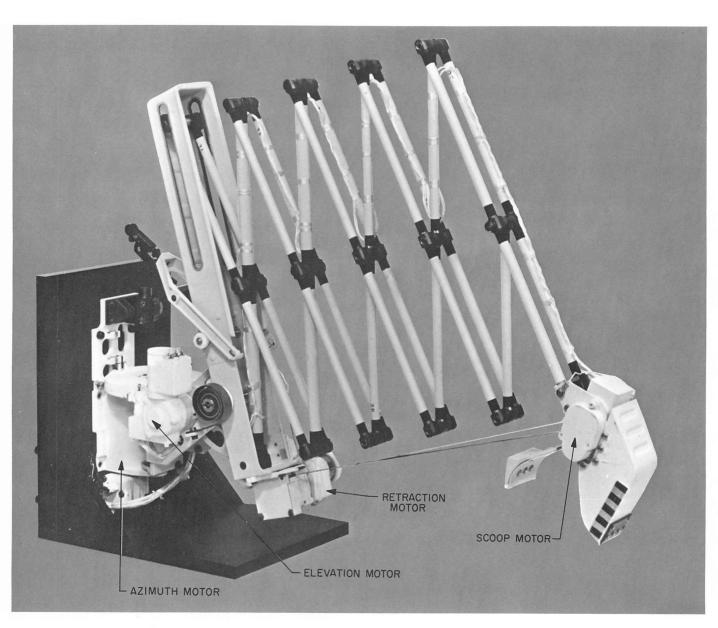
1. Subsystem Description

The physical design of the surface-sampler mechanism and its auxiliary electronics unit is the same as that of *Surveyor III* (Ref. V-1). The subsystem, as discussed here, includes the mechanism, its auxiliary, wiring harness, and mounting substructure.

- a. Mechanism, motors, and electronics. The extension/retraction mechanism, the motors, and auxiliary electronics unit are described in Refs. V-1 and V-2; the primary change made on Surveyor VII consisted of an increase in the capacity of the electronic auxiliary heater to 7.5 W.
- b. Scoop. The surface-sampler scoop is attached to the end of the extension/retraction mechanism (Fig. V-1). On Surveyor VII, the flat foot of the scoop door incorporated two embedded, rectangular horseshoe magnets. These magnets are shown in Fig. V-2, outlined by fine-grained material, after contact with the lunar surface. (See Sec-

tion VII-B of this Technical Report for a more detailed description of the magnet test.)

- c. Temperature sensors. In addition to the temperature sensor within the auxiliary electronics unit, the elevation and retraction motors have a sensor attached to each motor housing (Fig. V-1).
- d. Mounting substructure. The surface sampler is mounted below the survey television camera and to the right of the alpha-scattering instrument, as viewed from the position of the television camera. The relative positions of the surface sampler, television camera, and alpha-scattering instrument between footpads 2 and 3 of the Surveyor VII spacecraft are shown in Fig. V-3. The mounting substructure was designed to provide the surface sampler with the capability of reaching the alphascattering-instrument sensor head in its normally deployed position on the lunar surface and redeploying it to another selected location. The design of the azimuth drive prevents the surface sampler from reaching footpad 2. The areas of surface-sampler operations and alphascattering-instrument redeployment capability are shown in Fig. V-4.



 $Fig.\ V-1.\ \ Surface\ sampler\ on\ test\ stand,\ partially\ extended.$

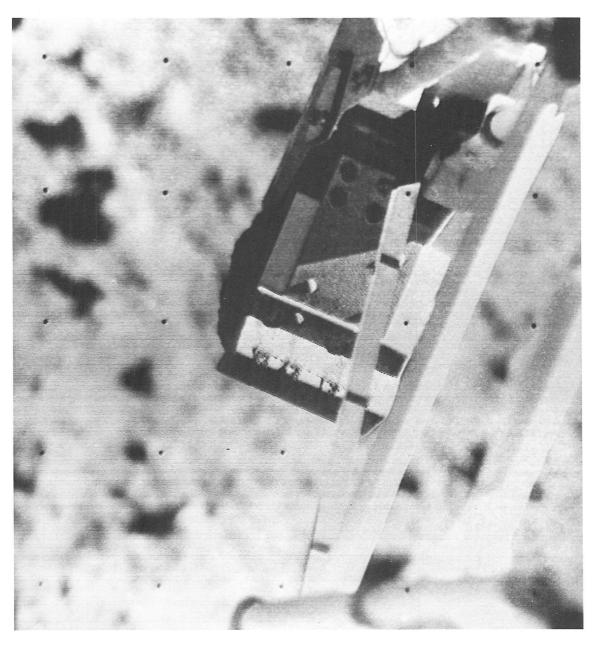


Fig. V-2. Surface-sampler scoop holding rock A. Note that the rock is slightly larger than the width of the scoop (Day 012, 02:52:15 GMT).

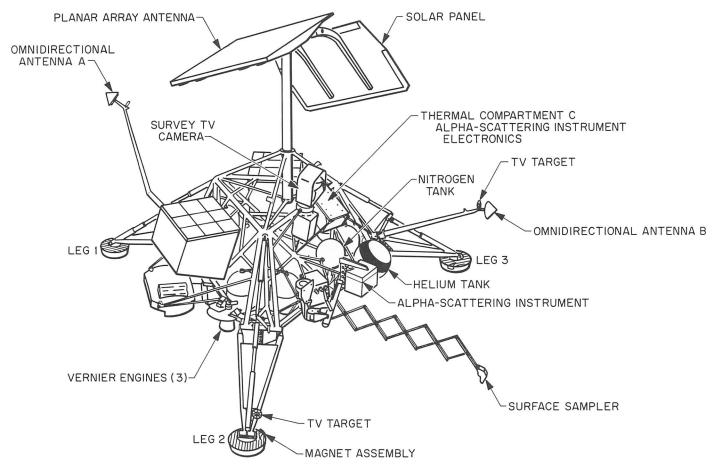


Fig. V-3. Surveyor VII spacecraft configuration showing surface sampler fully extended. The alpha-scattering instrument is in the stowed position.

2. Functional and Operational Description

The surface sampler, through the azimuth, elevation, and extension motors, can be driven in 0.1- or 2.0-sec steps left and right, up and down, and radially in extension and retraction. Figure V-4 shows the area that can be reached on a nominal surface.

a. Commands. Spacecraft commands listed in Table V-1 provide all surface-sampler subsystem operations. The heater commands are self-explanatory, as are the power on and off commands. The zero- and one-level input commands are used to generate functional commands within the auxiliary electronics unit. Table V-2 provides a dictionary of functional commands so generated. To command a single surface-sampler motion requires a minimum of five commands; a series of any given motions requires multiple commands (Ref. V-2). For operational convenience and to reduce the chances of operational error, command tapes are used to transmit the correct sequence of spacecraft commands.

A special-purpose command tape was used in the performance of several bearing tests during Surveyor VII lunar operations. Designated command tape 907, this tape first sets the 2.0-sec timing mode and loads the command to lower the surface sampler. Then, the execute and power off commands, separated by exactly 0.5 sec, are transmitted; this provides the surface sampler with the capability of applying loads to the surface for 0.5 sec. Command tape 907 continues, changing the spacecraft telemetry mode, taking a television picture, changing back to the original telemetry mode, and repeating the entire sequence. Figure V-5 presents a force vs penetration plot of such a bearing test (see Section V-B of this Report).

b. Telemetry and data display. During surface-sampler lunar operations, telemetry from the spacecraft is displayed in several ways. A computer (Univac 1219) processes spacecraft telemetry and provides a cathode-ray tube display. Selection of the proper format causes data

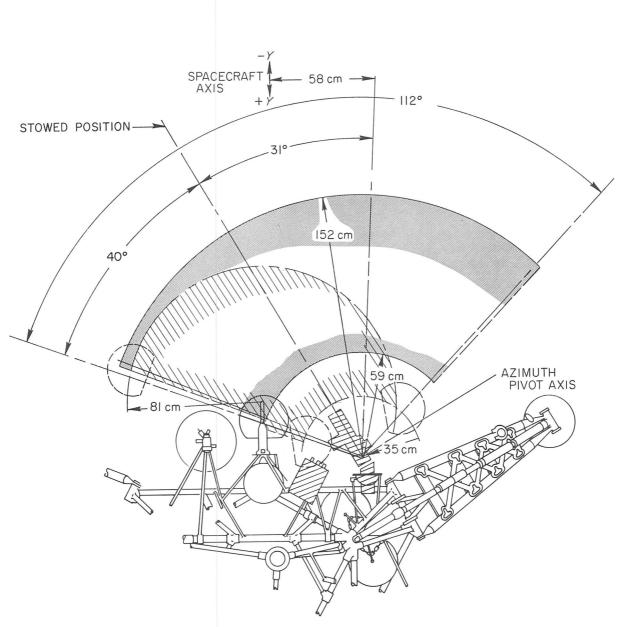


Fig. V-4. Plan view of surface-sampler area of operations for a nominal surface. The cross-hatch indicates the area within which the alpha-scattering-instrument sensor head can be manipulated by the surface sampler.

Table V-1. Surface-sampler subsystem commands

Spacecraft command	Designation	Function performed			
0131	Power on/execute	Turns subsystem power on; if power is on, executes the command in the register			
0132	Digital one input	Enters a one-level input to the command decoder shift register			
0133	Digital zero input	Enters a zero-level input to the command decoder shift register. If the register is full, a zero-level input clears the register and resets SS-2 ⁿ to low			
0134	Power off	Turns subsystem power off. Turning power off automatically resets the register, and sets fine timing mode			
0616	Heater off	Turns off power to auxiliary thermal control			
0614	Heater on	Turns on power to auxiliary thermal control			

Table V-2. Command glossary

Digital input	Function			
0111	Set fine timing (0.1 sec)			
0000	Set coarse timing (2.0 sec)			
1101	Enable squib firing			
0101	Enable squib firing (backup)			
0011	Release mechanism (fires squib)			
1111	Disable squib firing (protection of circuits)			
1001	Open scoop			
1110	Close scoop			
1000	Release clutch			
1010	All motors off			
0001	Extend			
0110	Retract			
1011	Left azimuth			
1100	Right azimuth			
0010	Lower			
0100	Elevate			

pertinent to the surface-sampler operations to be displayed. Teletype outputs provide command confirmation, and computer line printers provide hard copy data, again on a selectable format basis. Figure V-6 is an example of a printout available during operations for "quick-look" analyses. Telemetry pertinent to surface-sampler operations is listed in Table V-3.

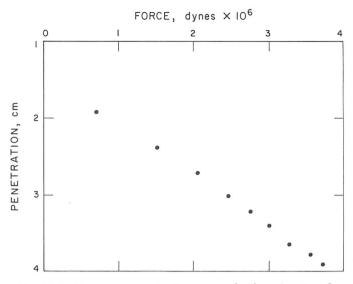


Fig. V-5. Force vs penetration curve for bearing test 2.

The motor current is assigned five symmetrically positioned commutator frames, while other pertinent data (voltage, temperature, etc.) are assigned a single frame. This provides motor-current data at 50-msec intervals and other data at 250-msec intervals at the highest spacecraft telemetry bit rate (4400 bits/sec). For a 2-sec motor command, nominally 40 motor-current samples are received; this sampling interval is apparent in the plot of Fig. V-7.

Table V-3. Surface-sampler telemetry assignments

Spacecraft telemetry designation	Data presented
SS-1	Digital bit indicates power on or off
SS-2	Digital bit indicates command register full or not full
SS-10	Motor current
SS-12	Electronic auxiliary temperature
SS-14	Retraction motor temperature
SS-15	Elevation motor temperature
EP-4	Unregulated bus voltage

Fig. V-6. Typical Univac 1219 computer printout for surface-sampler operations. Note 1: spacecraft commands are printed, and a program provides command recognition for surface-sampler sequences. Note 2: Surface-sampler motor-current samples are printed at 50-msec intervals while motor is running. Note 3: at completion of each motor operation, the motor-current average for that function is printed.

			S/C-7 DAY 1		SM/SS	2018			1
			UNR BUS E 2641-02	SS AUX T 5737-02	SS MECH T 1093-01	SS FL M T 1215-01	SS MOT I -1338-04	SS MI AVE 2470-04	
1.36.77.894	MIROOP (IP	1122		8 9000 000			● 0000700 30000		
1.37.13.887	XX.SPARE XFEP A LO	1737							
1.37.20.386	NEACXU DN	Ø126 Ø112							
1.37.24.386	PM 4 ON 2 MODE 4	Ø210 /4400							
01.37.27.83	5								
01.37.28.21	5								
01.37.32.95	14								
01.37.40.20	0								
01.37.41.45	9								
01.37.42.08	9								
01.37.43.08 01.37.43.83	4								
01.37.47.08	4								
01.37.47.58	4								
01.37.48.58	4								
01.37.52.883	SS 7 CMD	0133		7					
01.37.52.83 1.37.53.383	SS 2 CMD	Ø133	2647-92						
1.37.53.823	SS 7 CMD	0133							
1.37.54.3 ⁹ 3 01.37.54.20	A		2641-02						
1.37.54.883 01.37.55.08	3	9999	2647-02						
1.37.55.383 1.37.55.883	SS CLEAR	0133 0133		> NOT	ΕΙ				
1.37.56.383 01.37.56.28	SS 1 CMDN	0132	2644-92						
1.37.56.882	SS 2 CMD	Ø133	2641-02						
1.37.57.3 ² 01.37.57.19	SS A CMD	0133 NT ON							
01.37.57.62 1.37.57.882	B						-1969-94		
01.77.57.67	18						-1314-04		
1.37.58.3 ² 2 01.37.58.19	SS TLFAR	0133 NT OF							
01.37.58.63	7 A)			-1362-04 -1314-04		
01.38.00.15 01.38.00.15	PR +S CM F	NT ON					7988-04	NOTE 2	
01.38.00.67	7.8						5473-04		
01.38.00.70	8.8		2597-02				4008-04		
01.38.00.7	7.8						3715-04		
01.38.00.8	5.3		2606-02						
01.38.00.43 01.38.00.93							3153-04 2763-04		
01.38.00.9							2543-04		
01.38.01.0	7.8						2934-04		
01.38.01.1	7 R						2567-04 2128-04		
01.38.01.1		NT OF	F				2519-04		
01.38.01.2	7.8						2445-04 1835-04		
01.38.01.3	3.3		2612-02						
01.38.01.3	2.8						1762-04 2030-04		
01.38.01.4	7.R 2.R						2226-04		
01.38.01.5 01.38.01.6	7.8						2543-04 2128-04		
01.38.01.7	28						2348-04 2543-04		
01.38.01.7 01.38.01.8	28						2152-04		
01.38.01.8	7 A 2 B						2348-04 1933-04		
01.38.01.9 01.38.02.0	7.8						2152-04 2348-04		
01.78.02.0	78						1737-04		
01.38.02.1	78						2519-04		
01.38.02.2	7 R 2 R						2494-04		
01.38.02.3	78						2543-04		
01.38.02.4	7 R						2348-04 2543-04		
01.38.02.5 01.38.02.5	7.8				÷)		2152-04		
01.38.02.6 01.38.02.6	28						-1338-04	2665-84 NOTE	3
01.38.02.7 01.38.03.2	ØR		2636-02 2641-02						
01.38.21.2	82		2647-02 2641-02						
01.38.22.9 01.38.34.3	32		2647-02						
01.38.34.9	82		2641-02						
01.38.34.9 01.38.38.3	56		2641-02						
01.38.39.7	06		2641-02						
01.38.40.5 01.38.40.9	56		2647-02 2641-02						
01.38.41.8 01.38.45.7	31 06		2647-02 2641-02						
01.38.48.5 01.38.53.7	81		2647-02 2641-02						
01.38.54.5 01.38.54.5 01.38.54.9	81		2647-02						
01.38.56.9	68		2641-92	5014-02					
01.38.57.0 01.38.57.7	81		2647-02 2641-02						
	30		2647-02						

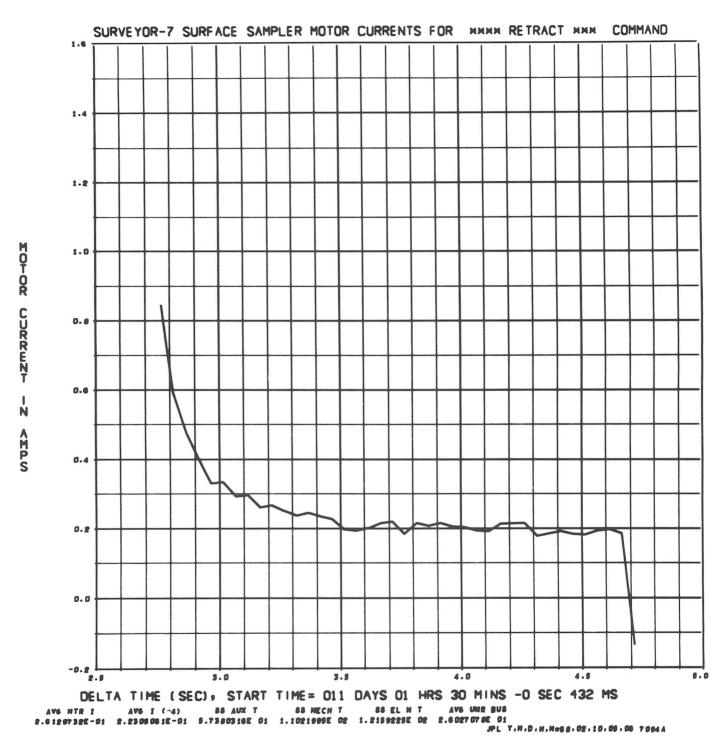


Fig. V-7. Typical computer output plot of post-mission, processed surface-sampler motor current.

A multichannel strip chart recorder (Brush recorder) provides real-time plots of motor current for evaluation of surface-sampler performance. The command register status and power on/power off status are also displayed in this recorder.

To assist in post-mission analyses of surface-sampler performance, the motor-current data are further processed and plotted (after the mission) for comparison with calibration data. An example of such a plot is shown in Fig. V-7. In addition to plotting the motor-current values, this output includes temperatures, bus voltage, average value of motor current, and an average of the motor current ignoring the first four samples in a given burst. These first four samples indicate a motor starting transient.

c. Calibration. Shortly before launch, the surfacesampler subsystem calibration was performed at Cape Kennedy, Florida. At a normal voltage of 22 V, the motor current required to drive the surface sampler against a series of forces was recorded for this calibration. The opposing force was varied in controlled steps from zero up to a force that stalled the drive motor. Both retraction, or trenching mode, and lowering, or bearing mode, calibrations were performed, each at extension distances of 106 and 148 cm. The motor-current data were recorded by a Univac 1219 computer, and printouts in the same format as flight data were provided. Plots of the current pulses were also processed, again as shown in Fig. V-7. For quick-look analysis in real time, a plot of average motor current vs force was used. A typical plot of a bearing calibration test at full extension is given in Fig. V-8.

d. Operations. The basic operations of the surface sampler are bearing, trenching, picking, and lifting of

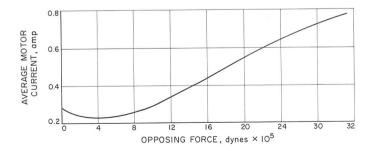


Fig. V-8. Calibration curve produced from pre-flight calibration performed at Cape Kennedy, Florida. This curve shows force vs current for the bearing test mode with the surface sampler at 147-cm extension.

objects. A bearing test can be performed with the scoop door open, thus presenting a narrow blade edge to bear on the surface, or with the scoop closed, to present a 2.5- by 5.1-cm bearing plate. Bearing tests are performed by selecting a test site from the television pictures, positioning the scoop above the point of interest, and commanding the lowering of the scoop. This can be accomplished with several 2.0-sec commands until a stall condition is reached, or by using the special command tape 907 (described in Section V-A-2) to provide a series of 0.5-sec commands. A 0.1-sec command is not used in a sequential bearing test because the motor-current readout occurs at 50-msec intervals at the highest spacecraft telemetry bit rate available, so that the 0.1-sec command does not afford sufficient current or force samples for a meaningful test.

A trenching test is performed by driving the scoop into the surface (normally, but not necessarily, with the scoop door open) in the same manner as in a bearing test. After the elevation motor is stalled, a series of retraction commands pulls the scoop back through the soil, digging a trench the width of the scoop (5.1 cm). Motor-current data yield information about the strength of the soil; current measurements during successive passes through a trench provide information about the variation of strength with depth.

A picking, or impact, test is performed by positioning the scoop above a desired surface point or rock, and releasing the solenoid-operated elevation drive clutch. This allows the mechanism to rotate freely at the elevation axis, so that a torque spring and gravitational acceleration cause the scoop to strike the surface.

Manipulating, grasping, or lifting objects with the surface sampler is the most time-consuming type of operation. Such an effort requires careful study of television pictures before and after any command sequence to evaluate the surface-sampler response and to select further commands to achieve the desired result.

Intended as an operational aid, Fig. V-9 is a plot of the surface-sampler area of operations, with a diagram of the surface areas viewed by the television camera at various camera azimuths and elevations. From the television data, the position of a selected object within the surface-sampler area can be plotted, and the commands required to move the surface sampler to the object may be chosen.

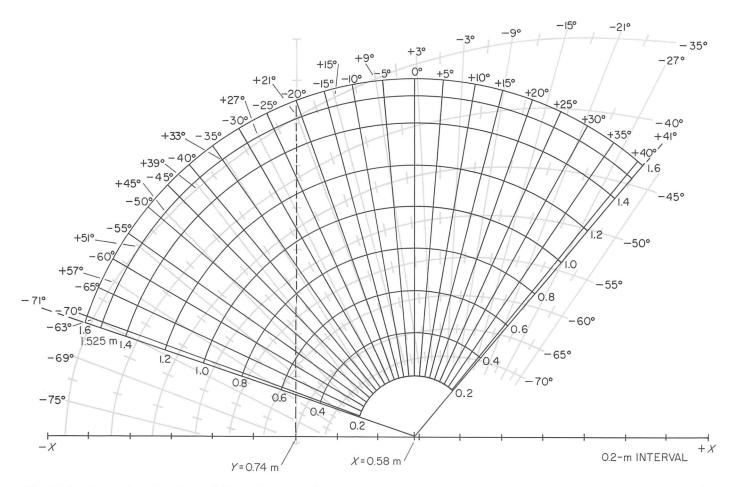


Fig. V-9. Operational aid used for selecting television camera position to view specific areas of surface-sampler operations.

3. Mission Description

a. Engineering performance. During Surveyor VII lunar operations, the performance of the surface-sampler subsystem was flawless under a wide range of operating conditions. Figure V-10 shows the temperatures of the elevation and retraction motors, and of the auxiliary electronics unit throughout the first lunar day. During the critical period around lunar noon (Days 015 through 018), the surface sampler was operated to provide shade for the thermal-control surfaces of the alpha-scattering instrument sensor head. Without this shade, it is possible that the sensor-head temperature would have exceeded its survival limits.

Several of the shading operations were performed when the auxiliary electronics unit of the surface sampler was above its upper operating limit. In these operations, the motors operated normally at temperatures up to 180°F. On the other hand, at one stage during post-sunset operations, retraction forces were applied to the lunar surface

at a time when the retraction motor temperature was $-167^{\circ}\mathrm{F}$.

Throughout the mission, the command decoding and telemetry outputs of the auxiliary electronics unit performed as designed. Table V-4 lists the total commands and operating durations for the subsystem during the first lunar day. Of the 36 hr, 21 min, of operational time, a total of 8 hr, 45 min, was used in deploying or redeploying the alpha-scattering instrument.

b. Lunar operations: first lunar day. Initial operations for the surface sampler were not scheduled to begin until the alpha-scattering instrument had been deployed to the lunar surface, thus ensuring an undisturbed lunar surface as the first sample. This delay would also provide adequate television coverage of the area for planning tests before initiation of activities. This preliminary television coverage is shown in Fig. V-11. The attempt to deploy the alpha-scattering-instrument sensor head to the

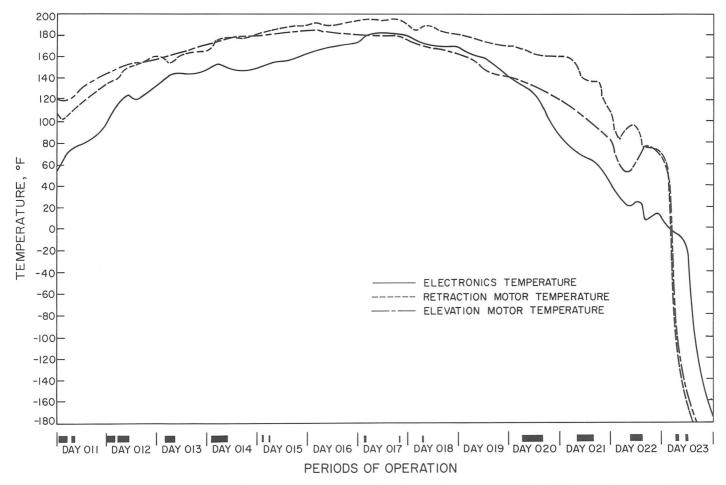


Fig. V-10. First lunar day surface-sampler temperatures. Periods of operation are noted by the bars at bottom of figure.

Table V-4. Surface-sampler subsystem performance summary for first lunar day

Day of 1968	Power on time, hr:min	Number of commands addressed to surface sampler	Number of surface-sampler functions performed ^a	Number of surface-sampler mechanism motions commanded	
011	03:59	806	371	184	
012	06:30	1,581	766	426	
013	03:29	1,499	853	561	
014	03:43	2,008	1,190	828	
015	00:09	73	38	22	
016	00:00	0	0	0	
017	00:10	42	18	6	
018	00:03	21	9	3	
019	03:07	1,364	898	590	
020	05:35	2,006	1,022	596	
021	04:37	1,289	713	463	
022	04:01	1,830	1,017	685	
023	00:58	120	61	33	
Total	36:21	12,639	6,956	4,397	
Functions performe	ed include such things as set timing mode	e, clear register, etc., and do not necess	sarily result in surface-sampler motions.		

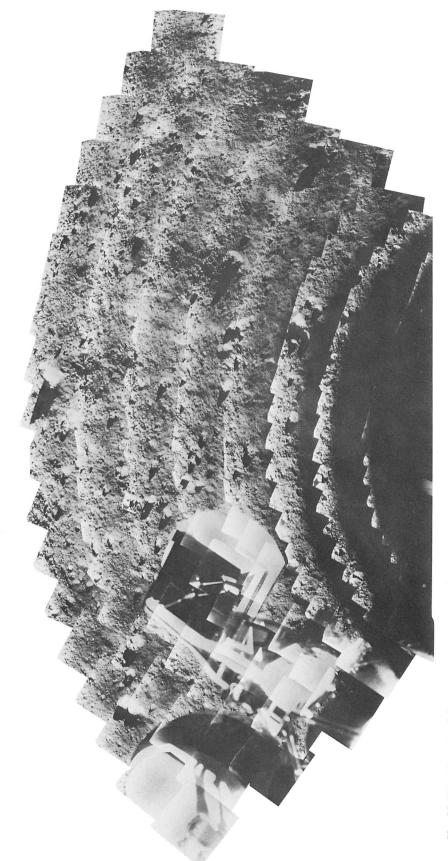


Fig. V-11. Mosaic of Surveyor VII pictures showing the surface-sampler area of operations before activities began (Catalog 7-SE-4).

lunar surface by normal means was unsuccessful. This led to decisions to start surface-sampler activities and, after certain minimal data were acquired, to attempt to free the alpha-scattering instrument.

Day 011. Surveyor VII surface-sampler operations started with the initial power on command at 01:00:28 GMT; after four 2.0-sec extend commands, the first television picture verifying proper response was received at 01:22:35 GMT. This initial checkout procedure continued with motor current and video verification that the azimuth, elevation, and extension drive systems were functioning properly.

Initial contact with the lunar surface occurred at bearing point 1, shown in Figs. V-12 and V-13. This bearing test was accomplished by driving the scoop down two 2.0-sec steps. Bearing point 2, located to the left of bearing point 1 and at a greater extension distance (Fig. V-12), was the first test using command tape 907. This test is shown in Fig. V-14a.

After these initial bearing tests, the first attempt was made to free the sensor head from its background position. In the hope that the problem was a minor frictional one, the attempt consisted of light taps applied to the circular plate of the sensor head. Although television

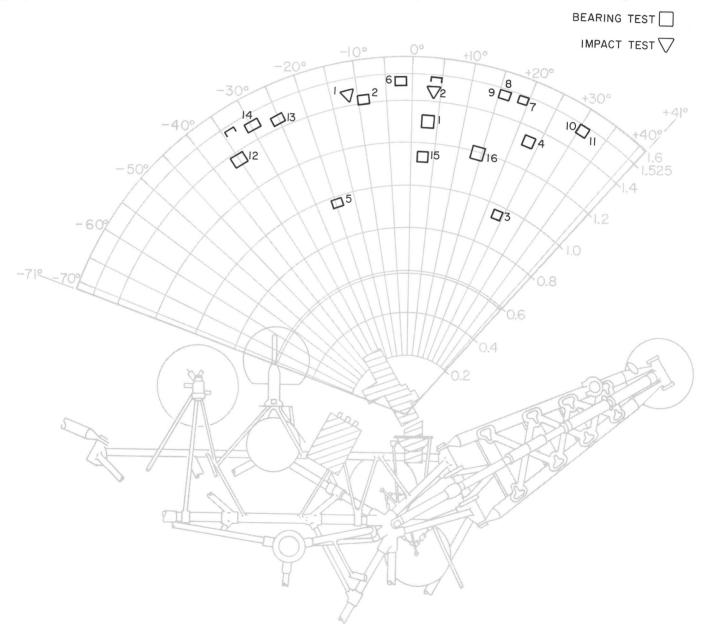


Fig. V-12. Plan view of surface-sampler operations showing location of bearing and impact tests performed.

pictures did show that the alpha-scattering instrument moved and swayed at the end of its nylon cord, it did not lower.

Day 012. Surface-sampler operations on Day 012 started with bearing point 3 (Fig. V-12). This test consisted of a 2.0-sec down command in which surface contact was made during the last one-third of the travel. The elevation motor was not stalled, thereby giving data on the initial penetration only.

Bearing point 4 followed at the same azimuth position at a greater extension (Fig. V-12). Again, command tape 907 and eight 0.5-sec steps were used. Bearing point 4 is seen in Fig. V-14b.

Bearing test 5 was performed by moving left and locating above the position noted in Fig. V-12. This bearing test was performed using a single 2.0-sec lower command and attempting to contact the surface during the steady-state part of the travel. This contact was achieved, and the result is shown in Fig. V-14c.

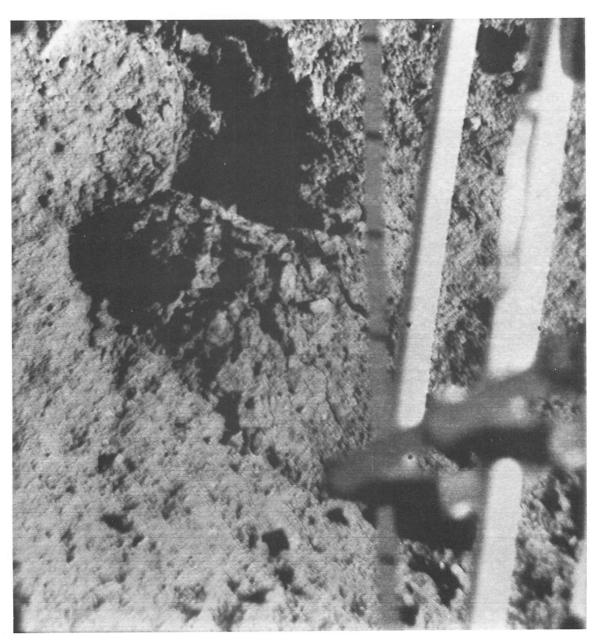


Fig. V-13. Bearing test 1. This picture shows the first surface-sampler contact with the lunar surface at the Surveyor VII landing site (Day 011, 03:55:42 GMT).

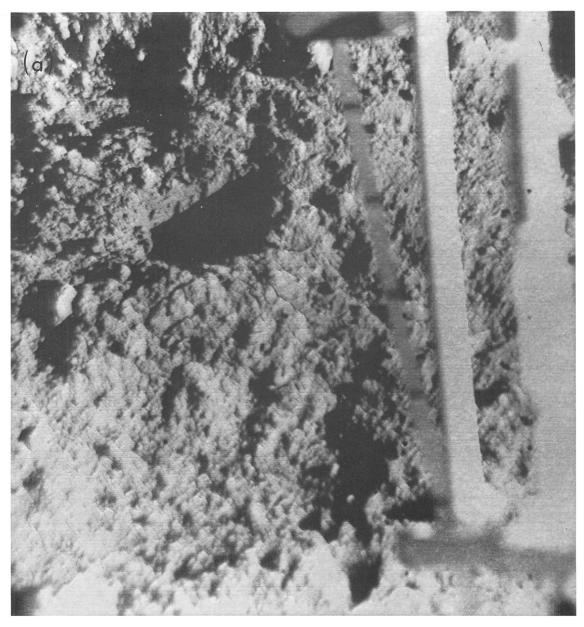


Fig. V-14. Surface-sampler bearing test results. (a) Bearing test 2 (Day 011, 04:52:24 GMT). (b) Bearing test 4 (Day 012, 01:58:08 GMT). (c) Bearing test 5 (Day 012, 04:38:26 GMT). (d) Bearing test 6 in progress (Day 019, 12:29:33 GMT).

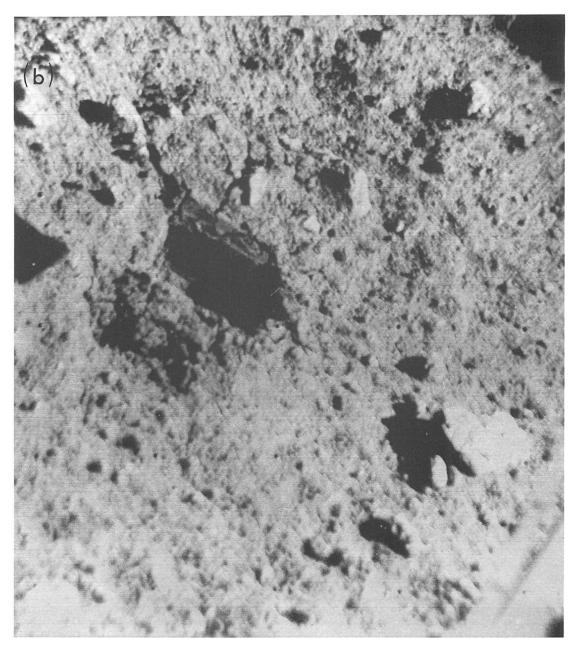


Fig. V-14 (contd)



Fig. V-14 (contd)

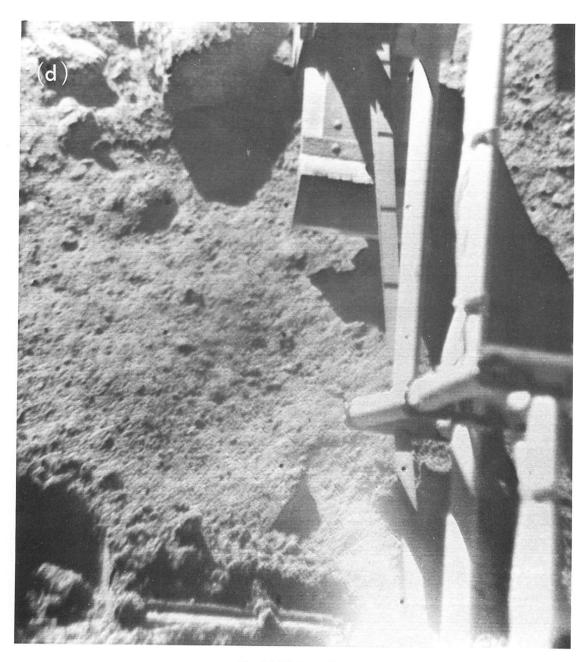


Fig. V-14 (contd)

The initial pickup of rock A (Fig. V-14d) followed bearing test 5. The rock was lifted and motor-current data taken to give weight information. The rock was dropped after this first pickup and landed at position A' in Fig. V-18. Figure V-2 shows the rock in the scoop before it was dropped.

In the Surveyor Experiment Test Laboratory, an analysis of the alpha-scattering instrument's position led to a plan for further attempts to free the sensor head. The surface sampler was positioned near the right side of

the sensor head and, by a series of extend and left azimuth steps, gradually rotated the sensor head and moved it left until it was in contact with the helium tank. In this position (shown in Fig. V-15), it appeared that the alphascattering instrument was wedged between the helium tank, the surface-sampler scoop, and some part of the alpha-scattering instrument's standard-sample bracket. In this condition, surface-sampler lower commands applied a downward force to the alpha-scattering instrument, which came free and moved down several centimeters. This allowed the scoop to be placed on top

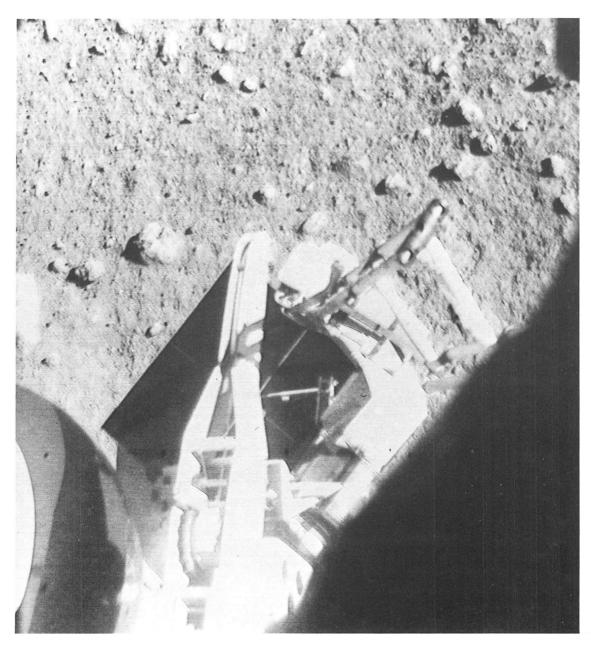


Fig. V-15. The surface sampler is shown forcing the sensor head against the helium tank, preparatory to applying a downward force to free it (Day 012, 06:57:30 GMT).

of the alpha-scattering instrument and a direct downward force to be applied to it. The thermal mirror on the sensor head was an aid in positioning the scoop and, as can be seen in Fig. V-16, afforded a view of the scoop interior. The alpha-scattering instrument was lowered to a point where it appeared to be on the surface, but a short test of the instrument counting rate showed it was not. The surface sampler was again positioned above the sensor head and continued to force it down until it was on the surface in the position shown in Fig. V-17.

Day 013. The first activity on Day 013 was an attempt to reach rock B (Fig. V-18) and lift it. Two attempts were made, and verified that the rock was beyond the maximum extension distance for the surface sampler. In further attempts to weigh another rock (in addition to rock A), rock C was picked up (Fig. V-18) and, in the course of being elevated for weighing, slipped out of the scoop. Though it was not immediately apparent, later television surveys revealed that it landed at location C' in Fig. V-18.

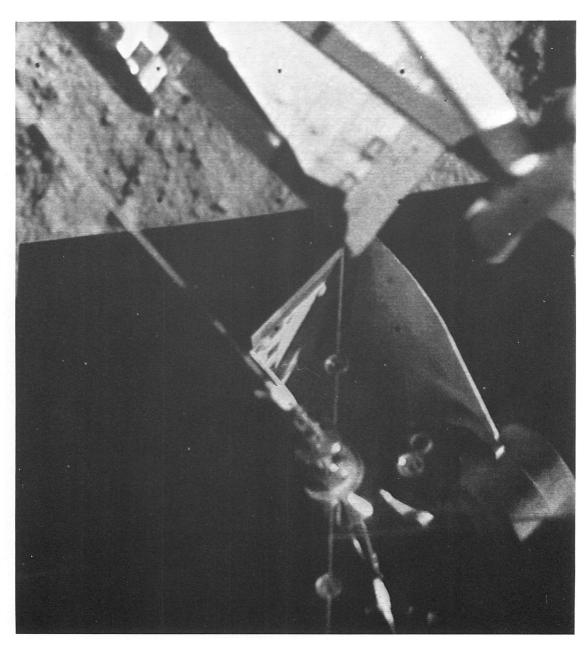


Fig. V-16. The thermal radiating mirror of the sensor head affords an excellent view of the surface-sampler scoop interior when the scoop is positioned above it (Day 012, 09:17:28 GMT).



Fig. V-17. The sensor head is shown on the lunar surface in position for its first analysis after the surface sampler has forced it down (Day 012, 10:28:32 GMT).

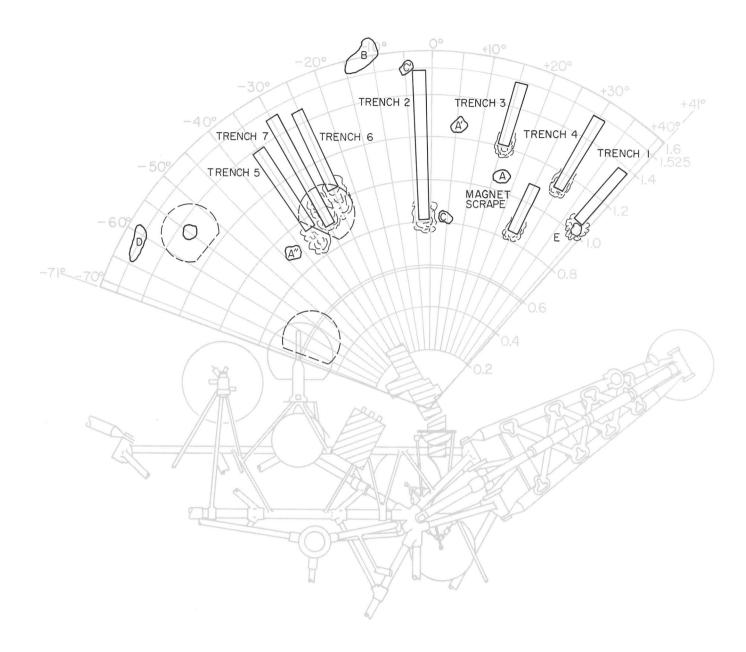


Fig. V-18. Plan view of surface-sampler operations showing trenches, rocks, and alpha-scattering-instrument positions.

Because the sun azimuth was progressing across the surface-sampler area, the first trenching operation was performed at the extreme right azimuth position. The position choice was also influenced by a desire not to disturb the surface near the sensor head of the alpha-scattering instrument and by the operational convenience of azimuth positioning accuracy for possible further passes through the trench. Trench 1, shown in Fig. V-19, was dug by going to the right stop, applying two 2.0-sec lower steps, at which point the surface sampler was

stalled, and retracting six 2.0-sec steps. The scoop was then lifted clear of the surface and extended back to the head of the trench. A second pass through the trench required a single lower command, and after four 2.0-sec retract commands, the surface sampler stalled. Two additional retract commands failed to break it loose.

The surface sampler was extended and lifted clear of the trench. Positioning the scoop to cast a shadow on the sensor head completed operations for Day 013.

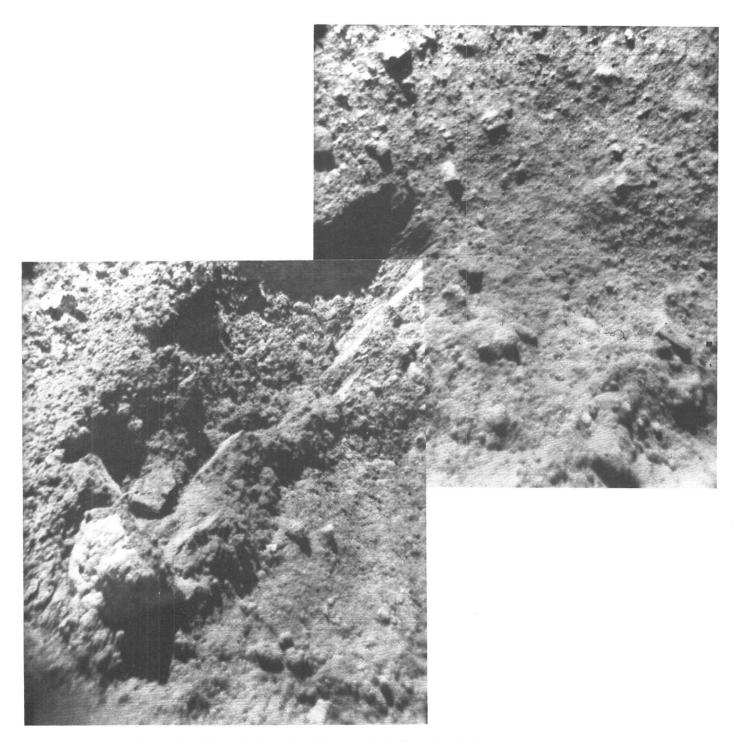


Fig. V-19. Mosaic of trench 1. Note the irregular shape and shallow depth of the trench (Day 019, 20:00:01 and Day 019, 20:00:59 GMT).

Day 014. In a further attempt to obtain a large rock for weighing, reinforced by a desire to make a rock available for analysis by the alpha-scattering instrument, the operations for Day 014 consisted entirely of working with rock D (Fig. V-18). At this time in the mission, television camera and spacecraft battery temperatures were high, and in fact dictated low-duty-cycle operations. The surface-sampler operations consisted of extending to the maximum distance at rock D, and closing the scoop on the rock. The rock was dislodged, as shown in Fig. V-20b,

and attempts to lift it resulted in its slipping from the scoop. Over a total period of 7 hr, attempts to move the rock closer for a better grip were unsuccessful.

Operations for the day were concluded with repositioning the scoop shadow on the thermal-control surfaces of the alpha-scattering instrument.

Day 015. Although the surface-sampler temperatures were high, the instrument was turned on and moved to

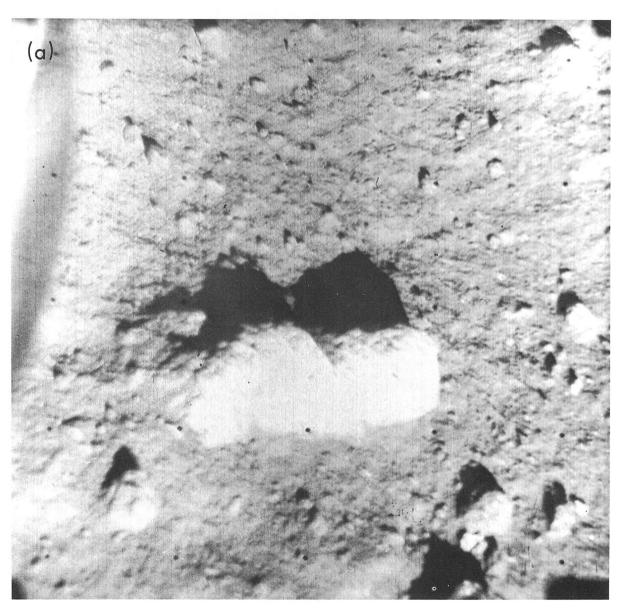


Fig. V-20. Two views of rock D. (a) Undisturbed view, showing exposed, smooth face (Day 012, 00:01:16 GMT). (b) After moving, showing angular, fragmented underside (Day 014, 05:32:25 GMT).

provide continued thermal relief for the sensor head. Surface-sampler operations were not effective under the severely limiting duty cycles imposed by camera temperature.

Day 016. No surface-sampler operations were performed.

Day 017. The surface-sampler scoop was moved twice to shade the sensor head. A total of six surface-sampler motions were commanded for this effort (Table V-4).

Day 018. On Day 018, spacecraft temperatures still precluded effective surface-sampler operation, and activity was again limited to shading the sensor head.

Day 019. With camera duty cycles increasing and general spacecraft temperatures improving, surface-sampler operations were resumed, starting with further weighing of rock A. The rock, at position A' in Fig. V-18, was lifted, recording motor current for weight data, and subsequently moved into the area of stereo view, using the auxiliary mirror for stereo coverage.

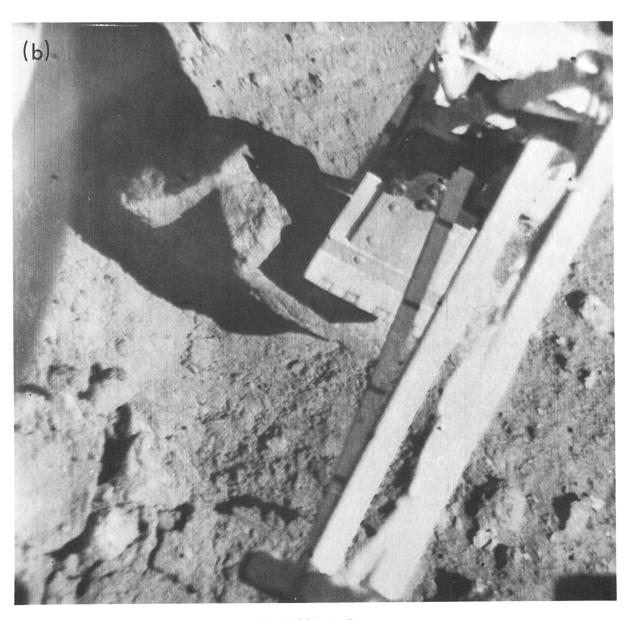


Fig. V-20 (contd)

Once in this area, the rock was viewed directly by the television camera, and viewed through the stereo mirror. Subsequently, the rock was picked up in the surface-sampler scoop, and stereo pictures were obtained. After dropping the rock, additional pictures were taken at the identical camera positions, to provide before and after coverage. Analysis of these pictures provided the information on surface-sampler deflection caused by the weight of the rock.

After the weighing exercise, the rock was again picked up and transported to a third location, point A" in Fig. V-18. This position was chosen for its proximity to the sensor head. The surface-sampler scoop was lowered to the rock at its new location, and a series of lower commands used to perform a bearing test on the rock.

From this position, the surface sampler was extended to its maximum distance; the scoop opened, and a 2.0-seccommand bearing test was performed at bearing point 6 (Fig. V-12). After the scoop was driven into the surface in this bearing test, a series of nine 2.0-sec retract commands completed the first pass through trench 2 (Fig. V-18). At the end of Day 019 operations, the surface sampler was left in place at the foot of trench 2.

Day 020. At the start of Day 020 operations, the surface sampler was lifted clear of its position at the foot of trench 2, extended, and lowered into the head of the trench for a second pass through the trench. After five 2.0-sec retract commands, a second lower command was given to maintain the scoop bearing force on the bottom of the trench. Three additional coarse (2.0-sec) retract commands completed the second pass through the trench.

After again extending to the head of the trench and lowering for the third pass through it, four 2.0-sec retract commands resulted in a stalled retraction drive. A fifth retract command failed to break it free, and some maneuvering of the scoop by extending and elevating slightly before continuing the retraction was necessary to clear the subsurface object causing the stall. After twice stalling on the object, the trench was lengthened to its maximum dimension. The third pass was completed after thirteen coarse retract steps, three of which were executed under stall conditions.

At the beginning of the fourth pass, near the head of trench 2, after the first two retract commands (2.0-sec timing mode), a slight increase in resistance was indicated by the motor-current data, and the scoop was observed to be forced laterally to the left, widening the trench as though the scoop were going around a buried obstruction. The remaining retraction met little resistance, and a total of seven 2.0-sec retract steps completed the effort in trench 2.

After completing trench 2, the scoop was extended and moved right to the point noted as bearing point 7 in Fig. V-12. With the scoop still open, a bearing test was performed, using command tape 907. A series of seven 0.5-sec commands completed bearing test 7. Bearing tests 8 and 9 were performed at the same site, just left of bearing point 7, as can be seen in Fig. V-12. Bearing test 8 was performed with the scoop closed, using command tape 907, for a total of four 0.5-sec lower commands. Figure V-21a and V-21b shows bearing test 8 in progress and after removal of the scoop, respectively.

Bearing test 9 was performed at the same location, after opening the scoop door. The test is shown in Fig. V-21c and V-21d, and consisted of two 2.0-sec lower commands. After the scoop was lifted clear of bearing point 9 for examination, it was lowered back in, at which time three 2.0-sec retract commands were executed, resulting in trench 3, located as shown in Fig. V-18. At the completion of the trench, the scoop was closed, and two 2.0-sec elevate commands were executed, with motor-current data to determine the weight of the soil in the scoop.

The scoop was extended to the maximum distance and moved right in preparation for bearing point 10, as located in Fig. V-12. As in bearing tests 8 and 9, bearing tests 10 and 11 were conducted using command tape 907, resulting in six 0.5-sec lower steps. These tests were followed by bearing test 11, performed with the scoop open, still using command tape 907, also resulting in six lower commands.

Trench 4 was dug by retracting three 2.0-sec steps from bearing point 11. The area noted in Fig. V-18 as the magnet scrape trench was the location of operations following trench 4. The scoop was lowered to the surface with the door closed and, by a series of 2.0-sec retract commands, was dragged across the surface in a trenching mode. After three such commands, the scoop was lifted clear of the surface and the scoop door opened. A rock fragment was observed, apparently adhering to the scoop door. To afford a closer television view, the scoop was elevated two 2.0-sec steps, and a narrow-angle television picture was taken. The result is shown in Fig. V-22,

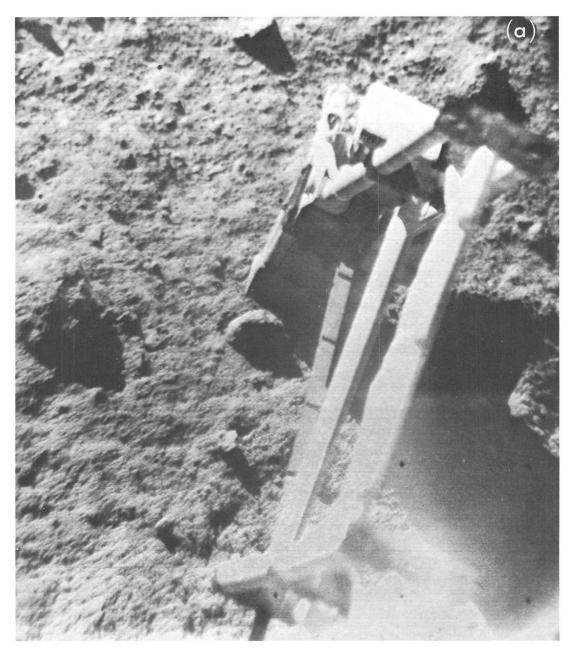


Fig. V-21. Bearing tests 8 and 9 in sequence. (a) Day 020, 11:41:05 GMT. (b) Day 020, 11:42:40 GMT. (c) Day 020, 11:55:42 GMT. (d) Day 020, 11:57:45 GMT.

and discussed in Section VII-B of this Report. Subsequent attempts to move the scoop into the stereo view area for closer television study of the fragment resulted in its loss before the stereo view was achieved.

To complete operations for Day 020, the scoop was again positioned to shade the sensor head.

Day 021. Operations for Day 021 started by performing 2.0-sec elevate commands at the final position of rock A, noted as position A" in Fig. V-18. These commands were

executed to gather no-load motor-current data before later lift tests with the sensor head at the same position.

Operations then proceeded with the positioning of the scoop above the sensor head and the closing of the scoop on the knob, or eye bolt, protruding at the center of the alpha-scattering-instrument thermal mirror. After grasping the knob, the sensor head was lifted clear of the surface and, after a series of elevate, extend, and right azimuth commands, was positioned above point A" (Fig. V-18).



Fig. V-21 (contd)



Fig. V-21 (contd)



Fig. V-21 (contd)

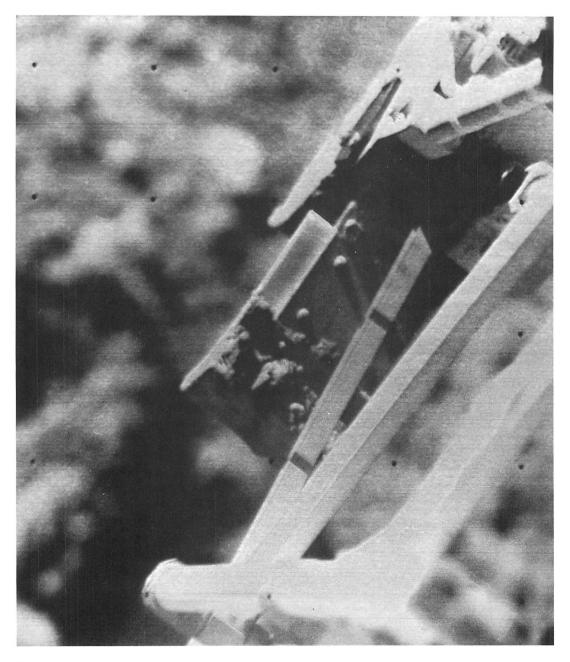


Fig. V-22. Fragment adhering to surface-sampler magnets after contacting lunar surface (Day 020, 14:57:46 GMT).

Two 2.0-sec elevate commands were commanded with the sensor head held by the scoop. The motor current provided a calibration by lifting a known weight to assist in analysis of similar data received while lifting rock A at this same position.

The continuation of extend and left azimuth commands led to the position shown in Fig. V-23, in which the target rock sample is seen at the lower-left corner of the sensor head. Continued maneuvering led to positioning the sensor head viewing port over this rock, as noted in Fig. V-18. In Fig. V-24, the ring around the rock shows the final position achieved.

Bearing point 12 (Fig. V-12) was the next site of operations; at this point, a bearing test was executed, using command tape 907. A total of six 0.5-sec lower commands was executed. At the completion of the bearing test sequence, trench 5 (Fig. V-18) was dug, requiring five 2.0-sec retract commands.

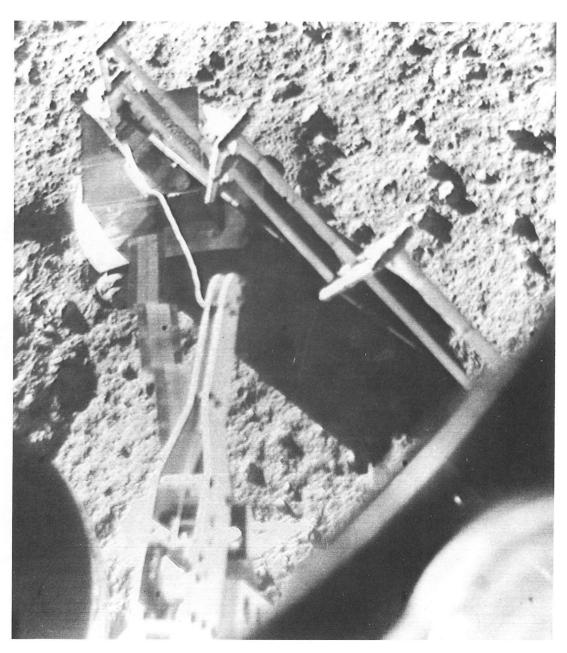


Fig. V-23. Surface sampler nearing final position in deploying sensor head to second sample on the lunar surface (Day 021, 11:44:53 GMT).



Fig. V-24. Surface sampler in process of moving sensor head from second to third lunar sample. Note ring around target rock at second sample location (Day 022, 11:21:12 GMT).

After closing the scoop, extend and right azimuth commands positioned the surface sampler for bearing point 13. This bearing test and trench were executed in the same manner as bearing test 12 and trench 5. Command tape 907 was used to execute five 0.5-sec lower commands, followed by four 2.0-sec retract commands. The surface sampler remained in contact with the surface at the foot of trench 6 at the end of operations on Day 021.

Day 022. Operations started by carefully completing trench 6, in the procedure used when the magnetic object was picked up on Day 020. No magnetic fragments were observed at this time.

To provide a large area of disturbed subsurface material as a third sample for the alpha-scattering instrument, a decision was made to dig a trench between trenches 5 and 6. To achieve this, bearing point 14 was contacted, and a bearing test consisting of two 2.0-sec lower commands was executed. The scoop was closed during this bearing test and during the subsequent retract commands, which produced trench 7.

The debris at the foot of trenches 5, 6, and 7 provided the third sample for chemical analysis, and efforts to redeploy the sensor head to this sample followed completion of trench 7. Redeployment again required positioning of the scoop above the sensor head and grasping the knob. Figure V-24 shows the sensor head after it had been lifted and partially moved to the third sample position.

The sensor head was placed on the debris at the foot of the trenches, and analysis of television pictures indicated the viewing port was directly above trench 7. A slight lateral movement of the sensor head was effected by placing the scoop against the side of the sensor head and commanding 0.1-sec left azimuth steps. The final position is noted in Fig. V-18.

After positioning the sensor head on its third sample, impact tests 1 and 2 were performed. These tests consisted of positioning the scoop above the points noted in Fig. V-18, elevating the desired height, and releasing the elevation drive clutch. Following the impact tests, bearing test 15 was performed, using command tape 907. Figures V-12 and V-18 show that bearing point 15 is very near trench 2. This test was performed with pictures of the trench wall taken between each bearing command to observe the wall behavior.

Bearing test 16 made use of command tape 907, and after each 0.5-sec bearing command, the scoop was lifted clear of the surface for television coverage. Low sun angles made interior views of the bearing point difficult; after three such 0.5-sec attempts, the bearing test was completed by executing two 2.0-sec commands, resulting in a stalled condition.

Using 0.1-sec right azimuth commands, the surface sampler was driven against the right azimuth stop, thus locating it above trench 1. The scoop was opened and positioned so that the blade was above rock E (Fig. V-18) at the foot of trench 1. After two 2.0-sec elevate commands, the clutch was released, allowing the scoop blade to strike the rock. As discussed in Section V-B-1, the rock fractured under the blow.

After careful television coverage of the fractured rock, including polarizing filter surveys, the scoop was extended and lowered into trench 2. Two 2.0-sec lower commands, followed by two 2.0-sec retract commands, resulted in the surface sampler being stalled against the subsurface rock previously encountered. It was left in this position in anticipation of post-sunset operations.

Day 023. Sunset occurred somewhat earlier than expected, resulting in a decision to operate the surface sampler while the spacecraft was being commanded by the Deep Space Station at Robledo, Spain (DSS 61). Without benefit of television, the trench 1 operation of the previous day was repeated, and again resulted in stalling against the subsurface rock. Motor current was transmitted and, at the low motor temperature, was high, as expected.

After Goldstone, California (DSS 11) acquired spacecraft control, the surface sampler was again stalled against the rock in an attempt to dislodge it or, as an alternative, to move the spacecraft.

c. Lunar operations: second lunar day.

Day 045. To verify that the surface-sampler subsystem had survived the lunar night, a single 2.0-sec extend command was executed. Both motor-current telemetry and emergency mode television verified normal response.

Day 051. Two 0.1-sec extend commands verified surfacesampler performance by motor-current telemetry. An attempt at one elevate and two left azimuth commands (all 2.0-sec) verified that the surface sampler seemed normal, but that the power system could not support operations.

B. Data Analysis

1. Discussion of Tests

Many tests of the mechanical properties of the lunar surface were conducted by the surface sampler, in addition to other manipulatory operations. This part of this section contains a discussion of these tests and preliminary analyses.

a. Description of area. Shortly after touchdown, a series of pictures was taken of the area of surface-sampler operations (see Fig. V-11). This narrow-angle mosaic shows the alpha-scattering instrument in the background position, from which it could not be successfully deployed to the surface by normal operations. It is seen that the lunar surface in the area of Tycho possesses more rocky fragments than did the Surveyor III site. Some of the fragments visible in the picture have dimensions of 6 to 10 cm across. Several of these fragments were moved during surface-sampler operations; one of them was weighed, and one broken.

Figure V-25 shows the accomplishments of the surface sampler by Day 021, toward the end of the first lunar day. In this mosaic, the alpha-scattering instrument can be seen in its second deployed position at the left-hand side of the picture; the surface sampler is in the process of excavating subsurface soil to provide the third sample for analysis. Some of the surface-sampler tests, identified in Figs. V-12 and V-18, may also be seen in Fig. V-25. In particular, just to the right of the surface-sampler position, a fairly large rock (rock B) is seen at the outer edge of the surface-sampler area. On the near side of the rock, two small trenches demonstrate that the rock was just outside the surface sampler's reach. To the right of the rock is a long, 15- to 18-cm-deep trench, identified as trench 2 in Fig. V-12.

Some shorter trenches are visible on the right-hand side of Fig. V-25; on the extreme right-hand edge lies a shallow trench, which was the first trench attempted. This trench could be excavated to a depth of only 2.5 to 5 cm because of the presence of rock immediately below the surface. At the foot of this trench is a small rock fragment (rock E), which was broken by the surface sampler into two fragments after the picture was taken. On the left-hand side of the diagram, just to the right

of the shadow cast by the sensor head is a somewhat rounded rock (rock A), which was weighed. Many surface-sampler operations involved this rock, which was finally positioned as shown in Fig. V-25 to permit analysis by the alpha-scattering instrument. However, an undisturbed rock, better suited to analysis, was located at the position of the alpha-scattering instrument in Fig. V-25; the instrument, as shown, is located on top of this rock. In the lower left of Fig. V-25, at the very edge of the sensor-head shadow, is seen a rounded mark or indentation in the lunar soil. This indicates the position of the sensor head at its first sampling site, and was the location to which the surface sampler deployed the sensor head following its release.

b. Bearing tests. There were 16 bearing tests of various kinds conducted by the surface sampler before and after deployment of the alpha-scattering instrument. Some of these bearing tests are described here.

Figure V-26 shows a view of the result of bearing test 1, which was performed by means of two 2.0-sec down commands in which the motor current was recorded. The disturbed soil shows a remarkable resemblance to the appearance of the lunar surface at the Surveyor III site following the first bearing test carried out at that location (Ref. V-1). The total depth of penetration of the surface sampler into the lunar soil in Fig. V-25 was about 5 cm in this test. The test was apparently located on the edge of a small surface depression, which became obvious in pictures taken later in the lunar day. Consequently, the surface subjected to the test (Fig. V-26) slopes downward to the right, which accounts for the unsymmetrical appearance of the deformed soil. At this location, the surface sampler was at an extension distance of about 103 cm from the spacecraft (see Fig. V-25), and consequently applied its force at an angle to the surface rather than directly downward. In the disturbed lunar surface material, a certain amount of minor cracking appears, together with an obvious general bulging of the area.

Since bearing test 1 and the previous calibration tests of the surface sampler on the moon indicated that it was in good operational condition, and in particular that the motor currents appeared reliable, it was decided to perform a second bearing test to the left of bearing test 1 and at greater extension, using command tape 907 (see Section V-A-2). Bearing test 2 was consequently performed; the appearance of this test is somewhat different from that of bearing test 1, although some bulging of the surface material in the vicinity of the bearing test was also evident.



Fig. V-25. Mosaic of area of operations on Day 021 (Catalog 7-SE-16).

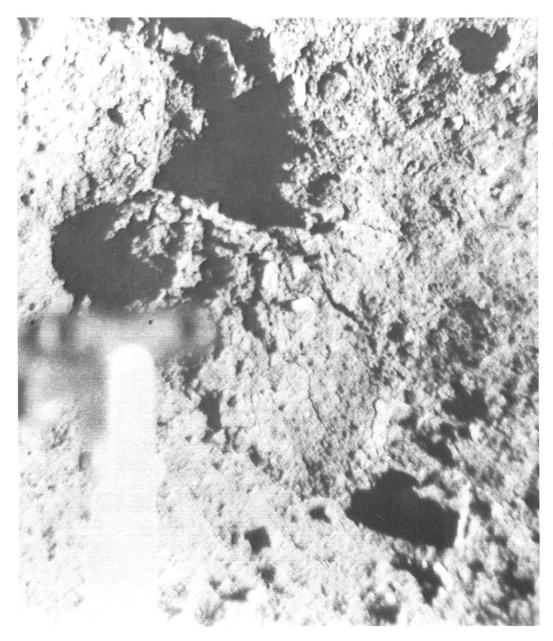


Fig. V-26. Results of bearing test 1 (Day 011, 04:09:54 GMT).

It is felt that the difference between these two tests probably results from the different angle of penetration of the surface-sampler scoop into the lunar soil in bearing test 1, which tended to drag the surface material toward the spacecraft. In addition, bearing test 2 appeared to have been performed on a level surface. Once again, in Fig. V-14a, it can be seen that the disturbed material cracks to some extent and exhibits displacement to some distance from the point of application of the force.

Careful analysis and comparison of the pictures of the soil in the area of bearing test 2 show that it appears to have been disturbed by the bearing test to a distance of at least 9 cm from the near edge of the surface sampler. The maximum depth of penetration in this test was in the vicinity of 4 cm. A preliminary analysis of force vs penetration data from bearing test 2 has been carried out from the motor-current data and pictures; the force vs penetration relationship is shown in Fig. V-5.

Another test (bearing test 4), also carried out with command tape 907 and exhibiting somewhat similar appearance to bearing test 2, is shown after completion in Fig. V-14b. Once again, in this test, a depth of penetration of about 2 cm was attained, and the soil was disturbed to a distance of approximately 8 cm from the near edge of the surface sampler. In this test, a piece of rock (or a rock fragment) seems to have been encountered near the surface at the left-hand top corner of the surfacesampler impression (Fig. V-14b), since there is some soil cracking, and the surface appears somewhat bulged beyond the surface-sampler impression. It appears that the surface sampler may have pressed down on one corner of the rock fragment that was slightly below the surface, and that this fragment tilted upward, thereby cracking the surface.

Bearing test 5 is shown in Fig. V-14c; bearing test 6, conducted with an open scoop, is shown in Fig. V-14d. In bearing test 5, only a relatively minor amount of surface disturbance in the vicinity of the surface-sampler scoop tip appears obvious, although some displacement of the surface and some bulging have occurred. The amount of penetration in this test was about 1 cm, which is considerably less than on the previous tests. Bearing test 6 was performed with the scoop door open; the test shows that the scoop at maximum force has penetrated a distance of about 6 to 7 cm into the soil.

Because there are indications that somewhat different surface disturbances and penetrations were being obtained from test to test during Surveyor VII surface-sampler operations, two special tests were performed to study this effect (see Fig. V-21). Figure V-21a shows bearing test 8, which resulted in an extremely small amount of penetration into the surface. In this test, the far edge of the surface-sampler scoop penetrated perhaps 1 cm, whereas the near edge of the scoop penetrated approximately 0.5 cm, and extremely little surface disturbance was manifested on the near side of the scoop. The impression left by the surface sampler is smooth and distinct (Fig. V-21b), and the various features of the scoop tip can be seen clearly. Because of the possibility that the small amount of penetration in this test was due to an underlying rock, it was decided to open the scoop and perform another bearing test in precisely the same location. In Fig. V-21c, the result is shown of driving the open scoop down into the surface. This was bearing test 9, and it can be seen that the scoop has penetrated a distance of 5 to 8 cm without causing any marked surface disturbance, which would indicate the presence of an underlying rock.

In Fig. V-21d, the lunar surface is shown in the vicinity of bearing tests 8 and 9 following the removal of the scoop from the surface; it can be seen that only a minimal amount of surface disturbance has taken place. The right-hand side of Fig. V-21d shows the surface at bearing test 7, which was a test carried out with the scoop full of soil from trench 2. The mass of soil, which appears on the spacecraft side of that test mark in Fig. V-21d, is, in fact, material that had been compressed in the scoop, but remained on the surface, still retaining the shape of the inside of the scoop, after the surface sampler was withdrawn.

Bearing test 13, which was performed with the scoop closed, is shown in Fig. V-27a; one retract command was given after the maximum downward force on the scoop in the bearing test had been obtained (Fig. V-27b). It is seen that, as a result of dragging the scoop backward, the penetration of the scoop into the lunar soil has been greatly increased as a result of the additional shearing stresses applied to the surface.

c. Trenching operations. Trenching operations during the Surveyor VII mission were carried out for a variety of purposes. The first trench (Fig. V-18) was performed at the extreme right-hand end of the surface-sampler operations area. This area was selected because it was possible to bring the surface sampler to the extreme right-hand stop very readily after moving it away from the trench. However, when trenching was attempted, it was



Fig. V-27. (a) Bearing test 13 (Day 021, 15:08:52 GMT). (b) Trench 6, performed in sequence at the sample point (Day 021, 15:11:51 GMT).

found that rock (or a large rock) lay under the trench, at a depth of only about 2.5 cm, so that larger penetrations could not be obtained. The rock had an irregular upper surface, and subsequent drag tests with the simultaneous recording of retraction motor current indicated fluctuations in current as the surface sampler rode over the underlying rock material.

Shortly after sunset of the first lunar day, the surface sampler, which had been left in a stalled position on the rock underlying the near end of trench 1, was operated in the retraction mode again at a motor temperature of about $-167^{\circ}\mathrm{F}$ in order to exert a very large retraction force on the rock. No movement of the rock was apparent in the pictures taken, although some deflection of the leg 2 shock absorber was achieved. Considering the retraction force of 1.8 to 2.0×10^{7} dynes that can be generated at very low motor temperatures, it would seem that the rock must have been a substantial fragment. Trench 1 is shown in Fig. V-19.



Fig. V-27 (contd)

Following deployment of the alpha-scattering-instrument sensor head, another trench was attempted in approximately the middle of the surface-sampler operations area (see Fig. V-18). Several trenching passes were made through this trench, which was eventually enlarged to a length of approximately 75 cm, a depth of about 15 cm, and a width of 5 cm. The occurrence of two obstructions in this trench was observed, one at the head of the trench where the surface sampler was deflected to the left around some subsurface object, and one at approximately two-thirds of the way down the trench toward the spacecraft, where a small protuberance again interrupted surface-

sampler operations. The retraction motor stalled on the object, which could not be extracted from the surface, and was thereupon avoided in trenching operations. The appearance of trench 2 at several stages in its construction is shown in Fig. V-28. In depth and general appearance, the trench is not dissimilar to trenches excavated by the surface sampler on *Surveyor III* (Ref. V-1).

Three trenching operations were performed at the left side of the surface-sampler area in order to provide subsurface materials for the third sample to be analyzed by the alpha-scattering instrument. The sensor head was

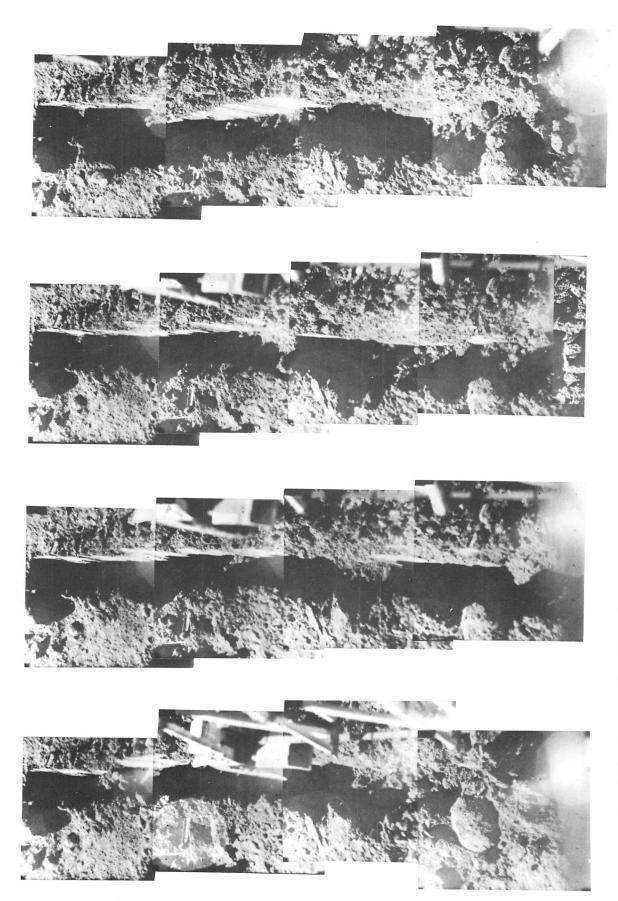


Fig. V-28. Four mosaics of trench 2, each after a successive pass through the trench, showing trenching progress, left to right (Catalog 7-SE-17).

subsequently positioned in this area. Other trenches were dug with the scoop closed (see Fig. V-27a and V-27b) in order to examine the change in penetration of the surface sampler by applying lateral shearing stresses after a drag test; a short trench was made for the purpose of locating a possible magnetic fragment on the surface.

d. Rock weighing. Early in the first lunar day, a rock (rock A) was observed in a position convenient for the surface sampler to pick up, and also of suitable dimensions

to be enclosed in the surface-sampler scoop. This rock was moved on a number of occasions to present its various surfaces to the camera for observation and to provide a possible alternate rock for chemical analysis. In the course of picking up the rock, the motor current required to elevate the surface sampler, both with and without the rock, was measured. On one occasion, the rock was picked up in the surface-sampler scoop; a pair of pictures was taken, both directly and through the auxiliary mirror on the spacecraft mast, to provide stereoscopic imagery;

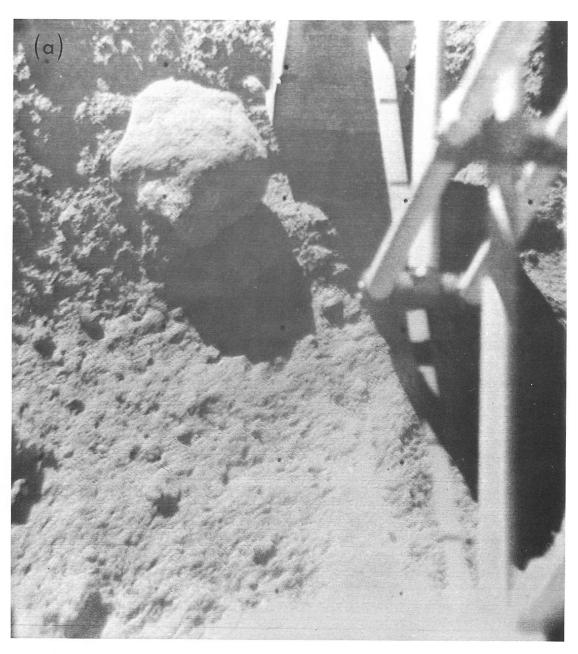


Fig. V-29. Rock A, after moving. (a) Direct view (Day 019, 09:28:36 GMT). (b) Through the stereo mirror (Day 019, 09:25:49 GMT).

the rock was dropped; and another pair of stereo pictures was taken. From these pictures, the deflection of the surface sampler can be measured so that, with the known force–deflection relationship of the surface sampler, the weight of the rock can be obtained. From the stereo pairs of pictures taken, the size of the rock can be measured, and the density of the rock calculated. At present, the volume of the rock has only been estimated from its overall dimensions, and its density will be discussed in a following section. The pictures of rock A used in the measurements are shown in Fig. V-29a and V-29b.

An attempt was made to pick up another rock (rock C), but it apparently flipped out of the jaws of the surface sampler, because of the coil spring in the scoop door, and landed at the extreme edge of the surface-sampler operations area. A third rock (rock D), appearing at the extreme left edge of the area had a rounded protuberance above the surface (see Fig. V-20) and was of such dimensions that an attempt was made to pick it up also. The rock, on excavation, revealed a substantial surface underlying the soil of a much more angular appearance than the surface projection, indicating that an erosion process had

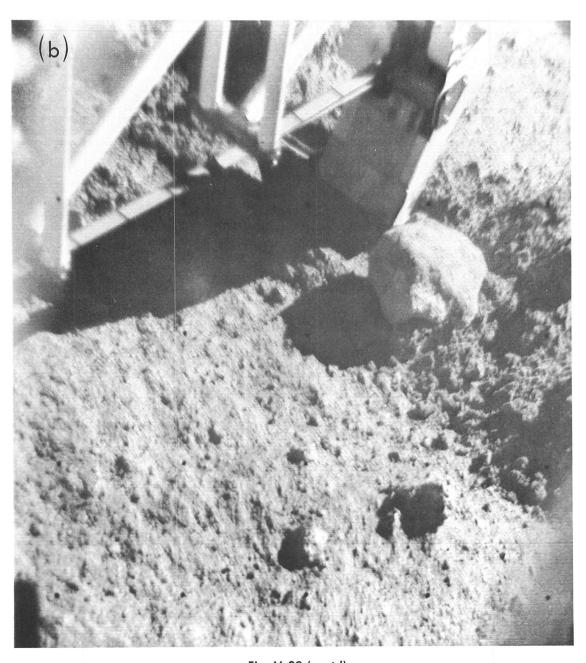


Fig. V-29 (contd)

occurred on the exposed part of the rock (Fig. V-20b). Unfortunately, this rock was slightly too large for the surface sampler to grasp, and consequently was not picked up. The attempt to weigh it was abandoned because of the time-consuming nature of the effort required.

Because of the presence of polarizing filters on the *Surveyor VII* television camera, it was considered of value to attempt to break one of the lunar rocks in order that a polarizing sequence of pictures could be taken on any fresh surface that might be revealed. For this purpose,

another rock (rock E), lying at the foot of trench 1, was selected because of the suitable viewing angle and nearness of the rock for pictures. Figure V-30a is a picture of rock E before it was broken by the surface sampler. After the open scoop was located appropriately on the rock's surface, the surface sampler was elevated to a height of about 35 to 40 cm above the rock and the clutch was operated. After the impact, the rock had moved slightly toward the spacecraft, and a fragment of the rock had been broken off (Fig. V-30b and V-30c); Fig. V-30c affords a slightly better view of the broken

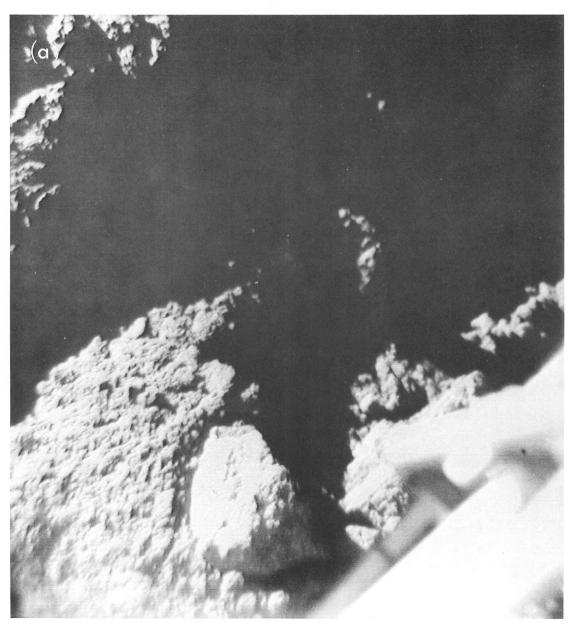


Fig. V-30. Rock E. (a) Before breaking (Day 022, 14:13:35 GMT). (b) After breaking (Day 022, 14:25:17 GMT). (c) After breaking (Day 022, 14:34:55 GMT).

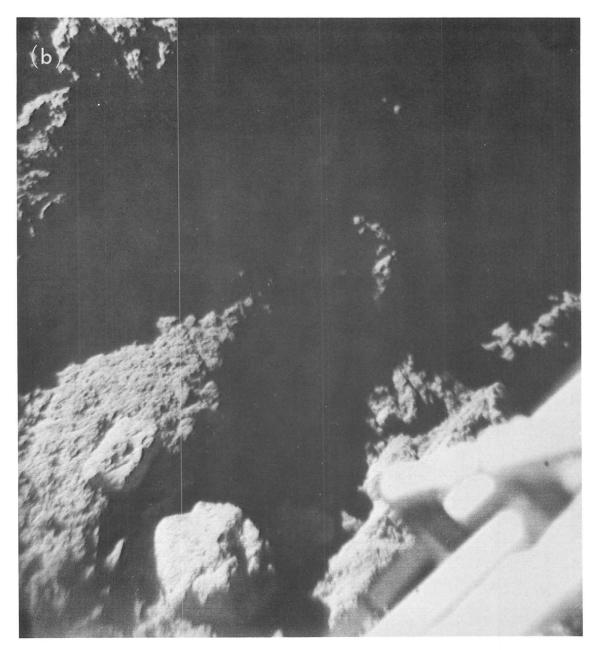


Fig. V-30 (contd)



Fig. V-30 (contd)

fragment. Following this operation, a polarimetric study was made of the rock.

e. Other operations. When the sensor head of the alphascattering instrument was being moved to its second location, a certain amount of soil, which had adhered to the surface-sampler scoop, was dropped on top of the mirror surface, giving it the appearance shown in Fig. V-31a. When the sensor head had been in its second sampling position for approximately 24 hr, it was moved by the

surface sampler to its third location. The sequence of operations involved first picking up the sensor head and then making a series of movements to the right in 0.1-sec steps. This type of motion is quite jerky, and the appearance of the sensor head after two of these right steps is shown in Fig. V-31b. It is seen that some of the soil on the alpha-scattering instrument has slid to one side during the motion, leaving a fairly clean surface with only a fine coating of dust. Since the mirror surface is made of Vycor glass, a comparison of Fig. V-31a and

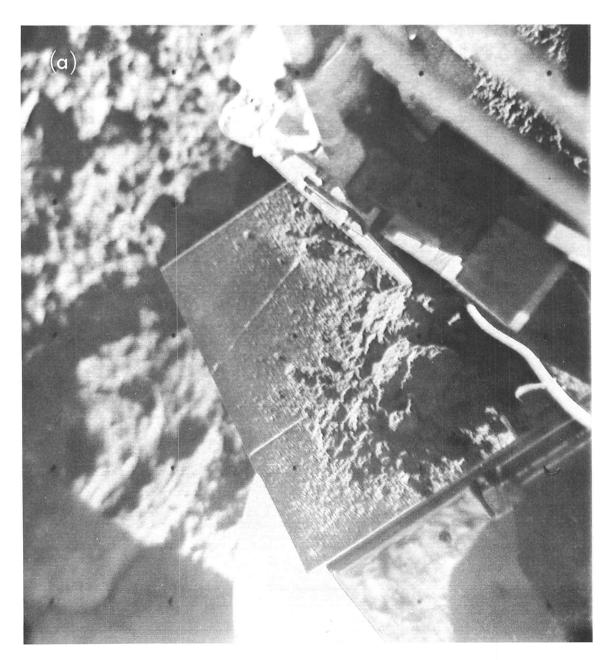


Fig. V-31. (a) Lunar soil dropped on the sensor-head thermal mirror (Day 022, 11:03:29 GMT). (b) After redeployment of sensor head, showing soil movement (Day 022, 11:31:42 GMT).

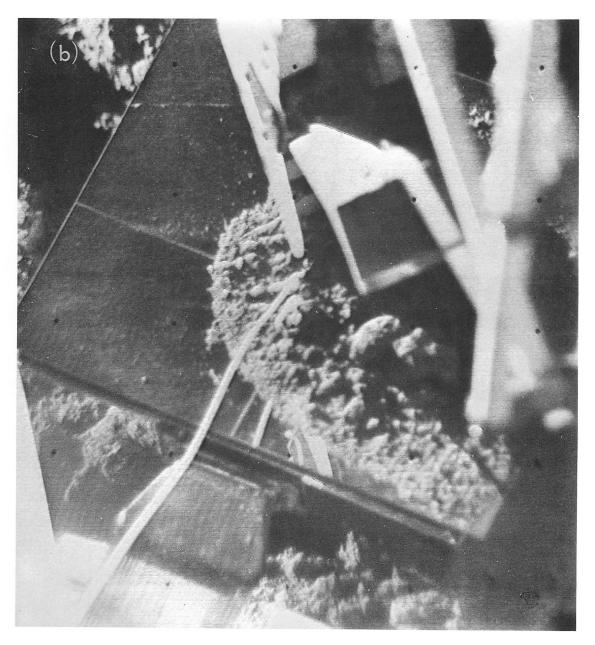


Fig. V-31 (contd)

V-31b would seem to indicate that, over a 24-hr period, strong adherence of the lunar surface material to the surface of the mirror did not develop.

Careful photographic studies were made of the two small horseshoe magnets, located in the base of the scoop door, both before lunar surface operations and at various times during the first lunar day. The magnets apparently picked up a coating of magnetic material from the lunar surface. In addition, the surface sampler was dragged through the surface at a selected location in order to determine if a small fragment of lunar surface had magnetic characteristics. A fragment was, in fact, found adhering to the surface sampler, which was elevated for better inspection of the fragment (see Fig. V-22 and Section VII-B of this Report).

2. Preliminary Analyses and Results

a. Soil properties. In general, it appears that the bearing tests carried out from Surveyor VII exerted forces on the lunar surface similar in magnitude to those of the tests performed during the Surveyor III mission (Ref. V-1), although the retraction forces on Surveyor VII were considerably larger than those on Surveyor III. However, the consequences to the lunar surface varied considerably from place to place as can be seen in Figs. V-14, V-21, and V-26. It appeared, from trenching tests, that a varying depth of lunar soil ranging from perhaps 1 cm to at least 15 cm existed over the operational area of the surface sampler at the Surveyor VII site, in contrast to a relatively uniform depth of material within the capabilities of the surface sampler at the Surveyor III site. Consequently, the variation in behavior of the bearing tests may be caused by a varying depth of lunar material over underlying rocks or a rock surface. In general, however, the material behavior was not substantially different from that exhibited in the Surveyor III surface-sampler operations; as a first estimate, it is considered that essentially the same density, friction, and cohesion values can be considered representative of the soil in the Tycho area.

To some slight extent, the soil around Tycho appears stronger or denser than the material in the maria. In general, the soil in the bearing tests and trenching operations in the Tycho area did not crack or split to the same extent as the soil in the Surveyor III mare area. During trenching operations, it appeared to yield or deform without breaking up into large, individual chunks or fragments of aggregated material, as did the soil near Surveyor III (see Ref. V-1). It is concluded, therefore, that the soil at the Surveyor VII landing site, although

cohesive, as evidenced by the smooth vertical walls of trench 2 and by other operations, did not exhibit the degree of cementing and brittle fracture evidenced by the first few centimeters of the lunar surface in the mare area. The contrasting behavior of the soils on the moon may be related to the difference in ages of the Tycho blanket (younger) and mare materials (older), or to the slight chemical difference observed by means of the Alpha-Scattering Experiment.

To date, only a preliminary analysis has been carried out with command tape 907 and motor-current information. Bearing test 2 has been analyzed in this way using motor currents in the form shown in Figs. V-7 and V-8. together with the step-by-step motions of the surfacesampler scoop, given by the sequential pictures to give the force vs penetration curve of Fig. V-5. In Fig. V-5, it can be seen that some amount of penetration occurred at relatively low load. This initial part of the curve is commonly referred to in soil mechanics as "seating," and may be due to either the irregular nature of the surface or to a layer of softer soil above underlying denser material. It will be seen that the curve has a tendency for the rate of penetration to increase at approximately $3.0 imes 10^6$ dynes force, and this may be interpreted as a bearing capacity for this size of footing. However, after this, the rate of penetration again decreases, and it seems likely that the increase is caused by an increasing strength or density of the material below a depth of a few centimeters. A more detailed interpretation of a number of bearing tests must be made before more general conclusions are drawn.

b. Rock density. Based on measurements of the deflection of the surface sampler before and after dropping the rock, a preliminary estimate of the weight of rock A has been made. From the dimensions of the rock on the lunar surface, by comparison with the dimensions of the surface sampler, its volume has been estimated. The weight appears at this time to be accurate to within ± 7 or 8%; at best, the volume can be obtained within about 30%. Since stereo pairs of pictures of the rock have been obtained, a more accurate calculation of its volume should be possible at a later date. Using the extremes of weight and volume obtained for the rock, it is estimated that its density lies within the range of 2.4 to 3.1 g/cm³. Although such a determination is not of sufficient accuracy to assist in an evaluation of the rock type, it does indicate that the material of which the rock is composed is not substantially porous, since the density lies within the range of common terrestrial rocks.

If it can be assumed that this rock was characteristic of many of the other fragments around the Surveyor VII landing site, and that the soil tested by the surface sampler in the same area was derived by meteoritic bombardment of these rock fragments, it must be concluded that the individual particles composing the soil are, in themselves, not highly porous. This would appear to reinforce the conclusions obtained from the Surveyor III surfacesampler operations (Ref. V-1) that, in fact, the strength and deformation characteristics of the lunar surface granular material can be explained by the presence of a material with a density comparable to that of common terrestrial soils, that is, in the range of 1.5 g/cm3 and greater. Bearing test data, such as shown in Fig. V-5, and other tests do appear to indicate the presence in some locations of a surface layer, possibly several millimeters thick, which is softer or more easily compressible than the underlying material. However, the material appears to gain in strength or density comparatively quickly as a function of depth in the first 1 or 2 cm. The increase with depth will be evaluated to greater depths from the motorcurrent data obtained during various passes through trench 2.

c. Observations. The lunar soil at the Surveyor VII landing site appears to be irregular in depth and relatively shallow, ranging in the surface-sampler area of operations from depths of less than 2.5 cm to a depth of at least more than 15 cm; it is underlain by substantial rock fragments. It is estimated that, in the first earth day following lunar sunset, the drag tests performed in trench 1 exerted a force of at least 180 N on the subsurface fragment underlying that trench. An individual rock fragment resisting a lateral force of this order of magnitude on the moon would have a very substantial size. In none of the trenching operations in the lunar surface were other soil fragments brought up comparable in size to the pieces lying about on the surface. A distinct impression is gained from the surface-sampler work that the surface rocks lie on a relatively fine-grained, granular material, and that this material does not contain rocks of comparable size to the fragments on the surface. However, it is underlain with substantially larger fragments. One normally expects in a granular material a gradation of fragments of all sizes distributed both horizontally and vertically through the material.

The rounded surface shape of rock D and its angular subsurface shape appear to be indicative of some process of erosion, probably meteoritic bombardment at the

surface. Although the undersides of some of the rocks excavated from the lunar surface were darker than the above-surface side of the rock, it appeared that this was due to a coating of fine-grained, granular soil on the underside.

It has not been possible, to the present time, to calculate a value for the strength of the rock broken by the surface-sampler impact; however, the impact delivered was not the most violent that the surface sampler was capable of delivering, and the implication is that the rock was relatively weak, either intrinsically or as a result of an existing fracture in it.

As in *Surveyor III*, little soil material appeared to adhere to the scoop early in the operations but, as the lunar day proceeded, the soil showed a greater tendency to adherence. It was, however, comparatively easily dislodged, as, for example, during the process of picking up the sensor head to move it to its second position.

C. Summary

- (1) The lunar surface at the *Surveyor VII* landing site is covered with a fine-grained soil whose depth over rock or rock fragments varies from 1 or 2 cm to at least 15 cm. Many rock fragments ranging in size up to 10 cm lie on the surface within the surface-sampler operations area.
- (2) The surface soil exhibits properties similar to those of the soil at the *Surveyor III* landing site. The behavior of the soil at a depth of several centimeters is therefore consistent with a material possessing a cohesion on the order of 0.35 to 0.7×10^4 dynes/cm², an angle of friction of 37 to 39 deg, and a density of about 1.5 g/cm^3 .
- (3) The resistance of the soil to penetration, and therefore its strength, increases with depth in the top 1 or 2 cm.
- (4) To a depth of several millimeters at the lunar surface, the soil appears less dense, softer, and more compressible than the underlying material.
- (5) The bearing capacity of the lunar soil to the 2.54-cm-wide area of the closed scoop of the surface sampler was about 2.1×10^5 dynes/cm², at a maximum penetration of about 3 cm.

- (6) Qualitatively, the soil at the Surveyor VII site was less brittle than at the Surveyor III site; there was less general cracking, and tests and trenching operations provided smaller lumps or aggregates of lunar soil.
- (7) Rock (or a rock) was encountered at two locations below the lunar surface, but was too large or firmly embedded to be moved. No movable subsurface rock fragments were excavated.
- (8) The density of a single rock, which was picked up and weighed, was in the range 2.4 to 3.1 g/cm³.

- (9) The excavation of one partially buried rock revealed that the subsurface portion was angular in contrast to the rounded visible portion.
- (10) One apparently intact rock was broken by a blow from the surface sampler.
- (11) The adhesion of lunar soil to the surface-sampler scoop appeared to increase with time on the lunar surface.
- (12) Little adhesion of lunar soil to the mirrored surface on top of the sensor head occurred in a 24-hr period.

References

- V-1. Scott, R. F., and Roberson, F. I. "Soil Mechanics Surface Sampler: Lunar Surface Tests, Results, and Analyses," Surveyor III Mission Report. Part II: Scientific Results, Technical Report 32-1177, pp. 69–110, Jet Propulsion Laboratory, Pasadena, Calif., June 1, 1967.
- V-2. Rouze, E. R., Clary, M. C., LeCroissette, D. H., Porter, C. C., and Fortenberry, J. W., Surveyor Surface Sampler Instrument, Technical Report 32-1223, Jet Propulsion Laboratory, Pasadena, Calif., February 1, 1968.

VI. Lunar Surface Temperatures and Thermal Characteristics

G. Vitkus, R. R. Garipay, W. A. Hagemeyer, J. W. Lucas (Chairman), B. P. Jones, and J. M. Saari

At 01:05:36 GMT on Day 010 (January 10, 1968), Surveyor VII, the last spacecraft in the Surveyor series, landed on an ejecta blanket north of the rim of the crater Tycho. The sun was approximately 12.5 deg above the eastern horizon. Position of the spacecraft, determined by matching features observed by the Surveyor VII television camera with features photographed by Lunar Orbiter V, was determined to be 11.41°W longitude, 40.95°S latitude, according to Orthographic Atlas coordinates. Temperature data for the Surveyor VII mission were obtained until Day 026 at 14:12 GMT, or about 80 hr after sunset.

The spacecraft, similar in design to the previous *Surveyors*, did not carry any instruments to measure lunar surface temperatures or thermal characteristics. Rather, the outboard-face temperatures of compartments A and B were used to obtain lunar surface brightness temperatures in the manner used for *Surveyors I*, *III*, V, and VI

(Refs. VI-1 through VI-4). Calculated temperatures after sunset were used to estimate the thermal parameter, γ , of the lunar surface.

A. Thermophysical Properties of Landing Site, as Determined From Earth-Based Observations

The total² solar (bolometric) albedo was determined to be 0.17 from earth-based measurements (Ref. VI-5). This albedo value was used to calculate the Lambertian temperatures of the site for the month of January (Fig. VI-1). Also shown in Fig. VI-1 are the earth-based (telescope) measured temperatures, which reveal the characteristic directional effects of the infrared emission of the lunar surface. During the lunar day, near local noon, the measured brightness temperatures were greater than the Lambertian temperatures, since the landing site region was observed from the same general direction as the sun.

The earth-based measurements were taken to a resolution of 8 and 10 sec of arc (14 and 18 km at the disk center). However, since the area of lunar surface, as viewed by the compartments, is considerably smaller, it

In all the *Surveyor* reports on lunar surface thermal measurements, brightness temperature is understood to be the temperature of a surface which obeys the blackbody radiation laws, assuming unity as the value of emissivity, and which gives the same radiant flux as the one actually measured. In this section, the lunar surface brightness temperature is specified as lunar surface temperature.

²Over the entire solar spectrum and reflected over 2π sterad.

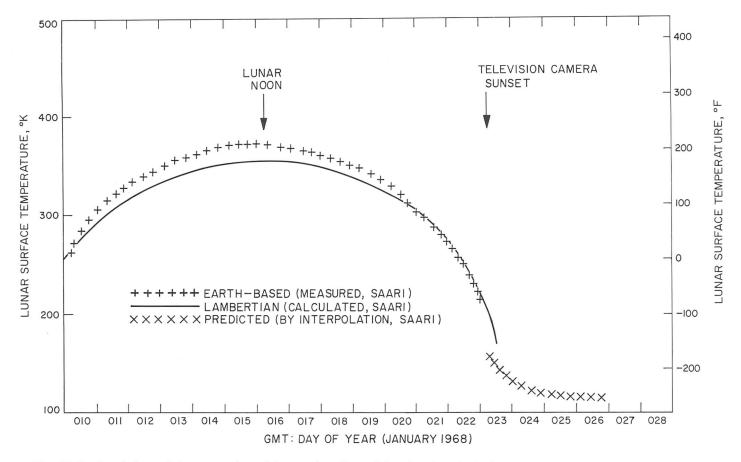


Fig. VI-1. Earth-based (measured and interpolated) and Lambertian (calculated) temperatures for Surveyor VII landing site region.

is possible that the thermal characteristics of the landing site may be considerably different than they appear as observed from earth.

If the lunar surface is assumed to consist of a uniform, semi-infinite solid with constant thermal properties (homogeneous), its surface temperatures during lunation depend upon the thermal parameter, defined as $\gamma = (k_{\rho}c)^{-1/2}$, where k is thermal conductivity, ρ is density, and c is specific heat. Actually, evidence exists supporting the fact that the thermal properties of a model consisting of a granular material are temperature-dependent; for example, $k = K_0 + K_1 T^3$, where K_0 and K_1 are constants (see Refs. VI-6 through VI-9). On-site observations from the Surveyor spacecraft have shown that the lunar surface consists of a granular material. These temperature-dependent effects should be considered in the lunar surface model in future calculations. However, γ is still useful as a reference constant for data comparison. The lunar surface temperatures for the Surveyor VII site have been calculated for a homogeneous model and are shown in Fig. VI-2 for γ of 240, 300, 385, 500, and 800 (cm² sec½ °K/g cal). Note that only after sunset is it possible to distinguish readily the temperature curves for thermal parameters in this range.

From the standpoint of the temperature difference over environs and areal extent, the crater Tycho is a prominent thermal anomaly on the lunar surface. Isotherms of the area (Fig. VI-3), obtained by Saari and Shorthill (Ref. VI-5) during totality of the December 19, 1964, eclipse, show that there are three maxima in the temperatures within the crater and that the anomaly extends approximately one crater diameter beyond the rim. The Surveyor VII landing site, as indicated in Fig. VI-3 is within the anomalous area surrounding the crater. During the same eclipse, Ingrao, et al. (Ref. VI-10), also made measurements on Tycho to 9 sec-of-arc resolution and until a few minutes before the end of totality. The observational data fit cooling curves for a homogeneous model with $\gamma = 450$ inside the crater and with $\gamma = 1100$ outside the crater (30 sec of arc east and west of Tycho).

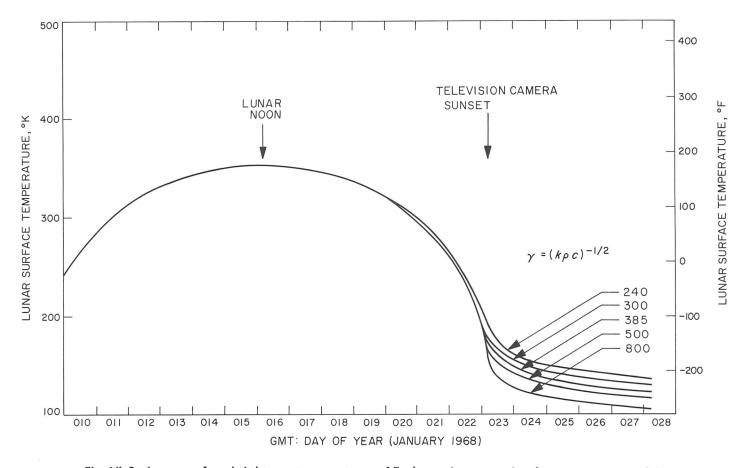


Fig. VI-2. Lunar surface brightness temperatures of Tycho region assuming homogeneous model.

No eclipse occurred during Surveyor VII operations on the lunar surface, so the post-sunset data are used to infer the thermal properties of the landing site. Unfortunately, no earth-based measurements of the landing site region have been made during the lunar night. However, it has been possible to obtain a post-sunset cooling curve by interpolation in the following manner. First, earthbased eclipse cooling curves were obtained from the data of Saari and Shorthill for the crater itself, the landing site region, and the environs outside the anomalous region surrounding the crater. These curves showed the landing site region had a temperature difference over the environs only 0.27 as large as for the crater itself. Secondly, postsunset cooling curves were available for the crater (Ref. VI-5); for the environs, a theoretical curve for the homogeneous model with $\gamma = 1091$ was assumed. Finally, a post-sunset curve for the landing site region was determined by interpolating 0.27 of the way from the environs curve to the crater curve, resulting in a predicted, X, curve shown in Fig. VI-1. This curve corresponds to a γ of 700 for the landing site region. It should be noted

that the time of sunset on the spacecraft television camera is shown in Fig. VI-1 and was 06:06, compared with 18:03 GMT on Day 023 predicted for sunset on a level landing site region.

B. Spacecraft Description

Surveyor VII is similar in overall structural and thermal design to Surveyors I, III, V, and VI. The basic frame (Fig. VI-4) is tubular aluminum, and serves as a tetrahedral mounting structure for the electronic gear and propulsion system. The three spacecraft legs are attached at the three corners of the base. The planar array antenna and solar panel, mounted on a mast approximately 1 m above the apex of the structure, cast varying shadow patterns on the spacecraft and on the lunar surface throughout the lunar day. Changes in shadow patterns occur as a result of the intermittent repositioning of the planar array antenna and solar panel and from the apparent movement of the sun.

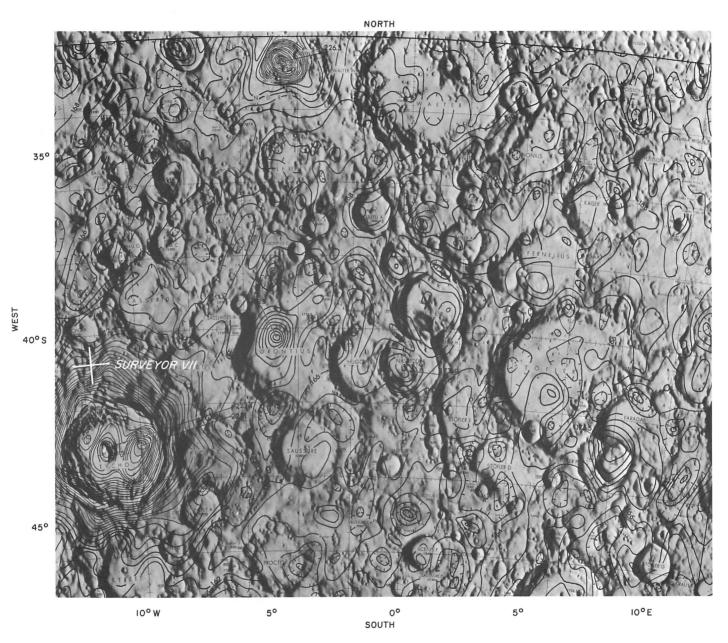
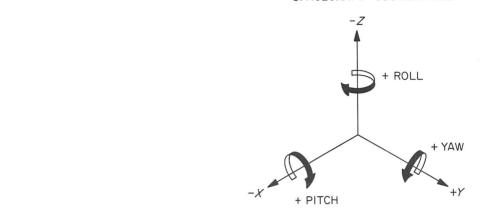


Fig. VI-3. Isothermal contours for landing site region obtained during totality of lunar eclipse of December 19, 1964. Temperature intervals are 2°K.

SPACECRAFT COORDINATES



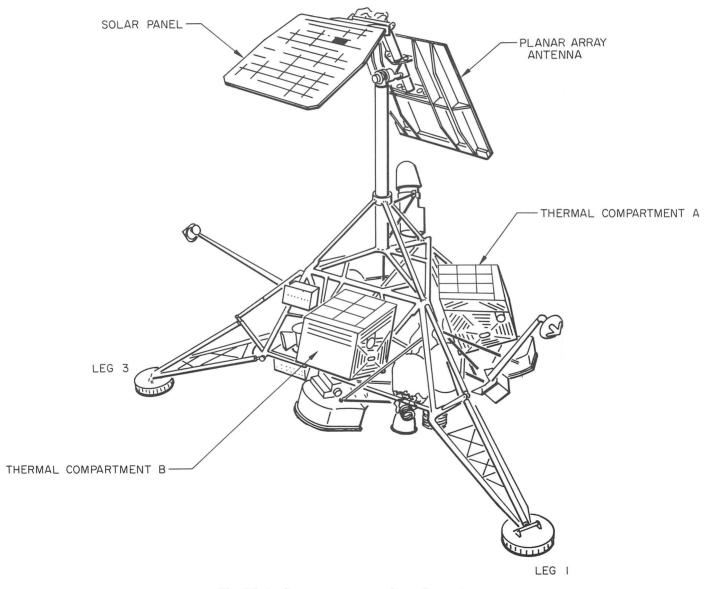


Fig. VI-4. Surveyor spacecraft configuration.

Generally, in the sun-illuminated areas, the spacecraft has white-paint surfaces that provide a low-solarabsorptance and high-infrared-emittance thermal finish. The polished aluminum underside greatly isolates the spacecraft from the lunar surface temperature effects.

The temperature data of various points in the space-craft are provided by platinum resistance temperature sensors. Each sensor is calibrated individually to $\pm 2^{\circ}$ C; other nominal system inaccuracies degrade the overall accuracy to $\pm 4^{\circ}$ C.³

Compartments A and B house the spacecraft electronics and battery. A blanket of superinsulation surrounds the components in each compartment, and in turn is covered with an aluminum panel. A temperature sensor is bonded to the polished-aluminum inner surface of the outboard face (i.e., the surface facing the superinsulation) of each compartment. The superinsulation isolates the panels from the inside of the compartments so that heat flux across the boundary is negligible during the lunar day; this, however, is not valid during the lunar night. A convenient analysis of lunar surface temperatures can be made, since the outboard faces of the compartments have a strong coupling to the lunar surface, but are virtually shielded from view of other spacecraft components.4 The parameters needed to obtain lunar surface temperatures from the compartment outboard-face temperatures by the methods described in this section are:

- (1) Angle between normal to outboard face and space-craft -Z axis.
 - (a) Compartment A: 71°4'.
 - (b) Compartment B: 70°30'.
- (2) Properties of the outboard faces before launch.
 - (a) Material: 2024 aluminum, 0.4-mm-thick panel with corrugations, coated with inorganic white paint.
 - (b) Solar normal absorptance: $\alpha_s = 0.20 \pm 0.02$.
 - (c) Infrared hemispherical emittance: $\epsilon_H = 0.87 \pm 0.02$.

The solar panel and planar array antenna are relatively low-heat-capacity planar surfaces that are also strongly

The temperature sensors were low resolution; a few sensors were calibrated to ± 1 °C with an overall accuracy of ± 3 °C over a narrow temperature range.

*Recent work indicates that the temperature of the compartment sides has an effect on the outboard-face temperature. This effect may modify the lunar surface temperatures calculated in this Report. coupled to the lunar surface. Using data from these components, it may be possible to derive lunar surface temperatures. The properties of the solar panel and planar array antenna are:

- (1) Solar panel properties.
 - (a) Surface area: front, 0.855 m²; back, 0.855 m².
 - (b) Heat capacity: 0.798 kg-cal/°C.
 - (c) Conductance (front to back): 50.3 kg-cal/hr °C.
 - (d) Solar normal absorptance of surface: front, 0.76 \pm 0.02; back, 0.30 \pm 0.02.
 - (e) Infrared hemispherical emittance of surface: front, 0.80 ± 0.02 ; back, 0.84 ± 0.02 .
- (2) Planar array antenna properties.
 - (a) Surface area: front (projected), 0.97 m^2 ; back (total), 1.40 m^2 .
 - (b) Heat capacity: 1.04 kg-cal/°C.
 - (c) Conductance (front to back): 16.8 kg-cal/hr °C.

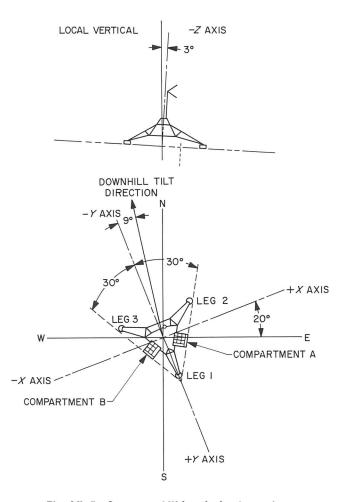


Fig. VI-5. Surveyor VII landed orientation.

(d) Solar normal absorptance: 0.80 ± 0.02 .

(e) Infrared hemispherical emittance: 0.88 ± 0.02 .

C. Spacecraft View of Lunar Surface

Surveyor VII landed on a generally level surface. The assumed orientation of the spacecraft with respect to lunar coordinates is shown in Fig. VI-5. This orientation was determined from solar panel positioning data and was used in all calculations of this section. Compartment A views to the east with a view factor of 0.337 to the lunar surface. Compartment B views in a southwest direction, with a view factor of 0.333 to the lunar surface.

Figures VI-6 and VI-7 show the lunar scene as viewed by compartments A and B, respectively. Large blocks may be seen near compartment B (see Sections III and IV of this Report). Figure VI-8 shows a closeup of these blocks. In television coverage, the lunar surface close to compartment B was either totally or partially obscured by the spacecraft structure. It is reasonable to assume that the blocks cover a greater portion of lunar surface than can be observed by the Surveyor VII television camera. The observed area and the assumed projected area of the surface covered with blocks (enclosed by dotted line) are shown in Fig. VI-9. The view factor from compartment B to the assumed projected area containing blocks is 0.053.

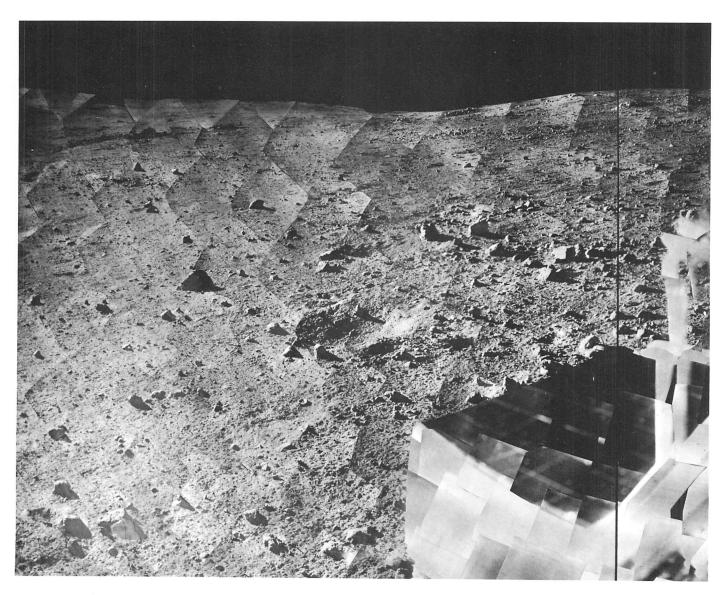


Fig. VI-6. Lunar scene viewed by compartment A.

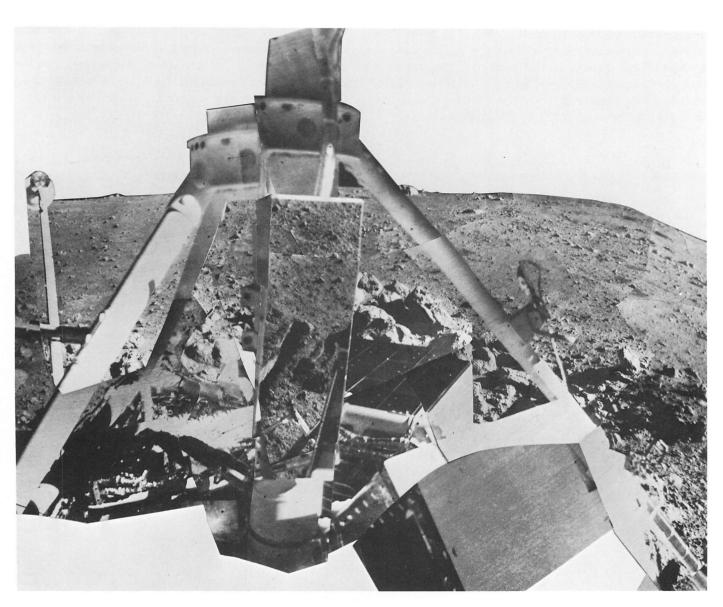


Fig. VI-7. Lunar scene viewed by compartment B.

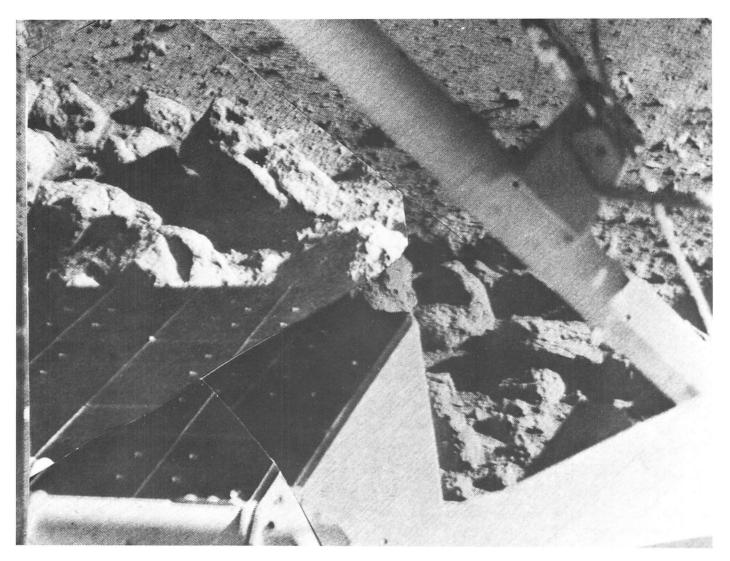


Fig. VI-8. Closeup of blocks near compartment B.

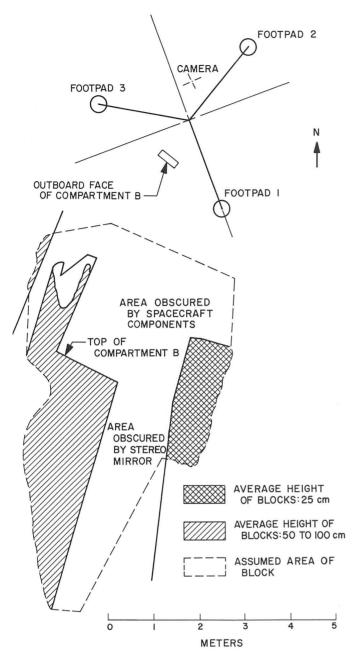


Fig. VI-9. Outline map of lunar surface covered with blocks near compartment B.

D. Compartment, Solar Panel, and Planar Array Antenna Data

The temperatures of the outboard faces of compartments A and B are shown in Fig. VI-10. Note that sudden changes in temperature occurred. These fluctuations were caused by shadows cast on the compartment faces, or on the lunar surface near the compartment, by the solar panel or the planar array antenna. The percentages of shadow on the outboard face of compartment A are shown

in Fig. VI-11. There was no shadowing on compartment B when it was sunlit. The view factor from compartments A and B to the shaded portion of the lunar surface is plotted in Fig. VI-12. The sun elevation and azimuth angles, relative to the spacecraft coordinates, are shown in Fig. VI-13. The angle, β , between the normal to the compartment outboard faces and the sun vector is presented in Fig. VI-14.

The temperatures of the solar panel and planar array antenna are presented in Fig. VI-15. Note that at sunset, temperature data of the solar panel were not obtained. The angles between the normal to the solar panel and both the sun vector and the spacecraft -Z axis are shown in Fig. VI-16. Figure VI-17 shows the angles between the normal to the planar array antenna and both the sun vector and the spacecraft -Z axis.

E. Calculation of Lunar Surface Temperatures

Lunar surface temperatures of the areas viewed by compartments A and B were obtained from the following heat-flux density balance equation (Ref. VI-1) of the outboard faces. F_{12} and F_{13} have been redefined here for clarity.

$$\sigma T_{2}^{4} = \frac{\sigma T_{1}^{4}}{\epsilon_{2} F_{12}} - \frac{F_{13}}{F_{12}} \sigma T_{3}^{4} - \frac{\alpha_{18} S}{\epsilon_{1} \epsilon_{2} F_{12}} (F_{12} \rho_{2} \sin \phi + \cos \beta)$$
$$- \frac{\dot{q}}{\epsilon_{1} \epsilon_{2} F_{12}}$$
(1)

where

 $T_1 = \text{compartment surface temperature}$

 T_2 = temperature of sunlit lunar surface

 T_3 = temperature of shaded lunar surface; 200° K was used in the calculations

S =solar insolation

 $= 1442 \text{ W/m}^2$

 F_{12} = geometric view factor from compartment to sunlit lunar surface

 F_{13} = geometric view factor from compartment to shaded lunar surface (from Fig. VI-12)

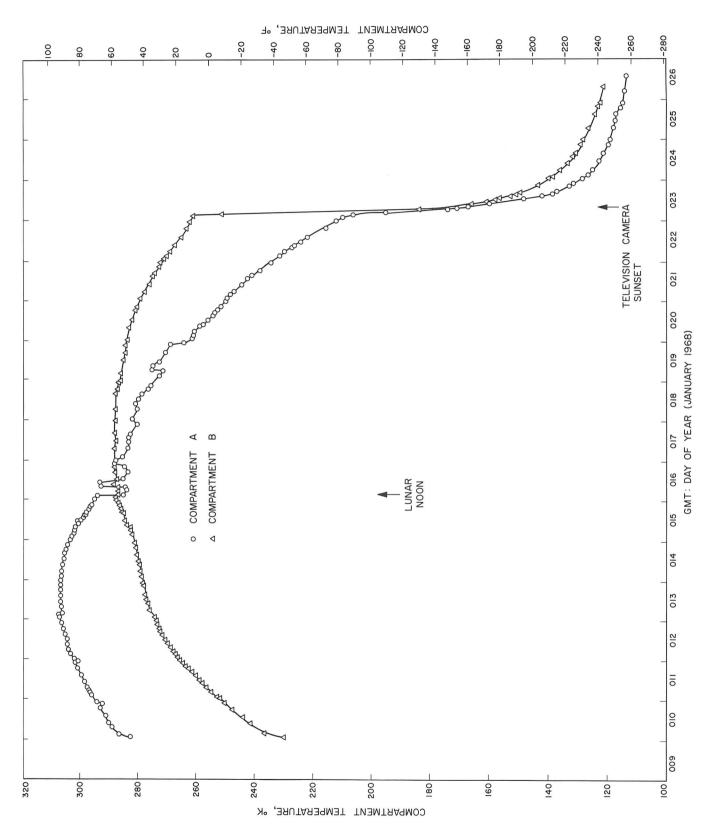


Fig. VI-10. Temperatures of outboard face of compartments A and B.

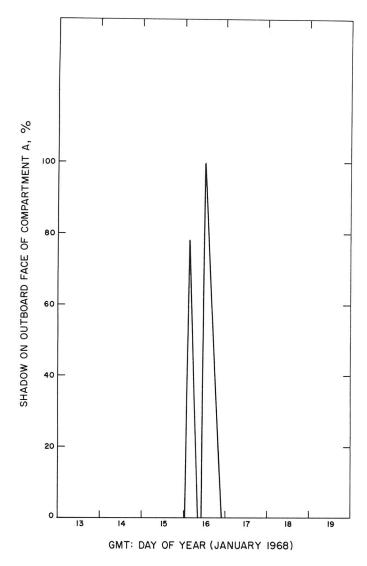


Fig. VI-11. Percentage of shadow on outboard face of compartment A.

 $F_{\scriptscriptstyle 12} + F_{\scriptscriptstyle 13} =$ geometric view factor from compartment to total lunar surface

= 0.337 for compartment A

= 0.333 for compartment B

 $\dot{q}= ext{heat flux from inside to outside of com$ $partment wall}$

 $= 3.5 \text{ W/m}^2$

 $\sigma = \text{Stefan-Boltzmann constant}$

 $= 5.675 \times 10^{-8} \,\mathrm{W/m^2 \, {}^{\circ} K^4}$

 ϵ_1 = compartment surface emittance

 $= 0.87 \pm 0.02$

 ϵ_2 = lunar surface emittance

= 1.0 (assumed)

 α_{1s} = compartment surface solar absorptance

 $= 0.20 \pm 0.02$

 $\phi = \text{sun elevation angle to lunar surface immediately surrounding spacecraft (from Fig. VI-13)}$

 β = angle between direction of sun and normal to compartment surface (from Fig. VI-14)

 $\rho_2 = lunar reflectance to solar irradiation$

= 0.17

The lunar surface post-sunset temperatures of the area covered with blocks near compartment B were obtained from the following heat-flux density balance equation:

$$\epsilon_1 \epsilon_R F_{1R} \sigma T_R^4 = \epsilon_1 \sigma T_{1B}^4 - \epsilon_1 \epsilon_2 \left(F_{12B} - F_{1R} \right) \sigma T_{21}^4 - \dot{q} \tag{2}$$

All nomenclature of symbols is the same as that used in Eq. (1), with the exception of:

 T_R = temperature of blocks in front of compartment B

 $T_{2A} = \text{lunar surface temperature as viewed by compartment A and computed from Eq. (1)}$

 ϵ_R = emittance of blocks

= 1.0 (assumed)

 F_{12B} = geometric view factor from compartment B to lunar surface without blocks

= 0.280

 F_{1R} = geometric view factor from compartment B to the assumed projected lunar surface covered with blocks

= 0.053

 $F_{12B} + F_{1R} =$ geometric view factor from compartment B to total lunar surface

= 0.333

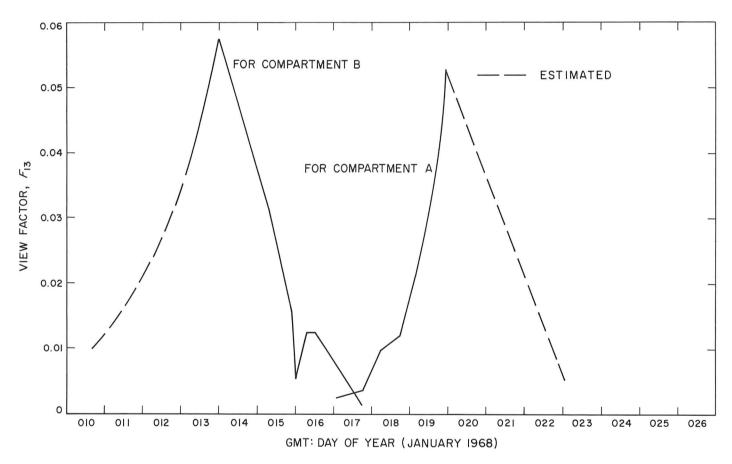


Fig. VI-12. View factor, F_{13} , from compartment outboard face to the shaded part of lunar surface.

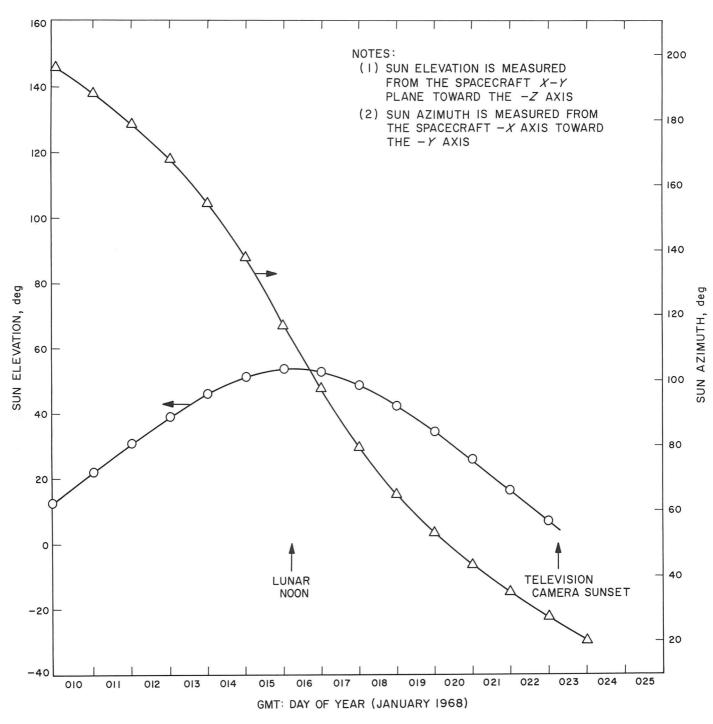


Fig. VI-13. Sun path during first lunar day in spacecraft coordinates.

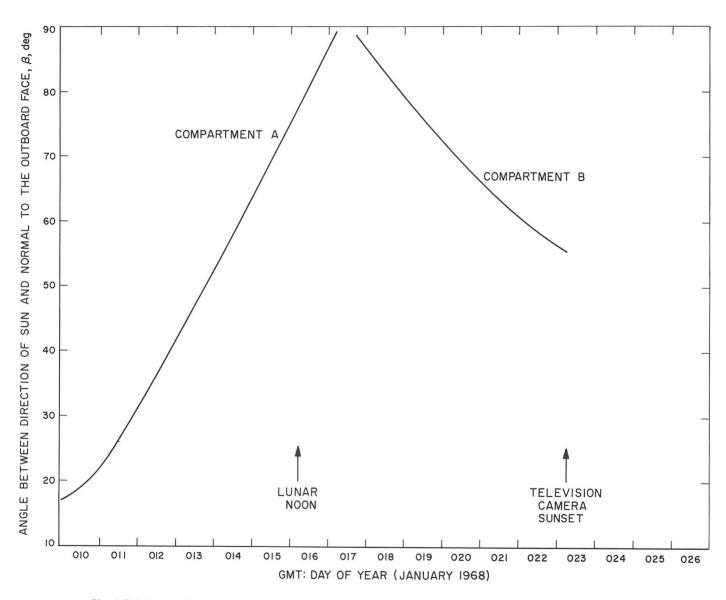


Fig. VI-14. Angle between direction of sun and normal to outboard face of compartments.

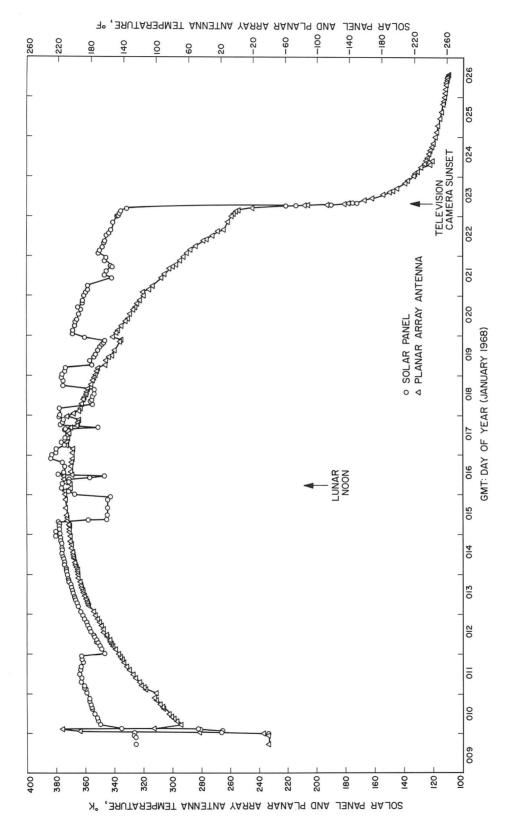


Fig. VI-15. Temperatures of solar panel and planar array antenna.

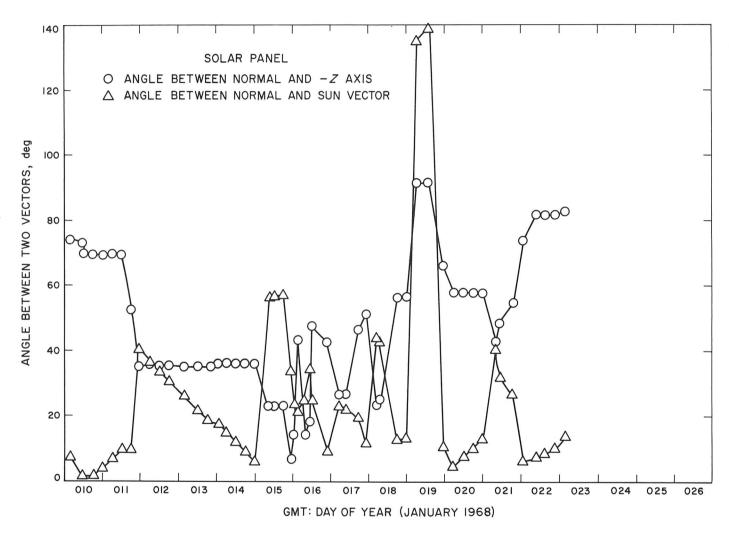


Fig. VI-16. Angle that normal to solar panel makes with sun vector and $-\mathbf{Z}$ axis.

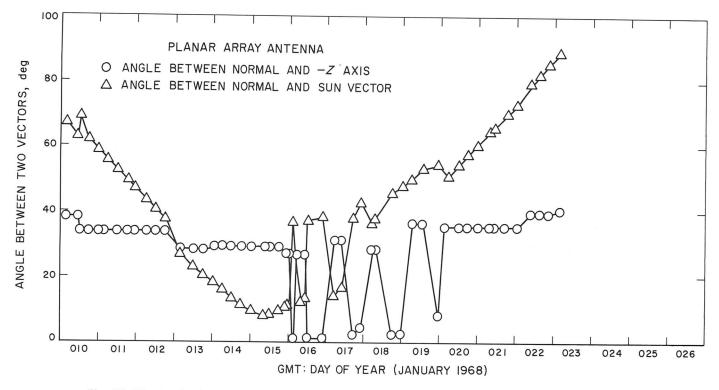


Fig. VI-17. Angle that normal to planar array antenna makes with sun vector and $-\mathbf{Z}$ axis.

F. Results and Comparisons

Figure VI-18 shows the lunar surface temperatures as calculated from compartment A and B telemetered temperatures. The temperatures derived from compartment B are considerably higher in the morning than those from compartment A. Later into the day, these two temperatures approach each other and cross in the afternoon. Immediately after sunset, the temperature curves cross again.

As previously noted, the lunar surface near compartment B was well covered with blocks (see Section III of this Report). It appears that these blocks were cooling more slowly after sunset than the lunar surface surrounding them, thus acting as hot spots and causing compartment B to sense higher lunar surface temperatures. Qualitatively, this indicates that the blocks have the thermal properties of solid rock.

In Fig. VI-19, lunar surface temperatures, as determined from compartments A and B, are compared with the Lambertian, earth-based, and predicted post-sunset temperatures, as given in Fig. VI-1. The results obtained from compartments A and B indicated higher lunar surface temperatures than were predicted at all times, except

in the morning when the results from compartment A indicated lower temperatures. Apparently, both compartments indicated results that were sensitive to directional thermal emission from the lunar surface.

In Fig. VI-20, lunar surface temperatures from compartments A and B are compared with theoretical homogenerous cooling curves, as given in Fig. VI-2. During the day, the results from both compartments indicated higher temperatures, except during early morning when the results from compartment A indicated lower temperatures. The temperatures of the lunar surface several days after sunset indicate that the lunar surface material viewed by compartment A has an effective γ of 385 and that compartment B has a γ of 240.

The block temperatures after sunset were calculated from Eq. (2) and plotted in Fig. VI-21. In the calculations, it was assumed that the area enclosed by dotted lines, as shown in Fig. VI-9, was covered with blocks. The temperatures obtained for the blocks depend very strongly on the view factor F_{1R} . Because the actual area covered with blocks is not known, the derived block temperature could be easily changed by assuming a different area.

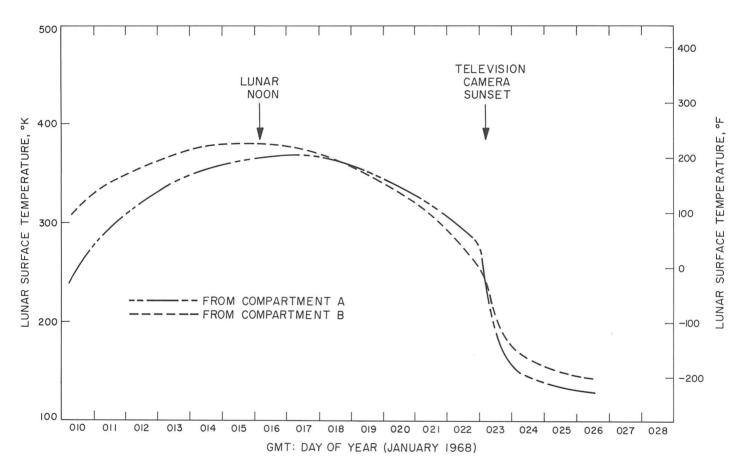


Fig. VI-18. Lunar surface brightness temperatures, as calculated from compartment telemetry data.

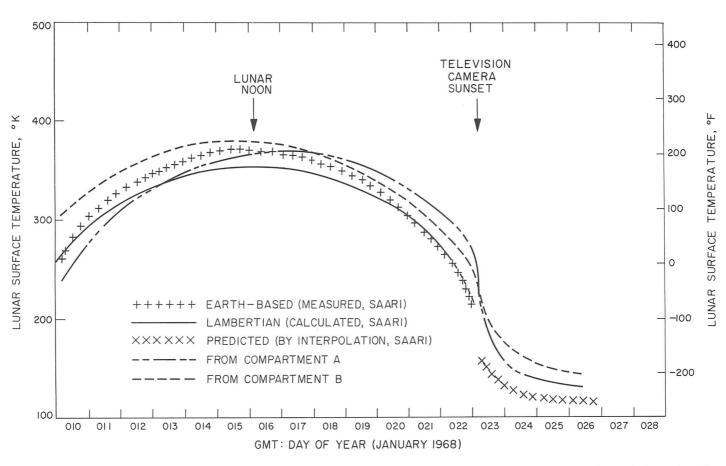


Fig. VI-19. Lunar surface brightness temperatures derived from compartment data, compared with earth-based and Lambertian temperatures.

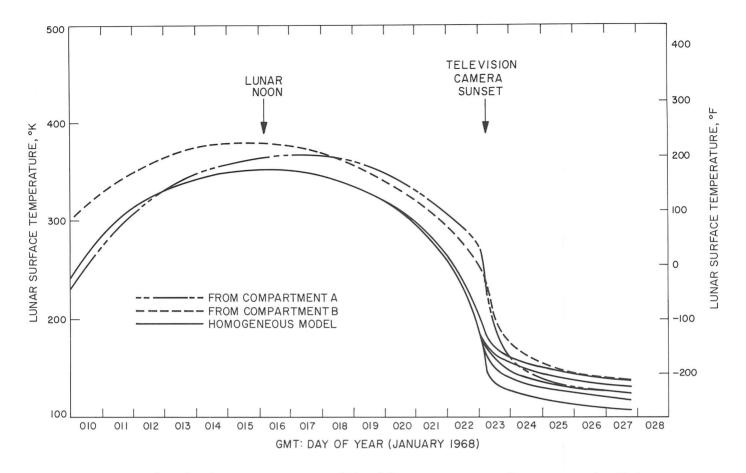


Fig. VI-20. Lunar surface brightness temperatures derived from compartment data, compared with homogeneous model temperatures.

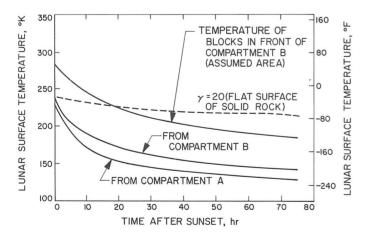


Fig. VI-21. Post-sunset temperature of blocks in front of compartment B.

G. Discussion

Lunar surface temperatures indicated by Surveyor VII during the day can be explained qualitatively in terms

of the directional effects of infrared emission from the surface. However, post-sunset data indicate that the surface viewed by Surveyor VII has an effective $\gamma=385$, as sensed by compartment A, and $\gamma=240$, as sensed by compartment B. This is in contrast to a value of approximately 700 predicted from earth-based data. This difference between lunar surface and earth-based data has several possible explanations:

- (1) An inaccurate heat flow value from the interior of the compartments may have been used.
- (2) Radiation from the spacecraft may be heating the lunar surface in the immediate vicinity.
- (3) The thermal characteristics of the local landing site may be different from those for the landing site region as viewed from earth.

Further analyses will be required to understand these results.

References

- VI-1. Lucas, J. W., Conel, J. E., Garipay, R. R., Hagemeyer, W. A., and Saari, J. M., "Lunar Surface Thermal Characteristics," Surveyor I Mission Report. Part II: Scientific Data and Results, Technical Report 32-1023, pp. 45–59, Jet Propulsion Laboratory, Pasadena, Calif., September 10, 1966.
- VI-2. Lucas, J. W., Conel, J. E., Garipay, R. R., Hagemeyer, W. A., Jones, C. B., Saari, J. M., Vitkus, G., and Wang, J. T., "Lunar Temperatures and Thermal Characteristics," Surveyor III Mission Report. Part II: Scientific Results, Technical Report 32-1177, pp. 155–188, Jet Propulsion Laboratory, Pasadena, Calif., June 1, 1967.
- VI-3. Lucas, J. W., Garipay, R. R., Hagemeyer, W. A., Saari, J. M., Smith, J., and Vitkus, G., "Lunar Surface Temperatures and Thermal Characteristics," Surveyor V Mission Report. Part II: Science Results, Technical Report 32-1246, pp. 89–113, Jet Propulsion Laboratory, Pasadena, Calif., November 1, 1967.
- VI-4. Vitkus, G., Garipay, R. R., Hagemeyer, W. A., Lucas, J. W., and Saari, J. M., "Lunar Surface Temperatures and Thermal Characteristics," Surveyor VI Mission Report. Part II: Science Results, Technical Report 32-1262, pp. 109–123, Jet Propulsion Laboratory, Pasadena, Calif., January 10, 1968.
- VI-5. Saari, J. M., and Shorthill, R. W., *Isothermal and Isophotic Atlas of the Moon*, NASA Report CR-855, National Aeronautics and Space Administration, Washington, D.C., September 1967.
- VI-6. Watson, K., "1. The Thermal Conductivity Measurements of Selected Silicate Powders in Vacuum From 150°K to 350°K; 2. An Interpretation of the Moon's Eclipse and Lunation Cooling as Observed Through the Earth's Atmosphere From 8-14μ," PhD Dissertation, California Institute of Technology, Pasadena, Calif., 1964.
- VI-7. Wechsler, A. E., and Simon, I., *Thermal Conductivity and Dielectric Constant of Silicate Materials*, Contract Report NAS 8-20076, Arthur D. Little, Inc., December 1966.
- VI-8. Wildey, R. L., "On the Treatment of Radiative Transfer in the Lunar Diurnal Heat Flow," J. Geophys. Res., Vol. 72, No. 18, September 15, 1967.
- VI-9. Halajian, J. D., Reichman, J., and Karafiath, L. L., Correlation of Mechanical and Thermal Properties of Extraterrestrial Materials, Grumman Research Report RE-280, Bethpage, New York, January 1967.
- VI-10. Ingrao, H. C., Young, A. T., and Linsky, J. L., "A Critical Analysis of Lunar Temperature Measurements in the Infrared," *The Nature of the Lunar Surface*, pp. 185–211, Johns Hopkins Press, April 1965.

VII. Lunar Surface Electromagnetic Properties

A. Radar Reflectivity Analysis

D. O. Muhleman (Chairman), W. E. Brown, Jr., and L. Davids

An integral part of the Surveyor terminal approach guidance system (radar altimeter and doppler velocity sensor, RADVS) consists of four continuous-wave radars, which includes one beam (beam 4, pointed along the roll axis of the spacecraft) whose signal is modulated to obtain range measurements in this direction. The other three beams (beams 1, 2, and 3, each oriented at a fixed angle of 25 deg from the roll axis) measure the doppler velocity components in these directions. The primary function of the RADVS is to supply velocity and range data to the spacecraft computer system, which automatically controls the spacecraft attitude and vernier-engine thrust during the final approach. The four separate receivers utilize an automatic gain-switching procedure in steps of 20 db. The signal strengths in each radar beam are telemetered at a sampling rate of about two/sec.

The signal-strength measurements, combined with a knowledge of the distance of the radars to the points of intercept of the beams with the mean surface of the moon (obtained from the telemetered range and velocity and a post-flight trajectory analysis), yield fundamental information regarding the backscatter characteristics of the lunar surface material over a range of incidence angles. These data, in principle, can be interpreted in terms of the electrical reflectivities and topographical roughness of the lunar surface material. The pre-flight measured values of the pertinent radar parameters are given in Table VII-1.

Table VII-1. Radar parameters

Parameter	Beam 1	Beam 2	Beam 3	Beam 4
Wavelength, cm	2.25	2.25	2.25	2.32
Power transmitted, dbW	34.02	34.92	34.07	24.32
Antenna gain, db	28.27	27.87	27.66	28.44

1. Signal-Strength Data

For the Surveyor VII mission, the various radars supplied useful scientific data as soon as their receivers reached an in-lock state, which occurred approximately 170 sec before impact. At this time, the spacecraft was oriented so that beam 4 was incident on the mean lunar surface at an angle of 36.0 deg from the vertical and at

a range of 23,664 m. At this time, the other beam orientations were:

Beamı	Beam. Angle of incidence, deg	
1	58.7	37,311
2	52.8	31,884
3	18.9	20,196

Shortly before touchdown, the terminal approach guidance system had reoriented the spacecraft so that beams 1, 2, and 3 were within a fraction of a degree of 25-deg incidence, and beam 4 was nearly vertical. The beam incidence angles and associated ranges, as a function of time from 170 sec to touchdown, were obtained using the range and doppler velocity data in the Hughes Aircraft Company six-degree-of-freedom computer program. The cartesian coordinates (centered at the final touchdown point) of the intercept points of the beams with the mean lunar surface were simultaneously obtained. The precision of these computations is difficult to judge, but the incidence angles to a hypothetical planar surface are believed to be accurate to a few tenths of a degree, and the beam intercept coordinates to a few meters relative to the touchdown point.

This information was used to reduce the signal-strength data to the radar cross sections per unit area, which are similar to albedo and are a function of the beam incidence angles. The procedure used is described in Ref. VII-1. The radar equation that defines the radar cross section is:

$$\sigma(\theta) = \frac{(4\pi)^2 P_r R^4}{P_t G_{\pi} (R\phi)^2 A_R}$$
 (1)

where P_r is the observed signal strength, R is the range along the beam, P_t is the transmitted power, G is the antenna gain, A_R is the effective receiver antenna area, ϕ is the beam half-angle, and θ is the angle between the incident beam and a vector normal (perpendicular) to the surface. They are given by

$$A_R = \frac{G\lambda^2}{4\pi};$$
 $\phi^2 = \frac{27,000}{4G} \left(\frac{\pi}{180}\right)^2$ (2)

where λ is wavelength. The cross sections, obtained as a function of time to touchdown, are shown in Figs. VII-1 through VII-4. The structure evident in these data are

due to the following factors, which are discussed in more detail in subsequent paragraphs:

- (1) Cross section $\sigma(\theta)$ varies as a function of θ .
- (2) Strong variations in measured signal strengths occurred when the spacecraft was being rapidly reoriented (from 150 to 120 sec), apparently because of rapid receiver gain-state switching.
- (3) Similar strong variations occurred in the last 30 sec when the beam was near vertical (particularly beam 4, shown in Fig. VII-4) and the spacecraft was near the lunar surface.
- (4) Slow variations occurred, apparently because of the tilt of the lunar surface from the mean plane (particularly beam 3, shown in Fig. VII-3).

2. Cross Section as a Function of Beam Incidence Angle

The values of $\sigma(\theta)$ as a function of θ are shown in Fig. VII-5. The variations of the various incidence angles with time to touchdown were obtained from the sixdegree-of-freedom computer program previously mentioned. Beams 1 and 2 indicate a variation in cross section as a function of incidence angle; this variation is similar to that obtained with earth-based radar observations at similar wavelengths. Considerable scatter is evident in the beam 3 data, apparently because of the fairly large variations in the local surface slopes over the region crossed by this beam. The beam 4 data show considerable data scatter, which is probably caused by the near-vertical incidence of this beam. In general, this near-vertical incidence data indicate a significantly higher cross section than that of the more oblique data, again consistent with earthbased observations of the moon.

It is evident from Figs. VII-1 through VII-8 that the data from beam 2 are everywhere consistently lower than the other data, although beam 3 is strongly affected by the surface topographic variations. This point was investigated by smoothing the data of beams 1 and 2 over intervals of several seconds. The smoothed values are shown in Fig. VII-9. Also shown in Fig. VII-9 is an empirical representation of the data of the form

$$\sigma(\theta) = \frac{k}{(\sin \theta + 0.42 \cos \theta)^3}$$
 (3)

where, for beam 1, k = 1.0; for beam 2, k = 0.7. Thus, the two data sets appear to differ by a constant value.

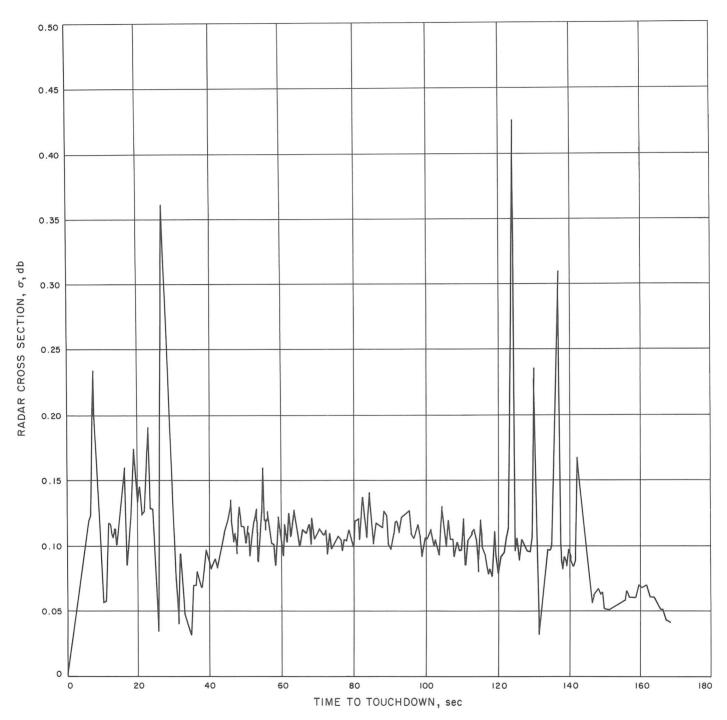


Fig. VII-1. Beam 1 radar cross section, computed from the measured signal strengths as a function of time to touchdown.

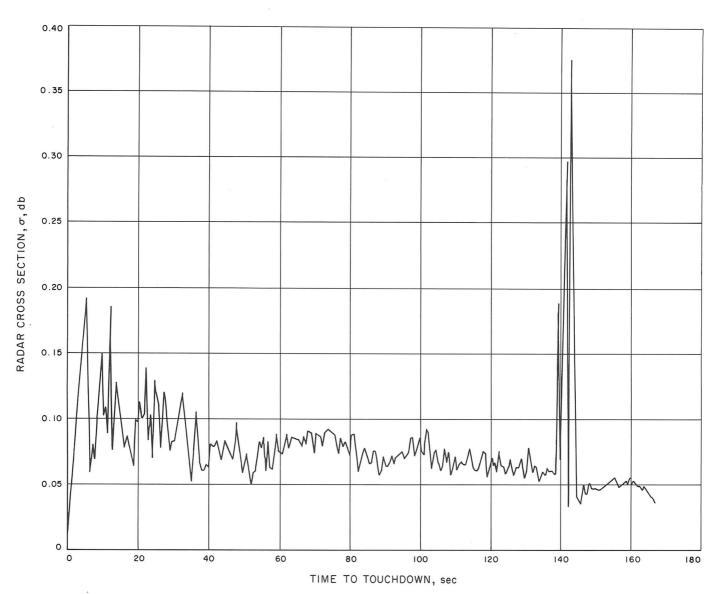


Fig. VII-2. Beam 2 radar cross section, computed from the measured signal strengths as a function of time to touchdown.

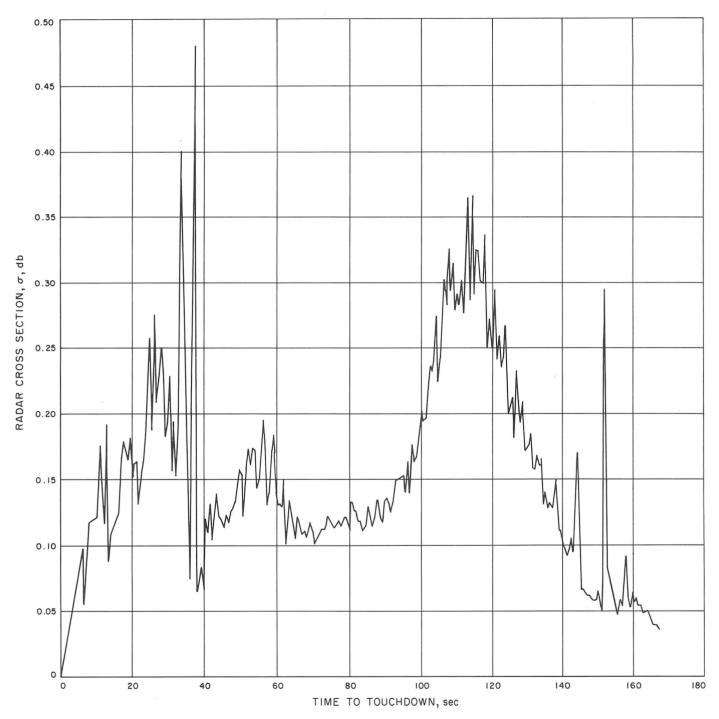


Fig. VII-3. Beam 3 radar cross section, computed from the measured signal strengths as a function of time to touchdown.

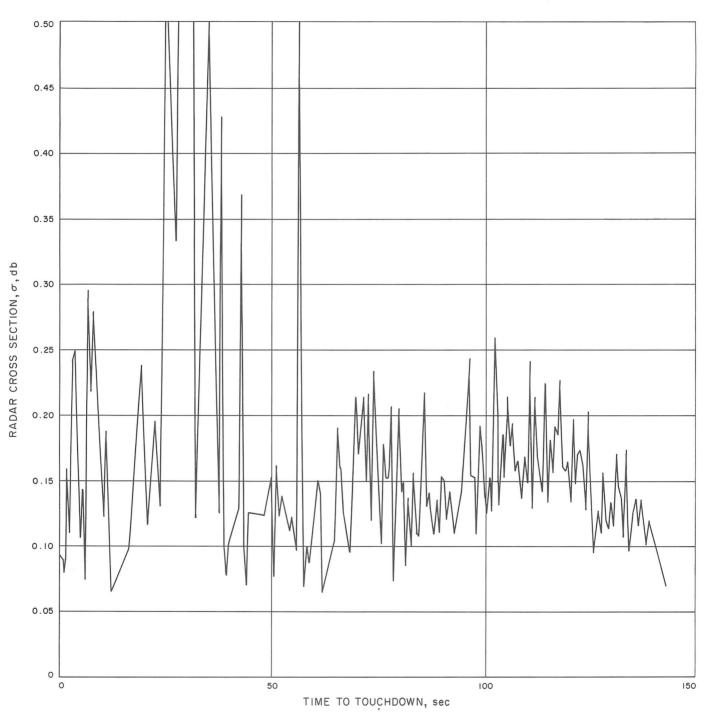


Fig. VII-4. Beam 4 radar cross section, computed from the measured signal strengths as a function of time to touchdown.

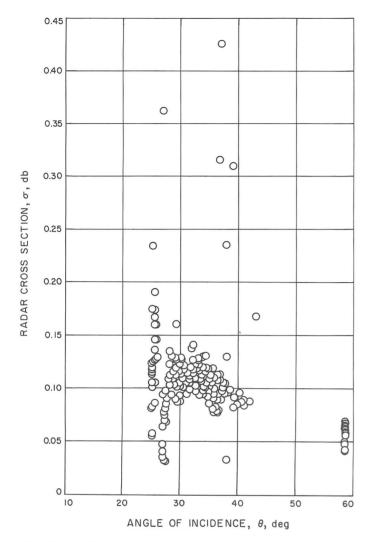


Fig. VII-5. Beam 1 radar cross section, computed from the measured signal strengths as a function of incidence angle.

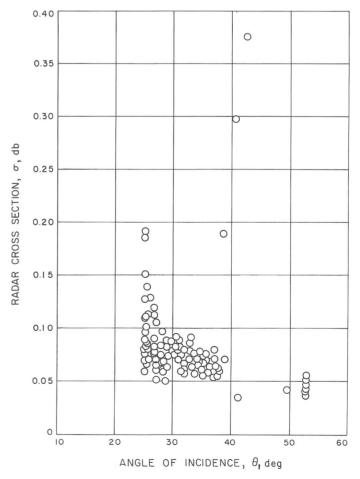


Fig. VII-6. Beam 2 radar cross section, computed from the measured signal strengths as a function of incidence angle.

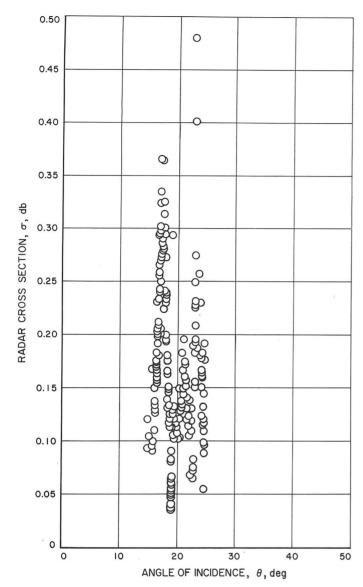


Fig. VII-7. Beam 3 radar cross section, computed from the measured signal strengths as a function of incidence angle.

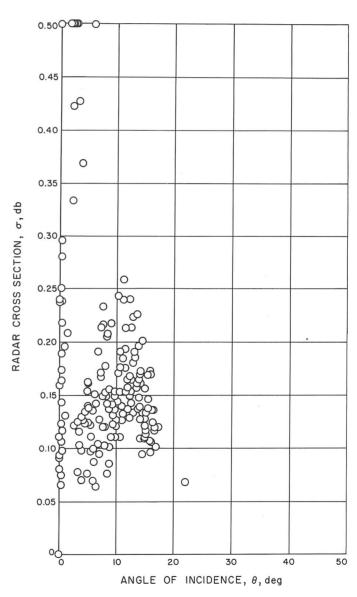


Fig. VII-8. Beam 4 radar cross section, computed from the measured signal strengths as a function of incidence angle.

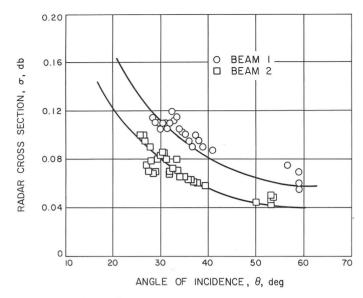


Fig. VII-9. Smoothed radar cross section for beams 1 and 2 as a function of incidence angle.

Although the two beams traverse different points on the lunar surface, the beam coverage converges near the touchdown point (incidence angle, about 25 deg). If the variation between the two beams were due to the lunar surface material itself, we would also expect the cross-section values to converge. The most likely explanation is an error in the radar parameters used in Table VII-1. Because beam 3 agrees generally with beam 1, we conclude that beam 2 is probably low by about 1.5 db because of an instrument calibration data error.

3. Tracks of Beams on Lunar Surface

The effective lunar surface area illuminated by each beam varied from a few square kilometers at the highest altitude to essentially zero at touchdown. The motion of the spacecraft laterally with respect to the final touchdown point plus spacecraft rotational motion about its axes caused the radar beams to sweep out a complex pattern on the lunar surface. Figure VII-10 is the resulting beam trace pattern mapped on a Lunar Orbiter V photograph. The angle of the sun in this photograph is about 9 deg; this low sun angle has the effect of greatly exaggerating one's impressions of the surface roughness. Apparently, beams 1, 2, and 4 traversed relatively flat regions, since little structure appears on the signal-strength data for these beams. However, the beam 3 data were obviously affected by variations in the local surface slopes. The variation of the incidence angle of this beam to the mean surface plane was relatively small. At 160 sec, the incidence angle was 19 deg:

the distance of the illuminated area from touchdown was about 7 km. The corresponding cross section was about 0.05, suggesting that the illuminated surface was tilted away from the beam and that the incidence angle was greater than nominal for a hypothetical planar surface. The cross section is seen to greatly increase, reaching a maximum of about 0.32 at 115 sec (distance, 43 km). Correlation with Fig. VII-3 suggests that the illuminated area was strongly sloped toward the sun, thus minimizing the true incidence angle. The cross section then decreased as the beam crossed the dark region in shadow (time, 70 sec; distance, 0.9 km), which may have been caused by a crater east of the touchdown point (see Fig. VII-11). It appears clear that the observed cross section should increase if the local surface is tilted to decrease the incidence angle; but it is not obvious why a crater would cause a stronger cross section. However, the sample effect was noted in the Surveyor I data. In the case of a crater, the signal increase could be caused by the additional local roughness, the exposure of more compact material (thus increasing the effective dielectric constant), or the presence of more terrain perpendicular to the radar line of sight.

4. Comparison With Other Surveyor Flights

Radar data of the same type reported here are available for *Surveyors I*, *III*, *V*, and *VI*, all of which landed in mare areas of the lunar surface. It is of some interest to compare the radar backscatter characteristics for the maria with those of the *Surveyor VII* highland site. Since this analysis is just beginning, general statements only will be made in this report.

- (1) The signal-fading characteristics are essentially the same for all flights. This suggests that the fading behavior is influenced primarily by the radar system design, which was identical.
- (2) The angular dependence of the cross sections is approximately the same for all flights and is consistent with earth-based lunar radar data. A much more complete analysis is required to determine the quantitative effects of roughness from these measurements.
- (3) The cross section at a given incidence angle is significantly higher (by a factor of about 2) for the Surveyor VII landing site than for the other sites. This circumstance would arise if the Surveyor VII area were considerably rougher at the effective radar wavelength, the surface material were of different composition, or the soil were more compact

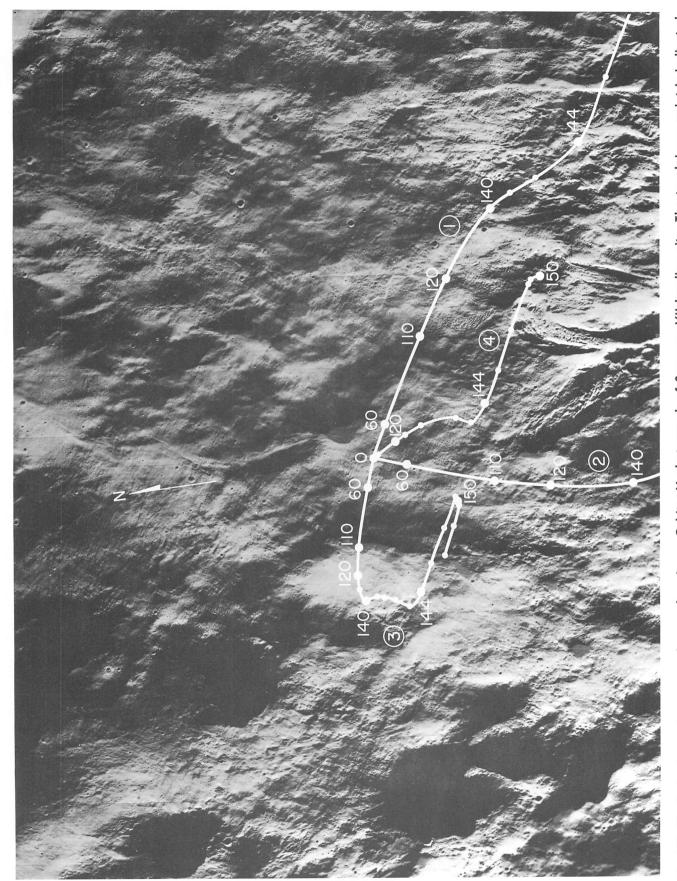


Fig. VII-10. Radar beam traces superimposed on Lunar Orbiter V photograph of Surveyor VII landing site. The touchdown point is indicated by circle; time to touchdown, in seconds, is indicated by dots.

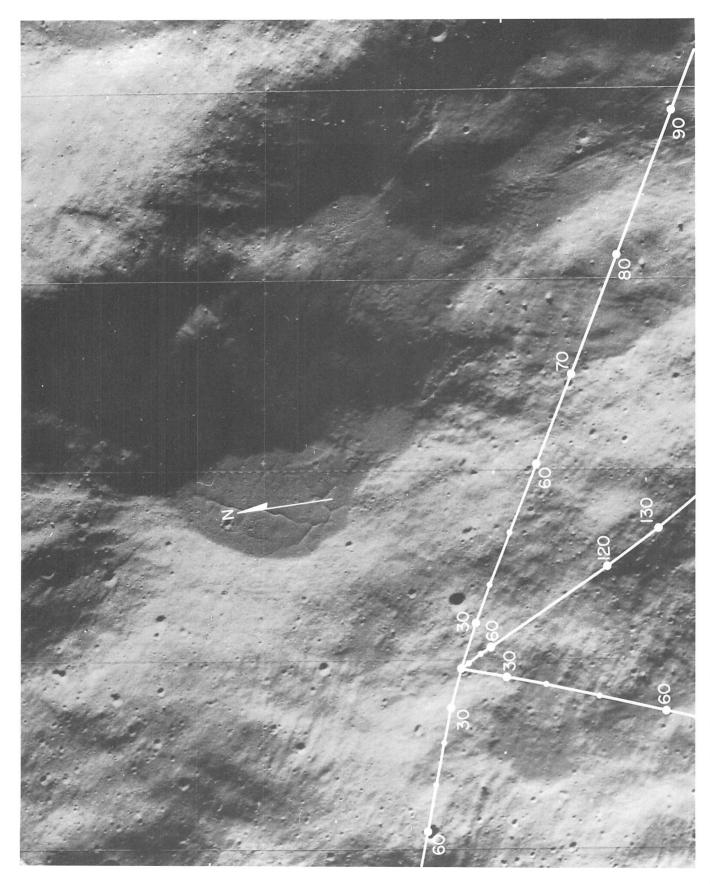


Fig. VII-11. Part of Fig. VII-10. The touchdown point is indicated by the intersection; time to touchdown, in seconds, is indicated by dots.

in this area. The last circumstance includes the possibility that the electrical parameters vary with depth, and that the material is more compact nearer to the surface in this area. The traverse of the new craters by the Surveyor I beam shows approximately the same increase (Ref. VII-1).

- (4) Only beam 3 of *Surveyor VII* passed over terrain which was "rolling" sufficiently to give meaningful structure in the signal-strength data.
- (5) Because of the fading characteristics of the data near normal incidence, it will be most difficult to obtain values of the normal-incidence cross sections.



Fig. VII-12. Photograph of the moon showing the Surveyor landing sites.

B. Magnet Data

J. Negus de Wys

Surveyors V and VI, each equipped with magnet assemblies on footpad 2, landed in typical mare areas, Mare Tranquillitatis and Sinus Medii, respectively (Fig. VII-12). Estimates of the amount, size, and probable composition of the magnetic particles attracted from the lunar surface material at these sites, as derived from the magnet test, were found to be compatible with laboratory studies in powdered basalt with no addition of pure iron. The most probable interpretation of the lunar magnetic material at these landing sites appeared to be primarily magnetite particles. Data derived by means of the Alpha-Scattering Experiment also indicated a basaltic composition at the mare landing sites (Refs. VII-2 and VII-3).

Surveyor VII, which landed north of the rim of the crater Tycho (Fig. VII-12), was the first spacecraft to land in a highland area. The possibility of a different chemical composition, suggesting further progression in magmatic differentiation, caused considerable interest. Such a chemical difference might well be reflected in the amount of magnetite present; an indication of meteoritic iron addition was also considered a possibility.

1. Purpose and Design Description

The Alnico V permanent magnets, with a magnetic pole flux of about 600 gauss, are capable of attracting magnetite (of which different rock types have varying percentages), pure iron, and meteoritic nickel-iron. With the magnets placed on the surface sampler, it was anticipated that a magnetic sample could be obtained from the surface layer, as well as at some depth, in the vicinity of the landing site. The maneuverability of the surface sampler also provided a means for testing rocks for magnetic attraction.

Magnet assemblies, similar to those flown on *Surveyors V* and *VI* (Refs. VII-4 and VII-5), were attached to footpads 2 and 3 of the *Surveyor VII* spacecraft (see Fig. VII-13a and 13b). As with prior assemblies, magnetic flux strength plots of 120 readings over the magnet surface were obtained.

The two rectangular horseshoe magnets, embedded in the door of the surface-sampler scoop, measured $1.6\times0.96\times0.32$ cm with magnetic flux strengths of about 700 gauss at the poles (Fig. VII-14a). The magnetic poles were oriented with the two south poles adjacent in the

center of the surface-sampler door. Mounted flush in the fiberglass door, bonded with RTV-60 bonding agent and attached by screws to the fiberglass, the magnets were capable of attracting a fragment of pure iron, magnetite, or meteoritic nickel-iron about 12 cm in diameter on the lunar surface. (The magnets in laboratory trenching operations in basalt may be seen in Fig. VII-15.)

2. Data

Footpads 2 and 3 penetrated the lunar surface less than 6 cm, an insufficient depth to cause magnet contact with the lunar surface material (see Figs. VII-16 through VII-18). However, the magnets on the surface sampler obtained data from two locations (near a in Fig. VII-19) following the first two bearing strength tests (Figs. VII-20 through VII-22). The surface sampler in both tests penetrated the fine-grained, homogeneous surface material to a depth of about 5 cm. A small amount of magnetic material is observed to outline the poles; a slight increase in amount is seen after the second bearing strength test. After several trenching operations, the magnets showed a considerable clumping of material on the magnetic poles. This is probably a result of increased exposure to material rather than an increase in magnetic material with depth (Fig. VII-23). From the sides of the trenches and footpad imprints, the surface material again appears to be very fine-grained and homogeneous. The size of magnetic particles is below camera resolution (about 1 mm); the shape of the particles cannot be determined.

Study of the area mosaic (Fig. VII-19) suggested that an object at location b might be worth testing for magnetic attraction. The albedo of this object was lower, the shape smoother and rounder than most other rocks in the area, and a slight luster could be observed in pictures taken with a low sun angle. After dragging the surface sampler toward location b with the scoop door closed, the object was observed to adhere to the south pole locations (Fig. VII-24) at about a 35-deg angle to the surface. The amount of retaining force necessary to keep the 1.2-cm-diameter object in such a position is about 1.8×10 dynes.

Studies are presently underway to determine the acceleration of the surface sampler in the subsequent motions which dislodged the fragment from its position of attraction. The results will aid in computing the possible range of magnetic susceptibility values for the attracted object.

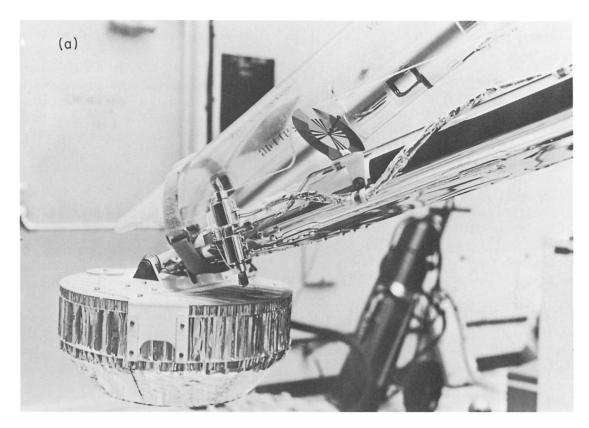
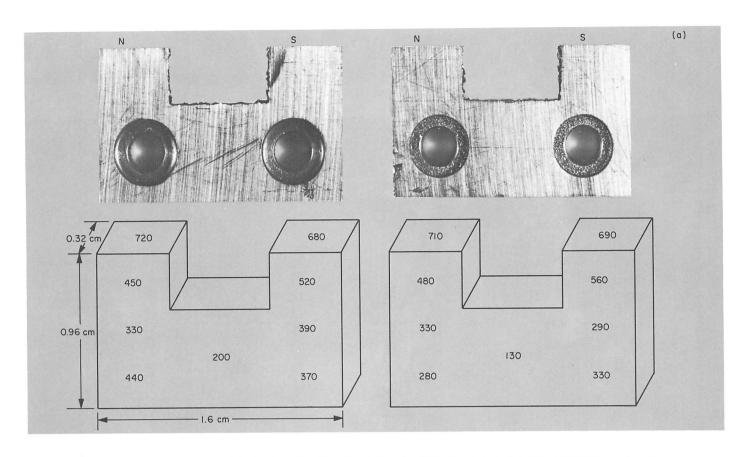




Fig. VII-13. Magnet assembly before flight. The magnetic bar is on the left; the nonmagnetic control bar is on the right. Magnetic flux along the pole edges is about 600 gauss. The control bar has flux readings of less than 0.1 gauss over the surface of the bar. Dark "S" on magnet side indicates the south pole. (a) Footpad 2 assembly. (b) Footpad 3 assembly.



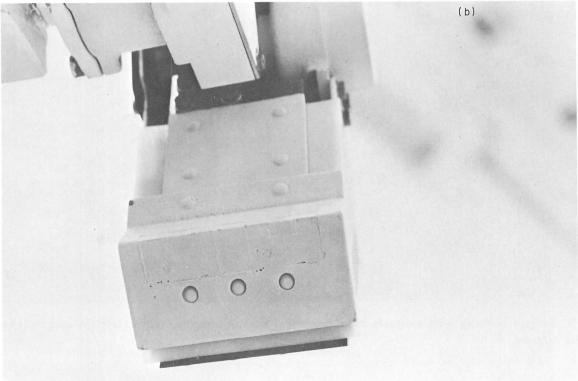


Fig. VII-14. (a) Horseshoe magnets embedded in the back of the surface-sampler door and magnetic flux plots (strength in gauss). (b) Bottom view of rectangular horseshoe magnets. All surfaces were painted with light blue paint.



Fig. VII-15. Surface sampler with magnets in laboratory studies in basalt powder. Note the magnetic material that outlines the magnet.

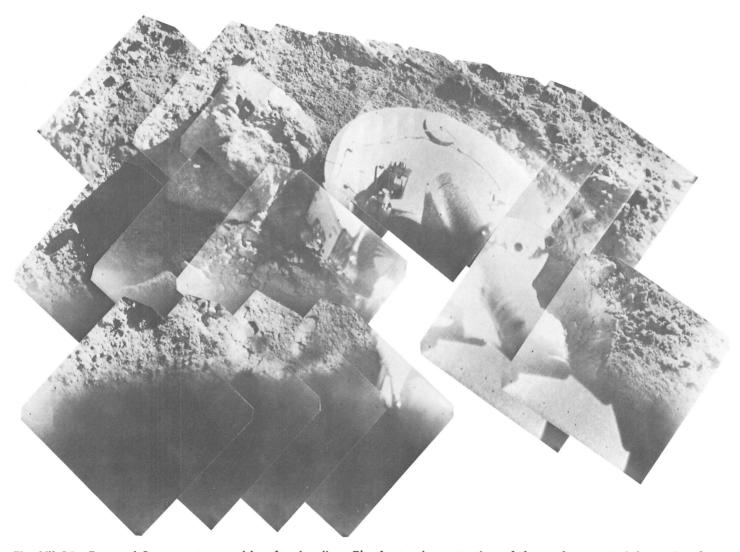


Fig. VII-16. Footpad 2 magnet assembly after landing. The footpad penetration of the surface material was insufficient to produce contact with lunar surface material. Dark mark on magnet side is south pole designation. Fine particles near the bottom are from material acquired during the landing (Catalog 7-SE-7).

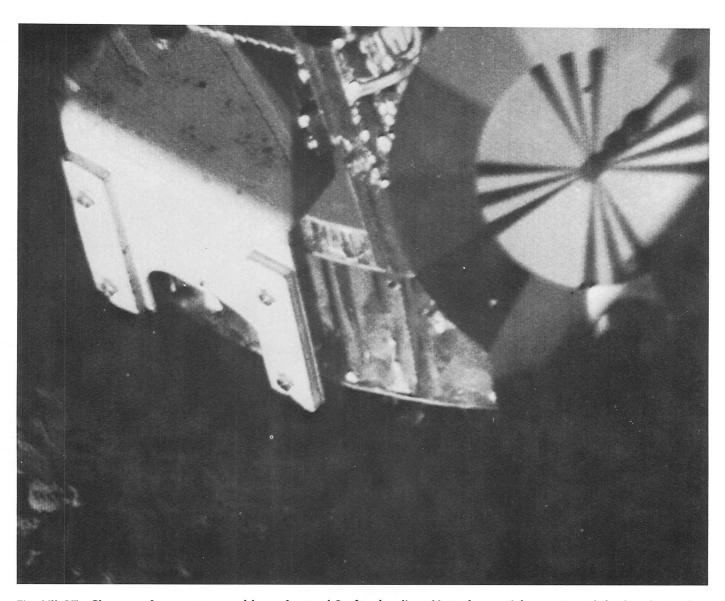


Fig. VII-17. Closeup of magnet assembly on footpad 2 after landing. Note the particles on top of the bracket; a few particles also adhere to the lower ends of the poles; these particles may also be caused by the landing disturbance (Day 022, 16:10:01 GMT).

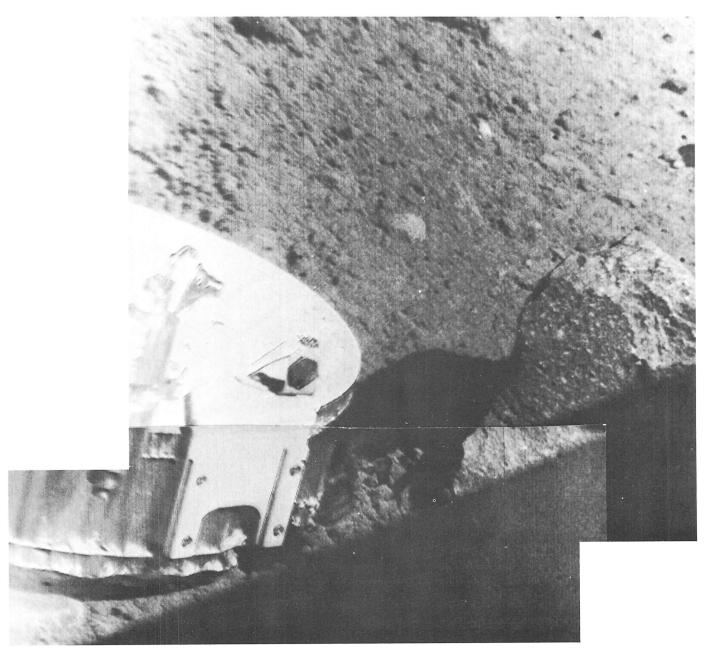


Fig. VII-18. Footpad 3 magnet assembly. No contact was made with the lunar surface material because of insufficient surface penetration.



Fig. VII-19. Mosaic of the area in which the surface sampler operated. Bearing strength tests 1 and 2 were in the vicinity of a; a rock thought worthy of testing was spotted at location b.

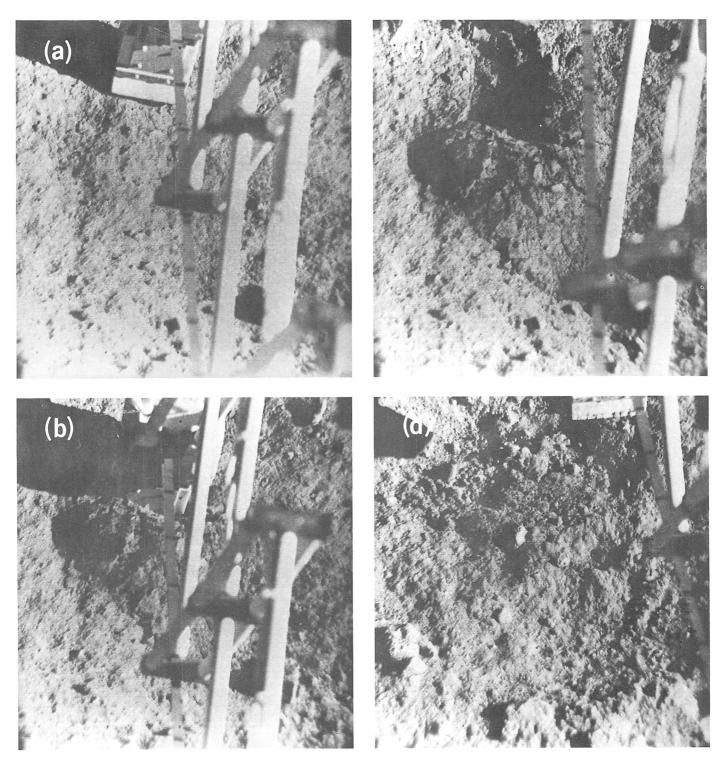
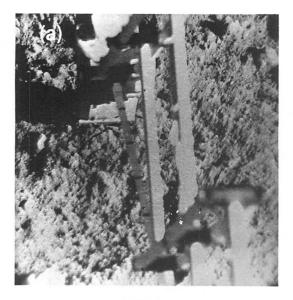


Fig. VII-20. Bearing strength test 1 sequence showing the scoop door. (a) Before contact. (b) During pressure. (c) After contact. The depth of penetration in b is about 5 cm. The amount of magnetic material collected on the magnetic pole faces may be compared with laboratory studies (Figs. VII-24 and VII-25).



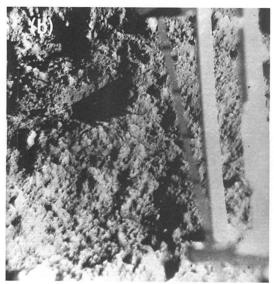




Fig. VII-21. Bearing strength test 2 sequence. The depth of penetration into the surface material is again about 5 cm (b). View (c) shows the magnetic pole face, which may be compared with laboratory studies (Figs. VII-24 and VII-25).

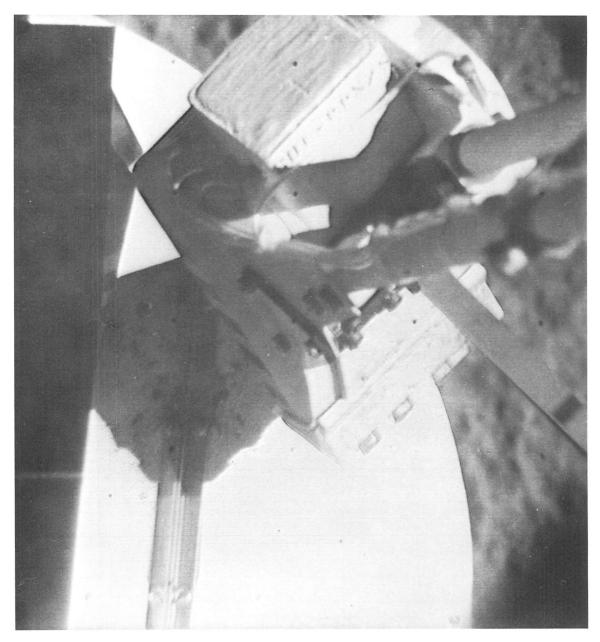


Fig. VII-22. Surface-sampler magnets after two bearing strength tests; compare with Figs. VII-25 and VII-26 (Day 011, 07:48:26 GMT).

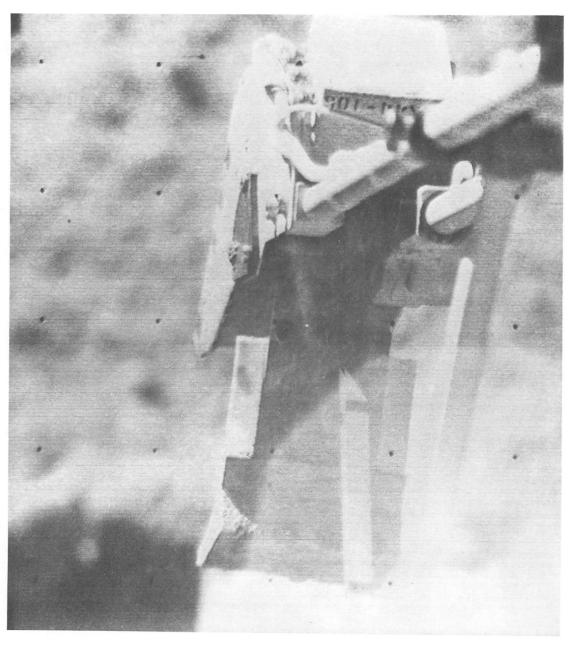


Fig. VII-23. Magnets on surface sampler after contact with material during operations. Note increase in the amount of magnetic material over that observed after bearing strength tests (Day 020, 15:08:28 GMT).

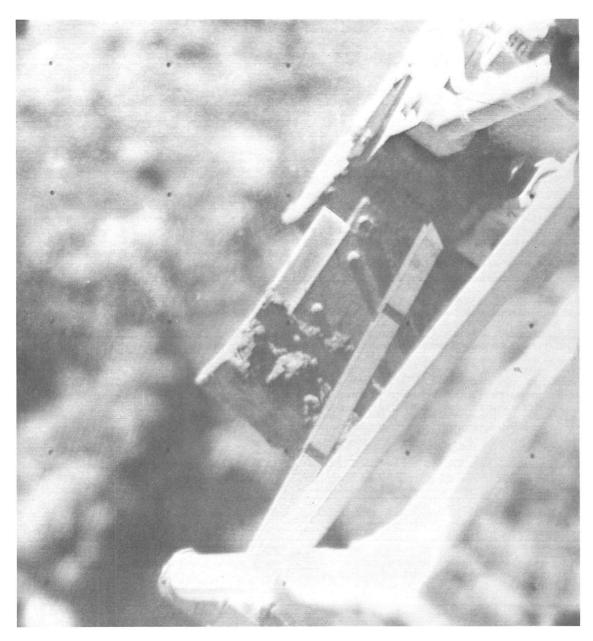


Fig. VII-24. Object attracted and suspended by the south pole of the horseshoe magnets on the surface sampler. The object is about 1.2 cm in diameter, has a darker albedo than most other rocks in the area, and a slight luster. From laboratory studies, this fragment is probably magnetite or a nickel-iron meteorite (Day 020, 14:58:39 GMT).

3. Laboratory Studies

Laboratory studies, similar to those conducted with the bar magnet assembly (Refs. VII-4 and VII-5), were conducted with the surface-sampler magnets (Figs. VII-25 and VII-26). Since the magnetic pole strengths were similar to those of the bars, the test results were similar.

In the powdered rock sequence, $37{\text -}50\mu$ powders of rhyolite, dacite, basalt, peridotite, and serpentine were used. Very little, if any, material is seen to adhere to the magnets when contact is made with rhyolite, dacite, or peridotite. Contact with the basalt powder (Little Lake basalt) showed the largest amount of magnetic material adhering to the magnets. Contact with peridotite powder resulted in slightly less material and a darker appearance.

The procedure used in testing the 1.2-cm-diameter object for magnetic attraction was simulated several times in the laboratory (Fig. VII-27) using 1.2-cm-diameter fragments of various materials (including pallasite, chondrites, basalt, nickel-iron meteorites, and magnetite). The only fragments attracted consisted of magnetite and meteoritic nickel-iron. Both could be held at an angle of about 35 deg to the surface. Other possibilities are under consideration. However, the laboratory studies appear convincing to the author that the lunar object must be magnetic. This is further corroborated by the Investigator Team on the Soil Mechanics Surface Sampler Experiment, who concluded that the general behavior of the object, when picked up by the surface sampler, could be explained only by magnetic attraction. No other object on the lunar surface has been picked up in this manner; this was the only object tested by the surfacesampler magnets for magnetic attraction.

4. Interpretation and Conclusions

The appearance of the surface-sampler magnets following bearing strength tests 1 and 2 is most similar to the laboratory studies using powdered (37–50 μ) Little Lake basalt. Peridotite powder studies showed a somewhat lesser resemblance to the lunar results.

The size of the material can be designated only as <1 mm (camera resolution), although, from laboratory comparisons, the $37{\text -}50\mu$ range appears to be similar to the lunar material. Thus, the shape of the fine particles cannot be determined. The amount of the fine, magnetic material is very similar to that found at the mare landing sites (Fig. VII-28). The Surveyor VII magnetic-particle sample represents contact down to about a 5-cm depth in the bearing strength tests and to about 50 cm in the

trenching operations. From the trenching operations, the material below the surface appears to be very homogeneous and fine-grained with no visible evidence of larger particles or fragments, or of lighter material, such as observed on the surface. From resistance to the surface sampler, a hard surface or rock was considered a possibility in the bottom of some trenches at the Surveyor VII landing site. From comparisons of Surveyor VII results with laboratory studies, the results appear compatible with basalt powder with no observable addition of meteoritic nickel-iron, i.e., <<0.25% by volume.

The chemical analysis obtained by means of the Alpha-Scattering Experiment shows about a factor of two decrease in iron at the Surveyor VII landing site (see Section VIII of this Report). There are several possible interpretations of this contrasting lower iron figure in comparison with the similar magnetic iron data from the magnet test in comparing the Tycho area results with mare area data. The top few microns of surface from which the alpha-scattering instrument obtained data in sample 1 at Tycho may be a mixture of several rock types. There is an abundance of lighter rocks of all sizes scattered in this vicinity. Fine powder from the light rocks is probably also present. However, below the surface, the material appears darker and very homogeneous, and may represent a different situation, i.e., one rock type, although such an interpretation has not been indicated by alpha-scattering data on sample 3 (disturbed surface). From interpretation of the magnet data, basalt is suggested, the source of which is usually considered to be volcanic extrusion.

The small amount of magnetic material in approximately the upper 5 cm does not indicate an observable meteoritic nickel-iron addition. Thus, churning of the upper layer by meteoritic bombardment is not evidenced by the magnet data. This could suggest that the material was fine-grained at the time of formation and deposition, or that it was reduced to a fine state in situ, by a process not yet defined.

The 1.2-cm-diameter object attracted to the south poles of the horseshoe magnets on the surface sampler may be composed predominantly of magnetite, or may be a nickel-iron meteoritic fragment. The structure observed on the object may represent exfoliation, not uncommon in nodular magnetite and a process which appears to be affecting other rocks on the lunar surface. However, the morphology is also compatible with that of some meteorites. It is interesting to note that before the object was picked up, it was protruding from surface material, with

¹H. Brown, private communication, 1968.

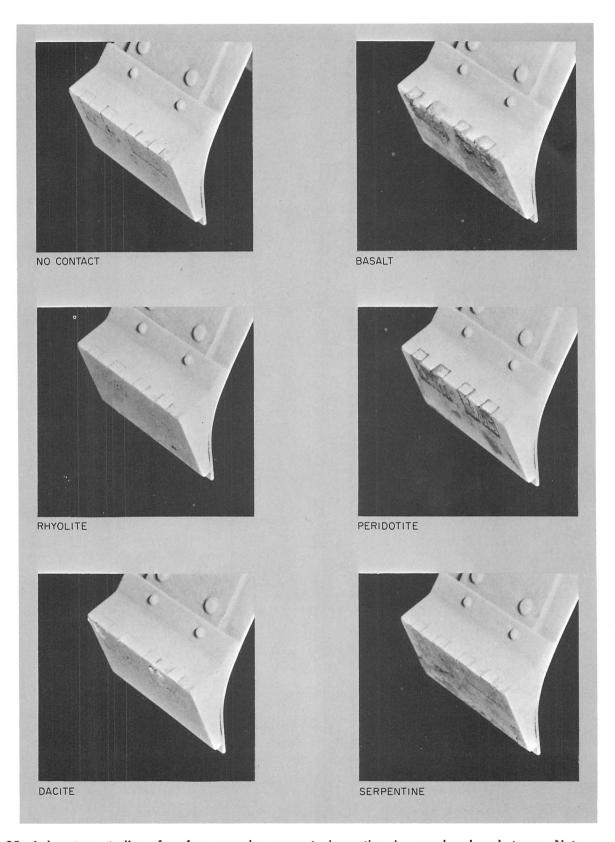


Fig. VII-25. Laboratory studies of surface-sampler magnets impacting in powdered rock types. Note amount of magnetic material collected on pole ends, compared with that observed after the first and second lunar bearing strength tests (Figs. VII-20 and VII-21).

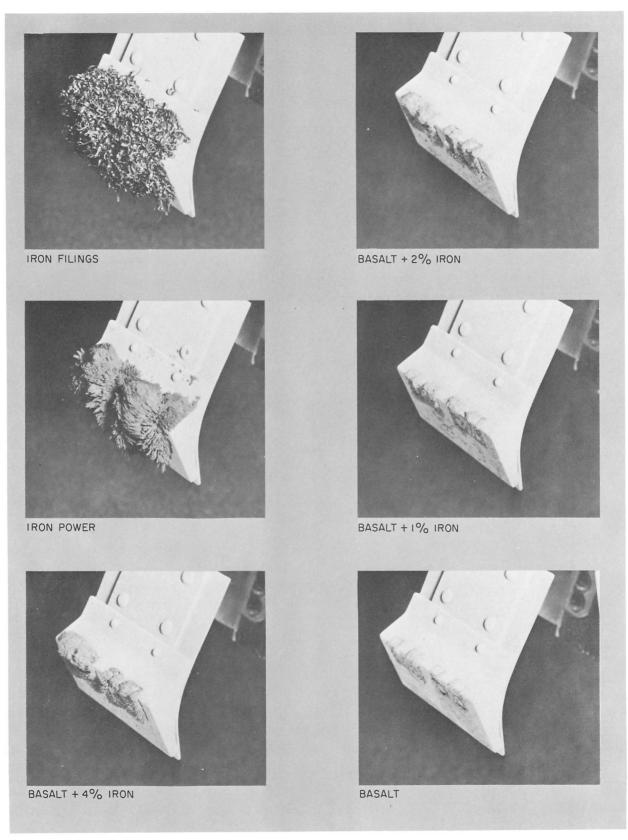


Fig. VII-26. Laboratory studies of surface-sampler magnets impacting in coarse iron filings, powdered iron, and various volumetric percentage additions of powdered iron to basalt powder (37—50 μ).

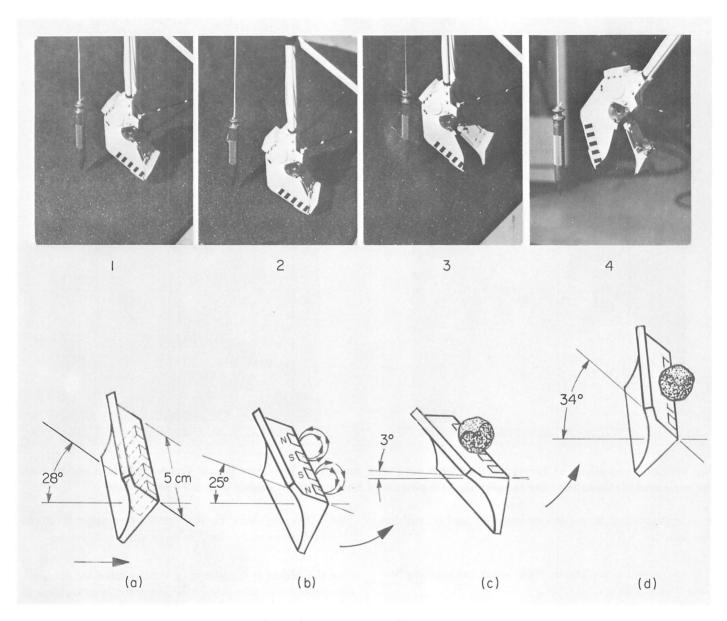


Fig. VII-27. Laboratory re-enactment of the surface-sampler pickup operation of the object. The plumb bob indicates the angular relationships. Between positions 2 and 3, the object was attracted. At position 4, the object was maintained at 34 to 35 deg (estimated minimum angle) after upward movement of about 36 cm. This operation was repeated numerous times in the laboratory with various types of material. Magnetite or nickel-iron meteorite were the only materials that were attracted and remained in this position.

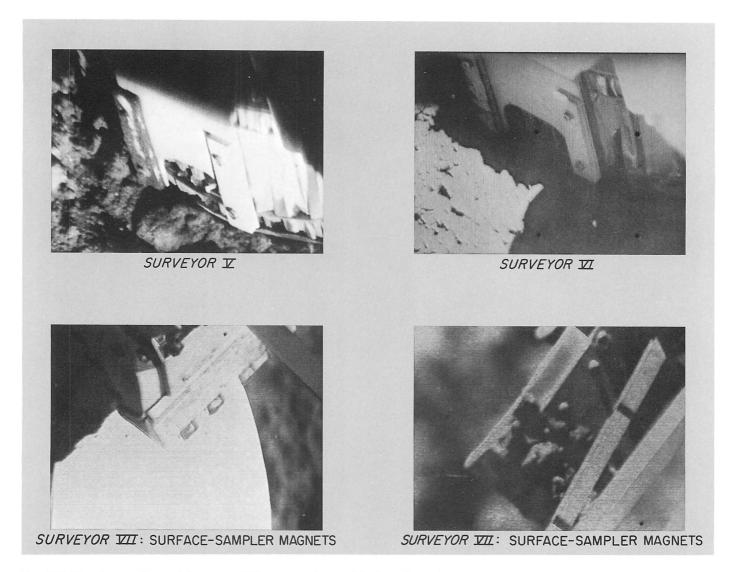


Fig. VII-28. Comparison of Surveyor VII magnet data with data from Surveyors V and VI. Magnet data results from the mare and highland sites are compatible with powdered basalt with no added meteoritic nickel-iron.

no accompanying depression or craterlet and no roll impression.

If the object is meteoritic nickel-iron, several implications would follow:

- (1) It would suggest that not all meteoritic material vaporizes on impact.
- (2) If this surface material is assumed to have been churned by bombardment, the data from the Alpha-Scattering Experiment should show an increase in iron. No such increase was observed; in fact, the iron content was low.
- (3) Some size distribution of particles in the upper layer of the lunar surface might be expected, rather than a layer of fine-grained, homogeneous material.

(4) This may have been a buried meteoritic fragment thrown out by the Tycho crypto explosion.

If the object is magnetite, a similar environment ecology problem is presented regarding the relationships to the surface, to the homogeneous substrate, and to a source area.

Further laboratory studies with solid fragments are being conducted. Whether predominantly magnetite or meteoritic nickel-iron, the object that adhered to the surface-sampler magnets is evidence of the presence of ore-grade iron fragments on the lunar surface. Studies of magnet contact with rock powders are continuing using a wide compositional range of basalts and varying additions of meteoritic powders.

References

- VII-1. Brown, W. E., Jr., "Lunar Surface Surveyor Radar Response," J. Geophys. Res., Vol. 72, No. 1, p. 791, January 15, 1967.
- VII-2. Turkevich, A. L., Franzgrote, E. J., and Patterson, J. H., "Chemical Analysis of the Moon at the *Surveyor V* Landing Site," *Science*, Vol. 158, No. 3801, pp. 635–637, November 1967.
- VII-3. Turkevich, Anthony L., Franzgrote, Ernest J., and Patterson, James H., "Chemical Analysis of the Moon at Surveyor VI Landing Site: Preliminary Results," Surveyor VI Mission Report. Part II: Science Results, Technical Report 32-1262, pp. 127–153, Jet Propulsion Laboratory, Pasadena, Calif., January 10, 1968.
- VII-4. de Wys, J. Negus, "Surveyor V Magnet Experiment," Science, Vol. 158, No. 3801, pp. 632–635, November 1967.
- VII-5. de Wys, J. Negus, "Electromagnetic Properties: Magnet Test," Surveyor VI Mission Report. Part II: Science Results, Technical Report 32-1262, pp. 155–169, Jet Propulsion Laboratory, Pasadena, Calif., January 10, 1968.

Acknowledgment

The programming of the radar data processing for the Science Computer Facility was completed by Mr. George Masters in December 1967. This processing has been a particularly tedious and time-consuming procedure; the successful efforts of Mr. Masters are greatly appreciated.

Appreciation is extended to Dr. Ronald F. Scott, Caltech, and Mr. Floyd I. Roberson, JPL, for their cooperation in articulating magnet tests with the surface sampler.

VIII. Chemical Analysis of the Moon at the Surveyor VII Landing Site: Preliminary Results

Ernest J. Franzgrote, James H. Patterson, and Anthony L. Turkevich (Principal Investigator)¹

The first direct chemical analysis of the lunar surface was provided by means of the Alpha-Scattering Experiment on Surveyor V (Ref. VIII-1). The Alpha-Scattering Experiment on Surveyor VI was almost identical to that of Surveyor V except for the location (Sinus Medii instead of Mare Tranquillitatis); the results obtained were in close agreement with those of Surveyor V (Ref. VIII-2). On Surveyor VII, however, the landing site was in a highland region near the rim of the crater Tycho, instead of in the equatorial mare regions as in previous Surveyor's. The surface material is considered to be part of the Tycho ejecta blanket, presumably situated far below the surface until the formation of the crater.

On Surveyors V and VI, there was little control over the sample to be analyzed. The surface sampler on the Surveyor VII mission provided a means of moving the alpha-scattering instrument from one position to another, thereby obtaining data from three samples: (1) an undisturbed soil, (2) a small rock, and (3) a disturbed soil area of the nearby lunar surface. During the mission, the surface sampler played an even more vital role in the Alpha-Scattering Experiment when it was used to lower the sensor head to the lunar surface after the usual method of deployment had been unsuccessful. In addition, it provided shade for the instrument when there was danger of exceeding specified temperatures during the middle of the lunar day. The method of analysis and the alpha-scattering instrument are described briefly here; emphasis has been placed primarily on the differences from the previous missions. Details of the method of analysis, instrument, and experiment control are described in Refs. VIII-1 through VIII-5.

Only a partial preliminary analysis has been made of the data from the samples at the *Surveyor VII* landing site. Nonstandard sample distances (for example, the rock protruded into the sample opening of the instrument) present more serious complications than in the previous missions. However, significant chemical characteristics can be seen even in the present crude state of the analysis.

¹See Appendix for authors' affiliations.

A. Instrument Description

1. General

As in the previous instruments, the sensor head, which is placed on the surface of the moon for the analysis, contains six capsules of Cm²⁴², which bombard the sample at the circular opening with a collimated stream of alpha particles. Two alpha detectors placed near these alpha-source capsules register and measure the energy of alpha particles scattered almost directly backward from the sample. Similarly, four larger detectors perform the same function for protons produced by nuclear interaction of alpha particles with some of the light elements in the sample. After amplification and energy sorting, the signals from these detectors are converted to a form suitable for transmission to earth by digital electronic circuitry in one of the spacecraft's thermal compartments.

Before the sensor head is lowered to the surface for the lunar analysis, it is calibrated in its stowed position by performing a chemical analysis of a standard sample. This is followed by a measurement of the local radiation background performed with the sensor head suspended above the surface of the moon.

2. Characteristics of the Surveyor VII Alpha-Scattering Instrument

In this mission, the instrument was modified from previous *Surveyor* instruments by the installation of a knob at the point on the top of the sensor head where the deployment cord is attached. This provided a handle for the surface sampler in moving the sensor head from one position to another on the moon.

In this instrument, the Es 254 , which was deposited on the mask of the detectors to determine a fixed point on the energy scale, had a broader energy spectrum than in the *Surveyor V, VI*, or the spare instruments. For this reason, the energy calibration by this means is more uncertain than in the previous instruments.

In the Surveyor V data, and more prominently in the Surveyor VI data, an increasing component of the background in the alpha mode was observed, with a break in its spectrum characteristic of gold. This was caused by the deposition by aggregate recoil of alpha radioactive material from the curium sources onto the thin films over the ends of the source collimators. The uncollimated alpha particles from this material were scattered into the alpha detectors by the gold-plating on the inside of the sensor head, giving rise to this background.

In preparation for the Surveyor VII Alpha-Scattering Experiment, the plates containing the curium were coated by vacuum evaporation with a film of carbon in an attempt to prevent the aggregate recoil. In the curium sources prepared for the spare instrument for this mission, the aggregate recoil was almost completely eliminated. In the sources used in the lunar mission, considerable aggregate-recoil contamination was observed, but it was less than that observed with uncoated sources. These sources were chosen in preference to the spare sources because they were approximately 70% higher in total alpha intensity. The spare sources would have had about the same intensity as the sources of the other two missions. This provided a more rapid accumulation of data, as the number of protons and alpha particles obtained is proportional to the incident alpha-particle intensity.

The assembly of the instrument (designated F-2 in premission tests) was completed on March 6, 1967. Science calibration of the instrument was finished April 4, 1967; the instrument was delivered to Hughes Aircraft Company about June 5, 1967. Final installation of sources took place on December 20, 1967. By the launch date (January 7, 1968), the instrument had been operated for 798 hr.

Table VIII-1 lists some of the characteristics of the sources and detectors used in the *Surveyor VII* instrument during the mission.

B. Mission Description

1. Pre-Launch Operations at Cape Kennedy

Final calibration of the flight instrument and preparations for launch were carried out in a special test facility at Cape Kennedy. These operations and the facility have been described in Refs. VIII-1 and VIII-2.

2. Launch and Landing

The Surveyor VII launch, transit, and landing operations proceeded normally. Alpha-scattering-instrument temperatures were monitored during transit to the moon, but the instrument was not activated before landing.

Touchdown of Surveyor VII occurred at 01:05:36 GMT on Day 010 (January 10, 1968). The spacecraft came to rest on a fairly flat surface (slope approximately 3 deg) with the outboard side of the sensor head facing about 20 deg west of north (see Section III of this Report). The landing site, less than one diameter north of the rim of

Table VIII-1. Characteristics of Surveyor VII alpha-scattering instrument

Alpha Source Characteristics		Proton Detectors	
Intensity as of Day 009	100	Gold foil thickness	10.5μ (equivalent to 20.3 mg/cm²
(total of six sources)	4.70 × 10 ¹¹ disintegrations/min	(Energy loss for 6.1-MeV alpha	
Mean energy, as measured through		particles)	5.5 MeV
source capsule protective films	6.02 \pm 0.01 MeV	(Energy loss for 2.0-MeV proton	
Energy spread range for six		particles)	1.13 MeV
sources (full width at half		Guard Detector System	
maximum)	1.3 to 2.2%	Approximate energy threshold	0.30 MeV
Thickness of secondary protective		Guard ratemeter response:	
film (energy loss for 6.1-MeV		10 events/sec	0.030 V
alpha particles)	0.026 MeV	30 events/sec	0.300 V
Alpha Detectors		100 events/sec	0.900 V
Thickness of evaporated-gold		300 events/sec	1.800 V
surface (energy loss for 6.1-MeV		1000 events/sec	2.500 V
,	0.039 MeV	Electronics energy scale	
alpha particles)		(Temperature of sensor head and	
Thickness of alpha mask films		of digital electronics = 25°C)	
(energy loss for 6.1-MeV alpha		Alpha	N = 18.98E - 10.9
particles)	0.026 MeV	Proton	N = 19.16E - 11.9

Tycho, was the only highland landing site of the *Surveyor* series. Assuming Tycho to be formed by an impact process, the gross topography of the landing area is believed to be dominated by debris ejected during formation of the crater. Local surface characteristics differed visibly from those of the mare sites of previous *Surveyor* missions; the local surface reflectivity and the abundance of rocks and fragments were significantly higher than found in the lunar maria (see Section III of this Report).

3. Post-Landing Operations

a. Stowed position (Day 010). Methods used for controlling the Alpha-Scattering Experiment during the mission have been described in Refs. VIII-1 and VIII-2. On Surveyor VII, the command to apply spacecraft power to the instrument was first transmitted at 09:27:31 GMT on Day 010. At that time, instrument temperatures were within operating limits (sensor head, 12°C; digital electronics, 2°C), instrument power-supply voltages were normal, and the guard-detector event rate was found to be comparable to the values measured on Surveyors V and VI.

Between 09:28:00 GMT and 15:29:00 GMT, accumulations of standard-sample spectra for a total duration of 5.2 hr were received via teletype from the tracking stations. These data, plus calibration spectra obtained using the commandable electronic pulser, showed that the instrument had survived the launch and landing and was capable of providing analyses in the lunar environment.

b. Background position (Days 010 through 012). When the sensor head is released from the stowed position, it swings outward and downward several centimeters and continues moving for some time like a pendulum. As during the Surveyor VI mission, a series of television pictures of this operation was planned primarily to provide a direct view of the eventual sample area on the lunar surface otherwise obscured by the sensor head. The sensor head was released from the stowed position by commands transmitted from the Robledo, Spain, tracking station at 15:48:52 GMT on Day 010. Personnel at the tracking station noted that successive pictures on their television monitor showed that the sensor head had been released and was moving. Approximately 100 pictures, commanded at 3.0-sec intervals, were obtained during the deployment operation.

When the sensor head was released to the background position, its temperature (which had been rising at a rate $>1^{\circ}\text{C/hr}$) decreased from 19 to 14°C over a period of about 3 hr. The digital electronics temperature at this time was 8°C.

The first accumulation of background data began at 16:13:00 GMT. From this time until 21:59:10 GMT, total accumulations of 4.8 hr were received. The data quality during this period was good except for a period of increased parity errors (possibly caused by high winds reported at the tracking receiver in Spain).

Because the amount of background data was considered adequate at this stage of the operation, a command to deploy the sensor head to the lunar surface was transmitted at 22:01:44 GMT. During the *Surveyor V* and *VI* missions, when this command was transmitted, tracking-station personnel had reported that the rate of analyzed events had increased, indicating that the sensor head had descended properly to the lunar surface. This time, no apparent change in counting rate was observed. The deployment command was retransmitted at 22:09:00 GMT; again, no increase in counting rate was observed. A 10-min accumulation of data verified that the instrument was still suspended above the lunar surface, and possibly had not moved at all.

When tracking operations were transferred to the Goldstone, California, Tracking Station (DSS 11), television pictures were taken to help diagnose the problem. The pictures showed that the sensor head was still suspended in the background position, but that a small retaining door (used to prevent premature deployment of the flat electronics cable) had opened correctly. This showed that the deployment command had been properly received by the spacecraft and that the squib-activated pin puller had operated. This information isolated the problem to the nylon suspension cord or its associated storage spool and escapement mechanism, affording hope that operation of one of the movable parts of the spacecraft would provide enough force to free the sensor head.

Although the surface sampler (with its versatility of movement and ability to reach the sensor head) offered the most promise of help, possible damage or entanglement of the surface sampler with the nylon cord had to be considered. The first parts of the spacecraft to be moved, therefore, were the solar panel and planar array antenna. Vibrations induced in the spacecraft by these motions, however, were not sufficient to lower the instrument.

After initial checkout of the surface sampler, and after minimal lunar surface bearing tests had been performed, an attempt was made to free the sensor head by pressing down on the edge of its circular plate. Sufficient force could not be exerted to deploy the instrument, however, because of the manner in which it was free to rotate away from the force. Further attempts were postponed until the following day.

Additional accumulations (7.2 hr) of background data were obtained while waiting until surface-sampler oper-

ations could be resumed. Three electronic-pulser calibration sequences were performed during the background phase of operation. During the following Goldstone visibility period (Day 012), the surface sampler was able to free the deployment mechanism and push the sensor head to the lunar surface by wedging the sensor head against the spacecraft and then exerting a downward force (see Section V of this Report). The fact that the sensor head was finally deployed and in an acceptable position on the lunar surface was established by the measured rate of reflected alpha particles and by careful analysis of *Surveyor* television pictures.

c. Lunar sample 1: undisturbed soil (Days 012 through 021). Figure VIII-1 shows the location of sample 1 (and succeeding samples) relative to the spacecraft. Figure VIII-2a is a television picture of the sensor head on the lunar surface in position for its analysis of sample 1. By the time accumulation of lunar surface data could be started (16:42:25 GMT on Day 012), the sensor-head temperature had risen to 35°C, the digital electronics temperature to 31°C. The intensity of scattering observed, as well as television pictures, indicated that the sensor-to-sample distance was somewhat greater than standard (or than observed on Surveyors V and VI).

By the end of Day 012, total accumulations of 6.2 hr of lunar surface data had been received. The sensor-head temperature had risen to 40° C by this time.

At 08:21:27 GMT on Day 013, the instrument was turned off because the sensor-head temperature exceeded 50°C, the upper operating limit. The surface sampler was then repositioned to shade the sensor head, and the instrument was turned on at 10:55:17 GMT. Because of rising temperatures, this procedure was repeated later on Day 013; the instrument was off from 20:21:32 to 22:36:12 GMT while the surface sampler was again moved to shade the sensor head. Despite these efforts, the sensor head again became too hot and the instrument was turned off at 23:33:07 GMT. By this time, accumulations (12.7 hr) of spectra from sample 1 had been received.

A decision was made to continue the accumulation of lunar surface data at higher temperatures as long as instrument performance remained within certain tolerances. The instrument was turned on at 16:46:10 GMT on Day 014, at a sensor-head temperature of 58°C. Data for an additional period of 6 hr (some of it with only three proton detectors) were obtained on Days 014 and 015 at sensor-head temperatures up to 62°C. The surface

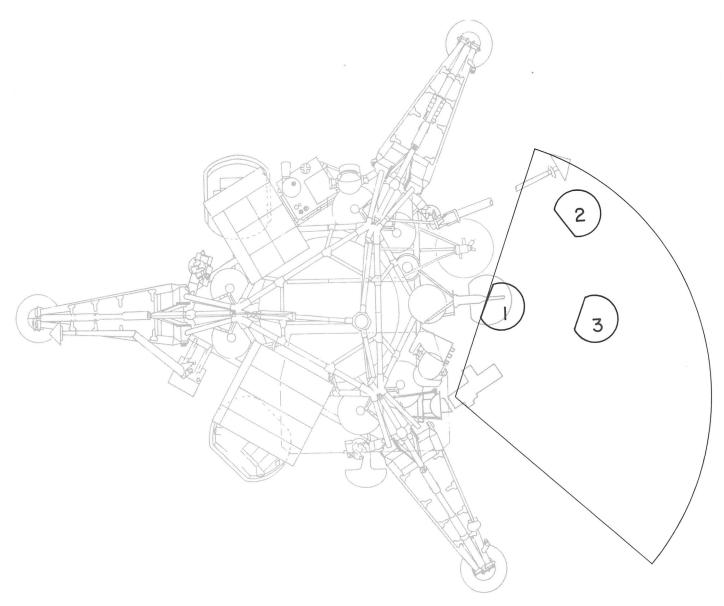


Fig. VIII-1. Plan view of Surveyor VII showing the three sample locations of the alpha-scattering instrument on the lunar surface. The large sector of a circle shows the area of operation of the surface sampler.

sampler was repositioned twice during this period to provide maximum shading. Some increase in noise in the proton spectrum was noted during this period, and when the guard-monitor voltage doubled (even with one protonguard combination off), the instrument was turned off.

While the instrument was off, temperatures remained above operating limits during the lunar-noon period for nearly 6 days. The surface sampler was used to shade the sensor head to keep its temperature below the survival limit of 75°C. At 21:14:41 GMT on Day 020, the instrument was again activated; the sensor-head temperature by this time had decreased from a maximum of 72 to

 42° C, the electronics temperature from 70 to 54° C. The instrument was found to be performing normally, and accumulation of data from sample 1 was resumed.

By 07:20:50 GMT on Day 021, data had been received for a total period of 27.4 hr. Seven calibration sequences were performed during sample 1 operations. Since only 2 days remained until sunset, the instrument was turned off and the sensor head was redeployed by the surface sampler to a second sample. Figure VIII-2b shows the sample 1 area of the lunar surface after the sensor head had been moved to the second sample location. Impressions of the circular plate of the sensor head can be seen

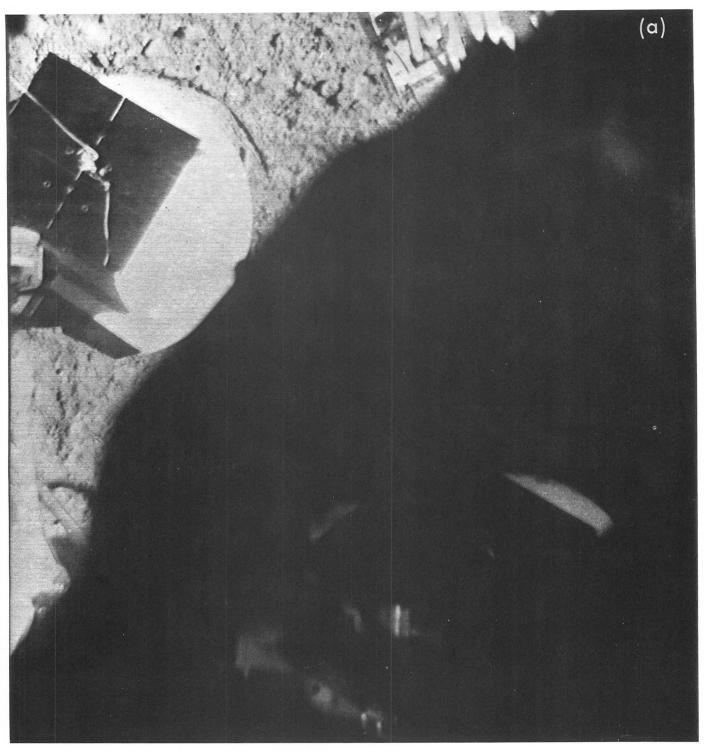


Fig. VIII-2. (a) The Surveyor VII alpha-scattering instrument on sample 1, an undisturbed area of the lunar surface (Day 012, 10:29:29 GMT). (b) Sample 1, after it was analyzed by means of the Surveyor VII Alpha-scattering Experiment.

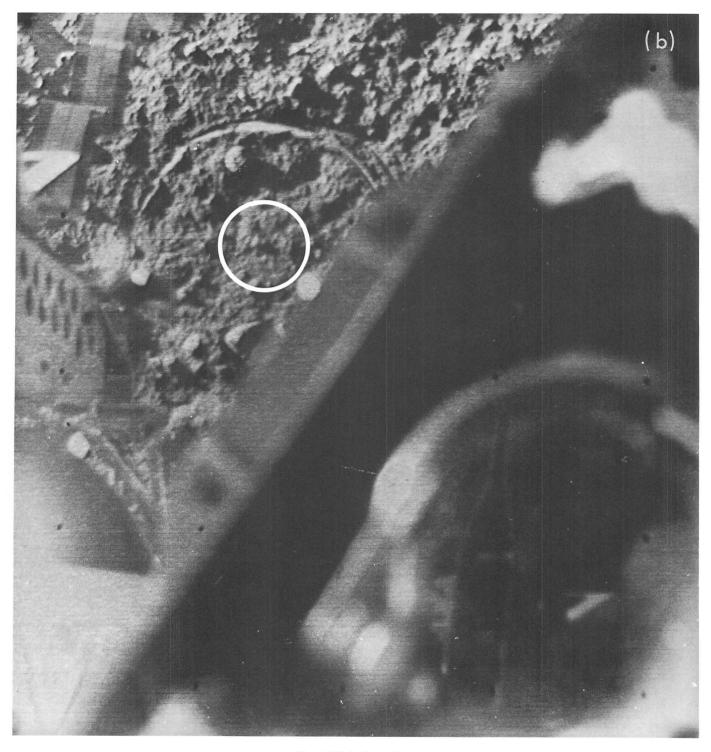


Fig. VIII-2 (contd)

in the lunar surface material. A rock, visible also in pre-deployment pictures, was located beneath part of the circular plate, holding the sensor head in a slightly elevated position on the side toward the spacecraft. The central outlined area, which is the actual sample, can be

seen to be relatively smooth; the largest particle in the sample 1 area is approximately 1.5 cm across.

d. Lunar sample 2: a rock (Days 021 through 022). A lunar rock was chosen as sample 2. This rock was about

5 by 7 cm in size, and was visible as an exposed object on the surface before the start of any surface-sampler operations. The redeployment by the surface sampler of the sensor head to sample 2 was completed at about 12:29 GMT on Day 021. Figure VIII-3a shows the sensor head in position for analysis of the rock; Fig. VIII-3b shows the same area of the lunar surface after subsequent removal of the sensor head. Impressions of the circular

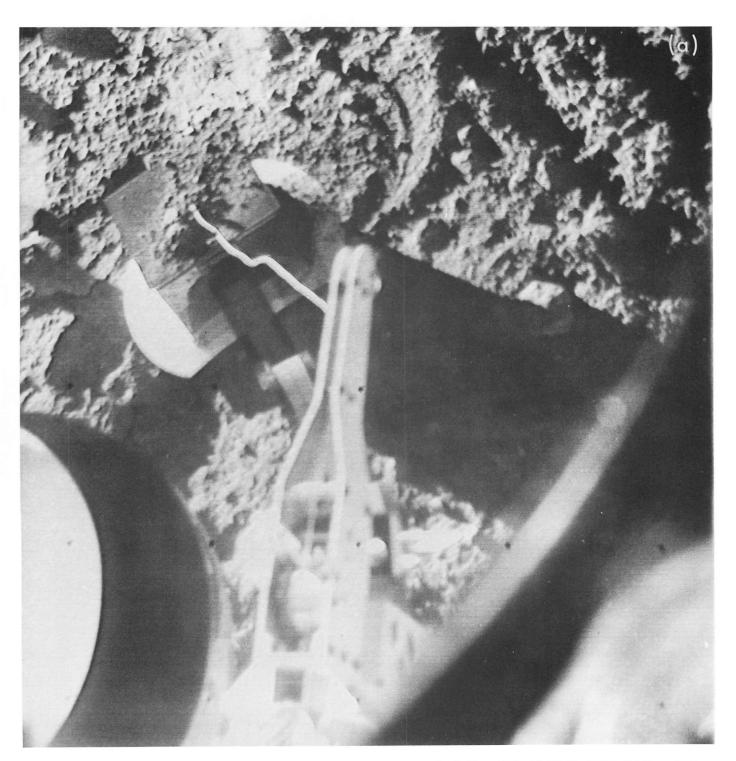


Fig. VIII-3. (a) The Surveyor VII alpha-scattering instrument on sample 2 (Day 022, 10:38:51 GMT). (b) Sample 2, a lunar rock, after it was analyzed by means of the Surveyor VII Alpha-Scattering Experiment.

bottom of the instrument in the lunar surface show its resting place during this analysis. The area outlined by the ellipse (including the rock) shows the size of the sample opening in the bottom of the sensor head. The rock can be seen to be somewhat brighter in appearance than the surrounding surface.

In the sample 2 position, the overall event rate in the alpha mode was found to be about double that observed for sample 1. This information, together with the television pictures, indicated that the rock was well centered in the sample area, protruding slightly inside the bottom of the sensor head.

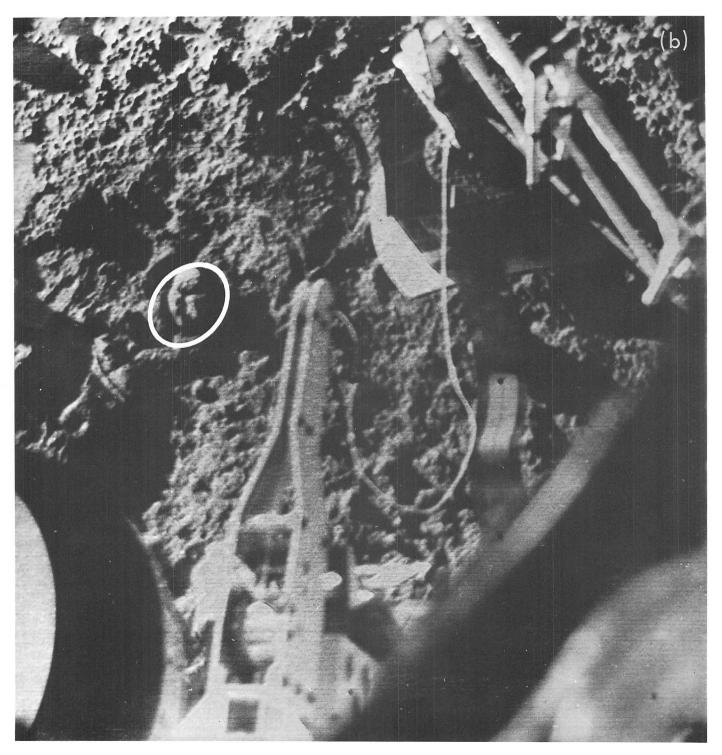


Fig. VIII-3 (contd)

Accumulation of alpha and proton spectra from sample 2 proceeded with normal instrument performance except for several periods of about 2-min duration when guard-monitor voltages increased temporarily to about

200 mV. The total accumulation time for sample 2 was 10.3 hr. This time included 0.3 hr of operation with individual proton detectors. Three calibration sequences were performed during this period.

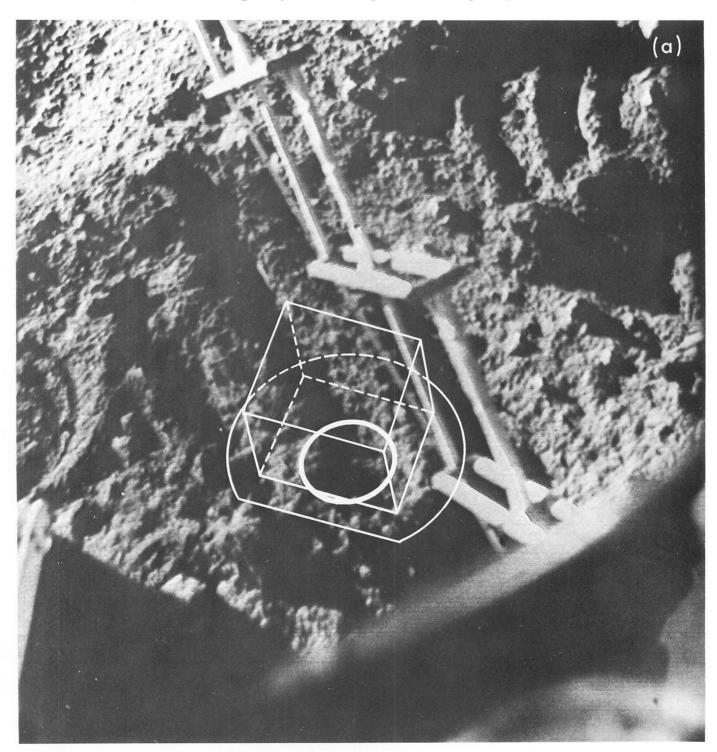


Fig. VIII-4. (a) Sample 3, an area of the lunar surface trenched by the surface sampler, later analyzed by means of the Surveyor VII Alpha-Scattering Experiment. (b) The Surveyor VII alpha-scattering instrument on sample 3 (Day 022, 11:51:02 GMT).

e. Lunar sample 3: disturbed soil (Days 022 and 023). At approximately 11:50 GMT on Day 022, the sensor head was again redeployed by the surface sampler. This third sample was in a trenched area previously prepared during surface-sampler operations. Figure VIII-4a is a

picture of this area with an outline of the subsequent sensor head and sample positions; Fig. VIII-4b shows the sensor head resting on sample 3. The observed alpha event rate in this sample position was again lower than nominal (as with sample 1). This indicates (together with



Fig. VIII-4 (contd)

the television pictures) that the actual sample examined was partially within one of the trenches. Sample 3, therefore, consists at least partly of subsurface material. Between 12:06:30 GMT on Day 022 and 14:40:10 GMT on Day 023, data accumulations totaling 6.7 hr were received from sample 3. One calibration sequence was performed. The instrument was turned off at 15:36:07 GMT on Day 023, approximately 9.5 hr after local sunset. At this time, the sensor-head temperature was -20° C; the digital electronics temperature was -49° C.

f. Sample 3 on second lunar day. Because only a minimal amount of data on sample 3 could be obtained before sunset on the first lunar day, it was fortunate that the spacecraft and alpha-scattering instrument survived the lunar night well enough so that useful data on this sample could be obtained during the second lunar day. A digital anomaly in the proton system prevented the accumulation of useful proton spectra. The alpha system, however, performed nearly as well as during the first lunar day, and between Days 044 and 051, total accumulations of alpha spectra of 34.5 hr were received; this is equivalent to 20 hr of normal alpha data. Interspersed among these accumulations were several pulser calibrations of the instrument.

C. Results

The Surveyor VII mission was extremely productive from the chemical analysis viewpoint. Data were obtained from three positions of the alpha-scattering instrument, each representing a different type of local sample: undisturbed local lunar surface, a lunar rock, and an extensively trenched area of the lunar surface. At the same time, the experiment was handicapped by time restrictions because of the delay in deploying the instrument to the lunar surface and by the longer high-temperature period during the middle of the lunar day when the instrument was above its operating temperature. Because of the latitude of the landing site, shading of the instrument during this period by the solar panel and planar array (which had been very effective in the equatorial landing sites of Surveyor V and VI) was not possible. Shading by the surface sampler helped, but was much less effective. In order to get as much data as possible, the instrument was operated part of the time above its prescribed high-temperature limit. It is felt that these data will be useful even though they will require more rigorous treatment to ensure their reliability.

As on previous missions at this stage of reporting, the results are based upon spectra relayed by teletype from

the Deep Space Stations. These spectra were transmitted in essentially "real time" for purposes of instrument performance analysis and mission planning. In addition to lack of positive evidence regarding their reliability, the data have, as yet, been corrected only approximately for non-nominal instrument behavior. Because of this, as in previous mission reports (Refs. VIII-1 and VIII-2), the interpretation has been made so far in terms of only eight chemical elements. Moreover, the three samples examined, especially the rock and the disturbed lunar surface, deviate considerably from the nominal geometry in which the instrument is usually used. This contributes to the uncertainty at the present stage of analysis. The possibility of systematic errors in this preliminary treatment is the reason for the larger errors assigned to the results than will be applicable at a later stage of data analysis. Moreover, at this time, relatively complete analyses will be presented only for the first sample examined by Surveyor VII, with general remarks about the composition of the other two.

1. Background Data

As in Ref. VIII-2, the data acquired during the second, background-measuring, phase of the experiment will be discussed first. Of the 12.0 hr of data obtained in this phase, 10.5 hr have been subjected to preliminary certification. It is essentially these background data that are presented for both alpha and proton modes in Fig. VIII-5. Plotted are the observed number of events, normalized to a counting time of 1000 min, with associated statistical errors (1σ) , as a function of channel number (energy). The ordinates are on a logarithmic scale.

The main features of the background, in both alpha and proton modes, are the same as in the Surveyor V and VI missions. The Es²⁵⁴ peaks at approximately channel 110 in both modes are of poorer quality, especially in the alpha mode, than in previous missions. In the alpha mode, more structure is visible in the main background spectrum. This is because, due to the higher-intensity sources and longer counting time than on previous missions, the effects of the low-probability reflection from the lunar surface, about 56 cm away, could be seen. The background, because of the scattering of alpha particles from the gold-plated interior of the instrument, was intermediate in intensity between those in the Surveyor V and VI missions; the carbon coating of the sources before encapsulation (see Section VIII-A of this Report) had apparently been moderately successful in reducing this cause of background. It was still sufficiently important that its change with time had to be considered.

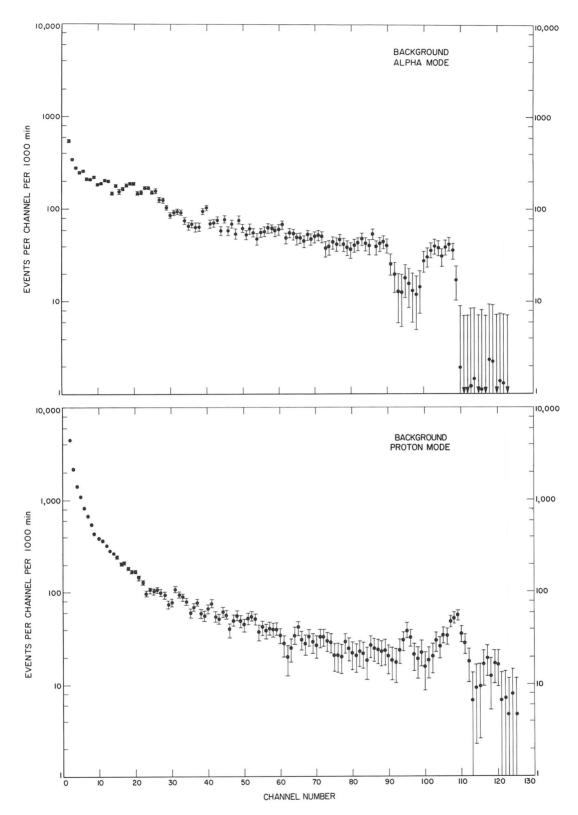


Fig. VIII-5. Results of background measurements on the moon. These data were taken on the Surveyor VII mission by the alpha-scattering instrument in the alpha and proton modes during the background phase of operations. The experimental points are shown with statistical (1σ) error bars. The data have been corrected approximately using the temperature coefficient of the instrument. The peaks at approximately channel 110 in both modes are due to Es²⁵⁴ placed near the detectors before launch.

The proton background rates in the main part of the spectrum were nearly the same as those in the Surveyor VI mission. In the overflow channel of the proton mode, the rates agree to better than 10% with those of Surveyor VI. This indicates that the flux of cosmic and solar protons in the energy range 50 to 150 MeV on the moon was the same at 40°S latitude at the time of the Surveyor VII mission as at the equator at the time of the Surveyor VI mission. The consistency of the background, together with the stronger sources used, meant that the signal-to-noise ratio in the proton mode during the sample measurements was significantly higher than in previous Surveyor missions.

2. Standard-Sample Data

Of the 5.2-hr of data accumulations while the instrument was still on the spacecraft, 5.0 hr have been certified by preliminary examination and have been corrected crudely for the temperature characteristics of the instrument. These data are plotted in Fig. VIII-6 in the usual units of events registered per channel per 1000 min as a function of channel number (energy). The ordinates are on a logarithmic scale with the statistical errors (1σ) indicated. Shown also is a smooth-curve version of the spectra observed in the subsequent, background, phase of the experiment (discussed above). The results in both alpha and proton modes are indicated.

Qualitatively, the data are similar to those observed in previous missions in the corresponding stages of the experiment. The higher source strength used in this mission leads to higher counting rates by about 70% and a better signal-to-background ratio, particularly in the proton mode.

The gross spectra also compare favorably (after appropriate background and instrumental corrections) with the pre-launch calibrations, which were performed at Cape Kennedy with the same sources but with a different standard sample and the electronic unit from a spare instrument. Specifically, the characteristic breakpoints in the alpha spectra, which were due to carbon, oxygen, silicon, and iron, are clearly visible in the gross spectrum as well as some of the features of the instrument response to silicon and sodium in the proton spectrum. As in previous missions, there was no evidence of radioactive contamination of the instrument, which would be caused by breakage of the thin, protective films over the sources during the spacecraft launch, transit, and touchdown conditions.

The data of Fig. VIII-6, after subtraction of the background, have been treated so far by preliminary calculational techniques only. These have included a library of only eight elements (C, O, Na, Mg, Al, Si, "Ca," and "Fe"), and only partial correction for detailed instrument characteristics. The calculational treatment was similar to that employed in the preliminary analyses of the *Surveyor V* and *VI* results (Refs. VIII-1 and VIII-2). An improvement was introduced, however, in programming the computer to correct, at least in first approximation, to the small differences in energy scale of the instrument as measured when on the moon and when the library of responses to individual elements was obtained.

The resulting representation of the standard-sample data in terms of the limited library is shown in Fig. VIII-7. The main features of both alpha and proton spectra are well reproduced. However, the energy scales have still not been matched adequately, and there are small systematic deviations between the calculated and observed data (such as in the alpha mode between channels 55 and 70) that appear to be outside of statistics and are not understood at present.

Table VIII-2 presents the resulting chemical analysis of the standard sample obtained under lunar conditions. Also shown, for comparison, are the results of a conventional chemical analysis of the glass part of the sample. Although the analysis under lunar conditions deviates somewhat more from the results by conventional techniques than desirable, it gives adequate assurance, at this stage of data analysis, that the instrument was in satisfactory condition to perform chemical analysis of lunar surface material.

Table VIII-2. Analysis of standard sample on Surveyor VII

	Percent of atoms ^a			
Element	Surveyor	Conventional		
	Total sample	Glass portion ^b	analysis of glass portion	
С	20.2	_	_	
0	44.0	55	59	
Na	8.0	10	8	
Mg	7.6	10	9	
Al	0	0	0	
Si	13.2	16	1 <i>7</i>	
"Ca"	0	0	0	
"Fe"	7.4	9	7	

a Excluding elements lighter than beryllium.

^bStandard sample was covered by a polypropylene grid. This column gives the analysis of the sample excluding the polypropylene.

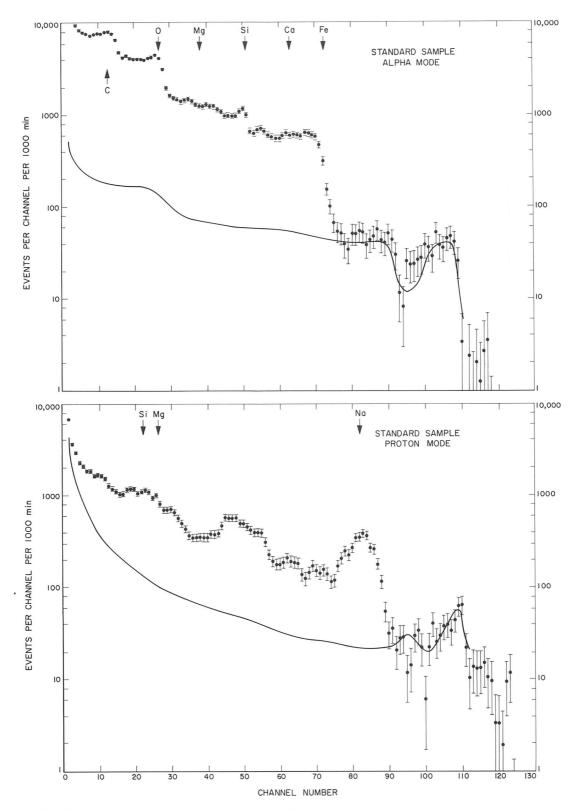


Fig. VIII-6. Results of standard-sample measurement on the moon. These data were obtained on the Surveyor VII mission by the alpha-scattering instrument in the alpha and proton modes during 5.0 hr of measurement of the standard sample after lunar landing. The experimental points are indicated with statistical (1σ) error bars. They have been corrected approximately using the temperature coefficient of the instrument. For comparison, the smooth curve shows the approximate magnitude of the background (Fig. VIII-5).

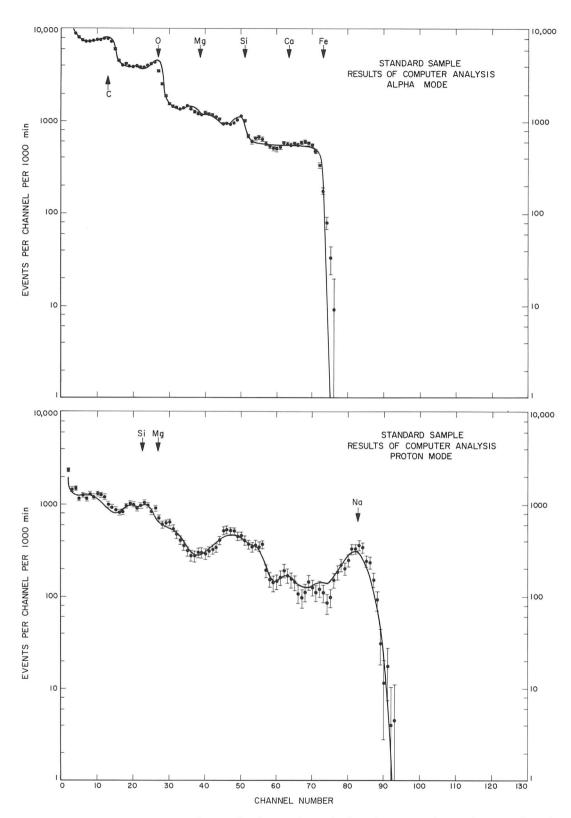


Fig. VIII-7. Computer analysis of standard-sample data. The calculated spectra (smooth curves), using an eight-element library, are compared with the data (points with 1σ error bars) taken during 5.0 hr of analysis of the standard sample on the Surveyor VII mission on the moon. The background (Fig. VIII-5) has been subtracted before the comparison is made.

3. Sample 1 Data

The first sample analyzed on the *Surveyor VII* mission was the relatively undisturbed lunar surface to which the instrument was finally deployed with the aid of the surface sampler. Measurements were made on this sample for about 27.4 hr both before and after lunar noon. From the data obtained before the instrument became too hot during lunar mid-day, those received during 11.2 hr have been examined in a preliminary way, and analyzed by first-cut calculational techniques, as described in Section VIII-C-2 of this Report.

The raw data from this period, corrected approximately to standard instrument response, are shown in Fig. VIII-8. The ordinates are in the usual units of events per channel per 1000 min, with statistical errors indicated. Shown also is the smooth curve version of the background observed while the instrument was still suspended over the lunar surface.

The gross features of both alpha and proton spectra are similar to those observed on the earlier *Surveyor* missions to the mare regions of the moon. This indicates that the chemical composition of this highland site cannot be very different from that in the maria. In particular, the higher signal-to-noise ratio in the proton mode on this mission makes clearly visible, even in the raw data, the presence of significant amounts of aluminum in the sample.

Computational analysis of the data of Fig. VIII-8 (after background subtraction), in terms of the standard library of eight elements, leads to the comparison with the observed data shown in Fig. VIII-9. In this treatment, the observed background was increased by 9.3 events per channel per 1000 min to correct approximately for the growth in the number of uncollimated alpha particles since the background measurement. Moreover, as in the treatment of the standard-sample data, the computer was programmed to shift the energy scales of the observed spectra very slightly to get the best match with the energy scale of the library. Figure VIII-9 shows that the synthesis out of the library spectra represents well the observed data. The main discrepancies at this stage of analysis appear to be the lack of sharpness in the oxygen and silicon peaks (at channels 27 and 49 of the alpha spectra) compared with that predicted from the library. Possible effects of the non-nominal sample geometry will be investigated at a later stage of analysis.

The results obtained in this way for the chemical composition of the first sample examined in the lunar highlands are presented in Table VIII-3. The composition is

Table VIII-3. Chemical composition of the lunar surface at the Surveyor landing sites: preliminary results

	Chemical composition, atomic percent ^a			
Element	Mare sites		Highland site	
	Surveyor V ^b	Surveyor VI ^c	Surveyor VII	
С	< 3	< 2	< 2	
0	58 ± 5	57 ± 5	58 ± 5	
Na	< 2	< 2	< 3	
Mg	3 ±3	3 ±3	4 ± 3	
Al	6.5 ± 2	6.5 ± 2	8 ±3	
Si	18.5 ±3	22 ±4	18 ±4	
"Ca"") "Fe" f	13 ±3 ^d	6 ± 2	6 ± 2	
"Fe" ^f ∫	13 13	5 ± 2	2 ± 1	

a Excluding elements lighter than beryllium.

expressed in atomic percent and normalized to include only elements heavier than lithium, since the instrument cannot detect hydrogen, helium, and lithium. In the present stage of analysis into only eight components, the "calcium" is to be taken as representing elements having masses in the approximate range of 30 to 47, and "iron" as representing those with masses between approximately 47 and 65. As in the reports on previous missions, at this stage of analysis, rather wide limits of errors are assigned to the results.

Table VIII-3 also shows, for comparison, the results found by the same technique on the first sample examined on the *Surveyor VI* mission, and the results from the *Surveyor VI* mission. It was concluded in the *Surveyor VI* report that the analyses of the samples at the two mare sites were essentially the same. The chemical composition at the *Surveyor VII* site, considering the errors assigned, is, in general, not strikingly different. There is no doubt, however, that the amount of the "iron" group of elements at the highland site is significantly lower, by about a factor of two, than at the two mare sites.

4. Sample 2 Data

The second sample analyzed on the *Surveyor VII* mission was a lunar rock that protruded a few centimeters above the originally undisturbed local lunar surface. With the help of the surface sampler, the alpha-scattering instrument was placed on this rock (see Fig. VIII-3a; also see Section V of this Report).

bSurveyor V results are from Ref. VIII-1.

CSurveyor VI results are from Ref. VIII-2.

dResults from Surveyor V, in this case, included both the ''Ca'' and the ''Fe'' groups. A lower limit for ''Fe'' was set at 3%.

e^{vv}Ca'' here denotes elements with mass numbers between approximately 30 and 47 and includes, for example, P, S, K and Ca.

f¹¹Fe'' here denotes elements with mass numbers between approximately 47 and 65 and includes, for example, Cr, Fe, Co, and Ni.

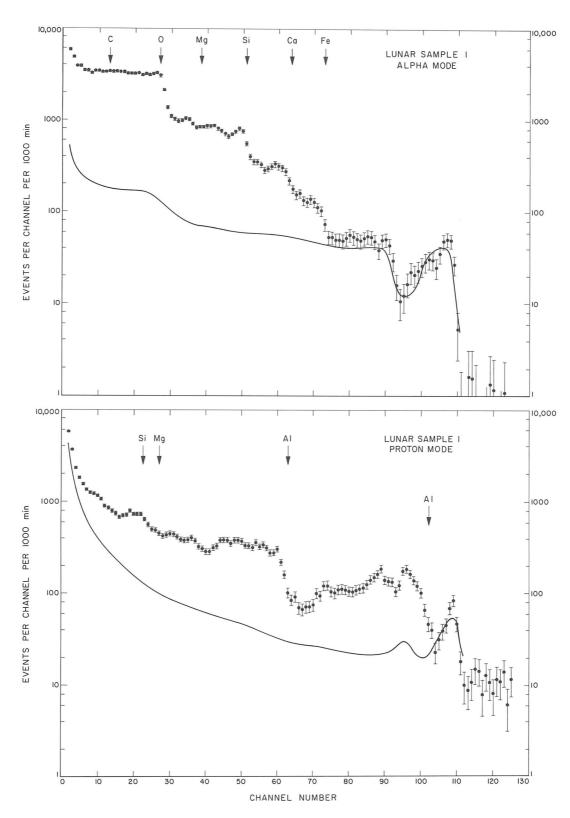


Fig. VIII-8. Surveyor VII lunar sample 1. These data were obtained by means of the Alpha-Scattering Experiment in the alpha and proton modes during 11.2 hr of measurement on the lunar surface. The experimental points are indicated with (1σ) statistical errors. The solid curve in each case is a smoothed version of the background observed in the previous stage of lunar operations.

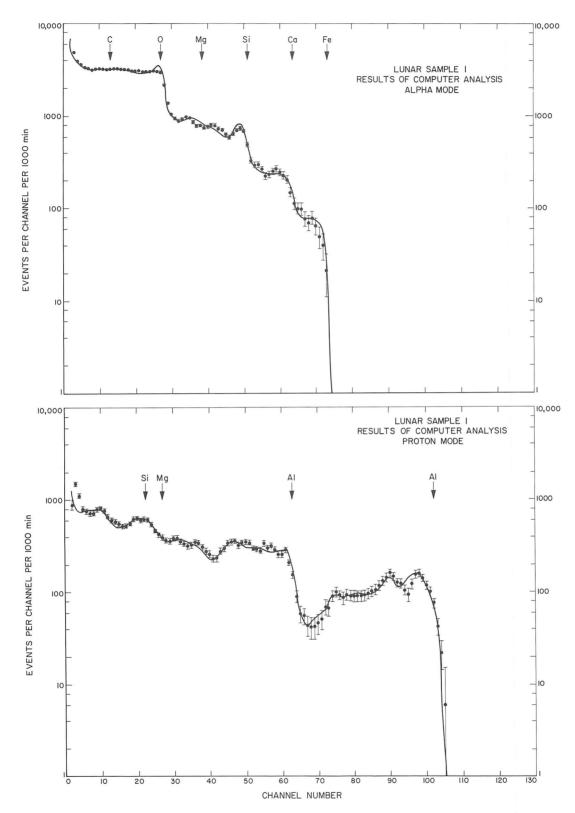


Fig. VIII-9. Computer analysis of Surveyor VII lunar sample 1 data. The calculated spectra (smooth curves), using an eight-element library, are compared with the data [points with (1σ) error bars] taken during 11.2 hr of analysis. The background (Fig. VIII-5) has been subtracted before the comparison is made.

In this position, about 10 hr of data were obtained (some with individual proton detectors). Because of the non-nominal geometrical relationship of the sample to the instrument (the rock definitely protruded into the sample opening of the instrument), the data show special characteristics which are not amenable to treatment by the crude techniques used in the analysis of data from sample 1. For example, the intensity of response in the proton mode, relative to that in the alpha mode, is much different in the case of the rock sample than in that of sample 1 or that of samples with close to nominal sample geometry. In addition, the proton spectra obtained from the rock show shifts of characteristic features to higher energies (from their positions in the spectra of sample 1) that are qualitatively understood, but not amenable to quantitative treatment at the present stage of analysis.

Thus, only qualitative statements will be made at present about the results obtained on the lunar rock. The chemical composition of this rock is not markedly different from that of the neighboring, undisturbed lunar material represented by sample 1. More specifically, the results from the proton mode definitely show the presence of aluminum in comparable amounts to those of sample 1. From the data in the alpha mode (which is much less subject to the geometrical considerations discussed previously), it can be concluded that the oxygen, silicon, and "calcium" contents of the rock are similar to those in sample 1.

The more quantitative calculational treatment of the entire data from this lunar rock will be supplemented, in the future, by laboratory studies to ensure that the geometrical effects (which can be simulated) are understood.

5. Sample 3 Data

Very little time (6.8 hr) was available for collecting data on the third sample (representing subsurface lunar material) before night fell at the *Surveyor VII* landing site. Fortunately, these data have been supplemented, in the alpha mode, by about 20 hr of data accumulated on the second lunar day. At the present time, all that can be said about this sample is that the gross chemical composition cannot be much different from that of sample 1. In particular, the lower "iron" content of sample 1 relative to that in mare material seems to be confirmed in this sample.

As in the case of the rock sample, it will be desirable to supplement the mathematical analysis of the sample 3

data by laboratory simulation studies, because of the unusual geometrical relationship of the sample to the instrument (see Fig. VIII-4).

D. Discussion

The preliminary results of the Alpha-Scattering Experiment on $Surveyors\ V$ and VI showed that the chemical composition of the two mare landing sites was essentially the same. This chemical composition was similar to that of some terrestrial basalts as well as to that of a rather rare type of meteorite, the basaltic achondrites. The chemical composition was unmistakably different from that of condensed solar atmospheric material or of terrestrial ultrabasic rocks such as dunite or of the great majority of meteorites (metallic or chondritic). It was also different from that of the acidic terrestrial rocks, such as granites, and that of tektites. The close similarity of the results of the two sites make it probable that many other mare areas of the moon will be found to have similar chemical compositions.

The Surveyor VII landing site was chosen to be as different an area as possible from the maria. Unfortunately, the highland regions of the moon, even though they represent the great majority of the lunar surface, show a much greater diversity in topography and optical properties than do the maria. Thus, the specific site chosen for the landing place of Surveyor VII, the ejecta blanket of the young crater Tycho, can, with much less confidence, be taken to represent the highland regions of the moon. Still, it shares with all of them the most prominent characteristics of a rougher topography and a higher albedo than those of the lunar mare regions.

The most complete analytical results from this mission (although still preliminary) are from the sample of undisturbed lunar material (sample 1). The chemical composition of this sample has been compared with that of the mare samples in Table VIII-3. It has been pointed out that, because of the large errors at present, the only significant difference between this highland sample and the mare samples is in the lower content of the iron group of elements.

Even this result might not be considered outside the limits of error of Table VIII-3; however, examination of the raw data confirms the reality of this difference. Figure VIII-10 shows, for both alpha and proton modes, a comparison of the relatively raw data from *Surveyors* V,

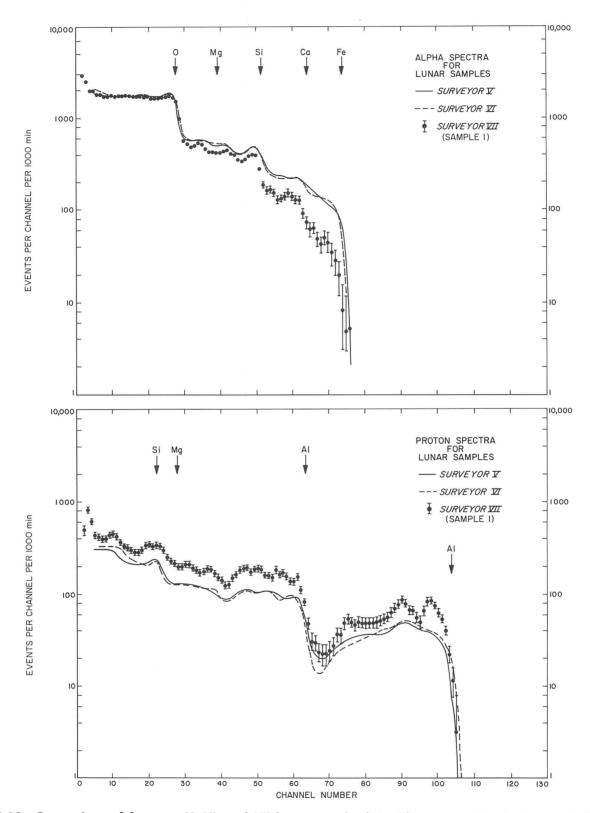


Fig. VIII-10. Comparison of Surveyor V, VI, and VII lunar sample data. The appropriate backgrounds have been subtracted. The Surveyor V and VII spectra are for the first samples from each of those missions. The data have been multiplied in both alpha and proton modes by factors that make them match in the oxygen region of the alpha mode.

VI, and VII. The data from the three missions (both alpha and proton) have been normalized to the oxygen region (alpha channels 8–25) to correct for differences in source strengths and sample distances. The appropriate backgrounds have already been subtracted in each case. The Surveyor V and VI data are represented by the smooth and dashed curves, respectively; those from Surveyor VII are indicated by the points with associated error bars.

In the alpha mode of Fig. VIII-10, it is seen that, though the data from the mare sites agree, those from Surveyor VII depart from the curves for the mare sites, particularly at the high-energy regions. The greatest difference is in the region of channels 65–73, which represents the contribution of the iron group of elements. The differences at lower channels are mostly a reflection of the different "iron" contribution. Thus, the basic data indicate a lesser amount of iron-group elements, on the order of a factor of two, at the highland site than at the mare sites.

The differences in the results from the proton mode (Fig. VIII-10) from the three missions are primarily in magnitude, rather than in spectral shape. These could be partially due to geometrical effects, and will be considered in detail at a later stage of analysis. Because the geometry would affect the results on the proton-producing elements, larger errors have to be assigned at this stage. The relative amounts of the major proton-producing elements (silicon, magnesium, and aluminum) appear to be not too different at the three sites.

As stated in Section VIII-C, cursory treatment of the data from the other samples examined on this mission supports the conclusion of general chemical similarity between the *Surveyor VII* surface material and that of the maria, except in the "iron" content.

Because of the gross similarity of chemical compositions, many of the conclusions made on the basis of the mare results (Refs. VIII-1 and VIII-2) apply at least to this particular highland site. In Fig. VIII-11, the chemical composition found for sample 1 is compared to the nonvolatile constituents of the solar atmosphere. As in Ref. VIII-1, the results have been normalized so that the silicon values agree. The relative amounts of magnesium, aluminum, "calcium," and now even "iron," do not agree with the solar ratios. Thus, none of the three *Surveyor* lunar landing sites examined by the alpha-scattering instruments have chemical compositions corresponding to that of condensed solar atmosphere.

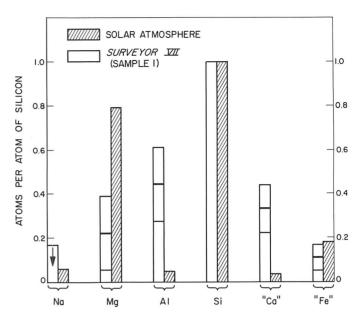


Fig. VIII-11. Comparison of the observed chemical composition of the Surveyor VII lunar sample 1 with that of the nonvolatile elements in the solar atmosphere. It has been assumed that the sulfur has escaped as hydrogen sulfide. The two compositions have been normalized so that the values of silicon are equal to 1. The solar values are from Ref. VIII-6.

As in Refs. VIII-1 and VIII-2, we can compare the results of the sample 1 analysis with those of various terrestrial and meteoritic samples. Of the innumerable comparisons of this type that can be made, six are shown in Fig. VIII-12. The correspondence with the chondritic (and, therefore, with ultrabasic terrestrial rocks) chemical composition is obviously poor. The composition of maretype material also did not correspond with chondritic composition. In the case of granites and tektites, there is (as in the case of the mare samples) not enough silicon and too much "calcium" in the sample examined by *Surveyor VII*, although now the "iron" abundances match better.

The agreement between the present results and the chemical composition of terrestrial basalts and of basaltic achondrites is better, although the lunar sample seems to have too little iron to match the average basalt content. A final comparison is made with the chemical composition of a terrestrial diorite. Here the "iron" matches, but the lunar sample has too much "calcium." It may be that, with the present results on only a limited group of elements and with large errors, comparison with only extreme types of terrestrial rocks is of significance.

Although the differences established between the chemical composition of the sample examined by *Surveyor VII*

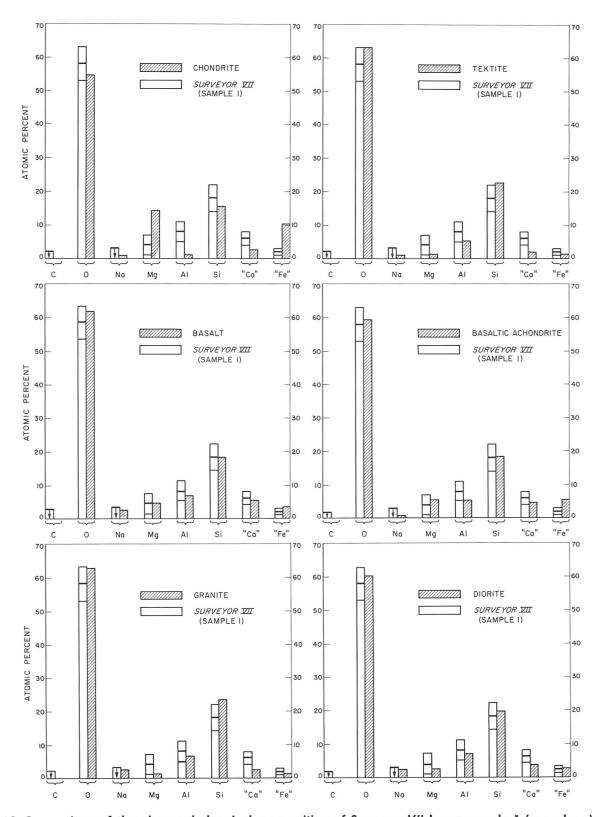


Fig. VIII-12. Comparison of the observed chemical composition of Surveyor VII lunar sample 1 (open bars) with the average composition of selected materials (cross-hatched bars). The diorite and basaltic achondrite values are from Ref. VIII-7; the basalt values are for Continental basalts from Ref. VIII-8; the granite values are for the North American Crust from Ref. VIII-9; the chondrite values are the averages of the low-iron group from Ref. VIII-10; the tektite values are those for the Indo-Malayan body quoted in Ref. VIII-7.

and the mare samples examined by earlier *Surveyors* is confined to the lower content of the "iron" group of elements at the highland site, this difference could be significant if it applies generally to the highland regions on the moon. It should be remembered that the "iron" group, at the present stage of data analysis from this experiment, includes the elements titanium, vanadium, chromium, manganese, iron, cobalt, nickel, and copper. These include elements which, in general, impart color to rocks. Terrestrial rocks that have more of these elements are usually darker and, therefore, at least in bulk form, have a lower albedo than do rocks with smaller amounts of these elements (see Fig. VIII-13).² Thus, although there are several

²We are indebted to Dr. Alden Loomis and Mr. Douglas B. Nash, JPL, for the use of the series of rocks shown in Fig. VIII-13.

possible reasons for the higher albedo of the highland regions of the moon relative to that of the maria, the lower content of the "iron" group of elements, as found in the *Surveyor VII* samples, may be a contributing factor.

Similarly, the lower "iron" group content of the Surveyor VII samples, if it is characteristic of highland regions in general, probably means that the bulk density of the subsurface rocks of the highland regions is less than that of comparable material in the maria. In this case, the very gross topographical relationships of the lunar crust would be similar to those of the planet earth, where, in general, the continental highlands are composed of material less dense than the basaltic ocean bottoms.

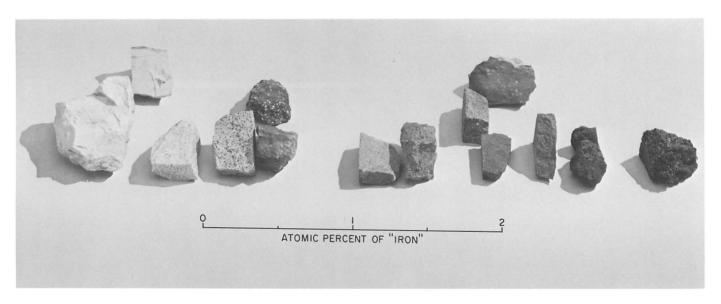


Fig. VIII-13. A series of terrestrial rocks, arranged according to the concentration of elements of mass number 47 < A < 65. In order of increasing concentration of these elements, the rocks are: aplite, 0.2%; Bishop tuff, 0.5%; Rocklin quartz monzonite, 0.8%; granodiorite, 1.2%; Lassen 1917 dacite, 1.2%; Puu Hulu trachyte, 1.3%; diorite, 2.2%; Mehrten andesite, 2.4%; quartz diorite, 2.8%; meta-basalt, 3.0%; Little Lake basalt, 3.1%; San Marcos gabbro, 3.3%; Pisgah basalt, 3.6%; 1960 Kilauea basalt, 4.1%.

References

- VIII-1. Turkevich, A. L., Franzgrote, E. J., and Patterson, J. H., "Chemical Analysis of the Moon at Surveyor V Landing Site: Preliminary Results." Surveyor V Mission Report. Part II: Science Results, Technical Report 32-1246, pp. 119–149, Jet Propulsion Laboratory, Pasadena, Calif., November 1, 1967. Also, "Chemical Analysis of the Moon at the Surveyor V Landing Site," Science, Vol. 158, No. 3801, pp. 635–637, 1967.
- VIII-2. Turkevich, Anthony L., Franzgrote, Ernest J., and Patterson, James H., "Chemical Analysis of the Moon at Surveyor VI Landing Site: Preliminary Results," Surveyor VI Mission Report. Part II: Science Results, Technical Report 32-1262, Jet Propulsion Laboratory, Pasadena, Calif., pp. 127–153, 1968. Also in Turkevich, Anthony L., Patterson, James H., and Franzgrote, Ernest J., "Chemical Analysis of the Moon at Surveyor VI Landing Site: Preliminary Results," Science, Vol. 160, No. 3832, pp. 1108–1110, 1968.
- VIII-3. Patterson, J. H., Turkevich, A. L., and Franzgrote, E. J., "Chemical Analysis of Surfaces Using Alpha Particles," *J. Geophys. Res.*, Vol. 70, No. 6, pp. 1311–1327, 1965.
- VIII-4. Turkevich, A., Knolle, K., Emmert, R. A., Anderson, W. A., Patterson, J. H., and Franzgrote, E., "Instrument for Lunar Surface Chemical Analysis," *Rev. Sci. Inst.*, Vol. 37, No. 12, pp. 1681–1686, 1966.
- VIII-5. Turkevich, A. L., Knolle, K., Franzgrote, E., and Patterson, J. H., "Chemical Analysis Experiment for the *Surveyor* Lunar Mission," *J. Geophys. Res.*, Vol. 72, No. 2, pp. 831–839, 1967.
- VIII-6. Urey, H. C., "The Abundance of the Elements With Special Reference to the Problem of the Iron Abundance," *Quart. J. Roy Astron. Soc.*, Vol. 8, pp. 23–47, March 1967.
- VIII-7. Palm, A., and Strom, R. G., Space Sciences Laboratory Research Report, Series 3, Issue 5, University of California, Berkeley, Calif., 1962.
- VIII-8. Turekian, K. K., and Wedepohl, K. H., "Distribution of the Elements in Some Major Units of the Earth's Crust," *Geol. Soc. Amer. Bull.*, Vol. 72, pp. 175–192, 1961.
- VIII-9. Condie, K. C., "Composition of the Ancient North American Crust," Science, Vol. 155, pp. 1013–1015, 1967.
- VIII-10. Urey, H. C., and Craig, H., "The Composition of the Stone Meteorites and the Origin of Meteorites," *Geochim. et Cosmochim. Acta.*, Vol. 4, pp. 36–82, 1953.

Acknowledgment

When the deployment mechanism on Surveyor VII did not lower the sensor head of the alpha-scattering instrument to the lunar surface upon command, a concerted effort to solve the problem was made by many members of the Surveyor Program at NASA, JPL, and HAC. The procedures that were eventually used to rescue the sensor head were devised by members of the Investigator Team on the Soil Mechanics Surface Sampler Experiment: Dr. Ronald F. Scott, Caltech, and Mr. Floyd Roberson and Mr. Maurice Clary, JPL. The surface sampler was also used to provide shade for the sensor head when there was danger of reaching too high a temperature. In addition to these unscheduled operations, the plans to use the surface sampler to move the sensor head from one location to another on the lunar surface were successfully carried out. Special thanks are due to Mr. Roberson for his expert manipulation of the surface sampler and to Dr. Scott and Dr. Eugene Shoemaker, U. S. Geological Survey, for relinquishing time from the Surface Sampler and Television Experiments so that the chemical analyses could be performed.

The Alpha-Scattering Experiment on the *Surveyor VII* mission has been the product of the work of many organizations and people. In addition to the authors, at the Enrico Fermi Institute of the University of Chicago, Mr. Ed Blume, Mr. Tom Economou, Mr. Ken Sowinski, and Mr. Bernd Wendring participated in the final tests and calibration of the instrument and in mission operations supporting the experiment.

The Laboratory of Astrophysics and Space Research, also at the University of Chicago, in addition to constructing the instrument, provided extensive support for the final testing and calibration of the instrument at Cape Kennedy, Fla., and mission support, especially via Mr. Wayne Anderson and Mr. Gene Drag. The detector status was continually monitored by Dr. Anthony Tuzzolino.

At the Argonne National Laboratory, Mr. Harry E. Griffin, Mr. Michael A. Essling, and Mr. Dale Henderson prepared and tested the curium and einsteinium alpha radioactive sources used. Mr. Dale Suddeth provided electronic support during the final calibration and during mission operations.

At the Jet Propulsion Laboratory, Mr. Robert Holman, Mr. Henry Giunta, Mr. Charles Fondacaro, and Mr. William Seeger participated in the final tests and calibration of the instrument at Cape Kennedy. Mr. James Carneghi, Mr. Carl Heinzen, Mr. Robert Imus, Mr. George O. Ladner, Jr., and Mr. Richard E. Parker provided support in controlling the instrument during mission operations, under the direction of Mr. Jack Lindsley and Mr. Donald D. Gordon. Dr. Stanley L. Grotch supervised the real-time calculational monitoring; computational support was provided by Mrs. Sally Rubsamen and Mrs. Margaret Simes.

IX. Lunar Theory and Processes

D. E. Gault (Chairman), J. B. Adams, R. J. Collins, G. P. Kuiper, H. Masursky, J. A. O'Keefe, R. A. Phinney, and E. M. Shoemaker

Whereas the previous Surveyor missions were undertaken to examine mare surfaces as potential landing areas for the Apollo Program, the primary objective of the Surveyor VII mission, based on purely scientific motivations, was to explore a contrasting highland region and, specifically, to determine the chemistry of the highland material for comparison with the Surveyor V and VI chemical analyses at the mare sites. Site selection was limited to some extent by Surveyor operational constraints, but primarily by the requirements of 10-mresolution photographs from the Lunar Orbiter Program for landing site certification. None of the nine sites studied in detail appeared capable of providing an unambiguous answer to the highland chemistry. The final selection of a site to the north of Tycho was based on the belief that the youthful character of the structure implied a minimum of contamination to the surface layers by foreign material via meteoritic processes. Moreover, the selection of a site near the rim of a major lunar crater promised insight into the "microscale" properties of a structure that represents the dominant morphologic feature on the moon.

The discussion here is divided into three parts. Because the interpretations of the results are dependent on the relationship of the landing site to the moon in general, and to the highlands in particular, a description of the regional and local geologic setting is given first; this description is then followed by a discussion of the results and implications from the Alpha-Scattering Experiment. Comments on the surface features and processes are considered last.

A. Geologic Setting

Surveyor VII landed north of the rim of the crater Tycho, a large bright-halo crater in the southern highlands of the moon. The crater is about 85 km in diameter and about 5 km deep. The crater shape, hummocky ejecta blanket, and extensive rays of secondary craters, indicate that the crater was formed by hypervelocity impact, as first suggested by Gilbert 75 yr ago (Ref. IX-1). The ray system, which extends for more than 1800 km, or 20 crater diameters (Figs. IX-1 and IX-2), is inconsistent with a volcanic origin. Magmatic gas pressures measured terrestrially and extrapolated to the moon are probably insufficient to throw projectiles to the observed distances. Of the proposed mechanisms for the crater origin, only hypervelocity impact can generate sufficient pressures to accelerate ray material to the required velocities.

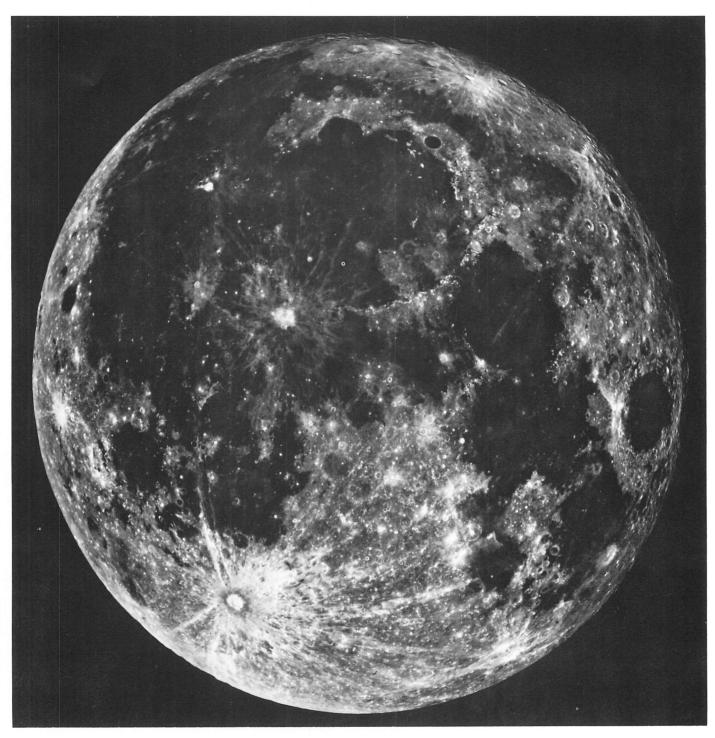


Fig. IX-1. Near-full moon photograph showing the conspicuous radial ray system and concentric albedo rings of Tycho (photograph by courtesy of U. S. Naval Observatory, Flagstaff, Arizona).

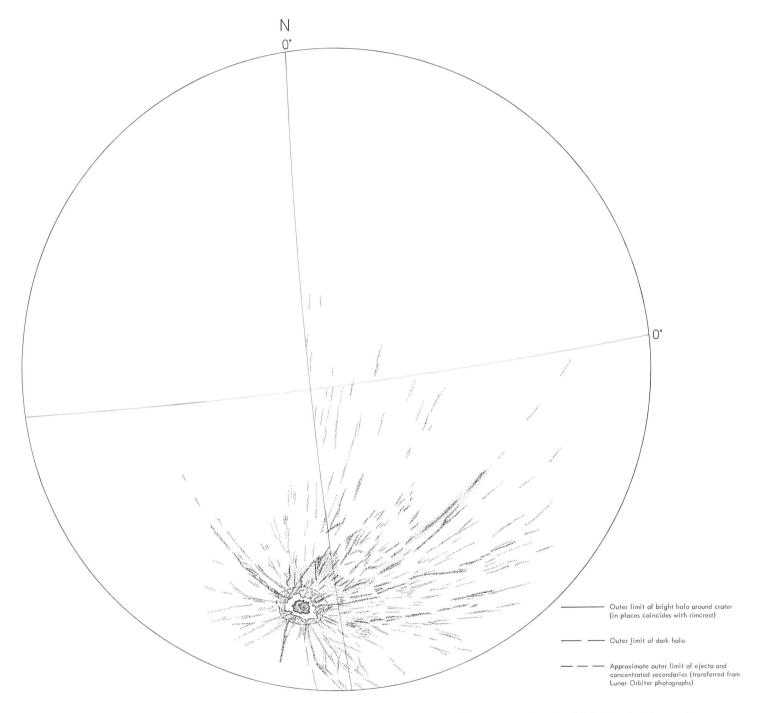


Fig. IX-2. Map delineating the principal albedo features relating to Tycho, as seen in Fig. IX-1. The bright regions are indicated by stipple; the stipple density is proportional to brightness.

The interpretations of this major lunar structure are diverse and open to many subjective decisions. Shoemaker (see Section III of this Report) interprets Tycho as an impact crater and attributes all the geologic units revealed in *Lunar Orbiter* photographs to various processes accompanying the impact event. A diametrically opposite point of view is given by Green, who interprets Tycho as a possible caldera. Intermediate interpretations involving impact and impact-triggered volcanism have also been suggested, and are included here to give a complete spectrum of the overall uncertainties concerning the geology of Tycho. The differences are, of course, fundamental to the interpretation of the chemical analysis.

The distribution of geologic units mapped by Masursky and associates¹ at a scale of 1:375,000, based on *Lunar Orbiter V* medium-resolution photographs and combined with albedo values from earth-based, full-moon photographs, is shown in Fig. IX-3. Units are shown which compose the bright, outer ejecta blanket (parts of the satellitic crater field); the intermediate ring of relatively smooth, darker deposits (several radial, flowlike units); the innermost ring of bright, mostly rugged units near the crater rim (concentrically lineated and hummocky rim and the leveed flows); the wall, floor, and central peak materials inside the crater.

A reproduction of the Lunar Orbiter V coverage of Tycho, medium-resolution frame 126, is shown as Fig. IX-4, with outlines of Figs. IX-5 through IX-8. Figure IX-5 presents the distribution of units for the interpretation given in Fig. IX-3 at a smaller scale of 1:60,000 for the north rim of the crater where the spacecraft landed. Several successive lobate flow units are interpreted to overlie the ejecta blanket with its rolling topography and secondary crater rays. The map is based primarily on Lunar Orbiter V high-resolution frame 128. Details in the vicinity of the spacecraft, based on an enlarged print of this frame, are shown in Fig. IX-6 at a still smaller scale of 1:8.000. The spacecraft is situated near what is considered to be the transitional boundaries of the outermost flow unit that overlies the continuous ejecta blanket. It is believed that the flows overlie, and are of a later period than, the continuous ejecta blanket. The flows have moved outward down the rim slope and inward down the crater wall. Three modes of origin have been proposed:

(1) The flows are part of the impact event and represent fluidized, suevite-like masses that overlie the continuous ejecta blanket.

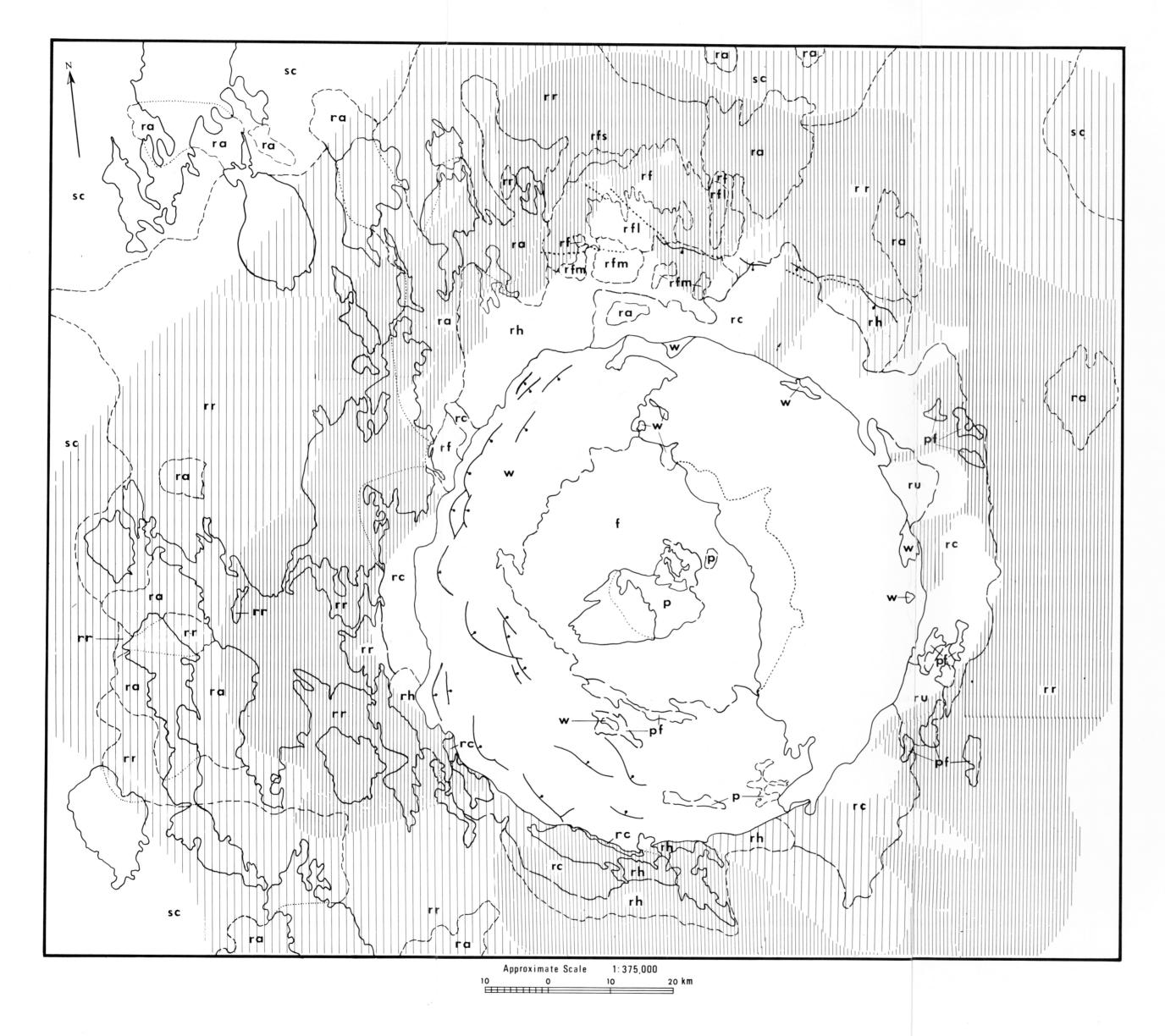
¹R. S. Saunders and D. E. Stewart-Alexander.

- (2) The flows are impact-generated, volcanic flows that continued erupting for some time after the event.
- (3) The flows are mass-wasting phenomena that represent movement of ejecta material much later and in a cold state down the sloping crater rim, activated by gravity, but triggered by seismic events.

A different interpretation of the Tycho region and the Surveyor VII landing site is proposed by Kuiper and associates.2 Regions considered to be major flows are mapped in Figs. IX-7 and IX-8 (see Fig. IX-4 for reference to Lunar Orbiter frame M-126). Figure IX-7 shows all craters more than 50 m in diameter and numerous fractures, particularly in the area surrounding the large crater in unit C; the location of the spacecraft is indicated. What is interpreted as the most recent flow is mapped in Fig. IX-8 as two lobes which, in Fig. IX-9, are seen to be part of the bright halo immediately surrounding the crater. These bright lobes protrude into the dark halo, which is thought to consist of a succession of flows. Numerous lava "lakes" are identified, several within the boundaries of Fig. IX-8, and some of these are clearly connected with adjacent flows on higher terrain. Counts of craters down to 25 m in diameter indicate that the average age of some 40 to 50 lava lakes around Tycho is similar to that of the crater floor. However, craters on the flows are more numerous by a factor of 1.8 on the average. Although this would seem to indicate that the lakes are more recent than the flows, Kuiper, et al. do not believe this true for the large lake 1 km northeast of Surveyor VII because they interpret the flow reaching the lake as protruding partly over its original surface. On this basis, therefore, the flow is considered to be more recent than the lake, the lake more recent than the Tycho impact, and the lake cannot consist of a mass ejected from Tycho during its formation.

The different flow units mapped in Fig. IX-8 show large differences in surface texture as to frequency and distribution of fractures, ridges, and roughness of terrain. These differences are thought to point to the separate origins for the flows rather than to part of a single major mass movement produced by the formation of Tycho. This conclusion is consistent with the time sequence noted before: Tycho \rightarrow lake \rightarrow flow. A study of the Aristarchus slopes, which are very similar to those of Tycho, leads to the same development pattern. Each crater is believed to have resulted probably from a major impact followed by extensive volcanism both on its crater floor and on its outer slopes.

²R. G. Strom, E. A. Whitaker, and G. Fielder.



pf Pond fill

Characteristics

Generally smooth, level material filling low areas. Blocks protrude through some areas; some exhibit a ropy texture. Slightly domed and terraced in places

Interpretation

Probably debris flow; may be volcanic

ra

Rim, angular

Characteristics

Landforms on high-resolution photographs are angular and irregular, characterized by sharp breaks in slope. Has small local lobes and mounds. Few blocks visible. The dominant radial pattern consists of grooves and ridges. An irregular cross pattern of ridges and a few mounds occurs within the grooves and is more conspicuous on moderate resolution than high. Larger mounds are superposed on the pattern

Interpretation

Early-stage ejecta, probably suevite. Differences in surface textures compared to rr probably are due to minor variations in fragment size, temperatures, percent of molten material, or other factors

Rim flows

Large, subparallel, anastomosing lobes surrounded by relatively level, but highly fissured surfaces. The reticulate fissure pattern is visible only on high-resolution photographs. Blocks present locally. Many lobes emanate from unit rfl. Relatively few craters

Interpretation Probably volcanic flows; alternatively may be debris flows

Rim, radially lineated

Characteristics

Radial pattern is dominant: in places seems superposed on a concentric pattern. Ejecta fragments are visible near crater in moderate resolution and become increasingly finer outward from the crater

Interpretation

Debris deposited by base surge. Concentric pattern in part "dunes" formed by piling up of fine ejecta and in part fractures

sc

Satellitic crater field

Characteristics

Areas of high density of 2 to 4 km subdued craters. Some craters elongate.

Interpretation

Secondary craters and debris formed by ballistically ejected fragments; part. filled by slightly later base surge material

rfm

Rim flows and mounds

Large, dome-like mounds alternating with ponds and elongate, reticulated flow lobes. Ponds are similar to those of unit pf, but are smaller; flow lobes are similar to unit rf. Ponds nearest unit rfl are generally ropy and coarse-textured; ponds nearer rim crest are generally smoother

Interpretation

Volcanic domes and flows and debris flows

rh

Characteristics

Coarse hummocks (> 1 km) or mound-like topography with interspersed, smaller smooth areas and localized flow-textured topography. Most mounds appear relatively smooth and rounded. High-resolution photographs show blocks on most of unit

Interpretation

Mounds may be large ejecta blocks that are partly covered by finer ejecta; flowlike areas may be partially mobilized suevite or later debris flows. Grades outward to unit rr

rc

Rim, concentrically lineated

Characteristics

Uneven series of ridges and grooves forming a strong pattern concentric to crater.

Blocks clearly visible on high-resolution photographs; the largest blocks just discernible at moderate resolution.

Interpretation

Relatively large discrete rock masses thrust outward or nearly in place; may include overturned ejecta. Concentric pattern probably fractures along which some movement has occurred.

rfl

Rim flows and levees

Alternating prominent, elongate, smoothtextured ridges and lumpy, highly textured depressions

Interpretation

Thick piles of material that formed channels and levees during flows. Best developed examples are probably volcanic; others may

rfs

Rim flows, smooth

Relatively smooth, nonfissured area adjacent to unit rf that terminates outward (away from crater) in lobes

Interpretation

Similar to those of unit rf, but older

Rim, undivided

Characteristics Surfaces near the rim crest that are covered only by moderate-resolution photographs and appear smooth in them. Unit interrupts the concentric pattern. Some blocks are visible

ru

Albedo units

Moderate

Interpretation

Covering materials, perhaps base surge or debris flow

Floor

Characteristics

Mounded, blocky, and highly fissured

Interpretation

Suevite, mixed breccia of highly shocked rock fragments and shock-melted rocks. Individual fragments mostly small (submillimeter to decimeter), but welded into cohesive mass. Texture may be in large part pumiceous. Surface mounds are produced by irregular flow patterns; fissures are produced on cooling or compaction Unlettered areas are in shadow on Lunar Orbiter V photographs

• · · · · · · · Fault; bar and ball on downthrown side; dotted where buried

Contact; long dash where approximate; short dash where gradational; dotted through shadowed areas

Wall

Characteristics

Series of arcuate benches inside rim crest with unevenly distributed mounds, blocks, and minor smooth patches

Interpretation

Slumped rim materials, talus, and local deposits of fallback. Smooth patches may be mass wasted debris or volcanic material

р

Characteristics Rugged peaks and hills near center of

Interpretation

Underlying rocks brought to surface by rebound. Rebound may be due to gravitational recoil, decompression of rock, shock wave rarefaction, or a combination of these

Fig. IX-3. Geologic map of the Tycho region at a scale of 1:375,000, based on Lunar Orbiter V medium-resolution photographs (geology by H. Masursky and associates).

Fig. IX-4. A reproduction of Lunar Orbiter V coverage of Tycho, frame M-126, with outlines of Figs. IX-5 through IX-8.

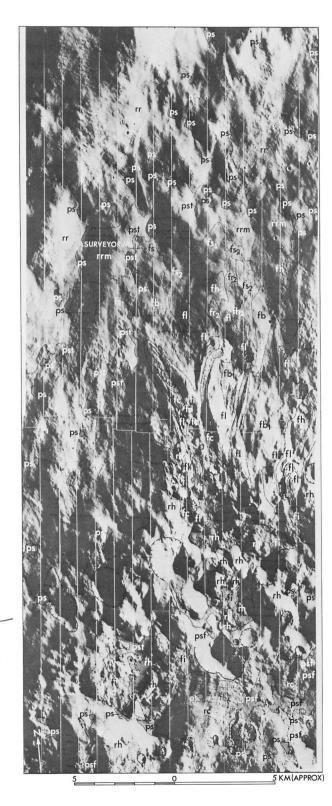


Fig. IX-5. Geologic map of the north rim of Tycho at a scale of 1:60,000, based on Lunar Orbiter V frame H-128 (geology by H. Masursky and associates).

Contact or flow front in flow units. Where dashed, contact is approximate and flow front is inferred







Circular to irregular depressions.

Dashed or incomplete where not well developed

fc

Flow channel material

Material between levees (fl) on large flow lobes. Fractured. Probably solidified molten material

fl

Flow levee material

Forms ramparts which bound the channels of the larger flow lobes. Range from about 500 m wide and 4 km long to only a few meters wide and several hundred meters long. Some show evidence of several outlets which have been sealed as the flow progressed



Flow materials, late

Flow surfaces with low crater density in comparison with surrounding areas. fs₂ has a smooth but not necessarily

planar surface. fh₂ surface is covered with small irregular hills (5 to 10 m) and many blocks. fb₂

has more blocks than fs₂ but a generally smooth surface. fr₂ is

covered with low, rope-like mounds which resemble the pressure ridges seen on some terrestrial flows. All the units are gradational into each other. Textures tend to grade down-slope from ropy to hummocky to smooth. These relations might be obtained in a lava flow, a debris flow, or a suevite-like mixture of molten and particulate material; the smoother distal flows would represent the more fluid fraction

Flow material, irregular

Flows with irregularly fractured surfaces. Flow fronts are generally high and abrupt. Formed of viscous material, either lava or suevite-like material



Flow materials, early

Flows with crater density about equivalent to the radial rim material. The flow features are more subdued than on the later flow material. fs₁ is smooth with abundant blocks. fh₁ has a hummocky, blocky surface and fb₁

has a blocky irregular surface. Unit fb₁ is gradational with unit rh. All the units typically have a superimposed reticulate fracture pattern. The material was probably emplaced as a flow after formation of the crater Tycho. The material may be fluidized ejecta similar to suevite



Flow dome material

Low, circular domes approximately 300 m in diameter on channel floor (near map center). May be tumuli on lava channel

ps pst psf

Pool material, smooth

Occupies low areas. Generally planar surfaces and well defined contacts with surrounding material. pst, thin pool material with blocks and protrusions of subjacent material. psf has structural features such as scarps and depressions. Some pools are connected by channels or have channels leading into them. Craters on the pools are generally irregular with many blocks. Probably a dense solid material such as basalt which came up from local vents



Rim material, hummocky Radial rim .material,

Terrain characterized by rounded irregular
hummocks up to 1 km across and circular
rimless unfilled depressions. Most hummocks
have abundant blocks. Hummocks may be
covered ejecta blocks. Depressions appear to
be collapse features and may indicate withdrawal
of fluid material, some of which formed the
surrounding fi unit

Occurs at the
(units fb₁, fs
rim, the
structures, ci
rim, which ar
than similar f
be thinly man
which accomp



Radial rim material, thinly mantled

Occurs at the distal ends of the flows (units fb₁, fs₁, fh₁, fs₂) but inside unit rr. The surface has dune-like structures, circumferential to the Tycho rim, which are slightly more subdued than similar features in unit rr. May be thinly mantled by particulate material which accompanied the flows. The subjacent material is probably fine Tycho ejecta



Rim material, radial

Outer rim unit covered with dune-like structures tangential to the Tycho rim. One strong lineation trends approximately NE and a second NNW. The material is probably fine ejecta deposited by base surge. The dune features may be deceleration dunes localized at concentric fractures in the underlying material



Rim material, concentric

Strong concentric lineation of discontinuous low ridges arranged as steps facing the creter rim. The material is probably thinly mantled bedrock. The ridges may be produced by faults

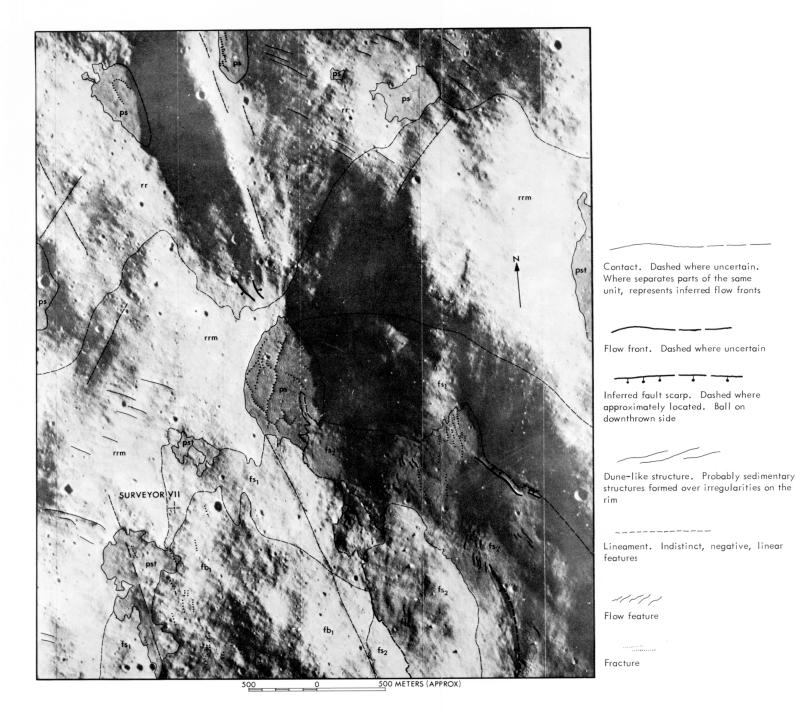


Fig. IX-6. Geologic map of details in the immediate vicinity of the Surveyor VII landing site at a scale of 1:8,000 (geology by H. Masursky and associates).

277

JPL TECHNICAL REPORT 32-1264

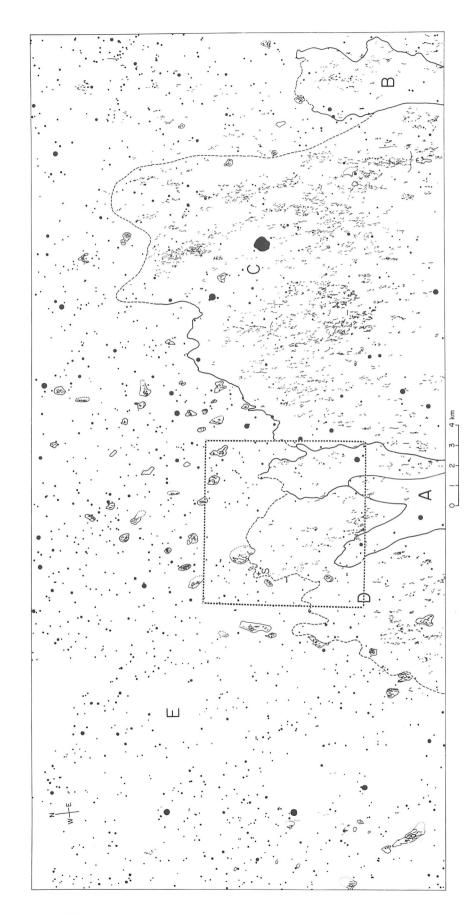


Fig. IX-7. Preliminary map and crater distribution of the central portion of Lunar Orbiter frame H-128. The filled circles are eumorphic craters more than 50 m in diameter, and the fine lines are fractures. The square, dashed outline is the area mapped in detail in Fig. IX-3 (geology by R. G. Strom).

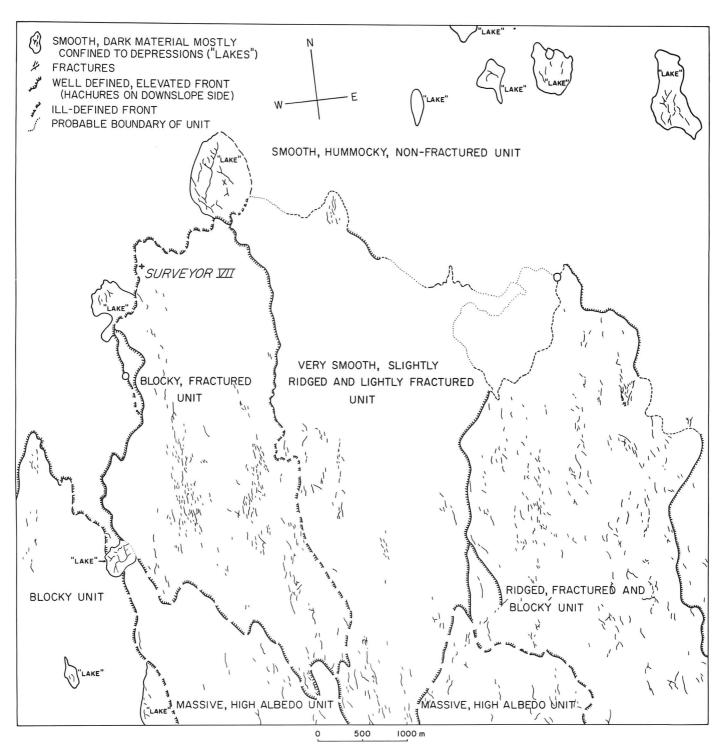


Fig. IX-8. Preliminary geologic map of Surveyor VII landing site (geology by R. G. Strom).

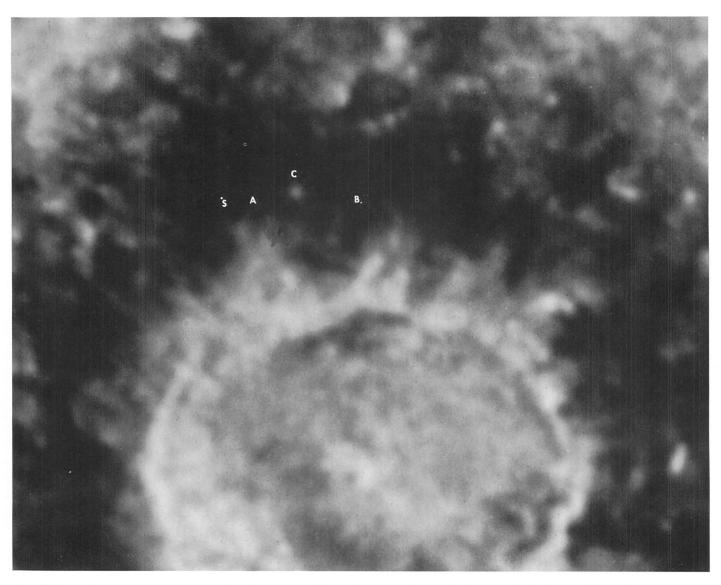


Fig. IX-9. Full-moon appearance of Tycho surroundings. The fork-shaped white patch below and left of A is unit A in Fig. IX-7 and the "massive high albedo unit" in Fig. IX-8. The elongated white area left of B is unit B in Fig. IX-7. The circular, bright patch below C is the largest crater on unit C in Fig. IX-7, and the S in the dark area is the approximate location of Surveyor VII (photograph by courtesy of U. S. Naval Observatory, Flagstaff, Arizona).

Additional evidence in support of this second interpretation is offered by the lava lakes near Tycho that have a meniscus-type surface, which is suggestive of a flow front, characteristic of lava flows. Sometimes the wall of the lake is breached, and minor fan-shaped flows result outside the breach. The sources of the flows themselves, while not obvious in all cases, are believed, in some instances, to be clearly associated with craters whose walls are breached in directions away from the central crater, with the flows issued through these breached walls. The same pattern is observed even more clearly on the Aristarchus slopes. It is not considered probable that these sources are impact craters, primary or secondary. The detailed structures of the walls are quite unlike those of impact craters, and their distribution on the Tycho (and Aristarchus) walls is peculiar, very far from random either radially or in azimuth. The sources are interpreted as appearing definitely volcanic.

In summary, the evidence derived from combining Lunar Orbiter V photographs and Surveyor VII pictures lead Kuiper and associates to believe that Surveyor VII landed on a lava flow that originated on the outer slope of Tycho sometime after the formation of the large crater.

This interpretation, in contrast to that offered by Shoemaker (see Section III of this Report), Masursky and associates, and Green clearly emphasizes that, while the chemical analysis at the *Surveyor VII* landing site refers to highland material in the broadest sense, it is not necessarily an "average" composition; care must be exercised in evaluating its significance to the moon and the processes active within it.

B. Discussion of Chemical Analyses

Preliminary results from the Alpha-Scattering Experiments on Surveyors V, VI, and VII are given in Table IX-1. For each of the elemental abundances, an error bar has been given; this error bar involves both the counting statistics and estimates of the uncertainties inherent in this preliminary stage of data reduction. In discussing the analyses, one must consider various compositions that lie within the given error bars. We point out here the problem involved in taking model compositions for which many of the elements lie at the extremes of their permitted ranges. If the likelihood of a single element at an extreme value is, say 0.1, then the joint likelihood that two elements so behave is 0.01, and so on. One may,

Table IX-1. Comparison of preliminary chemical analyses from Surveyors V, VI, and VII with representative rocks

	Element, atomic percent ^a							
	С	0	Na	Mg	AI	Si	"Ca'' ^b	''Fe'' ^b
Surveyor V (Ref. IX-4)	< 3	58 ± 5	< 2	3 ±3	6.5 ± 2	18.5 ±3	13 :	± 3
Surveyor VI (Ref. IX-5)	< 2	57 ± 5	< 2	3 ±3	6.5 ± 2	22 ±4	6 ± 2	5 ± 2
Surveyor VII (sample 1; see Section VIII of this Report)	< 2	58 ± 5	< 3	4 ± 3	8 ± 3	18 ±4	6 ± 2	2 ± 1
Chondrites								
LL group (Ref. IX-6)	_	58.0	0.7	15.2	1.0	16.0	1.0	8.1
Carbonaceous (type 1; Ref. IX-6)	6.6	55.4	0.6	8.4	0.7	8.4	12.3	7.8
Eucrites (Ref. IX-7)	_	60.7	0.5	3.6	5.7	18.8	4.2	6.9
Howardites (Ref. IX-7)	_	60.3	0.4	7.1	4.6	18.5	3.1	5.8
Dunite (Ref. IX-8)	_	59.0	0.1	23.9	0.3	14.1	0.2	2.3
Peridotite (Ref. IX-8)	_	58.9	0.4	19.3	1.9	15.5	1.4	2.5
Anorthositic gabbro (Ref. IX-9)		61.4	2.6	1.2	9.4	19.0	4.4	1.7
Basalt (tholeiitic)								
Average oceanic (Ref. IX-10)		61.3	1.5	4.1	6.3	18.1	4.5	4.3
Average continental (Ref. IX-10)	_	61.5	1.7	3.2	7.0	18.8	4.3	3.7
Basalt (alkalic)								
Average oceanic (Ref. IX-10)	_	60.8	2.1	3.8	6.7	17.2	4.8	4.3
Average continental (Ref. IX-10)	_	60.8	2.4	3.9	6.8	17.2	4.8	3.9
Andesite (Ref. IX-11)	_	61.2	2.9	0.1	6.9	21.1	3.1	3.0
Granite (Ref. IX-7)	_	63.4	2.3	0.4	5.9	24.4	2.7	1.0
Tektite (Indo-Malayan; Ref. IX-12)	_	64.0	1.0	1.1	5.4	25.2	3.4	1.5

^aExcluding elements lighter than beryllium.

b"Ca" and "Fe" denote elements with mass numbers between approximately 30 to 47 and 48 to 65, respectively.

therefore, ignore model compositions for which several elements are taken near the error limits.

Some rock and meteorite types are given in Table IX-1 for comparison with the Surveyor data. All of these, for one reason or another, are candidates for analogs to the lunar material. The LL chondrite and type 1 carbonaceous chondrite are presented as typical of stony meteorites. The Mg in all chondrites (in the minerals olivine and pyroxene, principally) is too high for any agreement to be possible. Chondritic and carbonaceous chondritic meteorites, thus, apparently cannot come from the surface of the moon, if the analyses are representative. The eucrites (Ca-Fe rich, monomict achondrites) agree better with the Surveyor VI analysis than any other of our analogs. The howardites (Mg rich, polymict achondrites) fail to agree, again by virtue of the high Mg. The tektites, represented by the Indo-Malayan type, do not fit at all, having too little Ca and excessive Si and O. The granite is not a good analog, although it is possible to find granite compositions that lie within the extreme error bars. The andesite is not as good a fit as some others, having too little Ca and Fe and comparably more Si and O. One of the best fits is an anorthositic gabbro, although Ca and O give marginal comparisons. Because the two mare areas investigated by Surveyors V and VI were found to be characterized best as basaltic with a high iron content, the simplest characterization of the Surveyor VII composition may be to describe it as basaltic with a low iron content; the precision of the analysis does not seem to warrant a much more detailed statement.

The central scientific questions about the moon, which might be answered by the compositional data, are:

- (1) What is the bulk composition of the moon? How does this compare with the composition of the earth and the meteorites?
- (2) What are the composition and mode of origin of the lunar crust? (This term is left ill defined, but it includes the surface itself and goes to a depth of at least 2 km, which is the scale of the topography.) Is it derived in ways similar to the terrestrial crust?
- (3) What is responsible for the known differences between highlands and maria, i.e., the difference in albedo, elevation, crater numbers, etc.?

In the discussion that follows, use is made of terrestrial and meteoritic analogs, both with respect to models of origin and compositional classes. This does not mean that the lunar rocks will be exactly like these analogs; in fact, these rocks are undoubtedly unique in many respects. But in following this approach, it is well to remember that we are in a position not unlike the biologist who first tried to describe the fauna of Australia to his colleagues, or of the biologist who takes the first 600-line picture of a Martian biped. Furthermore, it must be emphasized that the region in which Surveyor VII landed is found to consist of several flow units that originated from the direction of Tycho. The significance of the chemical analysis by means of the Alpha-Scattering Experiment is clearly dependent on a correct description of the mechanism by which these units were deposited, whether by some volcanic process or by a hot or cold, turbidity-like flow at the time of presumed impact. Nevertheless, this is the only available analysis for the highlands, which constitute more than 80% of the lunar surface. We will interpret the analysis, therefore, as being typical in some sense of the composition of these highlands, and discuss the contrasts between the maria and the highlands on the basis of the single Surveyor VII datum and the analyses from the mare sites of Surveyors V and VI. The density and albedo contrasts inferred in this comparison are quite reasonable in terms of the telescopically determined morphological and albedo contrasts. The possibility is accepted, however, that later analyses in this or other highland areas might show the Surveyor VII site to be quite atypical.

1. Contrasts in Albedo

The low iron content of the material at the Surveyor VII landing site provides a possible explanation of the high albedo of the lunar highlands. Iron is the most abundant of the elements (transition metals) that absorb strongly in the visible part of the spectrum. The change in iron content from the mare sites to the highland site is sufficiently large to account for a distinct change in the opacity, and perhaps in the amount, of the mafic silicate mineral(s). Such a change would, in turn, affect the albedo of the whole-rock powder.

From the present data, it appears unlikely that most of the iron measured by *Surveyor VII* occurs on the surfaces of the rock particles as free metal. We are not inclined, therefore, to ascribe the albedo contrasts between the highlands and maria to differences in amount of free metal on the lunar surface. Furthermore, low carbon abundances in analyses from the maria and highlands imply that carbon is not a major factor controlling albedo on the moon.

If it is correct that the iron content of the silicate minerals determines the albedo of large regions on the moon. it is also probable that this is not the only factor. For example, the numerous bright craters and rocks in the maria cannot all be intrinsically different in composition from the surrounding darker material. Shoemaker has proposed a "lunar varnish" alteration process (Ref. IX-2) to explain these differences in albedo. Adams (Ref. IX-3) has emphasized the importance of mean particle size where albedo contrasts are not the result of compositional differences. These ideas have not been tested conclusively by the Surveyor missions. However, the comparisons of analyses (when available) of the undisturbed soil, disturbed soil, and of the rock at the Surveyor VII landing site ultimately may provide evidence on the lunar varnish hypothesis.

2. Estimated Density of Lunar Surface Rocks

From the similarity of the atomic abundances in the *Surveyor* analyses to those of basaltic rocks, it seems reasonable to infer a mineralogy that includes some, or all, of the following:

Miner	Density	
Albite (Ab)	NaAlSi ₃ O ₈	2.62
Anorthite (An)	$CaAl_2Si_2O_8$	2.76
Pyroxenes	(Ca, Mg, Fe)SiO ₂	
Enstatite (En)	$MgSiO_3$	3.20
Diopside (Di)	$CaMgSi_2O_6$	3.28
Hedenbergite (Hd)	${ m CaFeSi_2O_6}$	3.55
Hypersthene (Hy)	$(Mg, Fe)SiO_3$	3.45
Olivines	$(Mg, Fe)SiO_4$	
Forsterite	$(\mathrm{Fo})\mathrm{Mg}_{2}\mathrm{SiO}_{4}$	3.21
Fayalite	$(Fa)Fe_2SiO_4$	4.39
Metallic iron	Fe	7.87
Magnetite	$\mathrm{Fe_{3}O_{4}}$	5.20
Quartz	$(Qtz)SiO_2$	2.65

The densities of these minerals and their solid solutions are determined almost entirely by the proportion of iron. Within the pyroxenes, the incidence of high Ca, despite its atomic weight, causes a density decrease. Estimates for the density of the pyroxene present may be made, however, with considerable confidence by ideal weighting in terms of the densities of the end members present. The distinction between the orthopyroxene and clinopyroxene is not significant because hypersthene is used here only to define a particular composition and density.

Plagioclase and olivine density may be estimated similarly in terms of two end members.

A series of putative atomic compositions that lie within the error bounds of the *Surveyor* alpha-scattering analyses is presented in Table IX-2. Computed norms for these compositions are given in Table IX-3, along with their estimated densities.

In computing the mineralogical norms, the *Surveyor* analyses do not provide a basis for any confidence in deciding whether or not olivines are present in any amount. Atoms are allocated, therefore, to pyroxene molecules insofar as it is possible. It is apparent from the derived density values that this assumption does not affect appreciably the mean density.

The densities are determined principally by the proportion of plagioclase to total rock and by the iron composition of the pyroxenes. The plagioclase proportion is, in turn, determined by the amount of Al in the analysis. Small amounts of free iron, or iron as magnetite, affect the density approximately as though the iron were in a pyroxene. The computed densities are, however, insensitive to the amount of excess iron, so that the question of whether all the metallic atoms are oxidized does not affect the density analysis.

Comparison of results (Table IX-3) for analyses from the highland site (models 1 through 11) with those from the mare sites (models 12 through 15) indicates that reasonable values for the rock grain density for the two regions are approximated by 3.0 ± 0.05 g/cm³ and 3.2 ± 0.03 g/cm³, respectively. The difference is significant and reflects the difference in the iron content between the two regions. It should be kept in mind, moreover, that Turkevich, et al. (see Section VIII of this Report) state that the rock (sample 2) analyzed at the Surveyor VII site contained about 30% less iron than that for the undisturbed lunar surface (sample 1), upon which Tables IX-2 and IX-3 are based. Thus, differences in rock densities of the highland and mare regions may be even greater than indicated in Table IX-3; note that Scott and Roberson (see Section V of this Report) estimate the density of the rock "weighed" by the surface sampler to be 2.4 to 3.1 g/cm^3 .

Regarding the analyses at the mare sites, the eucrites have been identified as having an atomic composition that falls within all the error bounds for $Surveyors\ V$ and VI

Table IX-2. Assumed atomic compositions

	Element								
Model	0	Si	Al	Na	Mg	"Ca''	"Fe"		
1	58	18	8	2	4	6	2		
2	59	18	8	1	4	6	2		
3	59	18	7	1	6	5	2		
4	59	18	7	1	5	5	2		
5	60	18	8	1	4	5	2		
6	60	18	8	1.5	4	5	2		
7	60	18	8	2	4	5	2		
8	58	18	8	2	4	5	2		
9	58	18	7	2	3	5	2		
10	58	18	9	1	3	6	2		
11	58	18	9	1	5	3	2		
Surveyor VII analysis	58 ±5	18 ±4	8 ±3	< 3	4 ±3	6 ± 2	2 ± 1		
12	58	20	6.5	2	3	6	5		
13	59	20	6.5	1	3	7	6		
14	60	18	5.5	1	4.5	5	6		
15	60	19	5.5	0.5	4.5	4	6		
Surveyor VI analysis	57 ± 5	22 ± 4	6.5 ± 2	< 2	3 ±3	6 ± 2	5 ± 2		
Surveyor V analysis	58 ±5	18.5 ±3	6.5 ± 2	< 2	3 ±3	$13\pm 3^{\rm a}$			
a''Cal'' and ''Fe'' taken together.									

Table IX-3. Estimated densities for assumed normative mineral compositions

Model Estimates density, g/cm³	Estimated	Normative composition ^a								
		Ab	An	Di	En	Ну	Hd	Fe	Fe ₃ O ₄	Other
1	2.95	2	3	3	_	_	_	2	_	
2	2.99	1	3.5	2.5	_	1.5	_	_	_	
3	3.03	1	3	2	3	1	_	1	_	
4	3.05	1	3	3	1	2	_	_	_	_
5	2.99	1	3.5	1.5	1	2	_	_	_	_
6	2.98	1.5	3.2	1.8	_	2	_	_		_
7	3.05	2	3	2	2	_	_	_	1.5	
8	2.96	2	3	2	2	_	_	2	_	_
9	2.92	2	2.5	_	_	2.5	_	_	_	_
10	2.97	1	4	2	_	1	_	1	_	_
11	2.98	1	4	2	2	_	_	2	_	
12	3.17	2	2.3	3.7	_	0.5	_	4.5	_	_
13	3.20	1	2.7	3	_	_	1.3	_	2.0	2.5 SiO ₂
14	3.20	1	2.3	_	3.2	1.3	2.7	2	_	
15	3.22	0.5	2.5	_	_	4.5	1.5	_	_	_
aUnits are arbitrary with coefficients proportional to the molar composition.										

(Refs. IX-4 and IX-5). For compositions taken arbitrarily from within the allowed *Surveyor V* and *VI* bounds, we find densities between 3.17 and 3.22 g/cm 3 . The higher densities, especially model 15, are found for compositions that are selected to agree with the most common eucrite compositions. Thus, the estimated densities are in essential agreement with the eucrite densities, although the latter may range up to 3.28 g/cm 3 .

In short, if the intrinsic density of the mare material is taken as 3.20, then the hypothesis of a eucrite mare composition is not counter-indicated. If some of the "Fe" (say about 1%) is really Cr or Mn, these elements would be found as impurities in the (already rather nonstoichiometric) pyroxene and plagioclase lattices and will affect the density in a way that cannot be distinguished from the effect of iron.

This analysis has been based on a fairly conventional interpretation of the chemistry. The possibility remains, however, that something rather strange may be masquerading as a basalt or a eucrite. For example, the possibility has not been included that there is 0.5% or more K in the "Ca," which would affect the mineralogy. This seems reasonable in view of the indicated low Na values and the usual Na/K ratios of 5 to 10 found in igneous rocks. There has been no discussion of Cl or C in this mineralogical model, nor has consideration been given to ensure that the minerals form a stable assemblage.

Many other questions that could be raised about the lunar surface involve effects that are too small for the chemical analysis to provide any answers in their preliminary form. It would be desirable to know whether 2% or more, by weight, H₂O is present in the surface material as water of hydration. If this were true, the amount of available oxygen for combination with the metals would be reduced by a few percent, thus presumably exacerbating the oxygen deficit. The present error bounds on the chemical analyses, as well as the bounds that must be placed on speculation, permit only the statement that 10% water of hydration appears fairly unlikely. The question may also be raised as to how much meteoritic iron is present in the surface soil. From the Alpha-Scattering Experiments, 0 to 4.5%, by weight, of the soil could be metallic iron, a result that establishes only an upper limit for the content. On the other hand, the magnet tests seem to indicate about 1% magnetic material; this could be all magnetite, if the analogy with terrestrial basalts is at all relevant. The single magnetic object that apparently adhered to the magnets on the surface sampler is spectacular, and may be a fragment of a meteorite; however, it seems inappropriate at this time to base any speculations upon a single datum of this kind.

3. Bulk Composition of the Moon

The *Surveyor* chemical analyses do not provide any definitive information on the bulk composition of the lunar body. Indeed, the composition of the lunar interior must always remain a matter of inference; evidence will always be circumstantial and remain open to alternate interpretations. At the present time, two questions are crucial to interpretations:

- (1) Is the Surveyor VII analysis typical of highland material?
- (2) To what depth is the estimated density representative of the lunar "crust"?

These questions obviously cannot be answered until additional highland sites are analyzed. The following circumstances prevail:

(1) The mean density of the moon (3.34) is very close to the mean density of the earth's uncompressed mantle material, about 3.35 or slightly higher. Under the pressure and temperature conditions expected in the lunar interior, the mean lunar density may be taken as the true, constant density of the lunar interior with an error less than 0.05 g/cm³, if the estimated density from the Surveyor VII analyses is valid for only a few kilometers of the lunar "crust" (i.e., no dense core or other structural inhomogeneity). In addition, the composition of the Surveyor VII lunar highland sample agrees closely with that of an anorthositic gabbro and reasonably well with that of oceanic and continental tholeiitic basalts (Tables IX-1 and IX-2). Analyses from the Surveyor V and VI sites are similar, but show twice as much iron; thus, the material from the maria also resembles terrestrial basalts, but bears a resemblance to the eucrites, which differ in major element chemistry from the terrestrial basalts in their high iron (as well as having lower alkalies, a matter which cannot be discussed on the basis of the preliminary results from the Alpha-Scattering Experiment). The obvious inference from the similarity between the mantle and moon densities is that the lunar body and the earth's mantle are composed of essentially the same substance.

The mantle may be thought of as a mixture of an olivine (80% Fo, 20% Fa) with a basalt in a ratio of about 5.1. Until some strong counter-evidence comes from the lunar surface, some heed must be paid to this inference because of the lack of any other obvious candidates for the 3.34 density. For this reason, it is especially interesting that the lunar surface, which we tend to regard as the prime derivative of the lunar body, should have a composition so similar to the basalts, which compose the prime derivative of the terrestrial mantle. The results from the Alpha-Scattering Experiment, therefore, may be viewed as additional circumstantial evidence in favor of the moon/mantle similarity.

The terrestrial analogy is imperfect, however, and the divergences provide very interesting scientific questions. In the Pacific Ocean, the basin extrusives are andesitic. These two varieties on the average show a density difference on the order of

- 0.1 or 0.2, which is of the same magnitude and sign as the density difference that has been estimated between lunar mare and highland materials. But the sequence of lunar materials is different: The basin deposits on the earth most resemble the highland deposits on the moon; the "ferrobasalt" of the lunar basins finds no common terrestrial analog, and the terrestrial andesite has not been found in any of the three *Surveyor* chemical analyses.
- (2) The Surveyor VII analysis bears a close resemblance to a terrestrial anorthositic gabbro (Table IX-1), such as may be found in layered basic intrusives, such as the Stillwater, Bushveld, or Skaergaard intrusives. Certainly the possibility should be considered that the layered gabbros and genetically related members are a ubiquitous feature on the lunar surface. In this respect, a geological mapping of the area north of the crater Tycho leads to remarkably consistent agreement that several distinct blankets of material can be identified and stratigraphically placed; only the origin of the various units has been subjected to multiple interpretations. If the units are ejecta deposited as a result of the impact that formed Tycho, then the material around the Surveyor VII site was probably derived from depths of 10 to 15 km. It would not be surprising, therefore, if plutonic igneous rocks were the main constituent of the deposits around the spacecraft. The observation of coarse, light/dark textures in rocks near the spacecraft is suggestive of, and consistent with, such an interpretation. The observations are, however, hardly conclusive. It is equally possible that the material analyzed at the Surveyor VII site is a post-cratering volcanic rock. The depth of origin of such material is a matter of speculation, but it seems likely that the source would be very much deeper than for impact ejecta.

Notwithstanding the origin of the Surveyor VII highland samples, if one posits that the density estimated for the material analyzed at the Surveyor VII site is representative of the highland provinces (corresponding to more than 80% of the lunar surface) and extends to depths approaching 100 km or more, the mean density of the moon would require interior densities significantly greater than the mean value. Recent results reported by Lorell and Sjogren (Ref. IX-13) from analysis of the Lunar Orbiter tracking data suggest that the moon has an interior density "moderately higher" than crust density. Because density increases produced by the modest interior pressures of the moon could be

compensated, or even offset, by the effects of increasing temperatures of depth, increased interior density may be interpreted as indicating material that is compositionally different from the *Surveyor* basaltic chemistry. Ultrabasic composition, high-pressure assemblages, and perhaps even the presence of an embryonic "core" as a result of chemical fractionation of the primordial lunar mass may provide, either individually or in partnership, an explanation for higher interior densities. Differentiation within the body of the moon, however, may not have proceeded as far as terrestrial processes; it is interesting to speculate that the moon in its present state may represent an evolutionary stage similar to that of a youthful earth.

4. On the Thermal Regime in the Moon

The Surveyor chemical analyses are strong circumstantial evidence that melting has occurred in the moon, and the Lunar Orbiter photographs suggest that this may have been true over a major fraction of the moon's history. The consequences of such melting in the lunar body are relevant to subsequent discussions and are of intrinsic interest.

It is possible to discuss the heating to be expected in an initially cold moon by decay of the long-lived radioactivities U238, U235, Th232, and K40. Temperatures estimated in this way are likely to represent the minimum possible temperature, since other effects, such as initial heating, tidal friction, etc., act to raise the temperature. Both time-dependent and steady-state calculations have been made, and all have certain features in common: (1) a nearly constant maximum temperature throughout the interior, decreasing to a nearly constant gradient region near the surface; and (2) a steady increase in the central temperature with time, given by the total heat added to the interior by radioactive decay. By relating the history of heat production to the concentration of heat-producing isotopes, it is possible to investigate whether or not melting in the interior is likely for a given type of material (Ref. IX-14). Melting is predicted if the concentration of K2O exceeds about 0.02%.

For oceanic tholeiites (Ref. IX-15), K_2O ranges between 0.06 and 0.26%; it ranges between 0.04 and 0.22% for eucrites (Ref. IX-7). Both of these are notable for having the lowest K_2O (and other alkalies) within terrestrial extrusive and stony meteorite groups, respectively. The amount of K_2O in the parent material is less by some factor which depends on the original proportion of the

magma in the parent. Factors of three to six have been suggested; it is then apparent that the range of uncertainty brackets the critical K₂O value of 0.02%. It is probably safer to heed the photographic and chemical evidence in favor of melting, and put a lower limit on the K2O in the moon. The values are not very different from the concentrations suggested for the earth's mantle in discussions of terrestrial heat flow; for that reason, it is convenient to set them equal and compare the steady-state heat flow to be expected. The moon's volume, and hence its total amount of heat-producing material, is smaller than that of the earth by $(R_m/R_e)^3$. The area is smaller by $(R_m/R_e)^2$. The heat flow should then be smaller in proportion to the radius, namely by a factor of four. In all numerical discussions of lunar temperature, the heat flow follows this approximation fairly well, and is insensitive to the transient aspects of the problem. On dimensional grounds then, the near-surface thermal gradient is found to be four times less than the terrestrial gradient. The pressure gradient, away from the center, is about six times less. Thus, approximately, the temperature and pressure gradients in the outer few hundred kilometers of the moon are expected to be about five times less than on the earth. The temperature (pressure), T(P), behavior can also be taken over from the terrestrial T(P), but must be scaled by a factor of five in depth. That upper portion of the terrestrial crust/upper mantle system that is cool enough to support long-term stresses and not creep is about 50 to 80 km thick, and may be called the lithosphere. The region extending from the lithosphere to at least 180 km is characterized by a low-velocity, high-attenuation zone, and is the locus of primary magma generation. Discussions of temperature indicate that this region is one in which the temperature is near, if not at, the melting temperature of the first melting component and has, in consequence, very little strength (asthenosphere). If these conditions are "mapped" onto the moon, the lithosphere must extend to depths of 250 to 400 km, and the remainder of the lunar interior will correspond to the low-velocity asthenosphere. The center of the moon corresponds to a depth of only 150 km in the earth.

5. On Chondritic Meteorites and the Moon

The possibility that some, or all, varieties of meteorites are derived from the moon has been a tantalizing prospect for many years (Refs. IX-16 and IX-17). However, from even a cursory examination of Table IX-1, it is apparent that the chemical composition at the *Surveyor V*, *VI*, and *VII* landing sites in no way resembles the composition of ordinary or carbonaceous meteorites; both types of chondrites have altogether too much Mg and too little

Ca and Al; in addition, carbonaceous chondritic meteorites have too much C. The evidence relating to the bulk composition of the lunar body remains circumstantial, however, and can be interpreted in a chondrite framework.

Suppose that ordinary chondrites, with a density of 3.6 to 3.8, comprise a major fraction of the moon. Two-thirds of this could be fully melted, in a core, without conflicting with present knowledge of the nonequilibrium gravity harmonics of the moon. Because the average density of such a moon could not be less than about 3.55, it is necessary to assume that volatiles, as exemplified by the constituents of the low-density (2.9) carbonaceous chondrites, are present in sufficient quantity to bring the mean density down to 3.34. Under the possible conditions of temperature and pressure in the moon, carbonaceous chondritic material would probably assume a density close to 3.25 when the water was taken into denser phases. The only chondritic moon that might be arranged to have the correct mean density by this mixture is composed almost entirely of carbonaceous chondrites.

A moon composed of carbonaceous chondrites in bulk differs principally from terrestrial mantle material in two ways:

- (1) The chondrites have significantly more iron, either as metal or in a silicate phase. The effect of this iron to increase the density is offset by the presence of a great deal of water, on the order of 10% of the total mass instead of 1%, or less, as is the case with the mantle.
- (2) The chondritic meteorites appear to be enriched in Na, K, etc., with respect to the earth's mantle.

It is possible to discuss implications of these differences, but not conclusively. From an analysis of the probable pressures and temperatures in the moon, there are indications that the $T\left(P\right)$ is very much like that of the earth, but with a depth scale about five times greater. From the center of the moon out to 1200 to 1400 km, temperatures appear to be at, or near, melting conditions for the first melting fraction. Under these conditions, with approximately 1% water, the earth's upper mantle is extremely mobile on geological time scales; this mobility is responsible for drastic displacements of crustal blocks, island arcs, mountain building, etc. No evidence for a similar tectonics of large-scale lateral displacement is seen on the lunar surface; however, this is compatible with the possibility that the lunar lithosphere (mechanically rigid crust)

is six times thicker than the terrestrial lithosphere, a situation which is likely to suppress large-scale displacements. To introduce 10% water, however, and retain such stability seems totally unreasonable. Moreover, it seems unlikely that a moon with a mobile, high-temperature interior could retain 10% water against outgassing over times of 10° yr or more. The circumstance most favorable to a chondritic moon is, therefore, that of an interior which has remained at temperatures significantly below the melting point; this does not appear to be compatible with the amounts of heat-producing K, U, and Th in chondritic meteorites.

If material of chondritic composition occurs in the lunar interior and does not come to the surface, the chondrites arriving on earth must have originated elsewhere. Although the possibility cannot be overlooked that chondritic material eluded three *Surveyors*, the fact remains that chondrites constitute the overwhelming majority of all meteorites, and the ordinary chondrites, high density and all, are still to be explained. (Carbonaceous chondrites are undoubtedly numerically more significant outside the atmosphere; they are easily broken apart and consumed by ablation processes on entering the earth's atmosphere.) If the *Surveyor* analyses are typical, it is difficult to see how some, or all, of the chondrites come from the moon, without conflicting with either the composition or the mean density.

The resemblance to eucrites, shown by analyses from the maria, has been cited in the past on circumstantial evidence in favor of the moon as an origin for the basaltic achondrites (Refs. IX-7 and IX-17). The Surveyor VII analysis does not support the lunar origin for these objects and, in fact, tends to refute the possibility. There are two difficulties: First, the basaltic achondrites constitute about 5% of the observed falls and, if they have a lunar origin, are derived from less than 20% of the lunar surface covered with mare material. Objects derived from the remaining 80% of the lunar surface, the highlands, also should be present in the meteorites arriving on earth. But there are no known meteorites with a composition similar to that indicated by the Surveyor VII analysis. Either the Surveyor VII analysis is not representative of the highlands or one must invoke the absurd conclusion that most meteorites are "filtered" by some unknown process that excludes all but those arriving on earth from the maria.

A second pitfall for the moon/eucrite analogy stems from the observation (Ref. IX-7) that eucrites might be

genetically related to the howardites and mesosiderites and they, in turn, might be representative of the highlands. It is clear from Tables IX-1 and IX-2 that the Surveyor VII analysis does not support such a possibility. It should be noted in passing that, with the potassium argon ages of eucrites 4.5 billion years, it is clear that the surfaces in the maria are either 4.5 billion years old or that the eucrites do not come from the moon (barring circumstances of surface heterogeneity). Lunar Orbiter photography provides a wealth of morphological and geological detail about mare surfaces; many mare areas are among the stratigraphically youngest places on the moon. Some members of this Surveyor Working Group are inclined to the view that the stratigraphic youth is equivalent to geological youth, with ages of some millions to tens of millions of years. However, others in this Working Group feel that the stratigraphically youngest areas are 4.5 billion years old. This question of age and eucrite origin should be settled beyond reasonable doubt when lunar samples are available for radiometric dating.

6. On Tektites

Chemical measurements at the *Surveyor VII* landing site (see Section VIII of this Report) add to the evidence (Refs. IX-4 and IX-5) that tektite material is not widely distributed on the lunar surface. The importance of such material in the formation of the mare surface, if any, is clearly not as great as indicated by O'Keefe in Ref. IX-18.

The analysis of the rock from the Surveyor VII site indicates a material that may have a density of 3.0 or as low as 2.9. The contrast in density between this rock and the material of the maria, which is much richer in iron and may have a density of 3.2, is conceivably sufficient to account for isostatic differences in the elevations of the two regions. On the earth, isostatic differences correspond to density differences of 2.7 vs 3.0. It follows that the argument for a silicic rock in the highland portions of the moon, contrasting with a basaltic rock in the maria, is not securely based.

On the other hand, it is well to keep in mind that large basaltic intrusions in the earth are normally accompanied by small volumes of silicic rock, the so-called granophyres. It should be expected, therefore, that acidic rock may occur somewhere on the lunar surface; the *Surveyor* analyses, therefore, do not rule out the possibility that tektitic material may be found in some portions of the moon.

7. Solar System Implications

The chemical analysis and the results of the data derived from the magnet test exclude the possibility that the Surveyor VII site is composed of chondritic material. This discovery, coupled with the findings of Surveyors V and VI in the maria, supports the conclusion that the moon is not the source of chondritic meteorites. This conclusion bears directly on our present knowledge of the chemical composition of the terrestrial planets.

The high density of Mercury (Ref. IX-19) and the generally lower (uncompressed) densities of the planets more distant from the sun have led to the idea that the dispersed material from which the planets accreted was somehow affected by solar irradiation early in the evolution of the solar system.

Urey (Ref. IX-16) suggested that chondritic meteorites might come from the moon. If true, this would mean that the bulk of the meteoritic data applies to a relatively restricted portion of the solar system. If the chondrites are now ruled out by the *Surveyor* evidence, it appears that most meteorites are samples from outside the earth/moon system. The source of the chondritic meteorites is, of course, undetermined. However, the existing chemical and isotopic analyses of meteorites, as compared with terrestrial and lunar data, now become more significant.

The *Surveyor* analyses raise doubts about whether any primitive lunar material is preserved at the surface. If the basaltic rocks measured by *Surveyors* are the product of magmatic differentiation, the moon probably has been extensively modified since accretion. A differentiated moon would imply that the (larger) terrestrial planets also are likely to be differentiated.

C. Rock Types

The area observed by *Surveyor VII* is littered with objects of a variety of shapes and sizes, which safely can be called rocks. Some are slightly rounded and look eroded; others are angular and look comparatively fresh; some show lineations, evidence of jointing, and even open fractures. When viewed at sun angles that minimize the effects of shadowing, these rocks are clearly seen to have a variety of albedos, fabrics, and textures that represent intrinsic differences within the class of these objects.

In views such as those of Figs. IX-10 and IX-11, fields of dark, rough-textured rocks are found in conjunction

with bright, more massive rocks. The albedo differences are extreme (e.g., Fig. IX-10) and suggest differences in composition. The dark rocks appear to have the same albedo as the lunar soil and seem to be in various states of physical disintegration (Fig. IX-12). On the whole, the brighter objects appear to resist disintegration more effectively and stand out as rounded, massive blocks against the dark background of the soil (Fig. IX-13). A strong impression is given that the greater susceptibility of the dark rocks to disintegrate means that the soil layer composition is biased toward their composition.

Closer to the spacecraft, one again finds dark, roughtextured rocks and brighter, massive rocks. The greater resolution permits some of the latter to be distinguished by various criteria. Some rocks show white blobs (crystals?) that stand out from the surface in three-dimensional viewing and by the shadows they cast (e.g., Fig. IX-14); such protuberances may be produced as the consequence of being more resistant to erosion than the basic matrix. For this reason, great caution must be exercised in attempting to infer actual differences based on the surface appearance; texture and surface roughness differences may be intrinsic to the rocks or related to erosion processes.

Figure IX-15 shows a pair of massive blocks less than 3 m from the television camera. A nonoriented pattern of millimeter- to centimeter-sized light patches is seen against a darker background. The overall appearance is that of an ordinary plutonic igneous rock; however, appearances frequently are deceiving and this rock might, in fact, be a porphyry, a breccia, or something else. The jointing and the particular way in which the surface is rounded suggests extreme isotropy for this rock.

In Figs. IX-16 and IX-17, these same rocks are viewed at lower sun angles to show their rough, pitted surface texture. Exposed edges have been rounded off, and two or three of the pittings are large enough to be called craters a few centimeters in diameter. This represents some of the most convincing direct evidence to date from the *Surveyor* pictures for the relevance of fine-particle impact in the evolution of the lunar surface material; unmistakable signs of erosion by impact are present in the surface texture of this and some of the more cohesive rocks. In addition to erosion by cratering, sufficiently energetic impacts may disrupt the block into several smaller pieces, either by spallation processes or by activation of joints or cracks which pre-existed the impact.

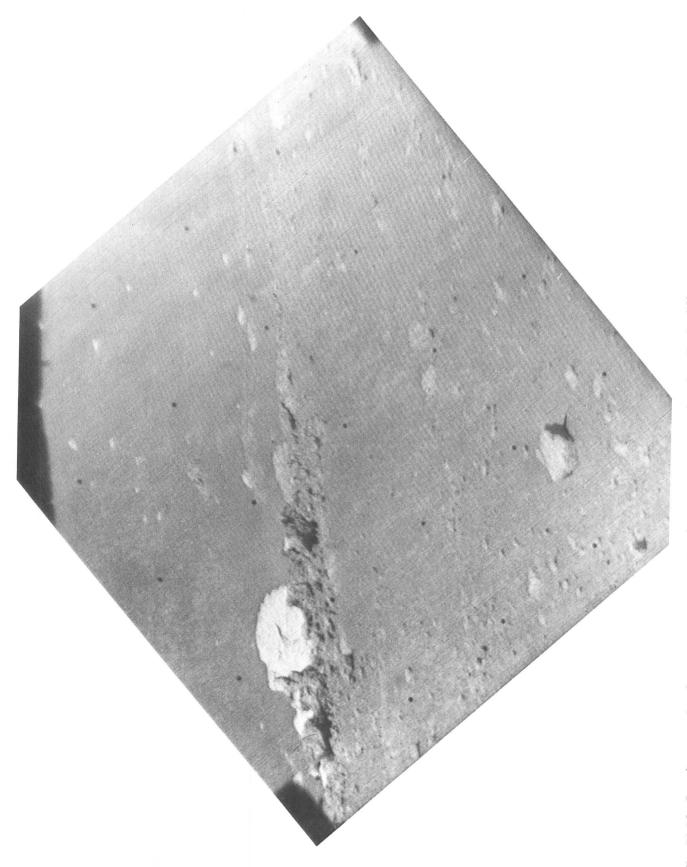
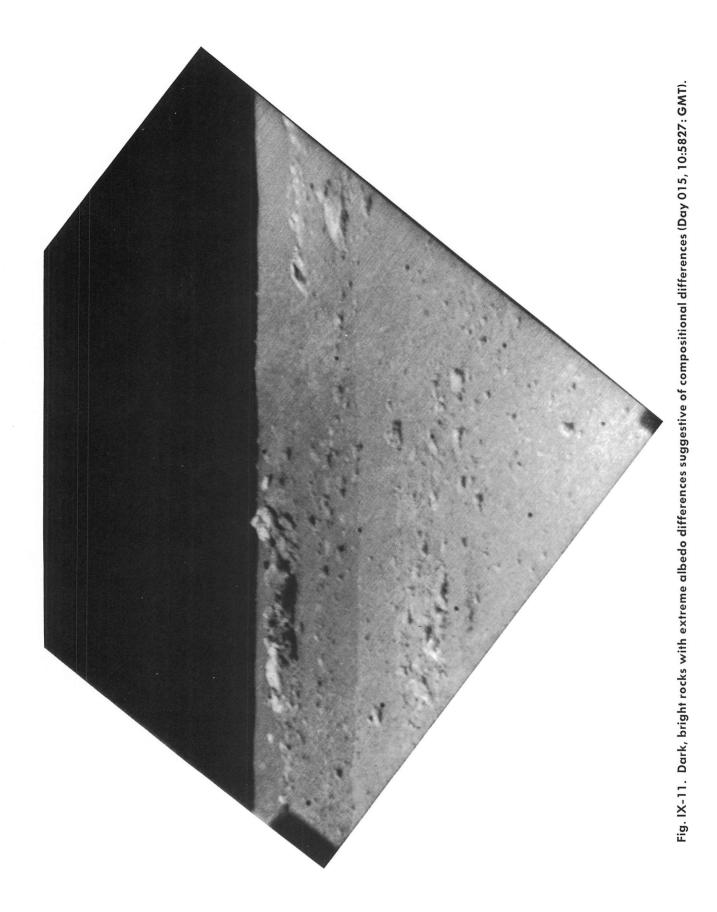


Fig. IX-10. Rough textured rocks in conjunction with bright, more massive rocks. The albedo differences are extreme and suggest compositional differences (Day 018, 12:16:22 GMT).



JPL TECHNICAL REPORT 32-1264

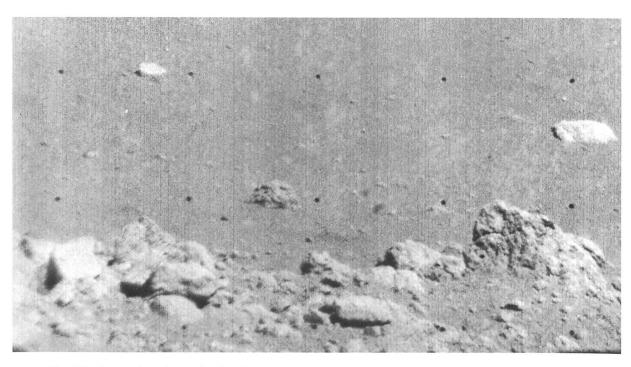


Fig. IX-12. Dark rocks with albedo similar to that of the lunar soil (Day 013, 14:02:17 GMT).

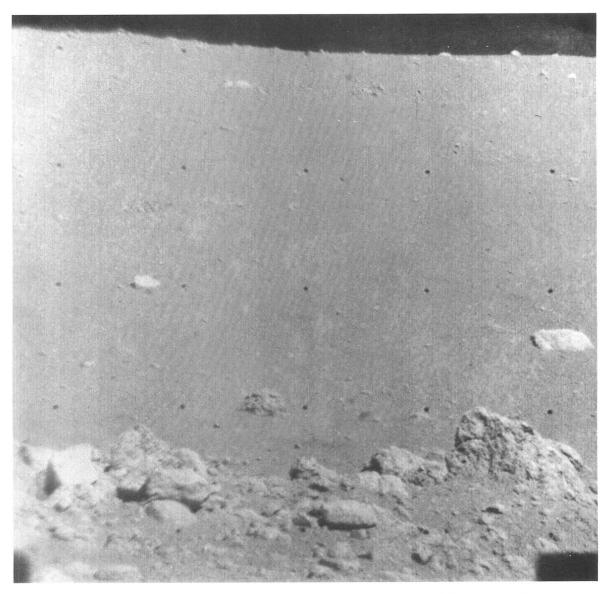


Fig. IX-13. The brighter rocks stand out against the darker background of the lunar soil and appear to resist distintegration (Day 013, 14:02:45 GMT).

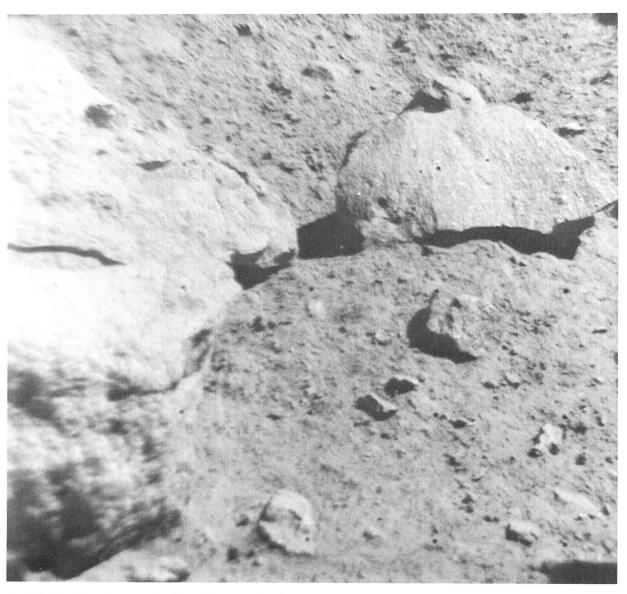


Fig. IX-14. Massive rock with white specks that appear to protrude from the surface, possibly as a consequence of being more resistant to erosion in the basic matrix (Day 018, 06:36:51 GMT).

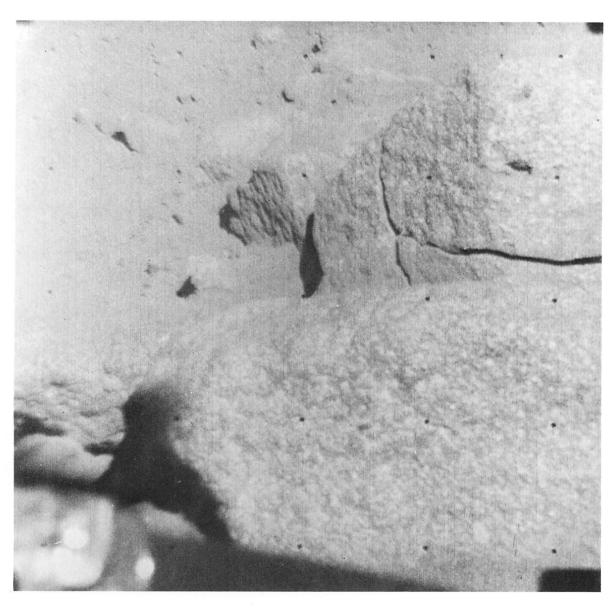


Fig. IX-15. Massive rocks with nonoriented pattern of millimeter- to centimeter-sized white patches in a darker matrix (Day 013, 13:59:22 GMT).

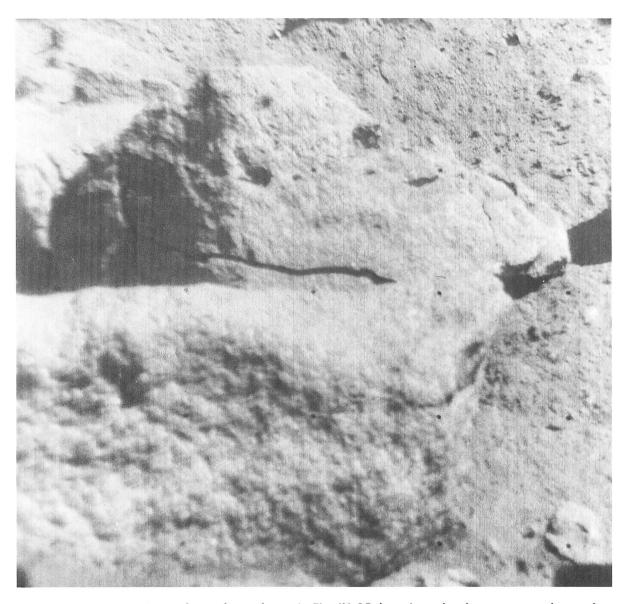


Fig. IX-16. Same massive rocks as those shown in Fig. IX-15, but viewed at lower sun angles to show rough, pitted surface texture (Day 017, 09:45:20 GMT).

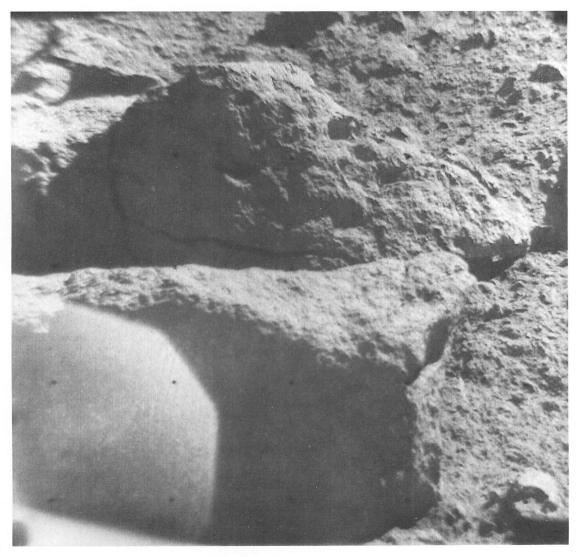


Fig. IX-17. Same massive rocks shown in Figs. IX-15 and IX-16, but viewed at lower sun angle to show the rough, pitted surface texture (Day 020, 17:07:50 GMT).

The fractures showing in one rock (Fig. IX-16) may have been produced by such effects of impact; it is in this manner that large rocks are broken down into smaller objects and the finest particles from the pits and small craters contribute to fine-grained surface material.

Rocks with fresh, conchoidal fracture surfaces are shown in Figs. IX-18 and IX-19; the rock shown in Fig. IX-19 may have been derived from the larger (fractured) rock below it in the manner just described. This rock appears to be composed of light grains (crystals or fragments) embedded in a darker matrix. Some orientation of fabric is visible, but the proportion of light grains is

less than in the previous example. Orientation in subparallel arrays suggests mechanisms such as flow and shearing, or deposition of hot pyroclastics. The angular rock in Fig. IX-15 is another example showing small light flecks embedded in a darker matrix, and some orientation of grains. Viewed by a distant camera, this rock would be regarded as "dark." The massive, bright rocks in Fig. IX-20 appear to be of the same general kind, with a barely resolvable flecked appearance, and a suggestion of orientation. Viewed at low sun angle (Fig. IX-21), it shows pitting and cratering that could have been caused by small-particle impacts. The rock in Fig. IX-22 is about 2 m from the camera and shows resolvable, oriented elliptical inclusions as a part of the light-on-dark texture.

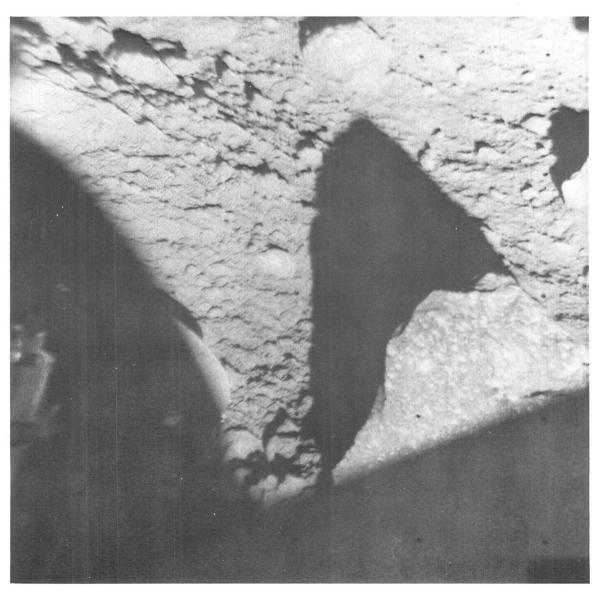


Fig. IX-18. Rock showing fresh, conchoidal fracture surface. It appears to be composed of light grains (crystals or fragments) embedded in a darker matrix (Day 011, 06:29:29 GMT).

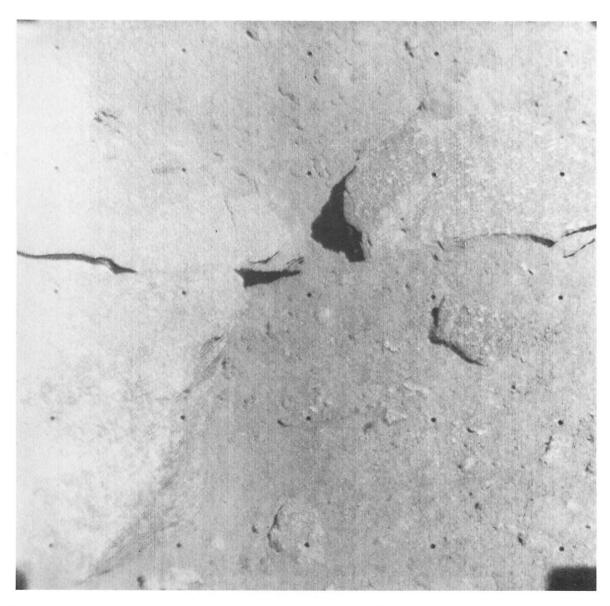


Fig. IX-19. Rock with fresh, conchoidal fracture surface, showing light grains embedded in darker matrix. Some orientation of fabric is visible (Day 013, 10:31:04 GMT).

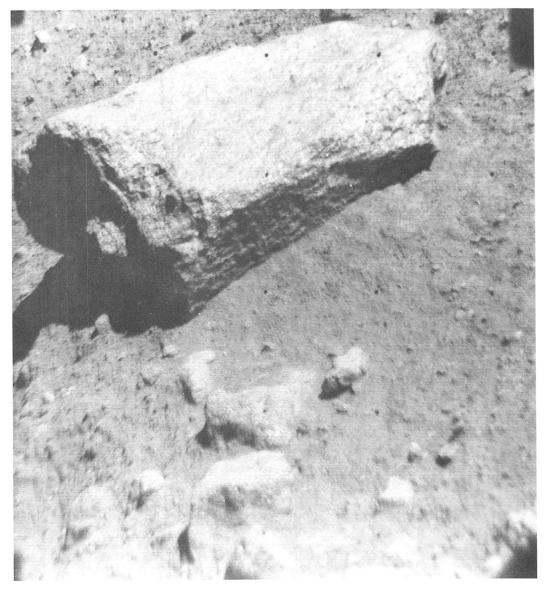


Fig. IX-20. Angular rock showing light flecks embedded in darker matrix. Some orientation of grains appears to be present (Day 013, 01:20:51 GMT).

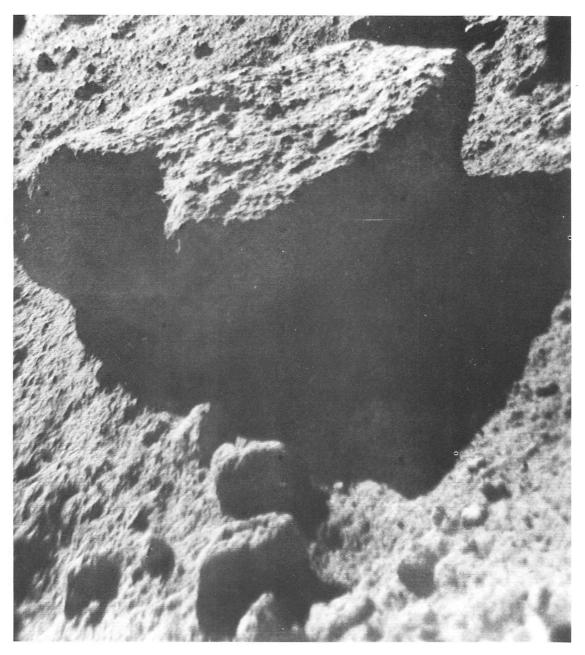


Fig. IX-21. Angular rock shown in Fig. IX-20, but viewed at low sun angle to show pitting and cratering caused by small particle impacts (Day 020, 16:55:36 GMT).

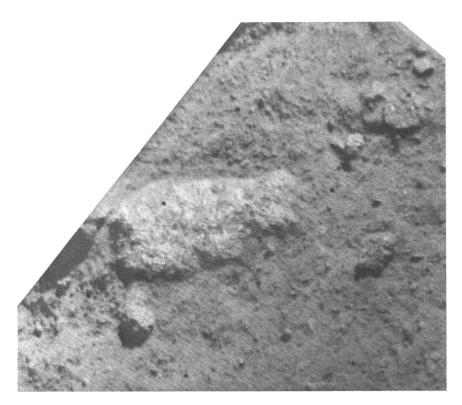


Fig. IX-22. Rock showing resolvable, oriented, elliptical inclusions as a part of light and dark texture (Day 013, 02:33:12 GMT).

Less striking, but quite common, are the dark, fragmental rocks, which appear to be kindred to the dark, and what have been interpreted as easily broken, objects in the far field. The objects seen in Figs. IX-23 and IX-24 are of this type. It is tempting to see vesicles in some of these rocks, but the effect of micrometeorite pitting on the softer rocks should be kept in mind. Figure IX-25 shows one rock containing an unmistakable band of vesicles; this rock is directly to the west of the spacecraft at a distance of about 8 m from the camera. The shape that this rock has assumed in response to erosion is quite characteristic of layered, extrusive, vesiculated basalt.

In summary, a diverse collection of rock types is observed, which suggests the presence of composition differences. Most of these rocks were presumably ejected from several craters (impact or volcanic) and some may have been carried by flows. These explanations allow large differences between the various rock types found in close proximity. In other cases, rocks appear to have a common origin by their present arrangement and their appearances are then indeed similar.

The presence of vesicular rock, presumably of volcanic origin, near *Surveyor VII* is consistent with the existence

of the numerous flows found on the outer slopes of Tycho on the *Lunar Orbiter* records. On the other hand, the presence of angular rock showing what may be crystals, would suggest that they originated at a considerable depth below the surface and perhaps that all rocks were ejected to their present location by meteoritic impact. The rock assembly also suggests, however, that they may have arrived on the surface not in a single event, but in a sequence of events that occurred since the deposition of the flow on which *Surveyor VII* is resting. The roundness of many rocks indicates the presence of erosion, probably the combined effect of the solar wind and micrometeoritic impact.

D. Surface Material

Earlier Surveyor missions established that the unconsolidated surface mantle of the moon consists of a dark, fine-grained powder containing a distribution of coarser fragments. It may be estimated that about 90% of this material consists of sub-millimeter grains, too small to be resolved by the television camera system, possibly as small as a few microns. The undisturbed surface of this material commonly is slightly brighter than fresh subsurface material brought up to the surface. In specific

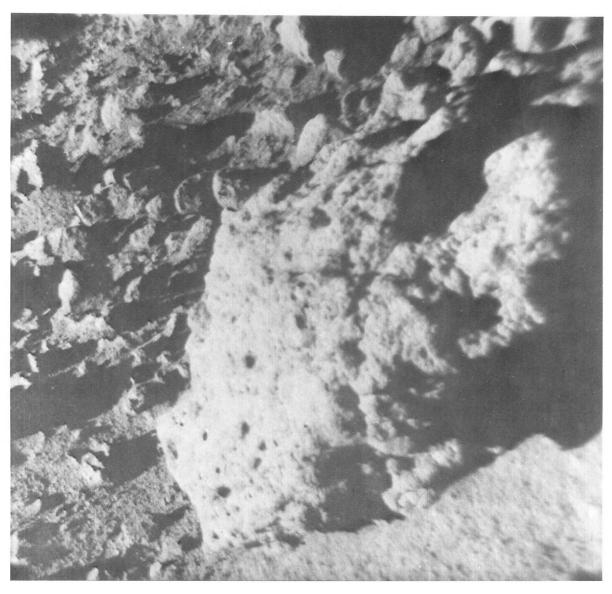


Fig. IX-23. Dark, fragmental rock. Note pitting and holes (vesicles ?) (Day 020, 16:41:20 GMT).

Fig. IX-24. Dark, fragmental rocks with surface pits and holes (vesicles ?) (Day 018, 06:46:05 GMT).

instances, the surface millimeter or so is seen to compose a crust, which apparently has slightly more cohesion than the substrate. The subsurface material manipulated by the surface sampler behaves incompressibly and appears to have a cohesive strength on the order of 10^4 dynes/cm². The texture of the surface shows the effects of repeated micrometeorite bombardment. This soil powder is responsible for the optical backscatter characteristics of the moon, as verified by Surveyor pictures. Telescopic and infrared evidence, coupled with all the previous Surveyor missions, show that this surface material, with its characteristic optical and thermal properties, composes all but

that very small fraction of the entire lunar surface that is covered with rocks.

Transportation of the powder is shown in *Surveyor* pictures by the small fillets of powder that are banked against rocks, primarily on the uphill side (Ref. IX-20). The transportation mechanism is clearly particle by particle, and most of the members of this *Surveyor* Working Group feel that this is by ballistic transport of particles stirred by micrometerite impact. The distance scale for transportation may be set by noting the sharpness of the maria/highland contact, as indicated by albedo contrast;



Fig. IX-25. Rock containing unmistakable band of vesicles with a shape characteristic of layered, extrusive, vesiculated basalt (Day 013, 14:53:38 GMT).

the particles cannot have been transported more than about ½ km in times appropriate to the ages of the principal mare surfaces.

In the area surrounding the *Surveyor VII* spacecraft, the powder layer is thin, of irregular thickness, and in places may vanish essentially altogether, exposing rock rubble. Its morphology is that of a blanket, which is gradually covering the rubble at the same time that the rubble is being eroded to form the powder. The preferential deposition of this material in topographic lows is indi-

cated both by the observed result and by the uphill powder fillets found banked against rocks (Figs. IX-26 and IX-27). The *Surveyor VII* surface-sampler area (see Section V of this Report) was nearly 100% covered by the powder layer. The fillets, which are of centimeter dimensions, have the same appearance as those seen at other *Surveyor* sites; this is consistent with an erosion/transportation/deposition process that has been acting long enough to create a powder layer at least several centimeters deep on the average. The form of the fillets would thus appear to be an equilibrium geometry controlled by the processes of deposition and erosion.

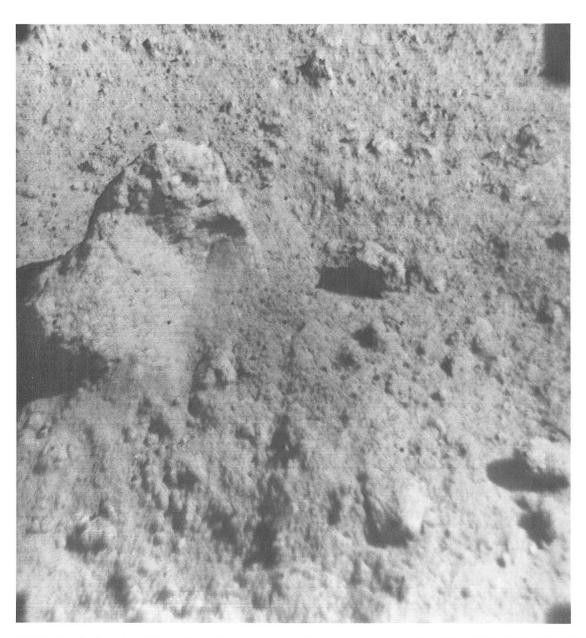


Fig. IX-26. Rock showing fillets of particulate material banked against sides (Day 013, 02:11:58 GMT).



Fig. IX-27. Rocky rubble covered with fine, particulate material and fillets banked against sides of rocks (Day 013, 13:58:10 GMT).

Figure IX-28 shows the illuminated side wall of a trench made in the surface layer by repeated manipulation of the surface sampler. Striations made by the surface sampler are clearly visible, as is the clean edge formed at the intersection of the trench wall with the surface. If we consider the dark striation in the center of the picture, the offset of the wall amounts to about 2 mm. The scintillation of the line produced by graininess may be estimated at about 20%. This would establish the grain size at about 200 μ if the scintillation is actually due to graininess and not to resolution limitations of the system. If the scintillation is a resolution limitation, 200 μ represent the maximum possible grain size.

E. Post-Sunset Horizon "Afterglow"

Observations of the western horizon shortly after sunset revealed a bright line of light along the crest of the horizon similar to that reported previously for the Surveyor V and VI missions (Refs. IX-17 and IX-21). Although not sufficiently well defined to be recognized at the time, the phenomenon also occurred during the Surveyor I mission. Although no sunset observations were made on Surveyor III, it appears that this post-sunset phenomenon along the western horizon (and probably the eastern horizon at sunrise) is not an unusual event, but occurs regularly as the natural consequences of some aspect of the lunar environment.

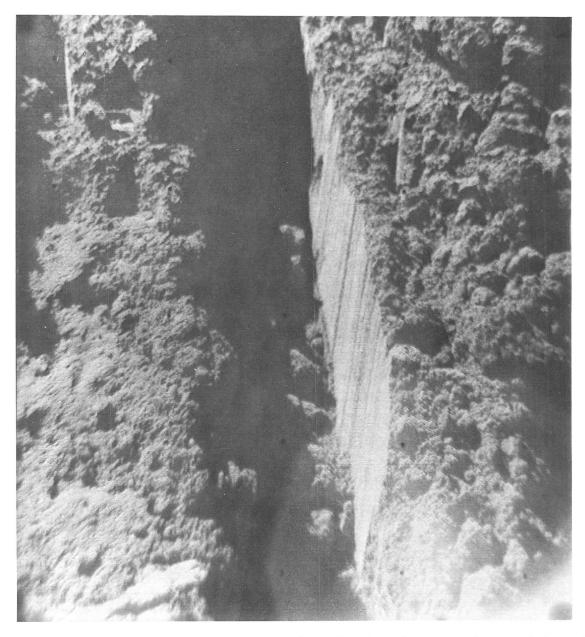


Fig. IX-28. Illuminated sidewall of a trench made in the surface layer by repeated manipulations of the surface sampler (Day 020, 09:51:50 GMT).

The light has been observed for periods of time up to about 2 hr after sunset. The center of the solar disk, therefore, is approximately 1.25 deg below the horizon when the "afterglow" either stops or the intensity falls below the limits of detection. Pictures of the light from the Surveyor VII missions are shown in Figs. IX-29 and IX-30 when the sun was centered approximately 0.4 and 1.0 deg,

respectively, below the horizon. In Fig. IX-29, the light intensity permitted normal shutter operation (exposure time, 0.15 sec); the bright line appears to extend only about 2 deg along and ½ deg above the horizon. The light intensity decreased rapidly; about 1½ hr later, a nominal 1.2-sec exposure (Fig. IX-30) showed a faint line of illumination extending at least 4 deg along the

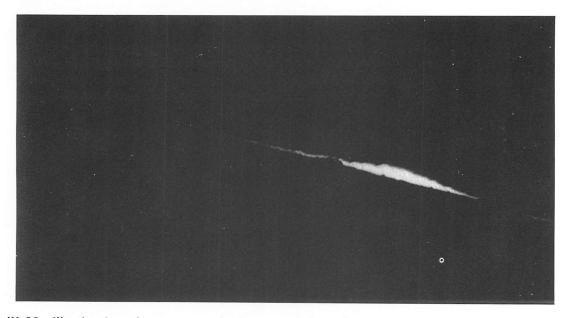


Fig. IX-29. Illumination along western horizon approximately 15 min after local sunset. Second disk; exposure time: 0.2 sec (Day 023, 06:18:32 GMT).

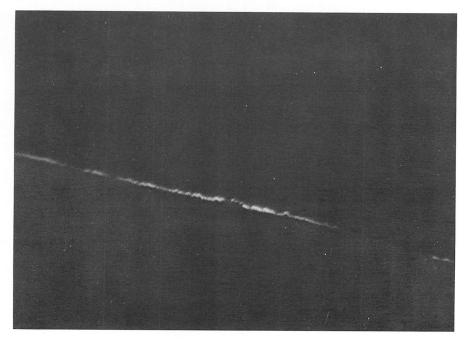


Fig. IX-30. Illumination along western horizon approximately 90 min after local sunset. Second disk; exposure time: about 1.2 sec (Day 023, 07:32:49 GMT).

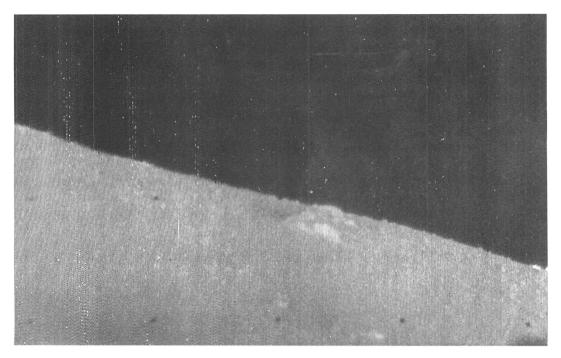


Fig. IX-31. Same field of view of western horizon as Figs. IX-29 and IX-30 about 160 min after local sunset. Second disk; exposure time: about 40 sec (Day 023, 08:46:56 GMT).

horizon. A 40-sec exposure (Fig. IX-31), taken about 2 hr, 40 min, after sunset, showed no edge of light along the horizon. This last picture (illumination provided by light backscattered from the ridges east of the spacecraft, and by earthlight) provides a valuable comparison of the rocks and horizon geometry with the shape of the bright regions in Figs. IX-29 and IX-30. A particularly striking facet of the phenomenon is the "mapping," or shadows, in the edge of light, apparently caused by the rocks extending along and above the moon horizon line.

Although no complete explanation can be offered at this time, the relative intensities of the light on *Surveyors VI* and *VII* suggest that scattering by small particles

above the lunar surface is not the mechanism for the phenomenon. This conclusion is drawn from the fact that, while the intensity of the bright edge appears to be greater for *Surveyor VII* than for *Surveyors V* or *VI*, the distance to the horizon and the path length of the light immediately above and along the surface is probably shorter. For equal spatial density of the particles above the surface, the longer path length, contrary to observations, should have produced a pattern of greater brightness. Alternatively, diffraction by small particles on the lunar surface, as discussed by O'Keefe, et al. (Ref. IX-18), may provide a mechanism for producing the phenomenon; however, further study is required before any explanation is considered firm.

References

- IX-1. Gilbert, G. K., "The Moon's Face—A Study of the Origin of Its Features," *Philos. Soc. of Washington Bulletin*, Vol. 12, pp. 241–292, 1893.
- IX-2. Shoemaker, E. M., Batson, R. M., Holt, H. E., Morris, E. C., Rennilson, J. J., and Whitaker, E. A., "Principal Scientific Results of the Surveyor III Mission," Surveyor III Mission Report. Part II: Scientific Results, Technical Report 32-1177, pp. 9–67, Jet Propulsion Laboratory, Pasadena, Calif., June 1, 1967.
- IX-3. Adams, J. B., "Lunar Surface Composition and Particle Size: Implications from Laboratory and Lunar Spectral Reflectance Data," *J. Geophys. Res.*, Vol. 72, No. 22, pp. 5715–5720, 1967.
- IX-4. Turkevich, A. L., Franzgrote, E. J., and Patterson, J. H., "Chemical Analysis of the Moon at the Surveyor V Landing Site: Preliminary Results," Surveyor V Mission Report. Part II: Science Results, Technical Report 32-1246, pp. 119–149, Jet Propulsion Laboratory, Pasadena, Calif., November 1, 1967.
- IX-5. Turkevich, A. L., Franzgrote, E. J., and Patterson, J. H., "Chemical Analysis of the Moon at the Surveyor VI Landing Site: Preliminary Results," Surveyor VI Mission Report. Part II: Science Results, Technical Report 32-1262, pp. 127–153, Jet Propulsion Laboratory, Pasadena, Calif., January 10, 1968.
- IX-6. Keil, K., "Meteorite Composition," *Hand book of Geochemistry*, Berlin, Heidelberg, New York, Springer-Verlag (in press).
- IX-7. Duke, M. B., and Silver, L. T., "Petrology of Eucrites, Howardites, and Mesosiderites," Geochim. et Cosmochim. Acta, Vol. 31, pp. 1637–1665, 1967. See also, Urey, H. C., and Craig, H., "The Composition of the Stone Meteorites and the Origin of the Meteorites," Geochim. et Cosmochim. Acta, Vol. 4, pp. 36–82, 1953.
- IX-8. Clark, S. J. (editor), *Handbook of Physical Constants*, p. 2, Geological Society of America, New York, 1966.
- IX-9. Turner, F. J., and Verhoogen, J., *Igneous and Metamorphic Petrology*, p. 325, McGraw-Hill Book Co., Inc., New York, Toronto, London, 1960.
- IX-10. Manson, V., "Geochemistry of Basalts: Major Elements," *Basalts, The Poldervoart Treatise on Rocks of Basaltic Composition*, Vol. 1, pp. 223–225, Interscience Publishers, 1967.
- IX-11. Average of seven from (1) Hatch, F. H., Wells, A. K., and Wells, M. K., The Petrology of Igneous Rocks, p. 271, Thomas Murby & Co., London, 1952, (2) Anderson, C. A., Volcanoes of the Medicine Lake, Highland, California, University of California Publications, Bulletin of the Department of Geologic Science, Vol. 25, No. 7, p. 392, 1941, (3) Williams, H., and Meyer-Orbich, H., Volcanoes in the Southern Part of El Salvador, University of California Publications in Geological Sciences, Vol. 32, No. 1, p. 50, 1955.

References (contd)

- IX-12. Palm, A., and Strom, R. G., *Space Sciences Laboratory Research* Report, Series 3, Issue 5, University of California at Berkeley, 1962.
- IX-13. Lorell, J., and Sjogren, W. L., "Lunar Gravity: Preliminary Estimates from Lunar Orbiter," Science, Vol. 159, No. 3815, pp. 625–627, 1968.
- IX-14. Phinney, R. A., and Anderson, D. L., "Present Knowledge About the Thermal History of the Moon," *Physics of the Moon*, AAS Science and Technology Series, Vol. 13, pp. 161–179, American Astronautical Society, Washington, D.C., 1967.
- IX-15. Engel, A. E. J., and Engel, C. G., and Havens, R. G., "Chemical Characteristics of Oceanic Basalts and the Upper Mantle," *Geol. Soc. Amer. Bull.*, Vol. 76, pp. 719–734, 1965.
- IX-16. Urey, H. C., "Primary and Secondary Objects," J. Geophys. Res., Vol. 64, pp. 1721–1737, 1959. Also see "The Origin of Some Meteorites From the Moon," die Naturwissenschaften, Vol. 55, No. 2, pp. 49–57, 1968.
- IX-17. O'Keefe, J. A., Adams, J. B., Gault, D. E., Green, J., Kuiper, G. P., Masursky, H., Phinney, R. A., and Shoemaker, E. M., "Theory and Processes Relating to the Lunar Maria From the Surveyor Experiments," Surveyor VI Mission Report. Part II: Science Results, Technical Report 32-1262, pp. 171–176, Jet Propulsion Laboratory, Pasadena, Calif., January 10, 1968.
- IX-18. O'Keefe, J., "Origin of Tektites," Space Science Reviews, Vol. 6, pp. 174–221, 1966.
- IX-19. Ash, M. E., Shapiro, I. I., and Smith, W. B., "Astronomical Constants and Planetary Ephemerides Deduced from Radar and Optical Observations," *Astron. J.*, Vol. 72, pp. 338–350, 1967.
- IX-20. Gault, D., Collins, R., Gold, T., Green, J., Kuiper, G. P., Masursky, H., O'Keefe, J., Phinney, R., and Shoemaker, E. M., "Lunar Theory and Processes," Surveyors III Mission Report. Part II: Scientific Results, Technical Report 32-1177, pp. 195–213, Jet Propulsion Laboratory, Pasadena, Calif., June 1, 1967.
- IX-21. Norton, R. H., Gunn, J. E., Livingston, W. C., Newkirk, G. A., and Zirin, H., "Astronomy," Surveyor V Mission Report. Part II: Science Results, Technical Report 32-1246, pp. 115–118, Jet Propulsion Laboratory, Pasadena, Calif., November 1, 1967.

X. Post-Landing Tracking Data Analysis

F. B. Winn

This section of this Report describes the Surveyor VII post-landing tracking data acquired by the Deep Space Instrumentation Facility and the utilization of that data to determine the selenocentric location of the probe and the geocentric locations of the Deep Space Stations (DSS) used in the tracking operations. The use of the data as a tool in the lunar ephemeris development and the refining of the atmospheric refraction model are also described. The discussion regarding data utilization encompasses the application of data rejection techniques and the relative weighting of observables and parameters. The lunar ephemerides used in the data reduction are identified, and the associated influences of each ephemeris on the solution are discussed.

The parameter solutions are presented in tabular form with formal standard deviations specified. The probe's position, as determined from *Lunar Orbiter V* photographs, and the cruise data reduction are presented for comparison. The terrestrial tracking positions, as calculated from land surveys and *Ranger* and *Mariner* spacecraft, are compared with the reductions of the *Surveyor VII* data.

A. Tracking Data Acquisition

To maximize the effectiveness of the tracking data sample that could be acquired, the following data acquisition policy was requested:

- (1) All tracking data collection periods to be a minimum of 30 min.
- (2) Tracking data collected during 1 lunar day to be equally distributed throughout the mean lunar pass, as opposed to being collected at the same points or portions during each pass.

An extensive effort was made to create these data characteristics; the resulting coverage is shown in Fig. X-1. Because of the desire to conduct video-oriented research over DSS 11 (Goldstone, California), spacecraft control was frequently transferred as soon as possible to DSS 11 by DSS 42 (Canberra, Australia) and DSS 61 (Robledo, Spain). The lunar rise over DSS 42 and the lunar set over DSS 61, as a consequence, were infrequently observed. Because DSS 11 was primarily obligated to television activities, DSS 42 and DSS 61 acquired most of the tracking data even though their view periods were truncated.

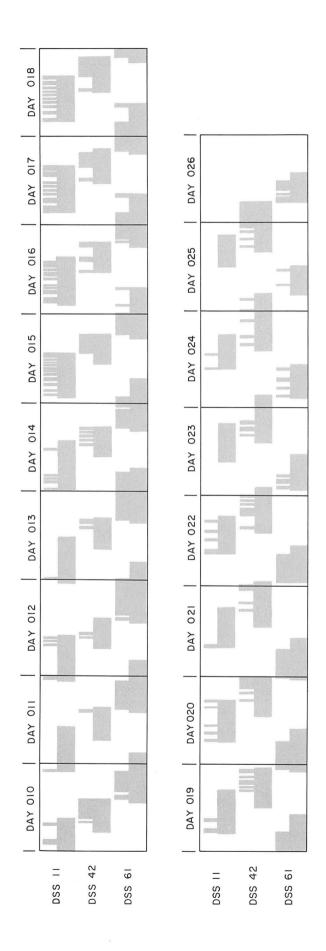


Fig. X-1. Tracking data acquisition times.

ACQUISITION TIMES LUNAR WINDOW

B. Tracking Data Validity and Weighting

Data acquisition procedures and associated influences on the solutions are reflected in the weighting techniques. The tracking data (coherent two-way doppler), as acquired, contained some blunder points which resulted from the existing state of hardware technology, e.g., various noise sources such as teletype communication lines and improper incrementing of the least-significant digits of the doppler cycle counter. In most cases, the invalid data points are recoverable; only a small percentage is invalid (see Table X-1). The detection of these characteristics was accomplished using the raw data in the Single Precision Orbit Determination Program (SPODP; see Ref. X-1) to perform a recursive least-squares fit and inspecting the "observed minus computed" (O - C) residuals. These initial residual sets adequately demonstrate any pronounced irregularities in the data sample (see Figs. X-2 through X-4).

Table X-1. Summary of data utilization

DSS	Data points received	Data points used	Blunder points
11	1547	1481	66
42	1900	1862	38
61	4519	4374	145

C. A Priori Parameter Constraints

It is possible to constrain the terrestrial tracking station position parameters in the SPODP tracking data reduction to those of some previous determination. However, such a constrained solution can lead to systematic distortion. There are many time-dependent variables incorporated in the theoretical model (e.g., E. W. Brown's lunar theory, lunar librations, terrestrial diurnal rotation, ionosphere, space plasma effects, etc.). There is a series

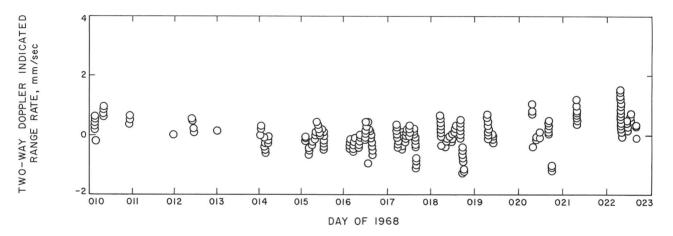


Fig. X-2. Surveyor VII, DSS 11 (Goldstone, California). First lunar day, O — C residual set (one data point/min). DE 29/LE 5 was used.

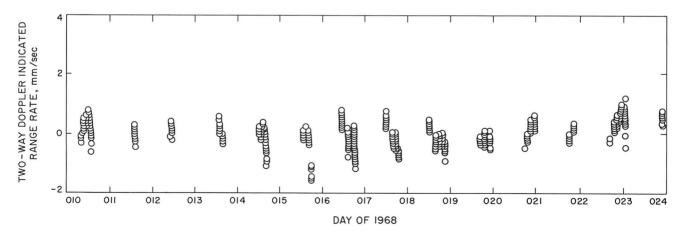


Fig. X-3. Surveyor VII, DSS 42 (Canberra, Australia). First lunar day, O-C residual set (one data point/min). DE 29/LE 5 was used.

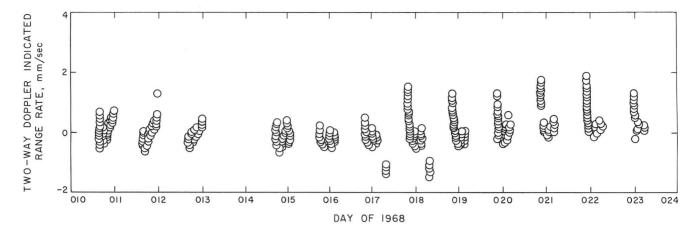


Fig. X-4. Surveyor VII, DSS 61 (Robledo, Spain). First lunar day, O — C residual set (one data point/min). DE 29/LE 5 was used.

of models used to provide values for some of these time-dependent parameters, and some are not modeled at all. Thus, there is always the danger of introducing systematic errors into a tracking data fit by constraining to the previously determined terrestrial tracking station positions in accordance with the associated variance/covariance matrix. It was with this perspective that the entire parameter list was assigned a priori standard deviations which, in effect, unconstrain the parameters. The a priori standard deviations associated with the parameters are:

- (1) Surveyor VII selenocentric distance: 10 km.
- (2) Surveyor VII selenocentric latitude: 5.0 deg (150 km).
- (3) Surveyor VII selenocentric longitude: 5.0 deg (150 km).
- (4) DSS 11 geocentric distance: 300 m.
- (5) DSS 11 geocentric longitude: 0.005 deg (0.5 km).
- (6) DSS 42 geocentric distance: 300 m.

- (7) DSS 42 geocentric longitude: 0.005 deg (0.5 km).
- (8) DSS 61 geocentric distance: 300 m.
- (9) DSS 61 geocentric longitude: 0.005 deg (0.5 km).

The initial estimate of the location of *Surveyor VII* was derived from the cruise tracking data reduction corrected for thruster braking, which occurred during *Surveyor VII* lunar descent (see Ref. X-2 and Table X-2). Station locations were those determined from *Mariner IV* data reduction (Ref. X-3 and Table X-3).

D. Lunar Ephemerides

Two lunar ephemerides were used:

(1) Lunar Ephemerides 4 (LE 4), which was coupled with the Jet Propulsion Laboratory planetary ephemeris to produce Developmental Ephemeris 19 (DE 19), and is currently being distributed to all NASA project ephemeris users (Refs. X-4 and X-5).

Table X-2.	Summary	of Surveyor	VII location	determinations

Source	Selenocentric latitude, ϕ , deg	Standard deviation of ϕ	Selenocentric longitude, λ, deg	Standard deviation of λ	Lunar radius, R	Standard deviation of R
1ª	40.95 S	_	348.59	_	_	_
2 ^b	41.01 S	0.069	348.59	0.054	_	_
3°	40.86 S	0.050	348.473	0.033	1741.695	1.752
4 ^d	40.76 S	0.049	348.658	0.033	1744.704	1.755
5°	40.86 S	0.050	348.473	0.033	1741.597	1.752

a Lunar Orbiter V photographs (see Ref. X-2).

^bTerminal cruise SPODP position (cruise data; see Ref. X-2).

 $^{^{\}mathrm{c}}$ SPODP post-landed Surveyor VII tracking data reduction using DE 29/LE 5.

dSPODP post-landed Surveyor VII tracking data reduction using DE 19/LE 5.

SPODP post-landed Surveyor VII tracking data reduction using DE 29/LE 5, coupled with refined tropospheric refraction model.

Table X-3. Summary of Deep Space Station locations

DSS	Source	Spin axis distance, m	Longitude, deg
11	Surveyor I	5206.3276	243.15085
	Surveyor III	_	_
	Surveyor V	.2670	.15114
	Surveyor VI (DE 19/LE 4)	.3317	.15081
	Surveyor VI (DE 29/LE 5)	.3315	.15083
	Combined Ranger position of DSS 12 corrected to DSS 11 by land survey	.3266	.15089
	Combined Ranger position of DSS 12 corrected to DSS 11 by Mariner IV deltas	.3275	.15090
	Surveyor VII (DE 29/LE 5)	.332	.15114
	Surveyor VII (DE 19/LE 4)	.339	.15063
	Surveyor VII (DE 29/LE 5 + refraction refinement)	.337	.15114
	Goddard survey	.3718	.15094
42	Surveyor I	5205.3474	148.98130
	Surveyor III	.3581	.98127
	Surveyor V	.3553	.98175
	Surveyor VI (DE 19/LE 4)	.3423	.98147
	Surveyor VI (DE 29/LE 5)	.3395	.98157
	Combined Ranger position of DSS 12 corrected to DSS 42 by Mainer IV deltas	.3403	.98157
	Surveyor VII (DE 29/LE 5)	.343	.98187
	Surveyor VII (DE 19/LE 4)	.348	.98135
	Surveyor VII (DE 29/LE 5 + refraction refinement)	.346	.98187
	Goddard survey	.2940	.98006
61	Surveyor I	_	_
	Surveyor III	4862.5993	355.75101
	Surveyor V	.5992	.75149
	Surveyor VI (DE 19/LE 4)	.6031	.75120
	Surveyor VI (DE 29/LE 5)	.6045	.75120
	Combined Ranger position of DSS 12 corrected to DSS 61 by Mariner IV deltas	.6077	.75122
	Surveyor VII (DE 29/LE 5)	.603	.75154
	Surveyor VII (DE 19/LE 4)	.606	.75103
	Surveyor VII (DE 29/LE 5 + refraction refinement)	.605	.75155
	JPL land survey	.6482	.75182

(2) Lunar Ephemeris 5 (LE 5), which was coupled with the Jet Propulsion Laboratory planetary ephemeris to produce Developmental Ephemeris 29 (DE 29), and is an extensive refinement of LE 4 (Ref. X-6).

The LE 4, regarded as the modern, evolved Brown lunar theory, has been discovered recently to have radial components of position and velocity that deviate from observations (see Refs. X-7 and X-8).

The LE 5 is a numerical integration of the equations of motion, that uses LE 4 positions as input observables (Ref. X-6). Essentially, this amounts to a smoothed LE 4, which is gravitationally consistent.

E. Parameter Solution Vector

Of the Surveyor VII post-landed tracking data reductions, three have undergone sufficient analysis to be reported on at this time. The three reported solutions involve two lunar ephemerides and subtle variations in

the tropospheric refraction parameter. The influence of such variations on the $\mathrm{O}-\mathrm{C}$ residuals is dramatically demonstrated and discussed in Section X-F of this Report. The influence of such manipulations on the parameter solution vectors is shown in Table X-4 with formal standard deviations specified.

Surveyor VII selenocentric positions, derived from the use of DE 29/LE 5 and DE 19/LE 4, are consistently displaced from each other. The selenocentric components of the displacement are:

Radial:

3010 m

Lunar latitude:

3000 m

Lunar longitude: 5550 m

The displacement is characteristic of the lunar ephemerides used in the reduction. Tracking data reductions for probe positions of $Surveyor\ I$ (Ref. X-7) and $Surveyor\ VI$ (Ref. X-9) using DE 29/LE 5 and DE 19/LE 4 also exhibit large relative displacements.

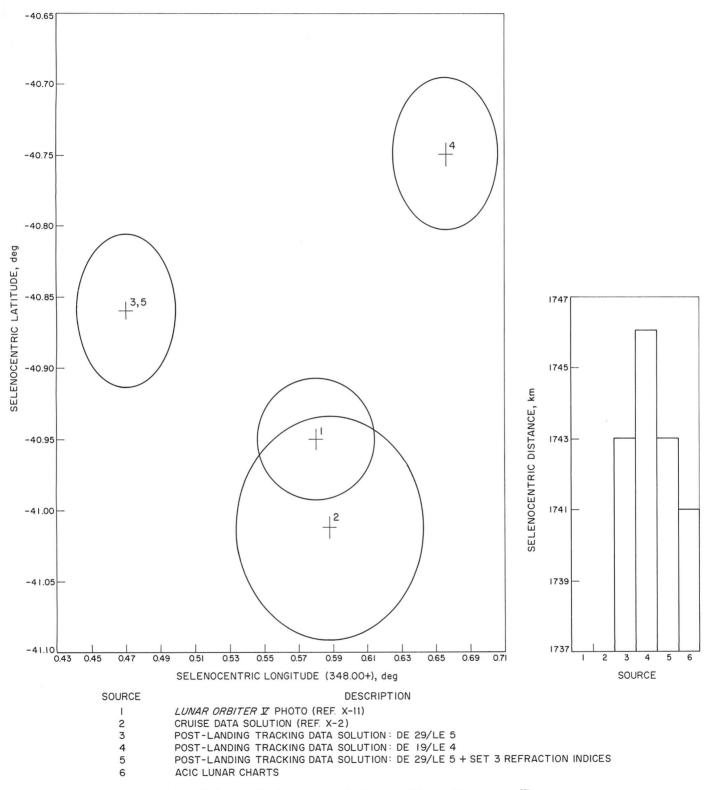


Fig. X-5. Relative displacements of selenocentric position error ellipses.

Table X-4. Surveyor VII parameter solutions

A priori		DE 29/LE 5 solutions			DE 19/LE 4 solutions		
Parameters ^a	Parameter estimates	Standard deviation	Without refraction refinement	Standard deviation	With refraction refinement	Without refraction refinement	Standard deviation
RADS, km	1736.0	10.0	1741.695	1.752	1741.692	1744.704	1.755
LATS, deg	-41.1	5.0	-40.858	0.050	-40.858	-40.757	0.049
LONS, deg	348.560	5.0	348.473	0.033	348.473	348.658	0.033
DSS 11 ^b							
rs, km	5206.333	0.24	5206.332	0.002	5206.337	5206.339	0.002
LO, deg	243.15070	0.005	243.15114	0.0001	243.15114	243.15063	0.0001
DSS 42 ^b							
rs, km	5205.348	0.24	5205.344	0.003	5205.346	5205.348	0.002
LO, deg	148.98140	0.005	148.98187	0.0001	148.98187	148.98135	0.0001
DSS 61 ^b							
r _s , km	4862.601	0.24	4862.603	0.001	4862.605	4862.606	0.002
LO, deg	355.75114	0.005	355.75154	0.0001	355.75155	355.75103	0.0001

aThe parameters are defined as:

RADS selenocentric distance of Surveyor VII

LATS selenocentric latitude of Surveyor VII

LONS selenocentric longitude of Surveyor VII

 $r_{\rm s}$ spin-axis distance of Deep Space Stations LO geocentric longitude of Deep Space Stations

bTerrestrial tracking station locations referenced to 1903.0 poles.

The error ellipsoids resulting from these data reductions have effectively the same respective dimensions. This is due to the use of one preliminary, scrubbed tracking data sample in all parameter solutions. The relative displacements of the *Surveyor VII* selenocentric position error ellipses are shown in Fig. X-5 along with the position determinations using *Lunar Orbiter V* photographs (see Section III of this Report) and *Surveyor VII* cruise data fits (Ref. X-2) for comparison.

The effect of tropospheric refraction-correction variations on the data fits is shown in Figs. X-6 through X-8. The primary influence of the refraction parameter is on the terrestrial tracking station coordinates. An examination of Table X-2 will disclose the fact that the probe's position remains fixed as the refraction mode is varied, and that the terrestrial tracking stations are displaced significantly. DSS 11 is moved radially away from the earth's spin axis, as is DSS 42 and DSS 61. The increased spin-axis distance is:

DSS 11: 5 m

DSS 42: 2 m

DSS 61: 2 m

The terrestrial station longitude response to the tropospheric refraction correction is effectively zero.

The statistical dependence of one parameter in relation to other parameters within a recursive least-squares fit can be inferred from the correlations of the parameter in question and the remaining parameter list. The small magnitudes of the parameter correlations in the correlation matrices (Table X-5) indicate the relative statistical independence of the parameters. A model weakness to be noted is the high correlation exhibited between all selenocentric and geocentric longitude determinations. In addition, the high correlation of the probe's selenocentric distance and latitude parameters should be noted.

F. Observed Minus Computed Residuals

The deficiencies of the data fits are demonstrated by the O-C residuals. In terms of past experience, these solutions are good; however, in an absolute sense, the model's evolution has not proceeded far enough. Diurnal periodicities and longer-term periodicities, coupled with data high-frequency noise and computer noise, are the obvious deficiencies. The standard deviation of the high-frequency noise associated with the residual sets is $0.13 \, \mathrm{mm/sec} \, (0.002 \, \mathrm{Hz})$.

The longer-term periodicities demonstrated by the residual sets (see Figs. X-9 through X-11) are as anticipated. The residual sinusoidal pattern is descriptive of the rangerate differences between LE 5 and LE 4 (Ref. X-7) after least-squares minimization has been attempted. The LE 5 is a better model of lunar motion than LE 4.

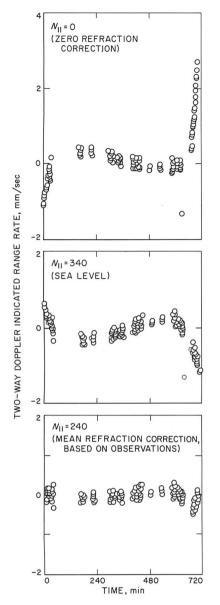


Fig. X-6. DSS 11, Pass 11. Refraction influence on SPODP residuals.

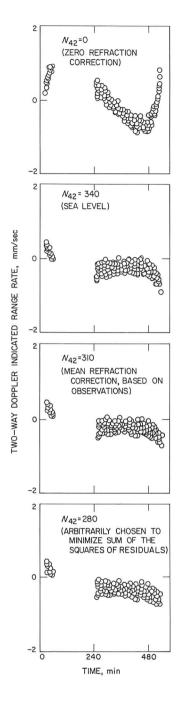


Fig. X-7. DSS 42, Pass 11. Refraction influence on SPODP residuals.

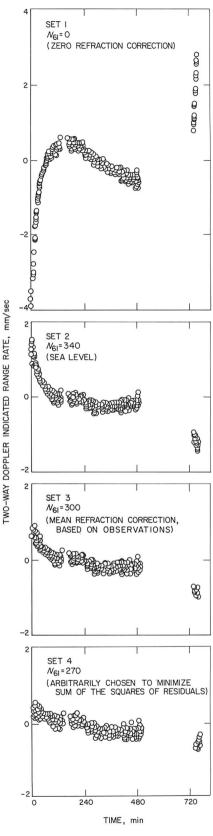


Fig. X-8. DSS 61, Pass 11. Refraction influence on SPODP residuals.

Table X-5. Correlation matrix (DE 29/LE 5)^a

D b	Standard		Surveyor VI	I	DS	S 11	DS	55 42	DSS	61
Parameter ^b	deviation	RADS	LAT	LONS	RI	LO	RI	LO	RI	ro
Surveyor VII										
RADS	1.752	1.0	0.964	0.396	0.346	0.062	0.121	0.073	0.256	0.049
LATS	0.050		1.0	0.153	0.422	0.310	0.179	0.321	0.352	0.300
LONS	0.033			1.0	-0.121	-0.878	-0.130	-0.875	-0.202	-0.892
DSS 11										
RI	0.002				1.0	0.316	0.128	0.313	0.234	0.308
ro	0.0001					1.0	0.028	0.976	0.356	0.982
DSS 42										
RI	0.003						1.0	0.128	0.134	0.208
ιo	0.0001							1.0	0.358	0.984
DSS 61										
RI	0.002								1.0	0.386
ιο	0.0001									1.0

[&]quot;No refinement of refraction model.

RADS selenocentric distance of Surveyor VII

LATS selenocentric latitude of Surveyor VII

LONS selenocentric longitude of Surveyor VII

RI geocentric distance of Deep Space Stations
LO geocentric longitude of Deep Space Stations

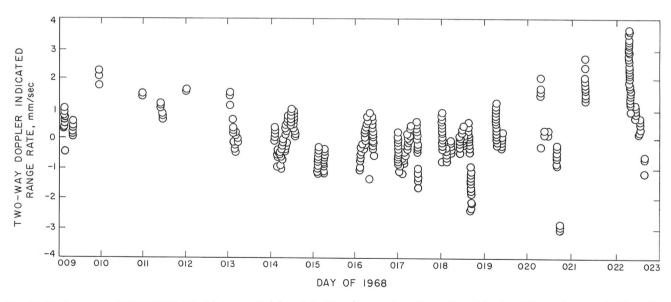


Fig. X-9. Surveyor VII, DSS 11 (Goldstone, California). First lunar day, O - C residual set (one data point/min). DE 19/LE 4 was used.

^bThe parameters are defined as:

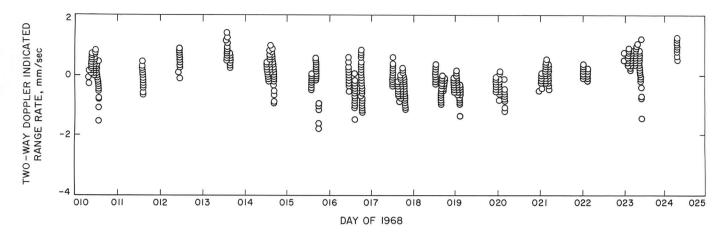


Fig. X-10. Surveyor VII, DSS 42 (Canberra, Australia). First lunar day, O - C residual set (one data point/min). DE 19/LE 4 was used.

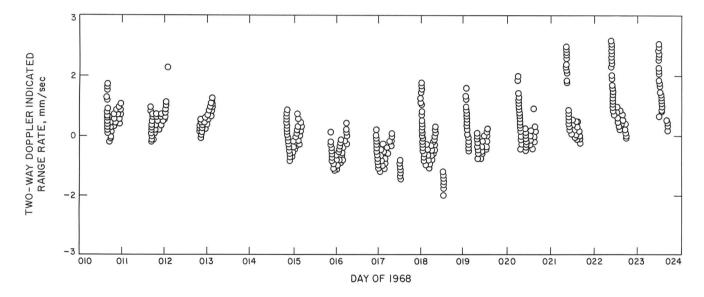


Fig. X-11. Surveyor VII, DSS 61 (Robledo, Spain). First lunar day, O-C residual set (one data point/min). DE 19/LE 4 was used.

The absence of any detectable long-term pattern in the DE 29/LE 5 O - C residual sets indicates the ability of LE 5 to model the lunar motion (see Figs. X-2 through X-4).

The diurnal nature of the Surveyor VII O - C residuals is of the same nature as the daily variations identified with the O - C residuals of Surveyors I, III, V, and VI. However, because of the acquisition of Surveyor VII low-elevation tracking data, a more complete picture of the residual behavior was made available. The diurnal signature in evidence is characterized by Figs. X-6 through X-8. This signature can be attributed to tropospheric

refraction (from deficient modeling), ionospheric charged-particle effects (not modeled), and/or station spin-axis distance, or latitude errors (suspected lunar ephemeris defect). Because of the high correlation between these variables, the majority of the influence of these combined errors on the O-C residuals can be effectively removed by simply incorporating any one of the three variables into the SPODP as a solution parameter. It is not the intent of such a procedure to numerically evaluate, in a physically meaningful manner, any one of the three parameters; this approach simply provides a means of increasing the accuracy of the data fit by using a combination parameter. Investigations by Liu (Ref. X-10) and

Mulholland (Ref. X-11) have ordered the three-error variables in accordance with the magnitude of each one's influence:

- (1) Tropospheric refraction: about 3 mm/sec per 100 index-of-refraction units at 0-deg elevation (maximum).
- (2) Suspected lunar ephemeris error functions: about 1.0 mm/sec (maximum).
- (3) Ionospheric charged-particle effect: about 0.5 mm/ sec (maximum).

The refraction errors in the tracking data have been empirically determined and programmed into the SPODP (Ref. X-1). The form of the empirical refraction function is:

$$\Delta r\dot{
ho} = rac{C_1}{ au} \left\{ \!\! rac{1}{\left[\sin\left(\gamma + rac{\dot{\gamma} au}{2}
ight) + C_2
ight]^{c_3}}
ight.
onumber \ - rac{1}{\left[\sin\left(\gamma - rac{\dot{\gamma} au}{2}
ight) + C_2
ight]^{c_3}} \!\!
ight\} rac{N}{340.0}$$

where C_1 , C_2 , and C_3 are empirically determined constants ($C_1=0.0018958$, $C_2=0.06483$, $C_3=1.4$) and

 $\Delta r\dot{\rho} = \text{refraction}$ correction applied to SPODP-calculated data types, Hz

 $\tau =$ doppler count interval, sec

 γ = elevation angle, rad

 $\dot{\gamma}$ = rate of elevation-angle change, rad/sec

N = index of refraction

The tropospheric refraction indices, N, used in the SPODP solution for the Deep Space Stations are all set at N=340.0. Recent research by Liu (Ref. X-10) has provided evidence that the following values for N are more precise:

DSS 11: $N_{11} = 240.0$

DSS 42: $N_{+2} = 300.0$

DSS 61: $N_{61} = 310.0$

The influence of atmospheric refraction is primarily a phase retardation plus a bending, and consequential lengthening, of the ray path. If a ranging data type is acquired, incorrect modeling of refraction is viewed as an apparent station-probe range change during the course of a pass. If a range-rate data type is acquired, refraction

model errors will indicate a station-probe relative acceleration as the elevation of the observation changes. By using Liu's formulation, an error of 100 units of N generates O - C residuals of 0.5 Hz (33 mm/sec) for horizon range-rate observations. The refraction-induced O-Cresidual signature contained in Ref. X-10 resembles a capital "S" rotated at +90 deg; this resembles the O - C residual characteristics of the Surveyor VII passes. Compared with other stations, DSS 11 most frequently acquired low-elevation tracking data. An examination of Fig. X-6 (DSS 11 residuals, pass 11) shows significant elevation-dependent O-C residual biases, which correlate remarkably well with the computed refraction-error functions. Examination of Figs. X-7 and X-8, pertaining to DSS 42 and DSS 61, reveals evidence of like influences. Future analyses will incorporate the more precise refraction indices; it is hoped that the O-C residual elevation-dependent characteristics will be diminished appreciably.

The ionospheric influence on the data type becomes a function of slant range and the effective electron density. Ionospheric charged-particle effects have been omitted from model consideration to the present. The residual signature resulting from this omission is similar to the tropospheric refraction-error signature; however, the ionospheric influence on the tracking data is of a lesser magnitude.

A history of ionospheric activity for the first lunar day of all successful Surveyor missions is being compiled. Once this information is available, the correlation of the O-C residuals and refraction and ionosphere will be investigated more fully.

Although the troposphere is an acknowledged major, but unevaluated, error source that warrants the evaluation efforts underway, there are other model limitations such as the lunar ephemeris. The lunar ephemeris is currently suspected of having two specific defects incorporated within its structure.

J. D. Mulholland is currently investigating this phenomenon (Ref. X-11). He has ventured to estimate the combined effects of the J_{2_0} defect (incorrect coefficient of the second harmonic term of the harmonic series used to describe the lunar gravitational potential) and the suspected faulty fitting of observations to Brown's lunar theory. Although Mulholland finds his present findings inconclusive, he has demonstrated a high correlation between the combined functions and the diurnal trait of the Surveyor I O — C residuals (Ref. X-7).

¹M. Davis, Stanford University Electronics Laboratories, California.

Mulholland has determined the possible influence of these functions for the first lunar day of the *Surveyor VI* mission. A comparison of residual sets and the suspected error functions fails to provide the assurance that there is a relationship between the residuals and these suspected error functions (Ref. X-9).

A similar comparison of these suspected error functions and $Surveyor\ VII\ O-C$ residuals (Fig. X-12) provides an inconclusive correlation between the functions and the residuals.

Mulholland is currently constructing a new integrated ephemeris (LE 8), which will contain the influences of the two error functions. Once available, a more detailed analysis can be conducted. All comparisons of the functions and the O-C residuals of Surveyors I, VI, and VII have been based upon approximations of the combined error function to one significant place.

The use of one "combinational parameter," as a means of fitting out of the O-C residual sets the influences resulting from tropospheric refraction, ionospheric charged-particle effects, and lunar ephemeris defects, is the only available approach at this time.

The results from the use of this procedure are most striking. The preponderance of the diurnal signature has been removed by the manipulation of the refraction-correction function. Figures X-6 through X-8 show that the O-C residuals emanating from the several SPODP Surveyor VII tracking data reductions used the following refraction indices:

(1)
$$N_{11} = N_{42} = N_{61} = 0$$
 No refraction correction
(2) $N_{11} = N_{42} = N_{61} = 340.0$ Sea-level refraction correction
(3) $N_{11} = 240$ Refraction correction based on observations of $N_{42} = 310$ based on observations of $N_{61} = 300$ Lunar Orbiter II (Ref. X-12)
(4) $N_{11} = 240$ Arbitrarily chosen to

minimize the sum of the

square of the residuals

G. Conclusions

 $N_{42} = 280$

 $N_{61} = 270$

Although substantial progress has been made in the analysis of the post-landing *Surveyor VII* tracking data, the investigation is incomplete. With the advent of a more refined *Surveyor VII* data sample currently in construction and the efforts presently in progress, the lunar ephemeris development, a more precise tropospheric refraction model, and the ionospheric charged-particle effects model are some of the anticipated major developments.

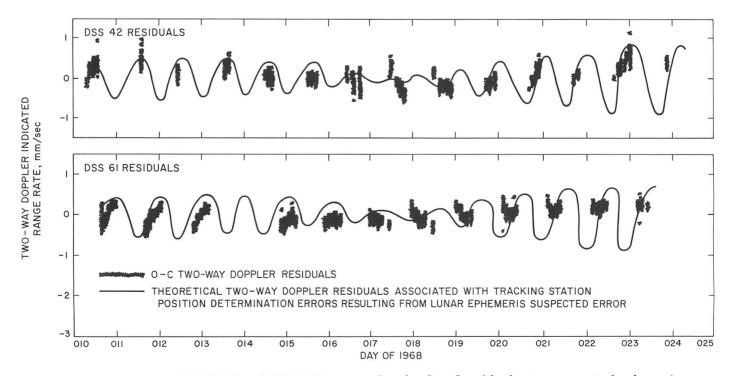


Fig. X-12. Surveyor VII, DSS 42 and DSS 61. Two-way doppler O - C residual set vs suggested ephemeris-dependent tracking station position error. DE 29/LE'5 was used, coupled with refraction refinement.

References

- X-1. Warner, M. R., and Nead, M. W., SPODP—Single Precision Orbit Determination Program, Technical Memorandum 33-204, Jet Propulsion Laboratory, Pasadena, Calif., February 15, 1965.
- X-2. Surveyor VII Mission Report. Part I: Mission Description and Performance, Technical Report 32-1264, Jet Propulsion Laboratory, Pasadena, Calif. (to be published).
- X-3. Mottinger, N. A., and Trask, D. W., "Status of DSS Location Solutions for Deep Space Probe Missions: I. Initial Comparisons," *The Deep Space Network*, Space Programs Summary 37-48, Vol. II, pp. 12–22, Jet Propulsion Laboratory, Pasadena, Calif., November 30, 1967.
- X-4. Lawson, C. L., Announcement of JPL Developmental Ephemeris No. 19, Technical Memorandum 33-162, Jet Propulsion Laboratory, Pasadena, Calif., April 13, 1967.
- X-5. Mulholland, J. D., and Block, N., *JPL Lunar Ephemeris Number 4*, Technical Memorandum 33-346, Jet Propulsion Laboratory, Pasadena, Calif., August 1, 1967.
- X-6. Devine, C. J., "Description of a Numerical Integration of Lunar Motion Employing a Consistent Set of Constants," Supporting Research and Advanced Development, Space Programs Summary 37-48, Vol. III, Jet Propulsion Laboratory, Pasadena, Calif., December 31, 1967.
- X-7. Sjogren, W. L., and Cary, C. N., "Lunar Ephemeris Errors Confirmed by Radio Observations of Lunar Probes," *The Deep Space Network*, Space Programs Summary 37-48, Vol. II, pp. 4–7, Jet Propulsion Laboratory, Pasadena, Calif., November 30, 1967.
- X-8. Sturms, F. M., Jr., "An Integrated Lunar Ephemeris," *The Deep Space Network*, Space Programs Summary 37-48, Vol. II, pp. 7–12, Jet Propulsion Laboratory, Pasadena, Calif., January 10, 1967.
- X-9. Winn, F. B., "Selenographic Location of Surveyor VI," Surveyor VI Mission Report. Part II: Science Results, Technical Report 32-1262, Jet Propulsion Laboratory, Pasadena, Calif., January 10, 1968.
- X-10. Liu, A., "Recent Changes to the Tropospheric Refraction Model Used in the Reduction of Radio Tracking Data From Deep Space Probes," *The Deep Space Network*, Space Programs Summary 37-50, Vol. II, Jet Propulsion Laboratory, Pasadena, Calif., March 31, 1968.
- X-11. Mulholland, J. D., "A Possible Explanation of Landed Surveyor Residuals," The Deep Space Network, Space Programs Summary 37-49, Vol. II, Jet Propulsion Laboratory, Pasadena, Calif., January 31, 1968.
- X-12. Mottinger, N. A., "Effect of New Tropospheric Corrections on *Lunar Orbiter II* Cruise Solution Vector," *The Deep Space Network*, Space Programs Summary 37-50, Vol. II, Jet Propulsion Laboratory, Pasadena, Calif., March 31, 1968.

XI. Laser Beam Pointing Tests

C. O. Alley (Chairman) and D. G. Currie

An opportunity to verify the ability of earth stations for directing very narrow laser beams to a specific location on the lunar surface was provided by the detection sensitivity of the Surveyor VII vidicon camera operating in its integration mode. Such tests were of interest primarily because of a planned Apollo lunar surface experiment in which an astronaut will emplace a corner reflector array to provide a fixed point for very precise laser ranging. The successful monitoring of point-to-point earth-moon distances to the expected accuracy of $\pm 15~\mathrm{cm}$ would provide: (1) a definitive test of the conjectured slow decrease of the gravitational constant; (2) an experimental study of whether continental drift is occurring now; (3) new knowledge on the physical librations, size and shape, and orbital motions of the moon; and (4) new information on the rotation of the earth (Refs. XI-1 through XI-4). An additional factor in testing narrow laser beam pointing and tracking techniques lies in their potential use in space communications systems.

The idea of using a *Surveyor* television camera for such tests occurred during a discussion on whether an astronaut could see the pulsed ruby laser beam planned for the retro-reflector ranging experiment. Measurements on the wavelength sensitivity of the vidicon surface were

conducted in November 1967 at the Jet Propulsion Laboratory (JPL) and indicated a decrease from the peak sensitivity by a factor 1/300 for the ruby laser wavelength of 6943 Å, making detection marginal for existing and planned ruby laser systems. However, the availability of argon-ion lasers operating in the blue-green (main wavelengths at 4880 and 5145 Å), within the peak of the vidicon sensitivity with average power of a few watts, suggested their use for the tests. The pointing and tracking techniques would be similar to those used with pulsed lasers.

Estimates of the power density on the moon of a 10-W (transmitted) argon-ion laser beam contained within a divergence cone angle (half) of 10 sec of arc yielded a value 2.25 times the power density of a magnitude 0 star, or nearly magnitude -1. The power density would scale directly as the power transmitted and inversely as the square of the beam angle. Experience with star observations on previous *Surveyor* missions (p. 15 of Ref. XI-5) indicated that the laser beams could be easily observed if they were directed to illuminate the spacecraft. The diameter of the illuminated area on the moon is about 2 km per arc second of divergence.

A. Laser Transmitting Stations

Six transmitting stations were established; each consisted of an argon-ion laser with a suitable optical system for collimating and aiming the laser beam. All six stations used the technique of directing the laser beam backward through a telescope to reduce the beam divergence. However, each station used a different method for aiming the laser beam. A brief description of each station is given below.

- (1) Kitt Peak National Observatory, Tucson, Arizona. The McMath Solar Telescope (60-in., f/60, heliostat configuration) and a 2-W laser were used. The telescope was used in the normal direction for aiming. The guide beam and the laser beam were separated by a specially constructed, divided-mirror beam splitter placed near the telescope focal plane. A reticle, which was designed for the purpose and which permitted offset guiding from nearby lunar features, and a field lens were placed in the focal plane.
- (2) Table Mountain Observatory, Wrightwood, California. The JPL 24-in. telescope, utilized at its f/36 Coudé focus, and a 2-W laser were used. A beam splitter with a pinhole was placed in the telescope focal plane to separate the guide beam from the laser beam. A 2.5 magnification microscope with a crosshair reticle was used as a viewing eyepiece.
- (3) Wesleyan University, Raytheon Research Laboratory, Waltham, Massachusetts. A 6-in. two-mirror coelostat directed the beam from a specially constructed 4-in., f/15, telescope toward the moon; a 60-W laser was used. The guide beam and the laser beam were separated using a clear pellicle beam splitter located ahead of the primary focal plane. The use of an appropriate glass film over the eyepiece permitted continuous viewing of the crosshair reticle.
- (4) Lincoln Laboratories, Lexington, Massachusetts. A beam from a 3.5-W laser collimated with a 3-in. telescope was directed using a special servo driven az-el flat mirror. Guiding was accomplished using a second 3-in. telescope, which was boresighted to the first telescope.
- (5) Goddard Space Flight Center, Greenbelt, Maryland. An existing mobile laser satellite ranging system was used; the pulsed ruby laser was replaced by a 10-W argon-ion laser. A series of mirrors guided the beam along the rotation axes of the az-el mount through a 5½-in. output aperture.

- Viewing of the moon was accomplished by an image orthicon television display from a bore-sighted 16-in. telescope.
- (6) Perkin-Elmer Corporation, Norwalk, Connecticut. A portable 2-W laser was attached at the Cassegrain focus of a 24-in. telescope. Aiming was accomplished by the 6-in. guide telescope, which was boresighted to the main telescope.

To aid in locating Surveyor VII on the lunar surface, Lunar Orbiter photographs of the region around Tycho and ACIC Lunar Chart LAC 112 were supplied to all stations. The initial estimates of the landing coordinates, as well as the accurate location of Surveyor VII (see Section III of this Report), were communicated with respect to both the Lunar Orbiter photographs and the lunar chart.

B. Schedule of Lunar Tests

The heavy demands on the Surveyor camera resulted in the initial allocation of only one 10-min block of laser observing time on each of four different nights. By combining the laser observations with the planned earthlight polarization observations, it was possible to increase the length of observing periods and to have a second period on Day 020. Time windows were chosen so that stations on both East and West Coasts could be observed simultaneously during control of the spacecraft by the Goldstone Deep Space Tracking Station; the primary constraint was that no station be too close to the terminator. During the window, the laser stations were responsive to the availability of the television camera. Communication was handled by a telephone network connecting all stations with the JPL Space Flight Operations Facility.

The first few days after touchdown were needed for other *Surveyor* activities and were used for final preparations at the stations. With the exception of the Norwalk and Greenbelt Stations, the first test period was held at 04:30 GMT on Day 014. It was necessary to interrupt the tests during the period near lunar noon because of glare in the camera caused by the proximity of the earth and sun. This time was used to modify techniques at some of the stations on the basis of the first test. Test periods were resumed on Day 019, and continued on Days 020 and 021. The time on Day 021 was chosen to maximize the probability of observing stations to the East Coast by having them far from the terminator even though, for the West Coast stations, it placed the moon very low in the sky.

During each test period, modes of operation for the stations were prescribed with definite on and off sequences to identify stations that were geographically close together. The aperture and exposure time were varied to produce on the A-scope display approximately one-half the saturation voltage level in the dark part of the earth crescent where laser beams were being transmitted, as this maximized the sensitivity. With this setting, repeated exposures were taken while the stations were directed to follow the above modes.

C. Detection of Laser Beams

Detection was achieved visually during the first observing period on Day 020 for both Tucson and Wrightwood. Suspected laser beam spots with the correct locations, as shown in Fig. XI-1, were observed at the JPL Space Flight Operations Facility. Further confirmation resulted when the earth image was shifted 3 deg within the 6.5-deg narrow field of view, the two spots shifting with it. The on-off sequencing discussed above also served to verify the detection of the beams. Full confirmation was obtained only with the subsequent, detailed study of correlations in projected enlargements from high-quality photographic negatives reproduced from the video tape recordings by kinescope film recorder. A positive print of one of the negatives, enhanced using a high-contrast process, is shown in Fig. XI-2. The spread of the images over several of the video scan lines is caused by aberrations in the optics (electron and visible) of the camera and also in the ground reproducing equipment.

Each of the stations detected was transmitting about 1 W, after telescope and atmospheric losses, with a beam divergence (full-angle) of about 3 sec of arc. Wrightwood was systematically scanning about the position of Surveyor VII and was limited by atmospheric "seeing," while Tucson had deliberately spread the beam. The spots appeared with an approximate star magnitude of -1, as originally calculated. Detection of these stations was accomplished again visually with about the same

intensity during the second run on Days 020 and 021. The approximate magnitude of the detected beams was determined by comparing pictures of the laser beams with those of Jupiter.

By digitization of the video pictures, it has been possible to increase the sensitivity of detection considerably beyond the visual. It is estimated that, by stretching the digitization in regions near station locations, intensities of laser beams directed to illuminate *Surveyor VII* can be detected with ½5 the intensity displayed by Tucson and Wrightwood. This technique enabled easy detection of the Tucson beam on Day 019. (Wrightwood was not operating on that day.)

A search for beams from the East Coast station has been made with the equipment at the University of Maryland, developed for visual scan of bubble chamber pictures. No positive results were found. Examination of the stretched digitized printouts has not given positive indication as yet, but the work is continuing with the technique of averaging successive frames for enhancement and looking for correlations at predicted locations. Although local weather conditions and structural obscurations interfered with transmission from East Coast stations (especially in the Boston area), there were periods when contact with *Surveyor VII* seemed possible.

D. Conclusions

The primary value of these tests lies in the experience gained in a variety of techniques for tracking and pointing laser beams with different types of telescopes. A report on this subject will be prepared by members of this *Surveyor* Working Group.

The potential value of well collimated laser beams for space communications is emphasized by noting that the 1-W laser beams appeared as bright stars, while the uncollimated light from major cities was not detected.

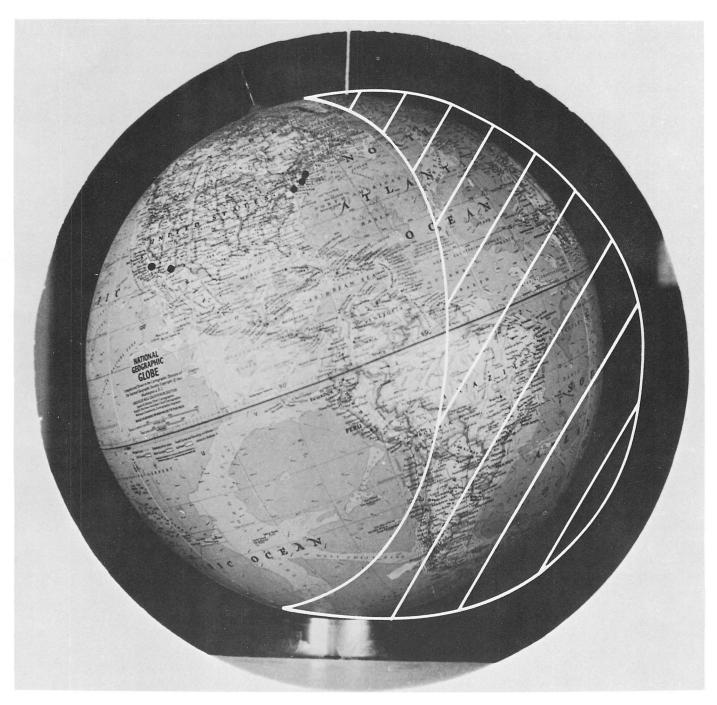


Fig. XI-1. This photograph of a globe, with the overexposed crescent indicated by cross-hatching, simulates the earth as seen from Surveyor VII at 09:00 GMT on Day 020. The station locations are indicated by black dots, and permit ready identification of the origin of the two laser beams in Fig. XI-2 as Table Mountain Observatory near Los Angeles, California, and Kitt Peak National Observatory, near Tucson, Arizona. Simulations similar to this photograph were prepared in advance by J. J. Rennilson, JPL, for each period of attempted laser detection.

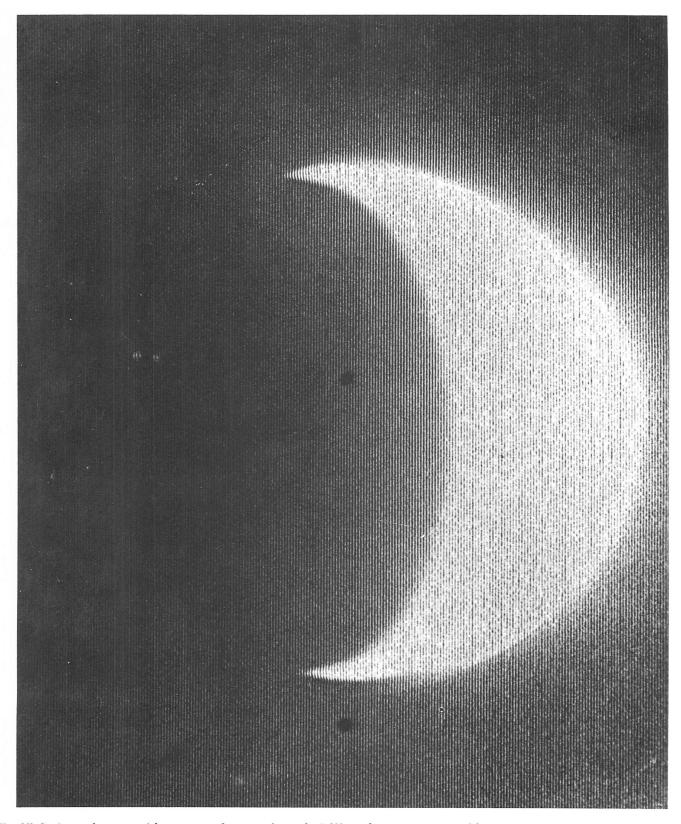


Fig. XI-2. Laser beams with powers of approximately 1 W each appear as starlike images comparable in brightness to Sirius (magnitude, -1.4) in this narrow-angle, f/4, 3-sec exposure of the earth. The crescent of the sun-illuminated earth is distorted because of overexposure. This was one of the first pictures in which the beams were readily visible (Day 020, about 09:06 GMT).

References

- XI-1. Alley, C. O., Bender, P. L., Dicke, R. H., Faller, J. E., Franken, P. A., Plotkin, H. H., and Wilkinson, D. T., "Optical Radar Using a Corner Reflector on the Moon," *J. Geophys. Res.*, Vol. 70, pp. 2267–2269, 1965.
- XI-2. Alley, C. O., and Bender, P. L., "Information Obtainable from Laser Range Measurements to a Lunar Corner Reflector," to be published in the *Proceedings of the IAU/IUGG Symposium on Continental Drift*, Secular Motion of the Pole, and Rotation of the Earth (William Markowitz and B. Guinot, editors), symposium held at Stresa, Italy, March 21–25, 1967.
- XI-3. Alley, C. O., Bender, P. L., Currie, D. G., Dicke, R. H., and Faller, J. E., "Some Implications for Physics and Geophysics of Laser Range Measurements from Earth to a Lunar Retro-Reflector," to be published in the Proceedings of the N. A. T. O. Advanced Study Institute on the Application of Modern Physics to the Earth and Planetary Interiors (S. K. Runcorn, editor), symposium held at the University of Newcastle upon Tyne, March 29–April 4, 1967.
- XI-4. MacDonald, G. J. F., "Implications for Geophysics of the Precise Measurement of the Earth's Rotation," Science, Vol. 157, pp. 204–205, July 21, 1967.
- XI-5. Rennilson, J. J., Dragg, J. L., Morris, E. C., Shoemaker, E. M., and Turkevich, A., "Lunar Surface Topography," Surveyor I Mission Report. Part II: Scientific Data and Results, pp. 7–44, Jet Propulsion Laboratory, Pasadena, Calif., September 10, 1966.

Acknowledgment

We wish to thank Mr. Benjamin Milwitzky, *Surveyor* Program Manager, and Mr. Steve Dwornik, *Surveyor* Program Scientist, for endorsing the laser pointing test and for providing the support of the National Aeronautics and Space Administration, which made the test possible.

Because of the short time between the initiation and the execution of the laser pointing test, many people and organizations voluntarily participated under adverse conditions and without compensation at each of the six stations. The essential contributions of the following persons are gratefully acknowledged:

Tucson: Dr. James Brault, Staff Astronomer of the Kitt Peak National

Observatory, and Professor S. K. Poultney of the University of Maryland, using a Spectra-Physics Laser loaned by the Aero-

space Corp.

Wrightwood: Mr. M. S. Shumate, JPL, and Mr. J. W. Young, Table Mountain

Observatory, using a laser constructed and loaned by Hughes

Research Laboratories.

Waltham: Professor J. E. Faller, Wesleyan University, using a laser from

the laboratory of Dr. George De Mars, Raytheon Research Laboratory. Ten undergraduate students from Wesleyan University, led by Mr. D. Burstein, and Mr. M. Hulett assisted Professor

Faller.

Lexington: Dr. Robert Kingston and Dr. Hoyt Bostick, Lincoln Laboratories,

using a laser loaned by Spacerays, Inc.

Greenbelt: Dr. H. H. Plotkin, Mr. H. Richard, and Mr. W. Carrion of the

Optical Systems Branch, GSFC, using an existing laser satellite

tracking system incorporating an RCA laser.

Norwalk: Mr. H. Wishnia and Dr. Morley Lipsett of the Perkin-Elmer

Corporation, using a Perkin-Elmer laser and Mr. R. Perkin's

telescope.

The test would not have been possible without the integration mode of the *Surveyor* vidicon camera. Work that led to the incorporation of the integration mode into the camera was initiated by Mr. L. H. Allen, JPL, who also performed the vidicon sensitivity measurements at the ruby wavelength and assisted in the overall test operations.

Appreciation is expressed to all members of the *Surveyor* Project at the Jet Propulsion Laboratory for technical help in the organization and performance of the tests. Special appreciation is extended to the following JPL personnel involved in the television aspects of the mission: Mr. J. Strand, Mr. T. H. Bird, Mr. J. J. Rennilson, Mr. D. L. Smythe, and Mr. C. Chocol; and to Dr. R. Nathan and Mr. E. T. Johnson of the JPL Image Processing Laboratory.

XII. Astronomy

R. H. Norton (Chairman), J. E. Gunn, W. C. Livingston, G. A. Newkirk, and H. Zirin

Seven pictures of the solar corona were obtained during the period between 8 and 14 hr after sunset. As on earlier Surveyor missions, attempts were made to photograph the bright, inner K-corona immediately after sunset on the spacecraft, which occurred at 06:06 GMT on Day 023 (January 23, 1968). On this date, however, there was unusually low activity on the solar disk, so that the K-corona was much fainter than on previous missions. The spacecraft latitude and uneven terrain resulted in the eastern horizon remaining sunlit for several hours after the television camera had gone into shadow. As a result, the western horizon was illuminated by enough back-scattered light from the eastern horizon to swamp the faint corona.

The eastern horizon finally went into shadow 8 hr after sunset, leaving the western horizon illuminated only by earthshine; at this time, the first solar corona picture was taken. This picture (Fig. XII-1) was a 15-min integration at f/4 using the clear filter. The earthshine-illuminated horizon appears in the lower-left corner, and the bright object above the horizon is the planet Mercury.

Figures XII-2 and XII-3 show 30-min integrations at f/4 with polaroid filters; the polaroid in Fig. XII-3 is crossed with respect to the polaroid in Fig. XII-2. On this date, the angular distance between Mercury and the sun was 15 deg; the field of view of all three pictures is 25 deg, and the horizon eclipses the solar corona at about 2 deg, or 8 solar radii from the center of the solar disk. The solar corona may be seen out to 10 deg or 40 solar radii on any one of the 30-min integrations. With computer processing and addition of pictures, it may be possible to measure the coronal radiance out to 50 solar radii.

For comparison, ground-based eclipse observations of the outer corona are limited to about 10 solar radii by scattering in the earth's atmosphere. Ground-based observations of the zodiacal light are limited to about 50 to 60 solar radii by atmospheric extinction and scattering in the twilight atmosphere. The observations from *Surveyor VII*, therefore, are most significant in that they should permit the determination of how the solar F-corona merges into the zodiacal light.

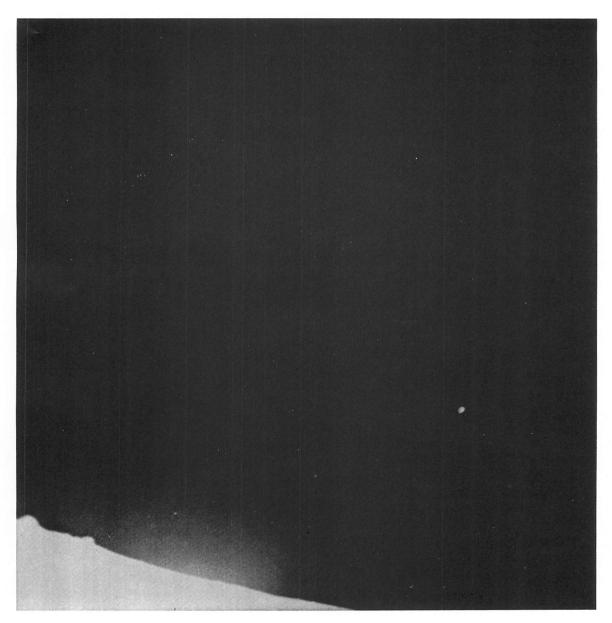


Fig. XII-1. A 15-min integration of the solar corona. The picture was taken at f/4 with the clear filter. The bright spot is the planet Mercury; its image is elongated because of the long exposure (Day 023, 14:46:08 GMT).

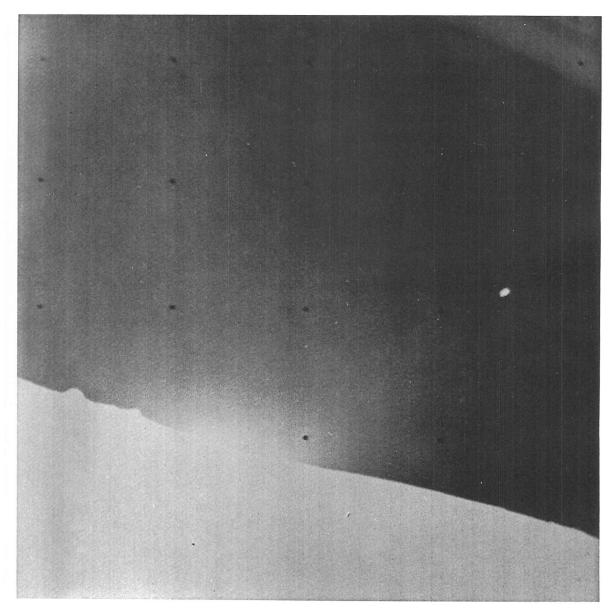


Fig. XII-2. A 30-min integration of the solar corona. The picture was taken at f/4 with a linear polarizing filter oriented parallel to the horizontal edge of the picture (Day 023, 15:23:13 GMT).

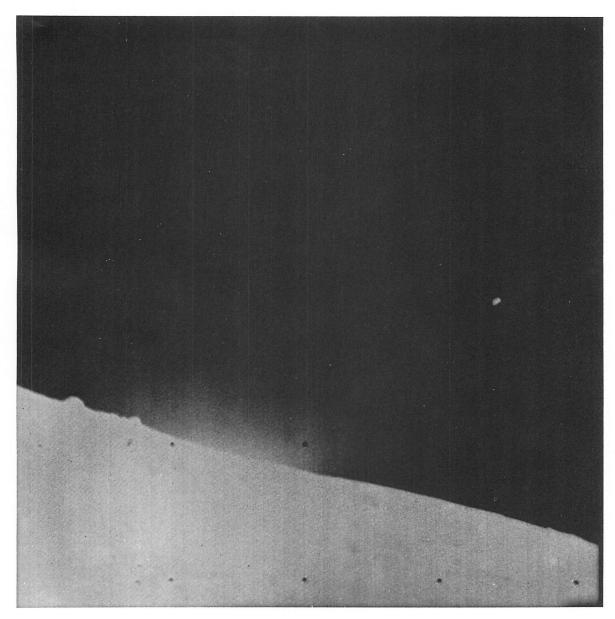


Fig. XII-3. A 30-min integration of the solar corona. The picture was taken at f/4 with a linear polarizing filter oriented parallel to the vertical edge of the picture (Day 023, 15:55:27 GMT).

Appendix

Surveyor Science Teams and Cognizant Personnel

Analysis of the scientific data for the *Surveyor VII* mission was conducted by the *Surveyor Scientific Evaluation Advisory Team*, Investigator Teams, and Working Groups. Membership for *Surveyor VII* was:

A. Surveyor Scientific Evaluation Advisory Team

C. O. Alley University of Maryland	
S. A. Batterson Langley Research Center	
E. M. Christensen Jet Propulsion Laboratory	
S. E. Dwornik NASA Headquarters	
D. E. Gault Ames Research Center	
J. W. Lucas Jet Propulsion Laboratory	
D. O. Muhleman California Institute of Technolo	gy
R. H. Norton Jet Propulsion Laboratory	
R. F. Scott California Institute of Technolo	gy
E. M. Shoemaker U. S. Geological Survey	
R. H. Steinbacher Jet Propulsion Laboratory	
G. H. Sutton University of Hawaii	
A. L. Turkevich University of Chicago	

B. Investigator Teams

1. Television

E. M. Shoemaker (Principal	U. S. Geological Survey
Investigator)	
R. A. Altenhofen	U. S. Geological Survey
R. M. Batson	U. S. Geological Survey
H. E. Holt	U. S. Geological Survey
G. P. Kuiper	University of Arizona
E. C. Morris	U.S. Geological Survey
J. J. Rennilson	Jet Propulsion Laboratory
E. A. Whitaker	University of Arizona

2. Alpha-Scattering

A. L. Turkevich (Principal Investigator)	University of Chicago
E. J. Franzgrote	Jet Propulsion Laboratory
J. H. Patterson	Argonne National Laboratory

3. Soil Mechanics Surface Sampler

son mechanics surrace sampler	
R. F. Scott (Principal Investigator)	California Institute of Technology
R. Haythornwaite	Pennsylvania State University
R. Liston	Detroit Arsenal

Appendix (contd)

C. Working Groups

1. Lunar Surface Thermal Properties

J. W. Lucas (Chairman)

Jet Propulsion Laboratory

J. E. Conel

Jet Propulsion Laboratory

Manned Spacecraft Center

Hughes Aircraft Company

W. A. Hagemeyer

H.C. Ingrao

Harvard College Observatory

B. P. Jones

Marshall Space Flight Center

J. M. Saari The Boeing CompanyG. Vitkus Northrop Corporation

2. Lunar Surface Electromagnetic Properties

D. O. Muhleman (Chairman) California Institute of Technology

W. E. Brown, Jr.

L. H. Davids

Jet Propulsion Laboratory

Hughes Aircraft Company

J. Negus de Wys

Jet Propulsion Laboratory

G. B. Gibson

Manned Spacecraft Center

W. H. Peake

Ohio State University

V. J. Poehls Ryan Aeronautical Company

3. Lunar Surface Mechanical Properties

E. M. Christensen (Chairman)
S. A. Batterson
H. E. Benson
R. Choate

Jet Propulsion Laboratory
Langley Research Center
Manned Spacecraft Center
Jet Propulsion Laboratory

R. E. Hutton TRW Systems

L. D. Jaffe Jet Propulsion Laboratory
R. H. Jones Hughes Aircraft Company
H. Y. Ko University of Colorado

R. F. Scott California Institute of Technology

F. Schmidt Bellcomm, Inc.

R. L. Spencer Jet Propulsion Laboratory
F. B. Sperling Jet Propulsion Laboratory
G. H. Sutton University of Hawaii

4. Astronomy

R. H. Norton (Chairman)

Jet Propulsion Laboratory

J. E. Gunn

Jet Propulsion Laboratory

W. C. Livingston

Kitt Peak National Observatory

G. A. Newkirk

High Altitude Observatory

H. Zirin Mt. Wilson and Palomar Observatories

Appendix (contd)

5. Lunar Theory and Processes

TORREST TORREST THE SECTION OF THE S	
D. E. Gault (Chairman)	Ames Research Center
J. B. Adams	Jet Propulsion Laboratory
R. J. Collins	University of Minnesota
T. Gold	Cornell University
J. Green	McDonnell Douglas Corp.
G. P. Kuiper	University of Arizona
H. Masursky	U. S. Geological Survey
J. A. O'Keefe	Goddard Space Flight Center
R. A. Phinney	Princeton University
E. M. Shoemaker	U. S. Geological Survey

University of California, San Diego

6. Laser Tests

H. E. Urey

C. O. Alley (Chairman)	University of Maryland
L. H. Allen	Jet Propulsion Laboratory
H. Bostick	Lincoln Laboratories
J. Brault	Kitt Peak National Observatory
D. G. Currie	University of Maryland
J. E. Faller	Wesleyan University
H. Plotkin	Goddard Space Flight Center
S. Poultney	University of Maryland
M. Shumate	Jet Propulsion Laboratory

The cognizant personnel of the various science and instrument aspects of the $Surveyor\ VII$ mission were:

D. Program and Project Scientists

S. E. Dwornik	Program Scientist
L. D. Jaffe	Project Scientist
R. H. Steinbacher	Associate Project Scientist
E. M. Christensen	Assistant Project Scientist

E. Cognizant Scientists and Science Staff

F. I. Roberson	Cognizant Scientist, Soil Mechanics Surface Sampler Experiment
E. J. Franzgrote	Cognizant Scientist, Alpha-Scattering
	Experiment
R. E. Parker	Alpha-Scattering Experiment
T. H. Bird	Cognizant Scientist, Television
	Experiment
J. J. Rennilson	Television Experiment
D. L. Smyth	Television Experiment
M. Benes	Television Experiment
	_

Appendix (contd)

J. N. Strand Television Science Data Handling

E. T. Johnson Cognizant Engineer, Image

Processing Laboratory

S. L. Grotch Non-Television Science Data Handling

C. H. Goldsmith Surveyor Experiment Test Laboratory

A. L. Filice Landing Sites

F. Instrument Development

D. H. Le Croissette Manager, Instrument Development

C. E. Chandler Project Engineer, Instruments

R. J. Holman Cognizant Engineer, Alpha-Scattering

Instrument

M. I. Smokler Supervisor and Cognizant Engineer,

Television Instrument

E. R. Rouze Cognizant Engineer, Soil Mechanics

Surface Sampler

G. Space Science Analysis and Command

J. N. Lindsley Director

D. D. Gordon Assistant Director

R. C. Heyser Director, Television Performance

Analysis and Command

D. L. Smyth Director, Television Science

Analysis and Command

E. J. Franzgrote Director, Alpha-Scattering Analysis

and Command

F. I. Roberson Director, Surface-Sampler Analysis

and Command

C. R. Heinzen Command Controller